



HAL
open science

Model based localization and estimation of an ellipsoidal object using artificial electric sense

Sylvain Lanneau

► **To cite this version:**

Sylvain Lanneau. Model based localization and estimation of an ellipsoidal object using artificial electric sense. Robotics [cs.RO]. Ecole nationale supérieure Mines-Télécom Atlantique, 2017. English. NNT : 2017IMTA0030 . tel-01713048

HAL Id: tel-01713048

<https://theses.hal.science/tel-01713048v1>

Submitted on 20 Feb 2018

HAL is a multi-disciplinary open access archive for the deposit and dissemination of scientific research documents, whether they are published or not. The documents may come from teaching and research institutions in France or abroad, or from public or private research centers.

L'archive ouverte pluridisciplinaire **HAL**, est destinée au dépôt et à la diffusion de documents scientifiques de niveau recherche, publiés ou non, émanant des établissements d'enseignement et de recherche français ou étrangers, des laboratoires publics ou privés.

Thèse de Doctorat

Sylvain LANNEAU

*Mémoire présenté en vue de l'obtention du
grade de Docteur de l'École Nationale Supérieure Mines-Télécom Atlantique Bretagne-Pays de la
Loire
Label européen
sous le sceau de l'Université Bretagne Loire*

École doctorale : Mathématiques et STIC

Discipline : Automatique, productique et robotique, section CNU 61
Unité de recherche : Laboratoire des Sciences du Numérique de Nantes (UMR6004)

Soutenue le 04/10/2017
Thèse n° : 2017IMTA0030

Localisation et estimation basées modèle d'un objet ellipsoïdal avec le sens électrique artificiel

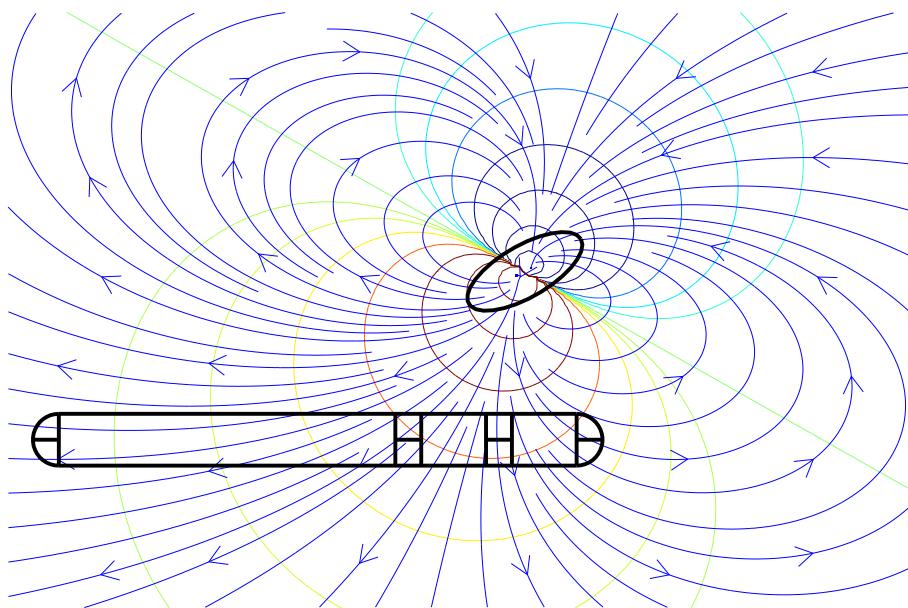
JURY

Rapporteurs : **M. Habib AMMARI**, Professeur, Eidgenössische Technische Hochschule, Zürich
M. Nicolas ANDREFF, Professeur, Institut Franche-Comté Electronique Mécanique Thermique et Optique - Sciences et Technologies, Besançon

Examineurs : **M. Stéphane VIOLET**, Directeur de recherche CNRS, Institut des Sciences du Mouvement, Marseille
M. Fabien CANDELIER, Maître de conférence, Institut Universitaire des Systèmes Thermiques Industriels, Marseille
M. Vincent CREUZE, Maître de conférence, Laboratoire d'Informatique, de Robotique et de Microélectronique de Montpellier
M. Luc JAULIN (PRÉSIDENT DU JURY), Professeur, Laboratoire des Sciences et Techniques de l'Information, de la Communication et de la Connaissance, Brest
M. François CHAUMETTE, Directeur de recherche INRIA, Institut National de Recherche en Informatique et en Automatique, Rennes

Invité :
Directeur de thèse : **M. Frédéric BOYER**, Professeur, Institut Mines-Télécom Atlantique, Nantes
Co-directeur de thèse : **M. Vincent LEBASTARD**, Maître assistant, Institut Mines-Télécom Atlantique, Nantes

Model based localization and estimation of an ellipsoidal object using artificial electric sense



Sylvain Lanneau

February 7, 2018

Et bien! en laissant errer cette imagination, en lui donnant la liberté de franchir les dernières bornes que voudraient lui prescrire la religion, la décence, l'humanité, la vertu, tous nos prétendus devoirs ; enfin, n'est-il pas vrai que ses écarts seraient prodigieux?

Donatien Alphonse François de Sade,
La philosophie dans le boudoir.

Remerciements

En premier lieu, je remercie mon directeur de thèse, Frédéric Boyer, pour son accueil dans l'équipe, pour la direction de mes travaux, pour la confiance et la grande liberté qu'il m'a accordées.

Je remercie aussi chaleureusement Vincent Lebastard, co-encadrant de ma thèse, pour sa disponibilité au quotidien, son écoute, sa patience et son soutien.

J'adresse mes sincères remerciements à Habib Ammari et Nicolas Andreff pour avoir accepté de lire cette thèse et d'en être les rapporteurs. Egalement, un grand merci à Fabien Candelier, François Chaumette, Vincent Creuze, Luc Jaulin et Stéphane Viollet pour avoir accepté d'être membre de mon jury de thèse.

J'ai une pensée particulière pour tous doctorants et post-docs que j'ai eu la chance de rencontrer à l'Ecole des Mines : Stéphane Bazeille, Bruce Ferrer, Axel Grimault, Renaud Henry, Léopold Houdin, Mohammad Maddah, Johan Mauny, et tous ceux que j'ai croisés sur ma route pendant cette thèse. C'est avec grand plaisir que j'ai partagé tous ces moments amicaux et philosophiques avec vous.

Je remercie aussi ceux avec qui j'ai travaillé sur des sujets autres que celui de cette thèse, mais qui ont significativement contribué à ma formation d'enseignant-chercheur : Philippe Chevrel, Fabien Claveau, Mathieu Porez et Mohamed Yagoubi, je vous remercie pour votre disponibilité, votre sympathie et pour ce que j'ai pu apprendre à vos côtés.

Egalement, je remercie sincèrement Gilles Chabert et Saïd Moussaoui pour avoir apporté leur expertise dans des moments-clés de mon travail de thèse.

Un grand merci au personnel de l'Institut Mines-Télécom Atlantique pour leur aide au quotidien, leur disponibilité et leur sympathie. Je remercie particulièrement Delphine Turlier et l'ensemble du personnel du centre de documentation.

Merci à tout mon entourage et mes amis, qui ont dû subir parfois les effets secondaires de cette thèse.

Enfin, je tiens à remercier Florian Lacroix et Matthieu Lescieux, pour leur coup de pouce sans lequel je n'aurais pas pu réaliser mon projet de thèse.

Contents

Résumé	4
1 Introduction and overview	12
1.1 State of the art	13
1.1.1 Underwater robotics	13
1.1.2 Underwater perception systems	14
1.1.3 Bio-inspiration	16
1.1.4 Active electro-sensing	16
1.1.5 Fish's performances	27
1.1.6 Technological applications of active electro-sensing	28
1.2 Addressed problem and contributions	33
2 Sensor, test bed and scene	36
2.1 Tank and Cartesian robot	36
2.2 Scene parametrization	38
2.3 Sensor's kinematics model	40
2.4 Sensor	42
2.4.1 Sensor's structure and dimensions	42
2.4.2 Implementation of the active electro-sensing	43
2.5 Currents measurements in practice	49
2.5.1 Noise characterization	49
2.5.2 Fly-by test	50
2.5.3 Object's support effect	52
2.5.4 Aquarium effects	55
3 Physics and models	57
3.1 The active electrolocation direct problem formulation	57
3.1.1 The electric potential in domains	59
3.1.2 Boundary conditions	61
3.2 Solving the direct problem	65
3.2.1 Boundary integral formulation	65
3.2.2 Boundaries discretization and direct problem solving	66
3.3 Analytical direct model	68
3.3.1 Axial and lateral currents	68
3.3.2 Model for the emission (Step 0)	70
3.3.3 Model for the 1 st reflexion (Step 1)	72
3.3.4 Model for the 2 nd reflexion (Step 2)	77
3.3.5 Currents model in polar coordinates	78

4	Object's inspection	81
4.1	Object's detection	81
4.2	Material discrimination	82
4.3	Left/right discrimination	83
4.4	Seek the object	84
4.4.1	Spherical objects	86
4.4.2	Ellipsoidal objects	87
4.4.3	First transition: stop while facing the object	88
4.5	Flee from the object's influence	90
4.6	Following the object's boundaries	92
4.7	Experimental implementation of the overall strategy	92
5	Localization	96
5.1	Principle of MUSIC algorithm	97
5.2	Implementation of MUSIC algorithm with analytical model data	100
5.3	Implementation of MUSIC algorithm with BEM data	102
5.3.1	Evaluation of a favorable area for the localization	103
5.3.2	Error behavior with respect to the object's properties	105
5.4	Implementation of MUSIC algorithm with experimental data	108
5.4.1	From small to large objects	109
5.4.2	New localization strategy for large objects	110
6	Shape estimation	114
6.1	Principle of the shape estimation algorithm	114
6.1.1	Step one : Estimation of the object's polarization tensor	115
6.1.2	Step two : Object's shape parameters estimation	118
6.2	Implementation of the shape estimation with BEM data	120
6.2.1	Neither localization error nor measurement noise	120
6.2.2	With localization errors and no measurement noise	122
6.2.3	With measurement noise and no localization error	125
6.3	Shape estimation with experimental data	126
6.3.1	Evaluation of the influence of the localization uncertainty on the shape estimation	130
6.3.2	Improved shape estimation strategy	132
7	Conclusion	134
A	Dielectric properties of materials	A1

Résumé

Les animaux et les hommes sont capable de se repérer, d'agir, de se déplacer et de réaliser des tâches complexes, y compris dans des environnements a priori inconnus. Cette capacité à continuellement adapter son comportement à la situation courante est remarquable. Dans le domaine de la robotique, une telle capacité d'adaptation est encore loin d'être atteinte et les robots d'aujourd'hui souffrent d'un manque d'indépendance dès que la tâche à réaliser n'est pas élémentaire ou lorsque l'environnement n'est pas bien connu [52, 68]. Comme l'animal qui possède des sens pour extraire de l'information de son environnement, un robot autonome a besoin de ses propres moyens de perception. Dans le cas particulier des robots sous-marins, il y a nombreux avantages à utiliser des robots autonomes, comme leur faible coût par rapport à une intervention humaine, une logistique réduite et une absence de risque pour le plongeur [20]. Quelques unes des principales applications sont donnée table 1.1. Les technologies employées le plus communément pour la perception sous-marine sont l'écholocation (sonar) [41, 65] et la vision par caméra [20, 47]. Souvent, ces deux technologies cohabitent [41]. Mais nous savons aussi que dans le cas d'eaux turbides et de milieux encombrés, ces technologies deviennent inopérantes [41, 92]. Or, depuis les années 1950, les biologistes étudient des espèces de poisson qui s'accommodent très bien de ces conditions, grâce à un mode de perception appelé *sens électrique* [61, 62]. Le principe de ce sens est de mesurer les distorsion d'un champ électrique auto-généré, ces distorsions étant façonnées par l'environnement proche.

C'est dans ce cadre que s'inscrit cette thèse. Le problème considéré est celui de l'implémentation de nouveaux algorithmes sur un capteur inspiré des poissons électriques, dans le but d'inspecter d'un objet ellipsoïdal et d'estimer sa localisation et sa forme. La stratégie proposée est représentée figure 1.28. Les résultats de ces travaux ont fait l'objet de publications [53, 54, 56].

Du sens électrique biologique au sens électrique artificiel

Les poissons électrique peuvent polariser leurs corps grâce à un organe dédié [70, 85]. Il en résulte un champ électrique dans l'environnement proche, dans un rayon de l'ordre de la longueur du poisson, soit $\simeq 10\text{cm}$. Ce champ, dit basal, est perturbé par la présence d'objets dans l'environnement [6, 49, 76], comme illustré figure 1.7b. Un des premiers modèles de perturbation a été proposé par Rasnow [75] (1.1). La perturbation du champ est perçue par le poisson grâce à des électrorécepteurs dispersés sur sa peau [15, 49, 70]. Il se forme ainsi une image électrique la peau de l'animal [93, 94, 28], qu'il sait décoder. Notamment, il a été démontré que le poisson utilise la position de la valeur maximale de l'image électrique sur son flanc ainsi que le rapport

entre la pente maximale de l'image et sa valeur maximale [34, 98]. Aussi, nous savons que le poisson utilise le déplacement conjointement à la perception, dans une boucle sensorimotrice [33, 90], représentée figure 1.15. De nombreuses études ont permis d'étudier les performances du poisson en terme de reconnaissance d'objet [80, 94, 95, 96, 97] et montrent que le poisson discrimine différentes formes d'objets, indépendamment du matériau.

Depuis la fin des années 1990, des chercheurs se sont inspirés du sens électrique des poissons afin de développer de nouveaux capteurs pour la robotique sous-marine, ainsi que des algorithmes associés. Les premiers capteurs étaient particulièrement élémentaires : de simples électrodes ponctuelles ou sphériques plongées dans l'eau [19, 66, 73, 83]. Grâce à des algorithmes de type filtre particulaire [83] ou beamforming [73], des techniques d'évitement d'obstacle et de localisation d'objets sphériques ont pu être mises en oeuvre. Puis, des capteurs intégrés ont été développés, permettant de naviguer dans un environnement complexe [13, 14, 25, 26, 57], ou de reconstruire une scène composée de murs et d'objets sphériques [8, 59]. Récemment, il a été démontré expérimentalement que l'on peut reconstruire un objet ellipsoïdal avec le sens électrique artificiel [9].

Le capteur, l'aquarium, le robot et les objets

Le capteur utilisé dans cette thèse est présenté figure 1.25. Il est plongé dans un aquarium cubique de 1m de côté, surmonté d'un robot cartésien qui possède trois degrés de liberté : deux translations horizontales et une rotation autour de l'axe vertical, voir figure 2.1a. Le système d'acquisition de données contrôle la position et/ou la vitesse des trois degrés de liberté grâce à des codeurs angulaires montés sur chaque axe. Le capteur est lié au robot par un tube rigide vertical. Puisque le capteur est fixé orthogonalement au tube rigide, il se trouve dans le plan horizontal et ses mouvements sont contrôlés par le robot dans ce plan, comme illustré figure 2.1b. Le paramétrage de la pose du capteur est donnée figure 2.2 et est connu à tout instant. Le modèle cinématique du mouvement du capteur est donné dans la section 2.3.

Des objets de différentes formes, tailles et matériaux peuvent être placés dans l'aquarium, représentés figure 2.3, et leurs caractéristiques sont données dans la table 2.1. Le maintien en position des objets est réalisé avec des fils de Nylon. Il est démontré dans la section 2.5.3 que leur effet sur les mesures est négligeable.

Les caractéristiques techniques du capteur sont détaillées section 2.4. Il est de forme cylindrique, et supporte quatre macro-électrodes, chacune d'elles étant composée de deux électrodes respectant une symétrie gauche/droite. Chaque macro-électrode peut être soumise à un potentiel électrique par rapport aux trois autres, offrant la possibilité de créer quatre champs différents, représentés figure 2.9. D'autre part, il est possible de mesurer les courants électriques traversant chacune des six électrodes de références indépendamment. Le tableau 2.2 résume les configurations de mesures possibles.

Ensuite, une étude démontrant le caractère résistif de la scène lorsqu'elle est composée d'objets conducteur et isolants est présentée. Seuls les objets dont les caractéristiques diélectriques sont suffisamment proches de celles du milieu conducteur sont susceptibles de produire un déphasage entre le signal de polarisation et les courants mesurés, ces objets n'étant pas étudiés dans cette thèse.

Enfin, un test standard, dit "fly-by test", ou "test à la volée", est décrit. Il consiste en un passage du capteur devant l'objet, en ligne droite et à vitesse constante. Ce test sera utilisé lors de la localisation de l'objet (chapitre 5) et pour l'estimation de forme (chapitre 6).

Physique et modèles du problème direct

Les équations du problème direct de l'électrolocation active sont celles de l'électrostatique [30, 31, 42]. Afin d'établir ces équations, nous partons des équations de Maxwell, que nous pouvons simplifier compte tenu des conditions particulières de notre problème : 1) chaque domaine de la scène est composé d'un matériau linéaire, homogène et isotrope (plastique ou métal) ; 2) le milieu conducteur est de l'eau du robinet dans lequel la loi l'Ohm est satisfaite ; 3) la fréquence du signal d'excitation est de 22.5kHz. Dans ces conditions, nous sommes dans le cas d'un problème d'électrostatique formulé en terme de potentiel électrique ϕ

$$\Delta.\phi = 0, \tag{1}$$

où Δ représente l'opérateur Laplacien. Cette équation n'est valide qu'à l'intérieur de chaque domaine. Les conditions de passage du champ électrique aux interfaces entre les objets et l'eau donnent les conditions aux limites. Ainsi, l'équation (1) peut être résolue. En pratique, nous utilisons la méthode numérique BEM (boundary elements method) [63]. Les courant traversant les électrodes peuvent ensuite calculés par application de la loi d'Ohm. Le modèle BEM constitue notre premier modèle des courant mesurés pour une scène donnée.

Avec des hypothèses supplémentaires, il est possible d'obtenir un modèle simplifié du problème direct [12]. Ces hypothèses sont les suivantes : 1) le capteur a une forme cylindrique et sa longueur est grande vis-à-vis de son diamètre ; 2) il y a un seul objet ellipsoïdal en présence du capteur ; 3) la distance de l'objet au capteur est grande vis-à-vis du diamètre du capteur ; 4) la dimension de l'objet est au plus celle du rayon du capteur ; 5) le capteur et l'objet sont dans le même plan horizontal. Dans ces conditions, la réponse électrique de l'objet est approximée par celle d'un dipôle, et que l'on modélise par un tenseur d'ordre 2, dit tenseur de polarisation de Polya-Szego [88]. Dans la base propre de l'objet il est représenté par une matrice diagonale de dimension $[3 \times 3]$ dont les coefficients s'expriment en fonction des propriétés géométriques de l'objet et de son matériau [5, 44]. L'expression de ces coefficients est décrite dans la section 3.3.3. Grâce à l'hypothèse d'une réponse dipolaire de l'objet, il est possible de définir deux courants pour chaque macro-électrode $k = \{1, \dots, 4\}$, nommés courant latéral et courant axial et respectivement notés $I_{lat,k}$ et $I_{ax,k}$. Le courant $I_{lat,k}$ est proportionnel à la composante normal de champ électrique provenant de l'objet polarisé, et $I_{ax,k}$ est l'image d'une polarisation axiale du capteur, sous l'effet du champ généré par l'objet. Voir les figures 3.4a et 3.4b. Ainsi, le second modèle décrit les courants $I_{lat,k}$ et $\delta I_{ax,k}$, $\forall k = \{1, \dots, 4\}$, il est appelé modèle analytique et est décrit par les expressions (3.93) et (3.97).

Sur la figure 3.9 sont superposés les courants latéraux et axiaux mesurés, calculés avec le modèle BEM et calculés avec le modèle analytique lors d'un passage en ligne droite du capteur le long d'un objet fixe.

Les algorithmes présentés dans cette thèse s'appuient sur le modèle analytique. Le modèle BEM sera particulièrement utile pour tester ces algorithmes en simulation.

Inspection d'objet

Nous considérons comme point de départ la situation dans laquelle le capteur navigue dans un environnement inconnu. Nous proposons ici plusieurs algorithmes qui permettent au capteur de détecter la présence d'un objet, d'adapter sa trajectoire afin de se diriger vers lui et de tourner autour de celui-ci. Également, nous montrons que le matériau et la position de l'objet par rapport à l'axe du capteur peuvent être discriminés. En résumé, le terme "inspection d'objet" est utilisé pour regrouper ces différentes tâches

1. détection d'objet,
2. discrimination du matériau de l'objet,
3. discrimination de la position de l'objet par rapport à l'axe du capteur,
4. se diriger vers l'objet et tourner au tour de celui-ci.

Les trois premières tâches correspondent à trois algorithmes simples qui consistent à vérifier si certaines valeurs de courant sont nulles, positives ou négatives. La quatrième tâche est réalisée grâce à un algorithme plus complexe, divisé en trois phases, et en partie inspiré du comportement du poisson électrique lorsqu'il se dirige vers une proie, représenté figure 1.14 et étudié dans [70, 78]. Les trois phases de l'algorithme sont représentées figures 4.2a et 4.2b. Chacune d'elle est réalisée de façon autonome grâce à une loi de contrôle proportionnelle. Pendant la première phase, le capteur s'approche de l'objet en suivant les lignes de champ créées par ce dernier et s'arrête à une distance donnée de l'objet. Lors de la seconde phase, le capteur effectue une rotation autour de l'axe vertical jusqu'à ce que l'effet de l'objet mesuré sur les deux électrodes aux extrémités du capteur soient égales. La troisième phase consiste pour le capteur à effectuer une rotation autour de l'objet.

Nous montrons expérimentalement que cet algorithme d'inspection est implémentable avec des objets sphéroïdaux et ellipsoïdaux (cf. figure 4.12), mais aussi avec des murs isolants (cf. figure 4.13). Composé de trois simples lois de contrôle proportionnelles et de simples détections de seuil sur les mesures, cet algorithme ne nécessite que de très faibles ressources en terme de calcul. De plus, il ne requiert aucun modèle physique. C'est un avantage pour une implémentation en temps-réel sur un robot autonome. Notons que la géométrie du capteur est essentielle : c'est la symétrie axiale qui permet de suivre les lignes de champ, et la position de la seconde macro-électrode (\mathcal{E}_2 figure 2.8) est un paramètre clé pour la distance d'arrêt lors de la première transition.

Cette inspection d'objet est particulièrement intéressante pour l'exploration et la reconstruction d'une scène avec le sens électrique. Cependant, elle ne permet pas de localiser précisément l'objet, ni de décrire sa forme. C'est pourquoi nous proposons dans les deux chapitres suivants d'autres algorithmes afin de traiter ces problèmes de localisation et d'estimation de forme.

Localisation

D'après les résultats présentés dans le chapitre précédent, nous pouvons considérer qu'un objet dans l'environnement du capteur a été détecté, son matériau et sa position par rapport à l'axe

du capteur discriminés. A ce stade, le problème consiste à localiser et à estimer ses propriétés géométriques. Ces deux tâches peuvent être découplées grâce à la mise en oeuvre de l'algorithme MUSIC (multiple signal classification). Ainsi, nous présentons ici la localisation du centre de l'objet avec MUSIC, indépendamment des propriétés géométriques. Les estimations de forme et d'orientation seront réalisées avec un second algorithme, présenté dans le chapitre 6. Un schéma de ce processus est donné figure 5.1. Cette stratégie en deux temps a été proposée par [2, 11] dans un contexte de modélisation du poisson électrique et a montré sa pertinence.

Nous montrons d'abord qu'il est possible d'implémenter MUSIC sur notre capteur grâce à des résultats obtenus en simulation. Cependant, en conditions expérimentales, il est particulièrement difficile de respecter les hypothèses du modèle. En particulier, des objets de volume suffisamment important doivent être utilisés. Ces conditions expérimentales n'étant plus en accord avec les hypothèses du modèle, nous montrons la difficulté de l'implémentation de l'algorithme. Nous mettons en évidence que c'est la non uniformité du champ basal dans l'objet qui fait chuter les performances de localisation. Cette non uniformité fait apparaître la composante quadrupolaire dans l'expression de la réponse de l'objet et qui n'est pas prise en compte dans le modèle analytique. Par conséquent, l'algorithme localise la partie de l'objet qui est soumise au champ basal le plus intense, c'est à dire, la partie de l'objet la plus proche du capteur. Egalement, le bruit de mesure et d'autres incertitudes expérimentales inévitables mènent à réduire la zone favorable, située face aux électrodes \mathcal{E}_1 to \mathcal{E}_3 . Parce qu'il est important que l'objet se trouve dans cette zone pour avoir l'erreur de localisation la plus faible, nous proposons dans la suite une stratégie basée sur des mouvements du capteur qui assurent cette situation. De plus, nous proposons une méthode basée sur la répétition de cette procédure quatre fois selon une trajectoire particulière autour du capteur. Ensuite, en prenant le barycentre de ces quatre localisations, nous obtenons une erreur de localisation significativement réduite, inférieure à 3mm pour des objets dont la taille est de l'ordre de 40 à 60mm.

Estimation de forme

D'après la stratégie représentée figure 5.1, nous devons à présent résoudre le problème de l'estimation de forme, compte tenu des courants mesurés et possédant une estimation de localisation. Ceci est en accord avec la stratégie utilisée par le poisson, qui est capable de séparer les tâches de localisation et d'estimation de la taille de l'objet, comme présenté dans la section 1.1.4.

Dans ce chapitre, nous prenons comme hypothèse de départ que le matériau de l'objet a été discriminé et sa localisation estimée en utilisant les algorithmes présentés dans les chapitres 4 et 5 respectivement. Si on se réfère au paramétrage de la scène donné sur les figures 2.4 et 2.5, les trois paramètres restant à estimer pour une complète reconstruction de scène sont les demi-axes a et b , ou bien, de manière équivalente, le volume \mathcal{V} et l'aspect ratio η , ainsi que l'angle entre l'axe principal du capteur et l'axe principal de l'ellipse, noté θ_o^c . L'algorithme qui permet d'estimer ces paramètres a été initialement proposé dans [2, 11], dans le cas de la modélisation du poisson électrique. Il est possible de le décomposer en deux étapes

Etape 1 Estimation du tenseur de polarisabilité de l'objet P_{11}^c , dont les composantes apparaissent explicitement dans le modèle des courants (3.96) et (3.101), grâce à un algorithme d'optimisation.

Etape 2 Estimation des paramètres \mathcal{V} , η et θ_o^c en utilisant le tenseur estimé à l'étape 1 et en inversant son expression analytique (3.84).

Cet algorithme a été implémenté en conditions expérimentales pour 7 distances latérales (entre 50mm et 110mm), 5 orientations de l'ellipsoïde (entre -30° et 90°) et pour quatre ellipsoïdes (objets 4 à 7 figure 2.3). Les résultats d'estimation de forme sont donnés dans les tableaux de la figure 6.9. Les distributions des erreurs sur l'estimation de forme proprement dite (erreur sur η et \mathcal{V}) et sur l'angle d'orientation (θ_o^c) sont données figures 6.11a et 6.11b respectivement. L'erreur de forme moyenne est de 16% et l'erreur maximale est de 47.7%. Pour l'erreur d'angle, on constate une valeur moyenne de 25° , et avec une étendue particulièrement importante, entre 0.2° et 85.7° .

Afin de réduire ces erreurs, un aménagement de l'algorithme est proposé. Il consiste à découpler l'estimation d'angle de celle de forme en alignant de façon automatique le capteur avec le petit axe de l'ellipsoïde. L'idée d'un tel alignement a été initialement proposée dans [9], implémenté en tant que séquence discrète de déplacements successifs. Ici, cette manœuvre est réalisée par une loi de commande réactive, du même type que celles qui sont présentées dans le chapitre 4. Une fois cet alignement réalisé, l'orientation de l'objet est connu. Ensuite, l'algorithme d'estimation de forme présenté ci-dessus est mis en œuvre, avec cette fois seulement deux paramètres à estimer (η et \mathcal{V}). Il s'ensuit une meilleure estimation de forme, avec une erreur moyenne inférieure à 15% lorsque l'objet se situe à une distance latérale entre 50mm et 90mm, voir figure 6.15.

Conclusion

Dans cette thèse, nous avons proposé de nouvelles méthodes pour l'inspection, la localisation et l'estimation de forme d'objets ellipsoïdaux en utilisant un capteur inspiré des poissons faiblement électriques. Nous avons montré leur pertinence à la fois en simulation et en conditions expérimentales.

Dans le chapitre 4, nous avons d'abord montré que l'objet pouvait être détecté, son matériau discriminé ainsi que sa position par rapport à l'axe du capteur. Ensuite, trois lois de contrôle ont été implémentées de sorte que le capteur se dirige vers l'objet et tourne autour de celui-ci en suivant ses frontières, en tirant partie de la symétrie axial du capteur. De plus, cet algorithme a été testé expérimentalement avec d'autres objets (cube et mur), démontrant ainsi sa polyvalence.

Afin de localiser l'objet, nous avons utilisés l'algorithme MUSIC. Les résultats sont présentés dans le chapitre 5. En faisant le choix d'utiliser des objets plus grands que les hypothèses de notre modèle ne le permettent, nous avons montré la difficulté d'obtenir une localisation précise. Nous avons clairement identifié la non uniformité du champ électrique basal dans l'objet cause de grandes imprécisions. Cependant, en utilisant des mouvements du capteur et quatre implémentations de MUSIC, nous avons pu obtenir une erreur de localisation inférieure à 3mm pour des objets dont la taille est de l'ordre de 40 à 60mm.

La forme et l'orientation ont été finalement estimés avec un algorithme basé sur les moindres carrés et sur l'inversion du modèle analytique du tenseur de polarisation de l'objet (chapitre 6). Grâce aux nombreux essais expérimentaux que nous avons mis en œuvre, nous avons extrait certaines tendances sur le comportement de l'algorithme. En particulier, nous avons montré qu'il

y a un intervalle favorable en terme de distance latérale dans laquelle l'estimation de forme est la meilleure : [60mm;100mm]. En dessous de 60mm, le modèle analytique n'est pas assez précis pour fournir de bonnes estimations. Au-delà de 100mm, le manque de précision vient de la faiblesse de la réponse électrique de l'objet par rapport au niveau de bruit. Si la distance latérale de l'objet est dans cet intervalle, l'erreur moyenne sur l'estimation de forme et sur l'estimation d'angle sont de 15.1% et 23.6° respectivement. Egalement, la difficulté pour obtenir une estimation d'angle précise avec cette méthode a été soulignée, en particulier pour les objets dont l'aspect ratio est de 1.5, c'est à dire proches d'une sphère. Une stratégie d'amélioration a été proposée, consistant à aligner l'axe du capteur avec le petit axe de l'ellipsoïde grâce à une loi de contrôle réactive. Alors que cette stratégie a besoin d'être validée expérimentalement, elle permettrait de descendre l'erreur de forme à 10.3%.

Ces résultats sont particulièrement encourageants pour la recherche dans le domaine du sens électrique. Les difficultés rencontrées pour l'implémentation expérimentale des méthodes proposées ont été mises en évidence. C'est pourquoi nous proposons en conclusion quelques thèmes de recherches à partir des résultats que nous avons obtenus.

Une des plus grandes difficultés de ce travail a été de gérer l'écart entre les courants calculés avec modèle analytique et les courants mesurés. Parce qu'il est difficile de respecter les hypothèses du modèle dans les conditions expérimentales (petitesse de l'objet), cet écart peut être grand et les résultats finaux en souffrent. Une première idée consisterait à affiner le modèle analytique ne lui ajoutant la composante quadrupolaire.

Pour la localisation avec MUSIC, cette contribution supplémentaire nous amènerait à définir de nouveaux steering vectors, associés à cette contribution. Nous suggérons pour les travaux futurs de calculer ces vecteurs et de définir la fonction coût associée.

Pour l'estimation de forme, parce que nous n'avons pas d'expression analytique du moment quadrupolaire, il ne serait pas possible d'utiliser directement le tenseur P_{22} comme nous l'avons fait avec le tenseur P_{11} . Mais le principe des moindres carrés pourrait être conservé, cette fois pour estimer les composantes de P_{11} et de P_{22} . On pourrait ainsi espérer une amélioration de l'estimation des composantes de P_{11} . Ensuite, la seconde phase de l'algorithme ne serait pas modifiée. La meilleure estimation de P_{11} pourrait mener à une meilleure estimation des paramètres géométriques.

En lieu et place d'une estimation de forme basée sur un modèle analytique, un autre paradigme pourrait être celui la reconnaissance de forme, par l'utilisation d'un dictionnaire faisant le lien entre un objet et un tenseur. Cette stratégie diffère significativement de celle qui a été proposée car la forme n'est pas estimée mais plutôt identifiée. Ceci a déjà été implémenté dans le domaine des mathématiques appliqués [4, 3, 11, 46]. Le dictionnaire pourrait être construit dans un premier temps grâce à la BEM et/ou à des mesures expérimentales et enregistrées dans la mémoire du robot. Ensuite, la méthode des moindres carrés pourrait être utilisée pour estimer les composantes du tenseur et la forme serait finalement identifiée par lecture dans ce dictionnaire.

Enfin, nous proposons une autre amélioration qui pourrait mener le système à un autre niveau d'autonomie. Bien que les algorithmes ont été présentés et implémentés de façon séquentielle (voir 1.28), ils pourraient facilement être implémentés l'un après l'autre dans cet ordre, dans une procédure totalement autonome. Nous avons donné dans cette thèse quelques prémices pour mettre ceci en oeuvre, qu'il serait particulièrement intéressant de tester en conditions expérimentales. Une variante de cette stratégie consisterait à fusionner les trois phases : inspection, localisation

et estimation de forme. La localisation et l'estimation de forme pourraient être réalisés pendant la phase d'inspection. En effet, si les mesures de la matrice δC peuvent être réalisées en continu pendant la trajectoire autour de l'objet, alors le principe des quatre localisations présenté dans le chapitre 5 serait applicable, éventuellement avec plus que quatre points. Egalement, avec un enregistrement continu des courants pendant le déplacement, l'algorithme des moindres carrés pourrait être implémenté et enfin, la forme estimée. L'objet serait alors localisé et sa forme estimée, simultanément avec la rotation du capteur autour de celui-ci.

Chapter 1

Introduction and overview

Animals and humans easily get their bearings, act, travel and perform complicated tasks in an unknown environment. This capacity to continuously and autonomously adapt its behavior to the current situation is remarkable. In the field of robotics, such a talent nowadays represents a Holy Grail, far from being reached yet. Instead, today's robots suffer from a significant lack of independence as soon as the task to perform is not basic or when the environment is not well known [52, 68]. The quest of autonomy for the robots go with researches in the field of world's perception. Indeed, just like an animal which possess senses to get information from its environment, an autonomous robot needs its own means of perception.

Particularly for underwater robots, the perception of the environment is generally performed using camera or acoustic systems (sonar), which allows self localization, cartography, obstacles' detection and objects' identification [22, 41]. The first part of this chapter is dedicated to the presentation of the main underwater robotics applications and related sensory systems.

But there exist some conditions in which vision and sonar become less efficient: turbid water [41] and cluttered environment [92]. A turbid water significantly perturbs the propagation of light which affects sensing by vision, and cluttered environments favor multiple propagation paths, which are challenging to deal with [1].

That is why, since two decades, researchers in the field of underwater robotics are interested in another perception modality which already exists in some fish species and do not suffer from these drawbacks. Named as the *electric sense*, or *active electro-sensing*, it is based on the measurements of the distortions of a self-generated electric field. It was discovered by biologists in the 50's [61, 62] and since then, it was extensively studied in the biology community [15, 49, 70]. In the second part of this chapter, the biological principles of the electric sense are developed, as well as the fish's performances in term of environment reconstruction.

In the 90's, a first device inspired by the electric sense was developed for obstacle avoidance [19, 29]. Since that time many other devices and associated algorithms were designed for obstacle avoidance and object's localization and shape estimation. The third part of this chapter is dedicated to introduce them.

Once these fundamentals will be given, the last part of this chapter introduces the problem that

is addressed in this thesis. It consists in describing the implementations of new algorithms on a sensor inspired by the electric fish for ellipsoidal object's inspection, localization and shape estimation.

1.1 State of the art

In this state of the art we firstly introduce some underwater robotics applications and the most commonly used perception systems in this field. We then show that in some cases these technologies are not well adapted and fail to provide accurate information of the environment. In order to find new technological solutions to that issue, one of the approaches is the bio-inspiration. It consists in taking inspiration from the nature for the purpose of designing new concepts and technological solutions. We firstly describe what a biological sensory system is in general and then introduce the active electric sense, a perception modality that some fresh water fish possess. Then, we show how this sense is part of a perception-behavior feedback loop. Finally, the bio-inspired applications of the electric sense are presented.

1.1.1 Underwater robotics

In the field of unmanned underwater vehicles, we can distinguish between ROV (Remotely Operated Vehicle) and AUV (Autonomous Underwater Vehicle). ROVs are hardwired linked to the surface from which it is controlled. On the other hand, AUVs are self-propelled and behaves according to preprogrammed scenario or real time adaptive control [20]. See examples of ROVs and

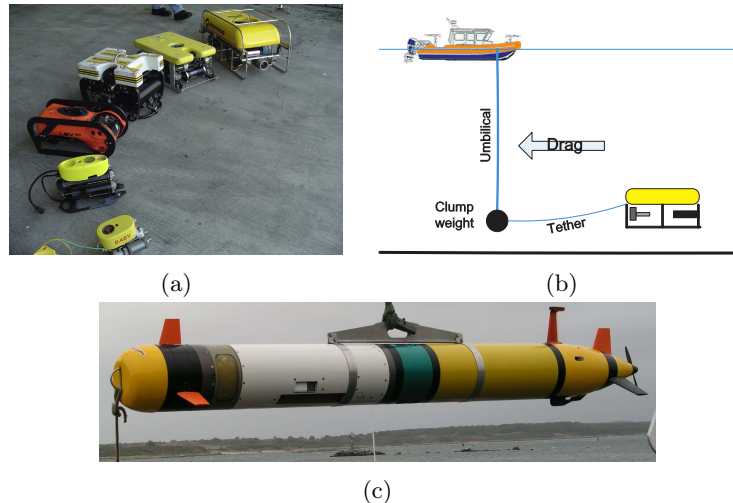


Figure 1.1: (a) Examples of ROVs, taken from [20]. (b) A ROV linked to the boat from which it is operated. A clump weight can be used to reduce perturbations due to the drag force, taken from [20]. (c) The REMUS 600 AUV, carrying mine countermeasures sensors, taken from [86].

AUV in figure 1.1. The advantages of using ROV or AUV are its lower cost compare to manned submersibles or divers, its lower requirements in term of logistics and absence of risk for human

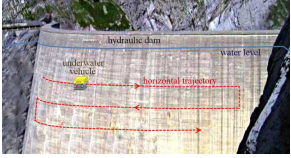
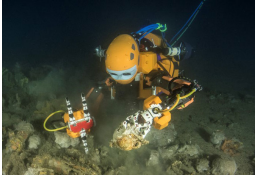
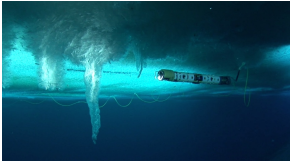
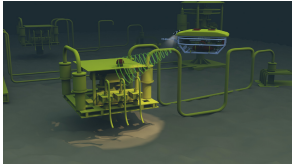
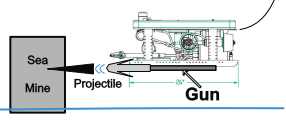
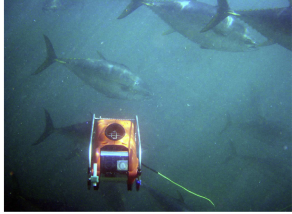
<p>Ship hull and hydraulic dam inspection</p> <p>Following the wall, checking for cracks or weaknesses [23, 38, 65]</p>  <p>Taken from [65].</p>	<p>Archeology</p> <p>Replacing underwater archaeologists in deep-sea [84].</p>  <p>Taken from [84].</p>
<p>Under sea ice exploration</p> <p>Making observations and measurements of biodiversity [18, 74]</p>  <p>Taken from [18].</p>	<p>Oil and gas exploitation</p> <p>Surveying and performing maintenance tasks for sub-sea systems, inspecting pipelines and cables [20, 41].</p>  <p>Taken from [20].</p>
<p>Sea mine countermeasures</p> <p>Detecting and neutralizing underwater unexploded ordnance [20, 86]</p>  <p>Taken from [20].</p>	<p>Fisheries and aquaculture</p> <p>Reducing fish farming constraints and costs [20].</p>  <p>Taken from [20].</p>

Table 1.1: A non-exhaustive list of underwater robots applications.

beings. There exist plentiful practical applications for underwater robotics. The most common ones are presented in table 1.1. Like any other robot on earth or in air, means of perception are required for any underwater robot for navigation, position or velocity regulation. The need of perception also concerns other tasks, such as obstacle avoidance, cartography or object detection [52]. The following section presents some of the most commonly used underwater perception systems.

1.1.2 Underwater perception systems

All of the applications of underwater robots require appropriate sensors. Two groups of sensors can be defined: vehicle sensors and survey sensors [20]. The former are involved in the telemetry system to manage the position, orientation, and physical status of the vehicle (for instance: depth gauge, water ingress sensor, inertial measurement unit). The latter are used to collect data from the environment and are directly related to the mission's goals (for instance: echolocation for cartography, metal detector for cable tracking or mine countermeasures). Some technologies are multipurpose and can be used for both robot's telemetry and cartography. This is the case of

echolocation, which can be used in a distance and orientation feedback loop for wall following [65], and also in underwater imagery [41]. This mode of perception is widely used for underwater robotics. Indeed, in the water the propagation of the electromagnetic wave, including light, is limited. On the other hand, sound waves easily propagate.

The principle of echolocation consists in sending out an acoustic signal and then listens for a reflection (echo) of that signal back to the receiver. Depending on the frequency of the emitting sound wave, the range can be large (1000km or more at 100Hz) or reduced but with better definition (50m at 1MHz) [20]. As an example, figure 1.2 shows a sea bed image obtained with

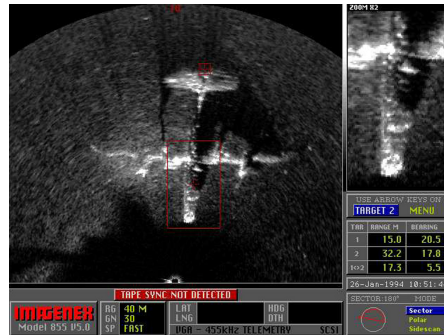


Figure 1.2: An image of a plane lying on the sea bed obtained with an echolocation system. Taken from [20].

an imaging echolocation system mounted on a ROV.

The second very commonly used mode of perception for underwater robots is vision, using a camera [20, 47]. Compare to echolocation, it is cheaper, resolution is higher and range shorter. For instance, vision can be used during approach phases or for object recognition. Often, raw



Figure 1.3: An image of the sea bed obtained with a camera. The left side is the raw image, the right side is the processed image. Taken from [47].

images require post processing, as shown in figure 1.3.

In fact, echolocation and vision are complementary technologies and they often cohabit on ROVs

and AUVs [41]. But, there exist situations in which neither echolocation nor vision is suitable. When the robot has to operate in a confined environment, with very close obstacles, the echolocation is submitted to multiple reverberations which significantly reduce the sensor's accuracy. Moreover, if the robot navigates in a turbid water, eventually because of stirred sediments, vision also shows its limitations. That is, a mode of perception is nowadays missing for underwater robots when navigating in murky water and cluttered environments. But, there exists in the nature some fresh water fish which live in these particular conditions (muddy water and environment full of plants and roots), with absolutely no difficulty. They have evolved a mode of perception adapted to this situation, based on electric fields generation and measurement. As with echolocation which is owned by some cetacean and reproduced by humans, the perception principle of these fish could also be taken as a source of inspiration. Hence, in the following we will firstly introduce the concept of bio-inspiration and then present in details the characteristics of this particular sense. Finally, technological applications based on that sense will be detailed.

1.1.3 Bio-inspiration

In the previous section we presented the needs in terms of underwater perception for robotics applications and some technological solutions. We also mentioned that some fish species possess a particular sense, based on electric fields, which allow them to solve some problems that have no solution yet in the field of underwater robotics.

Even though an animal does not aim the same goal (surviving, breeding) as a robot (perform a task), they share the same need of perception of their environment. Also, because the animals already possess means of probing their surroundings, an idea consists in observing the solutions that nature developed and take inspiration from them. According to [51, 67, 72], this approach is named as *biomimetics* when it consists in replicating a biological function by reproducing the biological structure. Often, the aim is to get a better understanding of the biological system by building models and robots [99]. On the other hand, another term, which is more appropriate to our strategy, is *bio-inspiration*. In this case, the understanding of biology is motivated by the design and the development of new technologies. A biological function is reproduced, but not necessarily the biological structure responsible of that functionality. This second terminology is well-suited to our approach in which we do not strictly copy the electric fish but rather derive and adapt the electric sense principles to our needs.

In the following we will present the active electro-sensing, a perception modality that some fresh water fish possess and from which we will take inspiration later in this thesis.

1.1.4 Active electro-sensing

In this section we develop the electric sensitivity owned by some fish, called electric fish, its discovery and the underlying biological principles. But, before that, we have to make clear our area of interest because there exist in the nature several species that sense and/or produce electric fields in order to achieve different goals. More precisely, we have to clearly distinguish between strongly and weakly electric fish on one hand, and active and passive electro-sensing on the other hand.

History and terminology

When dealing with electric fish, the first species that come to mind are those which produce strong electric fields in order to stun preys or escape from predators. For instance, electric eel in south America (*Electrophorus electricus*), electric ray in Atlantic Ocean and Mediterranean sea (*Torpedo*) and catfish in Africa (*Malapterurus electricus*) are some of the most well known electric fish species. Their discharges' amplitudes are between several tens and several hundreds volts. Since the ancient times, people knew these fish to have the particular ability to provide shocks, even if the nature of these shocks were not understood then [70]. During the 18th century, the link between these shocks and electricity was made and the electric organ was clearly identified and studied. In the same time, other fish species which live in fresh water in Africa and South America were known to have such organ, but smaller and providing no shocks. It was not until the middle of the 20th century that biologists discovered they produce low magnitude electric signals (between several hundred millivolts and a few volts). Lissmann and Machin [61, 62] studied one of them, the African fish *Gymnarchus niloticus*, and were the first who showed that it uses these electric signals to localize and recognize objects in their surroundings. Since then,

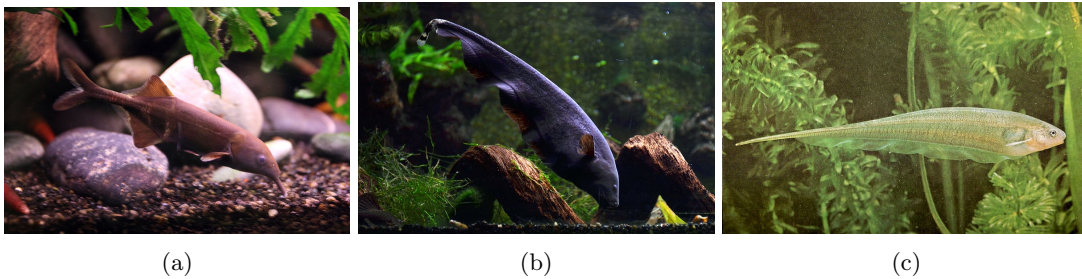


Figure 1.4: Three weakly electric fish species. (a) *Gnathonemus petersii* (Citron - CC-BY-SA-3.0) (b) *Aptereronotus Albifrons* (Vassil - CC0 1.0) (c) *Eigenmannia Virescens* (Luis Ruiz Berti - CC BY-SA 3.0)

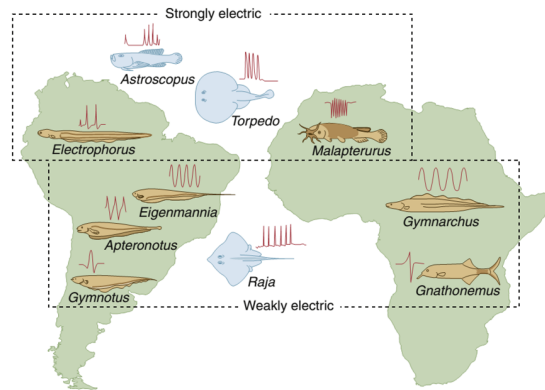


Figure 1.5: Electric fish map. Weakly electric fish live in rivers of Africa and South America. Taken from [71].

many other species enjoying this particular way of perception were discovered (see figures 1.4

and 1.5). The biological principles involve in this way of perception are detailed in the following section.

At this point, we clearly distinguish the *strongly* electric fish which produce high intensity electric fields as a weapon from the *weakly* electric fish which produce low intensity electric fields as a carrier of information. Throughout this thesis, we will only be interested in the weakly electric fish.

Moreover, we have to notice that another kind of electro-sensing exists in some species which do not produce electric field by themselves, but rather detect external fields that are produced by the neural and muscular activity of any living animal. For instance, some sharks, rays and some mammals like the platypus possess electroreceptors [82], generally located close to the mouth, helping to catch preys in the last phase of the attack [91]. This electric perception is said as *passive* electro-sensing because the sensory system only detects external fields [15, 49, 70]. No inert object can be detected with passive electro-sensing. On the other hand, with active electro-sensing, any object whose electrical properties differ from those of the surrounding water produces an electric response when it is submitted to an external electric field. Thus, it can potentially be detected and characterized. The underlying physics it will be detailed in chapter 3.

To sum up, the term *active electro-sensing* will refer to the weakly electric fish's mode of perception, which consists in generating low intensity electric field in order to get information from the environment. The term *electric sense* will also be use as an alternative.

Biological principles

Biologists highlighted two functions for the electric sense [15, 49, 70]:

- Communication: in a social context, electric sense enables self identifying to conspecifics, revealing its gender, finding a sexual partner, warning of danger, threatening. The generated electric field slightly differs from an individual to another. The own characteristics of the electric discharges of an individual is considered as its electric signature [36, 70].
- Electrolocation: in muddy waters and during the night, when visibility is significantly reduced, electric sense helps the fish to find its bearings and locate preys.

Even if the fish perform these two functions with the same electric field, we are interested in electrolocation only. Communication through electric field is not studied in this thesis.

Electric field generation and perception occur at the same time and are closely related to each other in the active electro-sensing process. But, for the sake of clarity, let us introduce the field generation first, then the field reception and finally the coupling mechanisms that occur, involving movements of the fish.

In order to submit its environment to an electric field, the fish uses a discharge organ, located in the tail in most of the species. This organ is composed of hundreds or thousands of cells, named as electrocytes. Their simultaneous discharges are controlled by the brain. The voltages of the electrocytes in series add up and as a result, it produces an electric discharge denoted EOD (electric organ discharge).

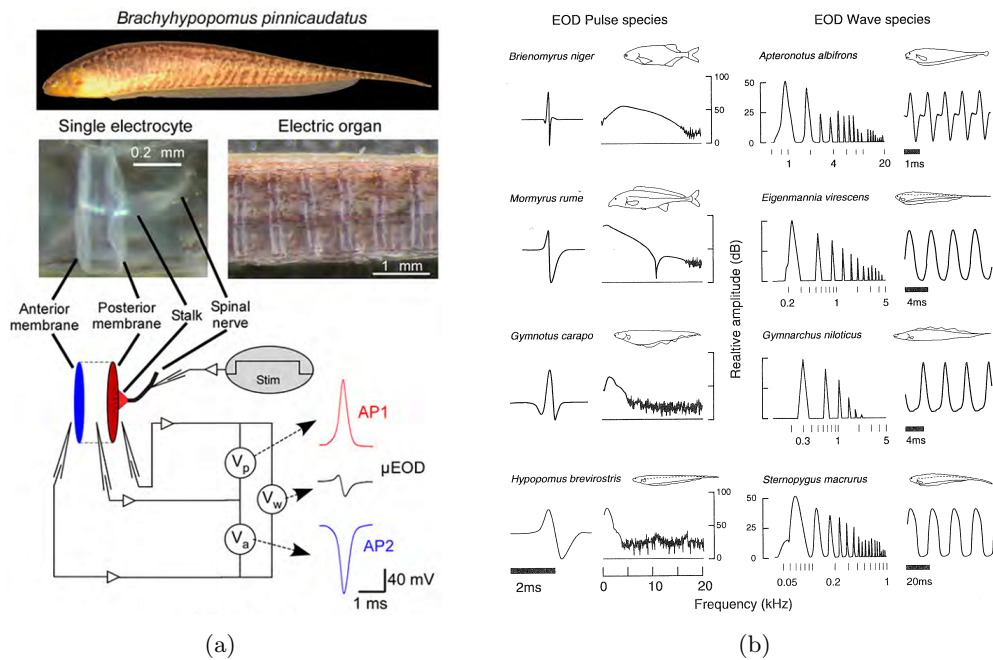


Figure 1.6: (a) The electric organ of a *Brachyhypopomus pinnicaudatus*. Each electrocyte is stimulated by a spinal nerve. Taken from [85]. (b) Some examples of pulse discharges (left column) and wave discharges (right column) with their respective frequency spectrum. Taken from [70].

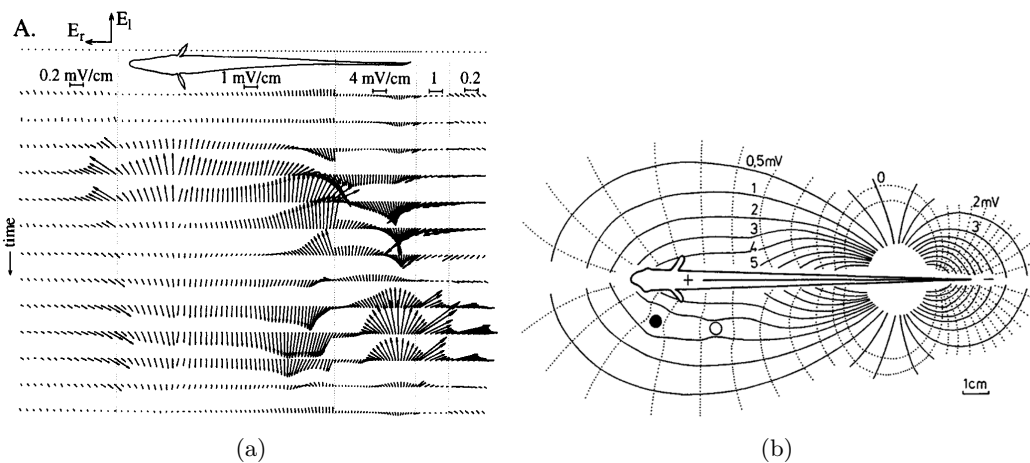


Figure 1.7: (a) The rostral component (along axis E_r) and lateral component (along axis E_l) of the basal field at 13 different instants during an EOD of a *Apteronotus leptorhynchus*. Taken from [76]. (b) Isopotential lines (solid lines) and electric field lines (dotted lines) at a given instant during the EOD. An insulating object (white) locally makes the field lines to divert, while a conductive object (black) locally makes the field lines to converge. Taken from [49].

Figure 1.6a shows the electric organ and the EOD of a single electrocyte (named as μ EOD).

Among all the weakly electric fish, there exist two kinds of temporal profiles of EOD: pulse fish produce brief discharges with controlled interpulse interval, whereas wave fish produce continuously sine-like signals. Figure 1.6b shows some examples of both kind on signals with their relative frequency spectrum.

During an EOD, the fish's body is electrically polarized: the electric organ is set to an electric potential which differs from the rest of the body. As a consequence, an electric field is generated in the surroundings, known as the *basal field*. At first glance, the fish can be considered as an electric dipole, but close to the fish, the spatio-temporal behavior of the basal field is more complex [6] and is determined by both the temporal profile and the morphology of the fish. As an example, figure 1.7a shows the the rostral and lateral field components during one EOD of a *Apteronotus leptorhynchus* [76].

Facing the tail, the electric field vector rotates during the EOD cycle, whereas facing the trunk and the head, the field has a relatively constant orientation while varying in magnitude. When an object is in the vicinity of the fish, it is submitted to the basal field and, as a consequence, distorts it as shown in figure 1.7b. Because the resistivity of an insulating object is significantly higher than that of the water, the field lines are locally repelled. On the other hand, the resistivity of a conductive object is significantly lower than that of the water, the field lines locally converge. This distortion of the field lines is due to the polarization of the object when it is submitted to the basal field. The polarized object produces an electric field which superimpose to the basal field. In the case of a spherical object of radius a submitted to a uniform external field \mathbf{E}_0 (see

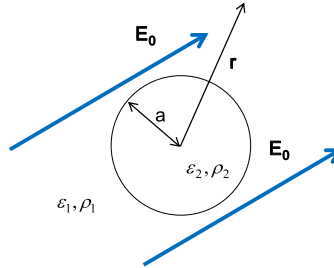


Figure 1.8: Configuration for the perturbation model proposed by Rasnow in [75].

configuration on figure 1.8), a model for the electric potential produced by the polarized sphere was given in [75]

$$\delta\phi(\mathbf{r}) = \mathbf{E}_0 \cdot \mathbf{r} \left(\frac{a}{r} \right)^3 \frac{\rho_1 - \rho_2 + i\omega\rho_1\rho_2(\epsilon_2 - \epsilon_1)}{2\rho_2 + \rho_1 + i\omega\rho_1\rho_2(2\epsilon_1 + \epsilon_2)}, \quad (1.1)$$

where \mathbf{r} refers to a point in \mathbb{R}^3 with respect to the center of the sphere, $\delta\phi(\mathbf{r})$ is the electric potential variation at the point \mathbf{r} , \mathbf{E}_0 is the uniform electric field in which the sphere lies, a in the sphere's radius, ρ_1 and ρ_2 are the resistivity of the medium and the resistivity of the object, respectively, ϵ_1 and ϵ_2 are the dielectric permittivity of the medium and the object, respectively, and ω is the angular frequency of the electric field \mathbf{E}_0 . The complex number $\frac{\rho_1 - \rho_2 + i\omega\rho_1\rho_2(\epsilon_2 - \epsilon_1)}{2\rho_2 + \rho_1 + i\omega\rho_1\rho_2(2\epsilon_1 + \epsilon_2)}$ is named as contrast factor, denoted χ . It represents the dielectric contrast between the object and the medium. A study of its behavior with respect to the respective properties of the water and the object was carried out and is presented in chapter 2.

This model being for the electric potential, the corresponding electric field can be calculated as the opposite of its gradient. A more extensive description of the underlying physics will be detailed in chapter 3.

In order to measure this distorted field, the fish possess electroreceptors, distributed over its skin, mainly on the trunk and the head [15, 49, 70]. They measure the transcutaneous electric field by converting it into neuronal messages. Depending on the species, there exist several kinds of electroreceptors but we can divide them into two groups: ampullary and tuberous electroreceptors.

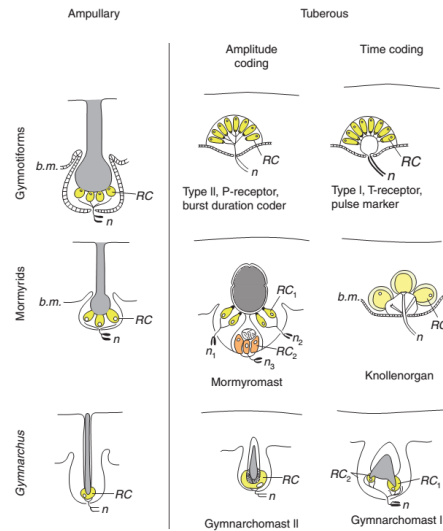


Figure 1.9: Different kinds of electroreceptors for three electric fish species: Gymnotiformes (top), Mormyrids (middle), Gymnarchus (bottom) [36]

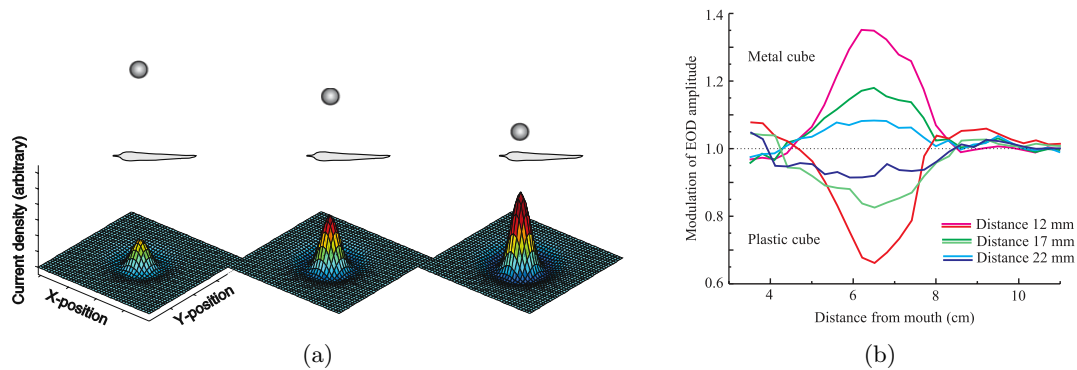


Figure 1.10: (a) 3D representations of electric images due to the presence of a conductive sphere at different lateral distances (simulation data). Taken from [28]. (b) Electric images measured along the mid-line of the fish for a metal cube (upper curves) and a plastic cube (lower curves) at three lateral distances. Taken from [93].

The ampullary electroreceptors are sensitive to low frequencies, between 0Hz and 50Hz, whereas tuberous electroreceptors are sensitive to stimulations between 100Hz and 10kHz (see figure 1.9).

Because the fish knows its own basal field, it subtracts it from the electroreceptors' measurements and only keeps the information that comes from the polarized object. The high density of electroreceptors on the head and the trunk of the fish creates a sensory surface onto which electric images of the object are projected, see figure 1.10a. The maximum value of the electric image is related to the object's distance, but not in a one-to-one relationship as we will see in next section. An insulating object produces similar shape, but inverted, as shown in figure 1.10b.

By analogy with vision in which optical images are projected onto the retina, the sensory surface of the electric fish constitutes an electric fovea [17, 28, 69]. However, electrical images fundamentally differ from optical images. Contrary to vision where the lens guide light to the photoreceptor layer, there are not any focusing mechanisms for the electric sense: electric images are out of focus and are necessarily blurry [60]. Whereas optical images are determined by object shape, size, and other geometrical parameters, electric images depend on several additional object properties, such as object depth, object distance, location along the fish's body and the properties of neighboring objects [28]. Hence, electric fish have to use particular mechanisms to extract information from the electric image. The next section introduces the strategies the fish is suspected to carry out for this information extraction.

Inverse problem solving

Like any other sensory system, electric sense aims to solve an inverse problem. This is clearly highlighted by Caputi in [16]:

"Sensory systems must solve the inverse problem of determining environmental events based on patterns of neural activity in the central nervous system that are affected by those environmental events".

The inverse problem for the fish consists in determine, or at least estimate, the properties of its environment from the electric image on its skin. Here, we consider the environment of the fish being composed of only one object. According to [15], this task can be split into three sub-problems:

- Detection: consisting in answering the question "is there an object in the surroundings?", which can be answered by "yes" or "no",
- Localization: for the estimation of the object's position relatively to the fish's body,
- Characterization: dedicated to estimate the properties of the object: size, shape and electrical properties.

Although performed in parallel by the fish, this sequential description of the electrolocation sub-tasks has a correspondence with the processes observed in the fish. These processes are based on the extraction of properties of interest from the electric image, named as *cues*. Firstly, biologists showed that the location of the electric image maximum value on the fish's skin is used as an estimator of the rostro-caudal and dorso-ventral coordinates of the object [6]. Indeed,

the object produces the maximum effect on the skin orthogonally to its position. This cue is named as the *peak position*. It is independent of the object's size and lateral distance, which only affect the image amplitude and width. The third coordinate (lateral distance) has to be estimated in a more sophisticated way. Indeed, as shown in the perturbation model (1.1), the triplet {object's distance \mathbf{r} , object's diameter a , contrast factor χ } is not unique for a given electric potential perturbation $\delta\phi$. As a result, two different objects could produce the same electric image on the fish's skin. This is illustrated in figure 1.11, where sub-figures (B) and

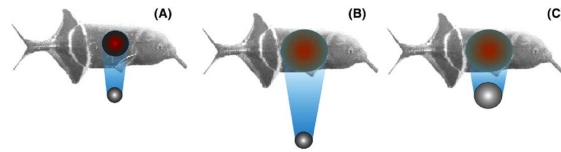


Figure 1.11: The electric images of a given object at two different lateral distances are different, compare (A) and (B). However, a larger but closer object possibly produce similar electric image, compare (B) and (C). Taken from [94].

(C) show similar electric images for two different objects at two different lateral distances. The biological mechanism for disambiguating such situations was first described in [98]. The fish uses the ratio between maximal image slope and maximal image amplitude. Figure 1.12a shows the

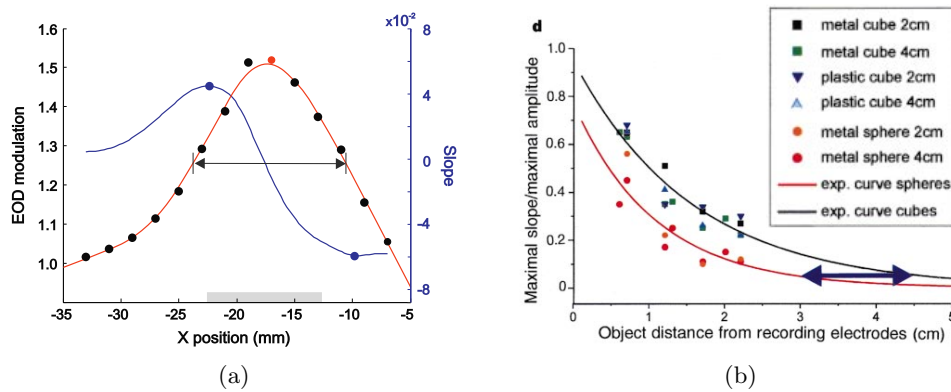


Figure 1.12: (a) Transect of the electric image (red) and its first spacial derivative (blue). Taken from [34]. (b) The SAR as function of the lateral distance for six different objects. The blue double arrow represents the difference in estimated lateral distances for a given SAR value. Taken from [98].

values along one height of the electric image, in red, and its first derivative, in blue. Named as SAR, for slope/amplitude ratio, it is independent of the object's volume and is only function of the lateral distance, at least for a given object's shape. This is illustrated in figure 1.12b, where the SAR is plotted against the lateral distance for cubes and spheres of different sizes and materials. One can see that the SARs which correspond to cubes are related to the lateral distance, independently of volume and material (blue curve). Same observation is made about the spheres, but according to a different relationship (red curve). This difference was used as an opportunity to validate the use of the SAR in the fish [98]. Indeed, when training fish to compare the distances of a metal sphere with those of a metal cube of the same diameter, they judged the sphere to be farther away than the cube, even though both objects were at the same lateral

distance. This is represented with the blue double arrow in figure 1.12b, corresponding to two different lateral distances for a given value of SAR. The fish, which is supposed to estimate the lateral distance according to the blue curve (cubes), indeed must over estimate lateral distance if the object is actually a sphere.

Until now, we have only considered static images. This static point of view and the related peak position and SAR requires a high density of electroreceptors. A recent study showed that it is possible for the fish to use the same principles for object's localization using only one electroreceptor and moving in a straight line with respect to a fixed object [34]. In these conditions, the electric image is said as temporal and denoted t-image. Figure 1.13A shows

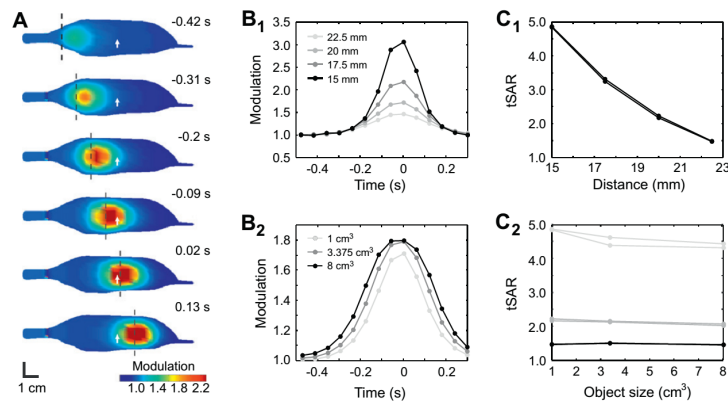


Figure 1.13: (A) shows the spatial electric images on the fish's skin, taken at different instants, when a 1cm^3 cube is moved from tail to head at a given lateral distance. The vertical dashed line represents the rostro-caudal position of the cube's center of mass and the white arrow indicates the electroreceptor on which the electric potential is measured. (B1) shows the t-images for a given object and four lateral distances. The corresponding tSAR as a function of the lateral distance is shown on (C1). For a given lateral distance (20mm), three t-images corresponding to three object sizes are plotted in figure (B2). Figure (C2) shows the tSAR for three lateral distances against the object's size. Taken from [34].

the experimental process and figures 1.13B1 and 1.13B2 the related t-images measured with one particular electroreceptor. The lateral distance estimation principle described above is still available on these t-images, this time using the temporal SAR, named as tSAR. Figure 1.13C1 shows that the tSAR decreases when the lateral distance increases whereas figure 1.13C2 shows that it is constant with respect to the object's size, for a given lateral distance.

When inspecting a novel object, weakly electric fish actually move in straight line, passing by the object as described above. But, this is just one typical movement, among many others, that can be observed in the fish. They intensively use others and more complex locomotion patterns to help perception [33, 35]. Motion and perception are deeply linked in a sensorymotor loop, which is described in the next section.

Active electro-sensing in the sensorymotor loop

As shown in the previous section, the sensory information can be acquired in both space and time. It was mentioned that the weakly electric fish use motion to influence sensory inputs. A relevant

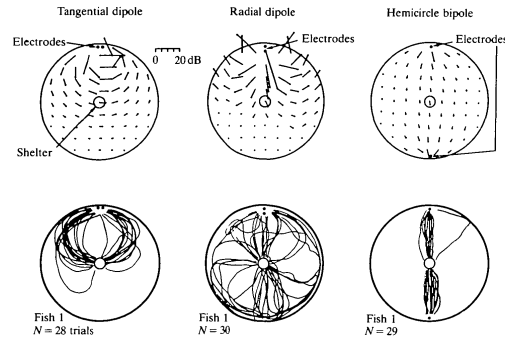


Figure 1.14: An experiment that highlights the strong link between fish's motion and sensory input. The fish starts from a shelter in the middle of a circular aquarium and reaches an artificial dipole by following the field lines. First row: the electric field lines depending for three dipole configurations (tangential, radial and hemicircle). Second row: the corresponding trajectories of the fish in the aquarium. Taken from [78].

example is given in [78], in which it is shown that the African active electric fish *Brienomyrus brachyistius* reaches an artificial electric dipole by aligning its body with the electric field lines. This behavior is represented in figure 1.14. One can see the correspondence between the shape of the field lines and the trajectories of the fish. The fish adapts its motion such that the normal electric field on its skin is minimized. Such a strategy ensures the fish to reach the dipole, even if it is not be able determine neither the distance nor the direction of that dipole. This

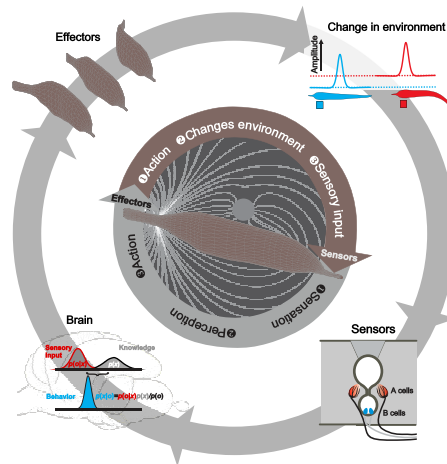


Figure 1.15: With the information provided by the sensors, the brain has knowledge of the environment, according to which it generates behaviors through the effectors. Movements modify the electric field pattern to which the object is submitted, thus changing the upcoming sensory input. Taken from [35].

example highlights the fact that motion and perception are both involved in a sensorymotor loop. Such a loop is schematized in figure 1.15. It shows that an action induces changes in the environment, thus modifies the sensory input and, as a consequence, updates the knowledge about the environment. This leads to a change in term of behavior and action.

In the active electric fish, the motor patterns observed when discovering a novel object are characteristic. Named as probing motor acts (PMAs), they were qualitatively described and linked

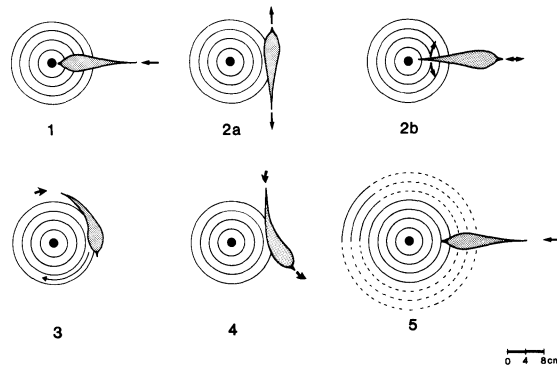


Figure 1.16: The probing motor acts (PMAs) displayed by mormyrid fish when exploring a novel object. 1: chin probing ; 2a: lateral va-et-vient 2b: radial va-et-vient ; 3: lateral probing ; 4: tangential probing ; 5: stationary probing. Taken from [90].

to the electrosensory probing of objects [89, 90], see figure 1.16. Recently, similar results were obtained on *Gnathonemus petersii* fish using a quantitative approach [33]. The extracted 2D

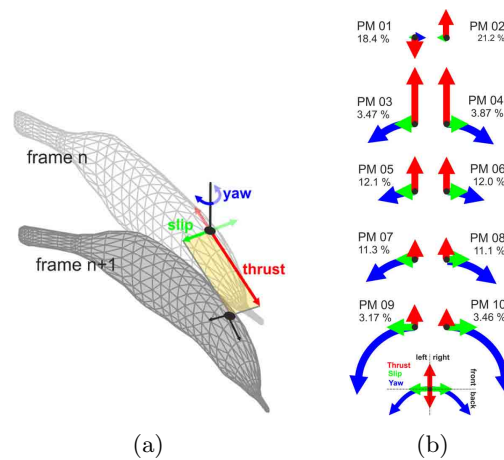


Figure 1.17: (a) The three extracted kinematic parameters for PMAs quantitative analysis: thrust, slip and yaw. They were exacted by filming the fish from above with a video camera, and comparing the fish's head position and body orientation between two frames. (b) The kinematic composition of prototypical movements (PM) when an object is explored (normalized velocities values), with the respective percentage of spent time during exploration. Both taken from [33].

kinematic parameters are presented in figure 1.17a. Thrust and slip correspond to the longitudinal and lateral velocities respectively and yaw correspond to the angular velocity about the

vertical axis. In figure 1.17b, the prototypical movements (PM) are listed, with their respective percentage of spent time during exploration. PM01 and PM02 were mainly thrust dominated, with negative thrust for PM01. PM03 to PM10 occurred in mirror-imaged pairs with respect to their slip and yaw velocity directions and occurred equally likely (see percentage of each PM). PM03 to PM10 describe a gradual transition from PMs with maximal translational amplitude (PM03 and PM04) toward those of maximal rotational amplitude and reduced thrust (PM09 and PM10). In addition, this study shows a strong correlation between the EOD frequency and the position and orientation of the fish with respect to the object during exploration.

This study highlights the fact that movements are deeply involved in active sensing strategies. Such movements are supposed to be used to satisfactorily shape the basal field and orient the sensory surface in a convenient way. However, how the fish solves the problem of discriminating between different object's shapes in its brain is not known yet. This is an open problem for biologists [97], while many studies have shown that the fish is able to solve that problem, even without vision, only using its electric sense. The next section presents some of the performances of the fish in term of shape recognition.

1.1.5 Fish's performances

As depicted above, we finally know very few things about how the fish extract information from their electric image, comparing to their observed performances in term of perception, which go far beyond locating objects only. Several studies were conducted to evaluate the ability of the fish in terms of object's shape recognition [80, 94, 95, 96, 97]. In this section, we present the methods and results given in [97], which are representative.

This study was conducted on eight African fish *Gnathonemus Petersii*. Fish were trained to discriminate between two metal objects of different shapes. The procedure to train a fish consists

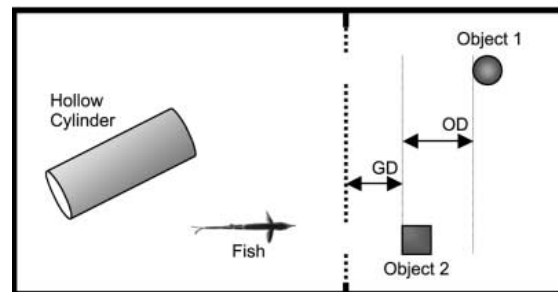


Figure 1.18: The experimental set-up for fish training (top view). The aquarium is divided into two parts using a plastic mesh screen, represented with a dotted line. The left compartment represents the fish's living area, containing a shelter (hollow cylinder) and plants. Two objects lie in the right compartment. The mesh screen has two gates, each one facing an object, and through which the fish can pass. Distance denoted GD represents the distance between the gate and the closer object, while distance denoted OD represents the inter-object distance. Taken from [80].

in dividing a tank into two compartments with a plastic mesh screen, as shown un figure 1.18. One compartment is used as a living area, containing plants and a shelter. In the second compartment,

the two objects are placed, each of them facing a gate made in the plastic net. The gate in front of which each object is placed is determined with a pseudo random schedule at each trial. The gates are wide enough so that the fish can pass through them. The distance between the net and the closer object is denoted as GD (standing for gate distance), and the distance between the two objects is denoted as OD (object distance). One of the object is defined as positive (object S+), the other one defined as negative (S-). Once the fish has inspected the two objects through the gates, if it passes through the gate leading to S+, it is rewarded with food, otherwise, it is frightened by knocking against the aquarium wall. Then, the fish goes back to its living area and a new trial is prepared by the experimenter. When the fish is able to make 75% of correct choices over 3 consecutive days, it is considered as sufficiently experienced. Each of the eight fish

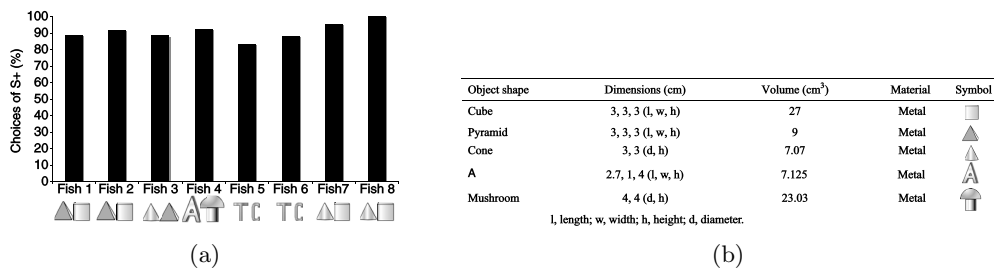


Figure 1.19: (a) The choice frequency for S+ of the eight fish after training. To each fish corresponds its pair of training objects. Left object: S+, right object: S-. (b) Description of the objects. Both taken from [97].

was trained with a particular couple of objects, see figures 1.19a and 1.19b. This training phase shows that fish are able to discriminate between two objects of different shapes, even in the dark. Note that the fish has to be at a distance from the object that is lower or equal to 4cm in order to obtain these results. Above 4cm, percentage of choice of S+ rapidly drops to 50% (random choice). In comparison, object detection (no characterization) works at one body length distance (≈ 10 cm) [70]. This suggests that shape recognition process requires more fine details in the electric image. Then, once the fish were trained, they underwent test trials, in which either S-, S+ or S+ and S- where changed with novel objects. These test trials showed that the object's shape discrimination performances were not significantly affected when the objects' scales and materials are changed, even when S+ is presented to the fish with different orientations [96].

Even though the underlying mechanisms of shape recognition are not known yet, these results prove the ability of the weakly electric fish to perform complex recognition tasks. Its performances make it a particularly interesting study subject, shows the high potential of this mode of perception and the great interest we would have in taking inspiration of it. In fact, bio-inspired electric sense devices emerged about twenty years ago in research laboratories. The following section is dedicated to present them.

1.1.6 Technological applications of active electro-sensing

Applications for underwater robotics inspired by electric sense began in the late 90s, motivated by the limitations of usual technologies (echolocation and vision) in muddy waters, waters with particles in suspension or navigation near obstacles. The first obstacle avoidance system inspired by electric sense was composed of one pair of electrodes emitting electrodes and another pair

of measuring electrodes [19]. Insulating and conducting spheres could be avoided by the robot. Then, in [66], a linear seven electrodes array was proposed, showing voltage measurement variations when a spherical object is moved in the array surroundings. In 2008, a sphere localization

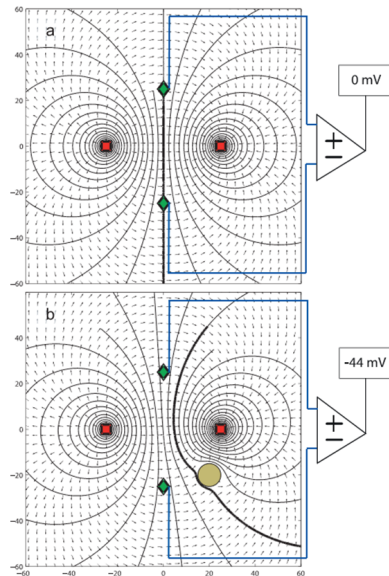


Figure 1.20: Measurement of an electric potential variation due to the presence of an object by two punctual electrodes (green diamonds). The emitters are represented with red squares. Top: without any object, the electric potential pattern is symmetric and the sensor measures 0V. Bottom: the presence of a 5mm radius sphere breaks the symmetry and the sensor measures -44mV. Taken from [83].

device composed of four punctual electrodes is presented in [83], see figure 1.20. The associated algorithm was a particular filter. This method requires a preliminary calibration of the electric potentials around the sphere, either by modeling or by measurements. A second method which doesn't need any calibration is also presented. It uses known characteristics of the electric potential which are independent of the object and the medium. Another punctual electrodes device was introduced in [73]. Two emitting electrodes generates the electric field, forming an electric

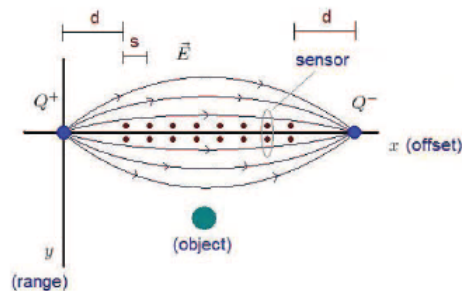


Figure 1.21: A linear active sensor for spheres localization. Taken from [73].

dipole, and eight measuring pairs of electrodes are placed symmetrically about the dipole axis, see figure 1.21. The associated algorithm is based on beamforming techniques [50] for objects localization. Another sensor geometry is proposed in [25], consisting of a point source located at

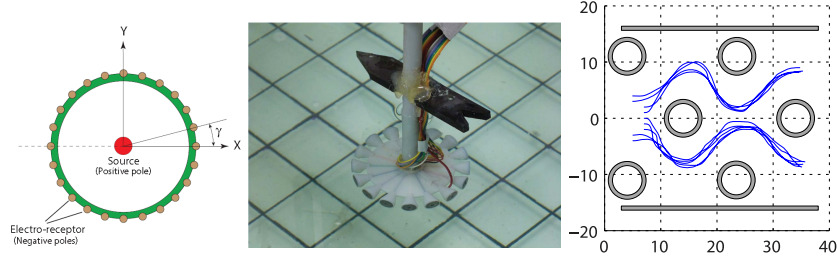


Figure 1.22: A circular active sensor for obstacle avoidance. Left: the electroreceptors are placed on a circle centered at the positive pole, with an angular resolution γ . Middle: actual sensor. Right: Trajectories of the sensor in a corridor with obstacles for different initial sensor's positions (experimental conditions, dimensions in inches). Taken from [26].

the center of a circular ring with electroreceptors on its periphery, see figures 1.22 left and 1.22 middle. This sensor is motion controlled for walls following and obstacle avoidance. To that end, an analytical model of the electric image is obtained by calculating the perturbation potential due to the wall using the method of images [42]. Then, this image is processed using Wide-Field Integration (WFI), as already used in the field of bio-inspired insect visuomotor system [39]. This processed image is used for state vector estimation in the feedback control loop. Figure 1.22 right, shows the trajectories of the sensor in a corridor with obstacles, for different initial positions of the sensor.

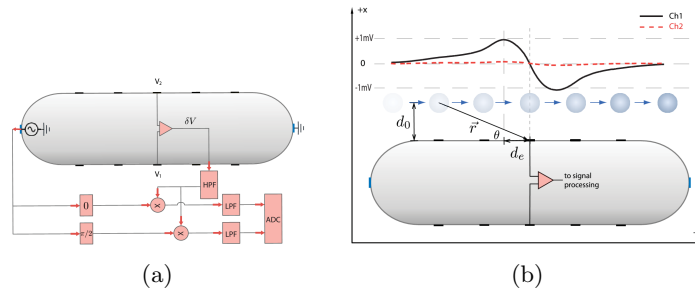


Figure 1.23: (a) The SensorPod device and its demodulation circuit. HPF: high pass filter, LPF: low pass filter, ADC: analog to digital converter. (b) The object is moved parallel to the SensorPod at a given lateral distance d_0 . Ch1 and Ch2 are the demodulated signals which represents the amplitude and the phase, respectively. Both taken from [8].

Some cylindrical shaped experimental platforms were also designed, such as the SensorPod [8] which polarizing and measuring configurations are represented in figure 1.23a. The two electrodes at each end are connected to a sine wave voltage generator. This produces the electric field in the surroundings. Five measuring electrodes on each side are coupled by pairs and differential voltage is recorded ($\delta V = V_2 - V_1$ in figure 1.23a). Measurements are demodulated twice: with the reference signal and with the reference signal that is $\pi/2$ out of phase. Gain and phase are extracted from the two resulting signals with trigonometric operations. The experimental setup consists in fly-by tests: an object is moved parallel to the SensorPod at a given distance (see figure

1.23b). Various objects were tested: cubes of plastic, metal and fresh meat, grape, tomato, rock, aquatic ribbon plant and rolled Nylon net. The results showed that the objects could be identified with their phase and/or amplitude behavior over a frequency range from 0Hz to 10^5 Hz. Also, amplitude was shown to be a function of distance and size. Still using the SensorPod, another algorithm was presented in [9] for ellipsoidal objects identification. It consists in estimating

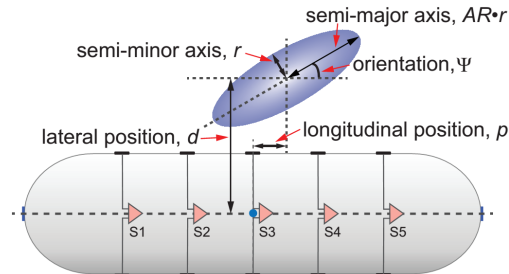


Figure 1.24: The scene parametrization for ellipsoidal object identification using the SensorPod. Taken from [9].

five parameters: two for the object's localization in the horizontal plane (d and p), two for the object's geometrical properties (r and AR) and one for its orientation (ψ), see figure 1.24. The method is decomposed into three stages. Firstly, the parameters p and ψ are estimated with an iterative process involving rotations and translations of the sensor. The process is stopped when a symmetry in the voltage measurements, encoded by the symmetry ratio η , is reached. For $\eta = 1$, the sensor is parallel to the object's main axis ($\psi = 0$) and its center faces the sensor mid-length ($p = 0$). Secondly, the aspect ratio AR is estimated using a map, relating η to AR , which was previously determined with a numerical model. This relationship being bijective for a given ψ , AR is estimated by reading on this map. Finally, using a supervised learning model the lateral position d and the semi-minor axis r are disambiguated. Whereas the SensorPod technology is said U-U because voltages are applied to the water and voltages are measured, another technology which consists in applying voltages and measuring electrical currents (U-I technology) was developed as well. It is cylindrical shaped, made of a succession of insulating



Figure 1.25: The bio-inspired sensor using U-I technology. Left: four macro-electrodes version, right: three macro-electrodes version.

tubes and conductive elements. See figure 1.25. More precisely, the conductive elements (one hemispherical at each end and zero, one or two cylindrical depending on version) are denoted macro-electrode. Each of them is divided into two symmetrical left and right electrodes. Each macro-electrode can be set under an electric potential with respect to the three others, and the electrical current that flows through each electrode can be measured. A complete description of this sensor and the related Cartesian robot is given in [81] and in chapter 2 in this thesis. An

analytical model for the sensor's measurements was proposed in [7, 43], showing the feasibility of walls avoiding and localization in experimental conditions using extended Kalman filters. A similar strategy was implemented in [57] for localization and size estimation of a sphere and navigation around a sphere. This method for sphere estimation was experimentally proven in

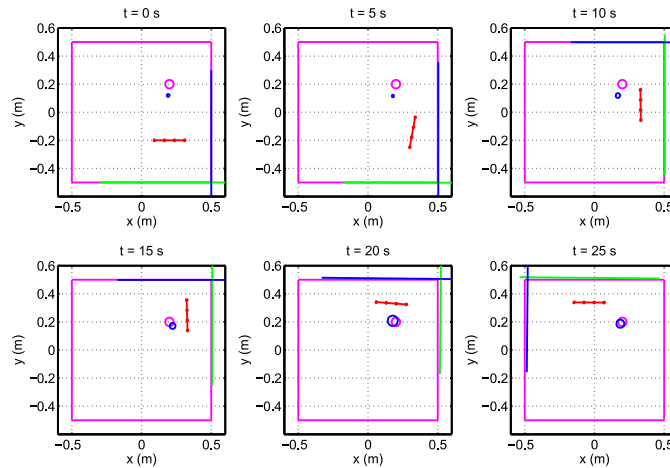


Figure 1.26: A sphere estimation in presence of insulating walls from $t=0s$ to $t=25s$. Actual sphere and walls are pink, estimated sphere is blue and estimated walls are blue and green. The sensor is red. The sensor adapts its trajectory in order to avoid the walls while the estimated sphere tends toward the actual sphere. Taken from [59].

[58, 59], even in presence of walls in the surroundings, see figure 1.26 Moreover, it was shown that the process also works for a cube, which electrical response can be approximated to that of a sphere. All these methods are based on an analytical model with the assumption of spherical electrodes.

In [12], a new analytical model is proposed taking into account the actual electrodes' shapes (that are hemispherical and cylindrical) and the insulating parts which it is composed of. This model is presented in chapter 3. It describes the relationship between the polarization of the macro-electrodes and the measured currents. For each macro-electrode, two kinds of current

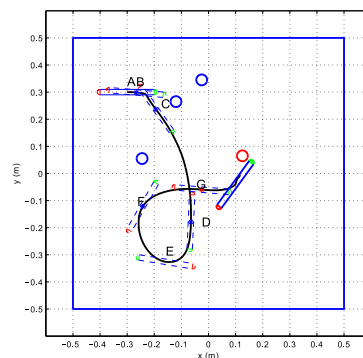


Figure 1.27: The trajectory of the sensor, reaching a conductive object (red) while avoiding insulating objects (blue). Taken from [14].

are defined: the axial current, denoted I_{ax} , which is the sum of the currents that flow through the two left-right electrodes and the lateral current, denoted I_{lat} , which is the difference of the currents that flow through the two left-right electrodes.

Using the I_{ax} and I_{lat} currents and sensory motor loops, it was shown in [14, 55] that the sensor can reach a conducting object, avoiding insulating objects, by following the electric lines produced by the polarized conducting object, see figure 1.27. This strategy is inspired by the electric fish's behavior when it heads toward a prey.

Another simple and low computation algorithm can also be implemented to know whether the object is conducting or insulating and if it is on the left or on the right side of the sensor [14, 55]. It is only based on a study of signs of I_{ax} and I_{lat} currents. Implemented on two macro-electrodes versions of the sensor at first, it was recently extended to a four macro-electrodes sensor in [53] and detailed in chapter 4 of this thesis.

At this point, we have presented the most relevant bio-inspired electric sense devices. Since about twenty years, these technologies have progressed from simple punctual electrodes systems for spherical object's avoidance to embedded systems able to navigate in unknown environment. But, comparing to the fish's performances presented in the previous section, there is still a significant room for improvement, especially in object's localization and shape estimation. Based on that observation, new methods could be developed and implemented in order to improve actual performances of artificial electric sense. Actually, this is the purpose of this thesis, and the next section introduces it in details.

1.2 Addressed problem and contributions

Comparing the fish's performances to the actual bio-inspired sensors' results described above, we can see that there is a huge gap between them. The fish explores and recognizes the objects in total autonomy. The actual bio-inspired systems are far from being at this stage.

Hence, we describe in this thesis new methods for achieving the object's detection, localization and characterization tasks, using the U-I technology sensor presented in the previous section. Also, we prove their relevance with simulation and experimental results. Moreover, whilst the results obtained in the previous works with that sensor concerned spheroidal objects (spheres and cubes), the results presented in this thesis concern ellipsoidal objects. These objects being extended in one direction, they are appropriate for a first step toward some more complicated shapes, especially because it introduces the concept of object's orientation.

The results presented in this thesis are organized according to the sequential process shown in figure 1.28. As a starting point, we consider the sensor navigating in an unknown environment. The first step, named as "object's inspection", gathers several algorithms. The first one consists in detecting the presence of an object in the sensor's surroundings. Then, a second algorithm discriminates its material, and a third one discriminates the left/right position of the object with respect to the sensor's axis. Finally, a reactive control loop allows the sensor to navigate toward the object, automatically stops the sensor motion at a given distance and performs a trajectory around the object. These algorithms, gathered in the block named as "Object's inspection" in figure 1.28, are described in chapter 4.

February 7, 2018

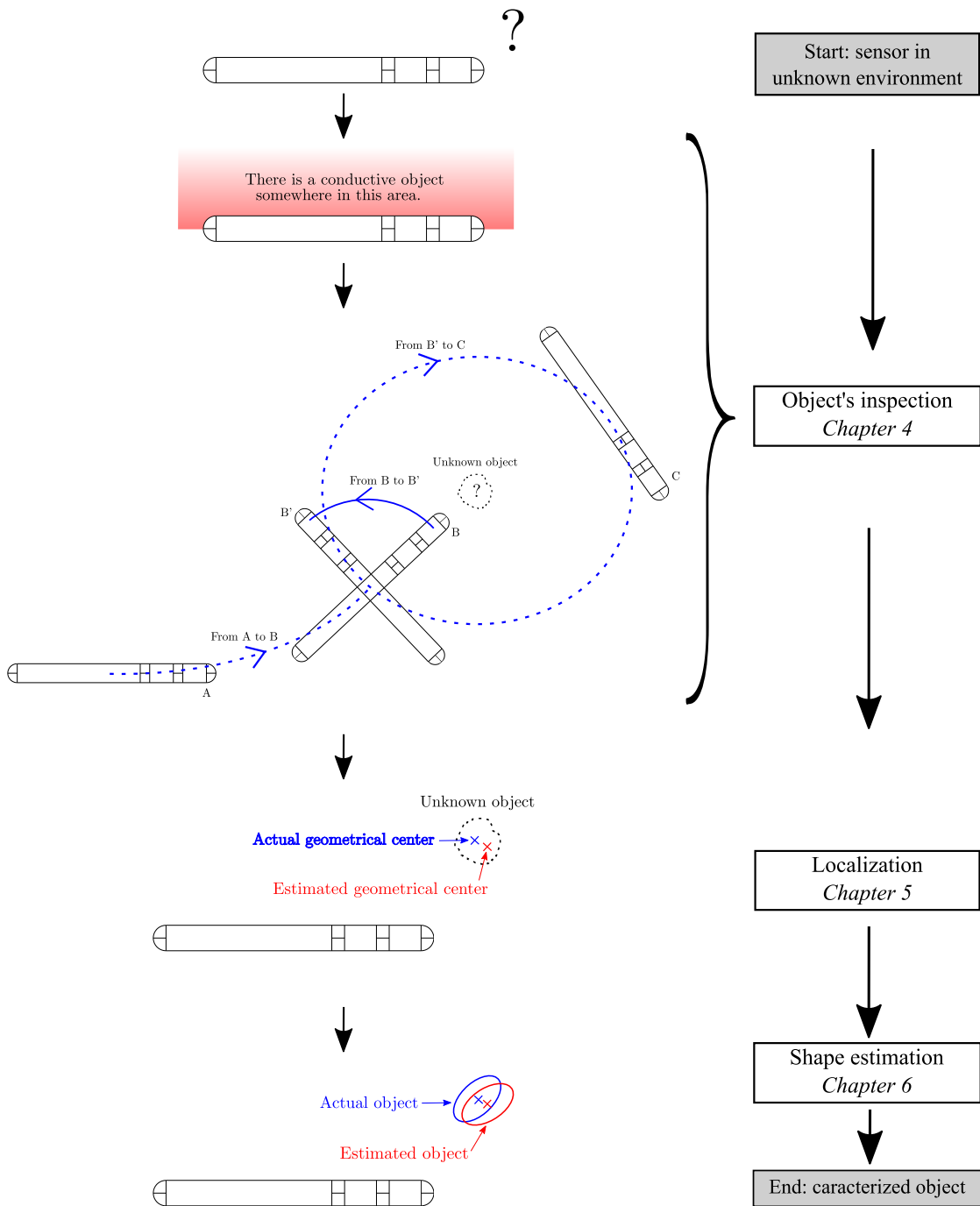


Figure 1.28: The sequential process (from top to bottom) for the inspection, localization and shape estimation that is followed in this thesis. All the figures represent the sensor and the object from above.

These results were published in

LEBASTARD, V., BOYER, F., AND LANNEAU, S. Reactive underwater object inspection based on artificial electric sense. *Bioinspiration & Biomimetics* 11, 4 (2016).

Even if the object's inspection step gives an approximation of the relative position of the object with respect to the sensor, it does not provide an accurate object's localization. This is the purpose of chapter 5. The localization of the object is estimated using the MUSIC (multiple signal classification) algorithm, which allows the localization of an object independently of its geometrical properties, at least theoretically. Indeed, the implementation of MUSIC on our sensor in experimental conditions is particularly difficult, and we propose a new strategy to circumvent the problems.

Finally, once the object is localized, its geometrical properties are estimated using an least squares procedure and by inverting the model of the object's electrical response. This is the purpose of chapter 6. At this point, the object was detected, localized and characterized. Like the experimental implementation of MUSIC, the shape estimation in actual conditions suffer from non negligible imprecisions in some cases. The reasons are studied and understood, and some additional methods are given in order to improve the results.

The results of these localization and the shape estimation algorithms were published in

LANNEAU, S., LEBASTARD, V., AND BOYER, F. Object shape recognition using electric sense and ellipsoid's polarization tensor. In *In Proceedings of the IEEE International Conference on Robotics and Automation (ICRA)* (2016), pp. 4692–4699.

and in

LANNEAU, S., BOYER, F., LEBASTARD, V., AND BAZEILLE, S. Model based estimation of ellipsoidal object using artificial electric sense. *The International Journal of Robotics Research* 36, 9 (2017), 1022–1041.

In order to carry out these algorithms, some more material is needed about the sensor and the underlying physics. In chapter 2, the sensor, the tank in which it navigates and the Cartesian robot are described. This chapter is also dedicated to the polarization and the measurement principles, the description objects as well as the scene. Then, in chapter 3 the needed physics is presented and the models are described.

Chapter 2

Sensor, test bed and scene

The sensor that will be used throughout this thesis was introduced in chapter 1 (see figure 1.25) and this chapter aims to describe it in details. The water tank and the Cartesian robot which enables its movements are firstly presented. Then, a parametrization of the scene and a kinematic model of the sensor are given. Finally, the performances of the sensor in term of electric field generation and electric current measurements are detailed, as well as the electric circuit that implements these functions.

2.1 Tank and Cartesian robot

The sensor navigates in a 1m x 1m x 1m dimensions water tank, on which is attached the fixed frame denoted $R = (O, \mathbf{i}, \mathbf{j}, \mathbf{k})$, vector \mathbf{k} being vertical, see figure 2.1a. This tank is topped with

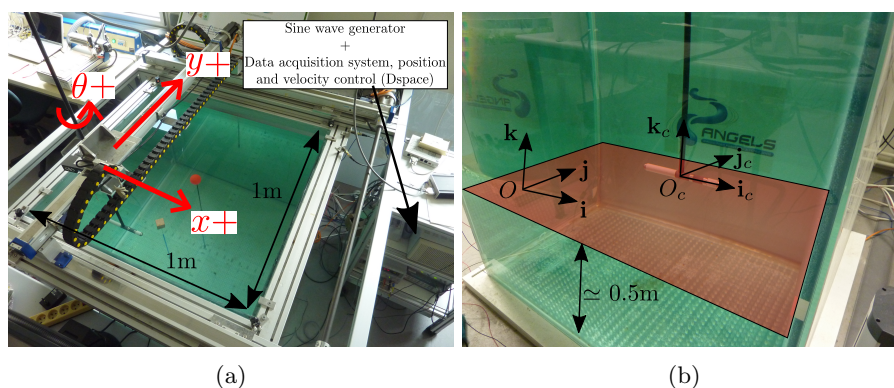


Figure 2.1: (a) Top view of the tank and the Cartesian robot. (b) In red, representation of the horizontal plane in which the sensor and the object lie, at mid-height of the tank. Frames $R = (O, \mathbf{i}, \mathbf{j}, \mathbf{k})$ and $R_c = (O_c, \mathbf{i}_c, \mathbf{j}_c, \mathbf{k}_c)$ are linked to the tank and the sensor respectively.

a Cartesian robot which has three degrees of freedom: two horizontal translations (x and y axis

parallel to axis \mathbf{i} and \mathbf{j} respectively), and one vertical rotation (angle θ about axis \mathbf{k}). The data acquisition system controls the position and/or the velocity of the three degrees of freedom using incremental encoders mounted on each axis. The maximum speed for both of the translations is 300mm/s and $80^\circ/\text{s}$ (13.5 rot/min) for rotation.

The sensor is linked to the robot with a rigid epoxy fiber tube which is parallel to axis \mathbf{k} . The sensor being orthogonally fixed at the end of that rigid tube, it lies in the plane $(O, \mathbf{i}, \mathbf{j})$ and its movements are thus controlled by the robot, see figure 2.1b. The sensor frame $R_c = (O_c, \mathbf{i}_c, \mathbf{j}_c, \mathbf{k}_c)$ is attached to the sensor, O_c being located at the geometrical center of the sensor, \mathbf{i}_c being parallel to the sensor's main axis and \mathbf{k}_c being vertical, as shown in figure 2.2. The rigid tube length is

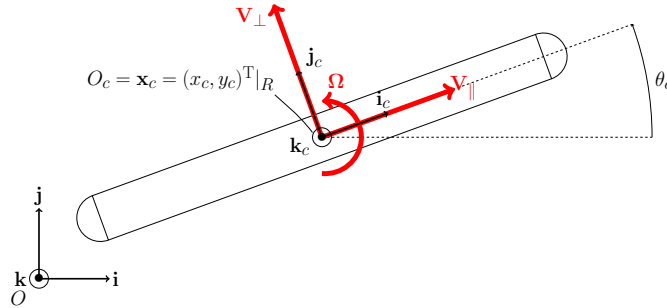


Figure 2.2: The coordinates defining the sensor pose in the fixed frame. \mathbf{V}_{\parallel} is the longitudinal velocity, \mathbf{V}_{\perp} is the lateral velocity and Ω the angular velocity about vertical axis \mathbf{k} .

adjusted so that planes $(O, \mathbf{i}, \mathbf{j})$ and $(O_c, \mathbf{i}_c, \mathbf{j}_c)$ coincide and are at mid-height of the tank. The sensor's pose in R is described with two Cartesian coordinates x_c and y_c and an angle θ_c , as shown in figure 2.2.

Throughout this thesis, the pose of the sensor (x_c, y_c, θ_c) will be considered as known at any instant.

Objects of different shapes, sizes and materials can be placed in the tank. In this thesis,

Object number	Material	a ($\text{m} \times 10^{-3}$)	b ($\text{m} \times 10^{-3}$)	$\eta = a/b$	$\mathcal{V} = 4\pi ab^2/3$ ($\text{m}^3 \times 10^{-6}$)
Object 1	Conductive	10	10	1	4.19
Object 2	Insulating	10	10	1	4.19
Object 3	Conductive	20	20	1	33.51
Object 4	Conductive	33	16	2	35.39
Object 5	Insulating	33	16	2	35.39
Object 6	Conducting	27	18	1.5	36.64
Object 7	Insulating	27	18	1.5	36.64
Object 8	Insulating	20	20	1	64

Table 2.1: The characteristics of the objects used in this thesis. In columns: material, semi-major axis a , semi-minor axis b , aspect ratio η and volume \mathcal{V} . For the cube (object 8), a and b are defined as half the edge length. Conductive and insulating objects are made of aluminum alloy and PVC (polyvinyl chloride), respectively. See the corresponding pictures in figure 2.3.

eight different objects are used for the experiments. They are presented in figure 2.3 and their

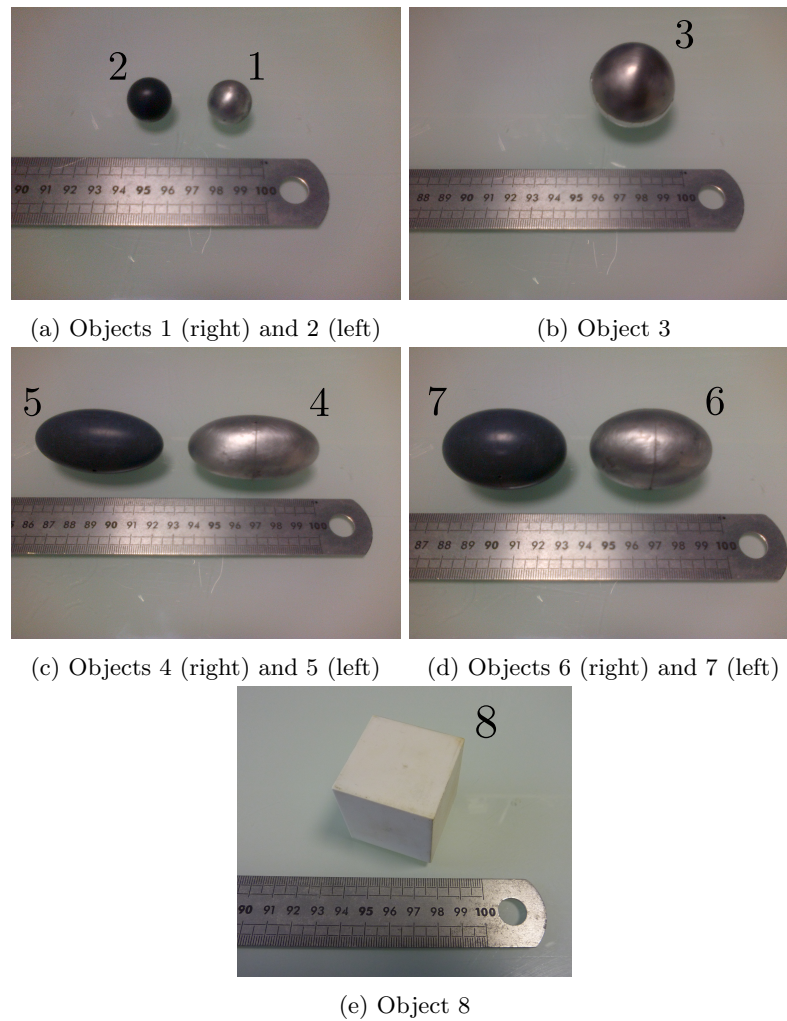


Figure 2.3: The objects used in this thesis for the experiments. Their characteristics are given in table 2.1.

characteristics are given in table 2.1. These objects have to be held fixed in the scene. A close attention has to be paid to the support of these objects, so that it does not perturb the currents' measurements. This issue is dealt in section 2.5.

2.2 Scene parametrization

Throughout this thesis, there will be only one object in the sensor's surroundings. Moreover, the shape of this object will be a prolate ellipsoid, that is, it has two semi-minor axis of equal values

and one semi-major axis. Its equation in Cartesian coordinates is

$$\frac{x^2}{a^2} + \frac{y^2}{b^2} + \frac{z^2}{c^2} = 1, \quad (2.1)$$

where a , b and c are the semi axis, with $a \geq b = c$ for prolate ellipsoids. The specific case where $a = b = c$ corresponds to the sphere of radius a . The cube (object 8) is an exception, but it can be approximated at first glance as a sphere.

Let $R_o = (O_o, \mathbf{i}_o, \mathbf{j}_o, \mathbf{k}_o)$ be the object's frame aligned with the three axis of the object, as shown in figure 2.4. Also, the main axes of the sensor and of the object will always lie in the same

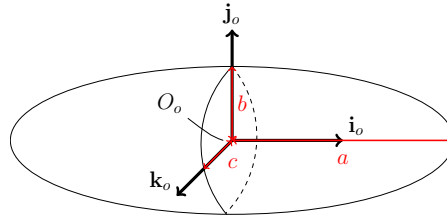


Figure 2.4: The object's frame and the three parameters that define its dimensions.

horizontal plane, leading to a top-bottom symmetry of the problem. Thus, the pose of the object in the fixed frame and in the sensor frame is defined with the Cartesian coordinates and angles (x_o, y_o, θ_o) and $(x_o^c, y_o^c, \theta_o^c)$ respectively.

Figure 2.5 shows the complete scene with these sets of parameters. The Cartesian coordinates

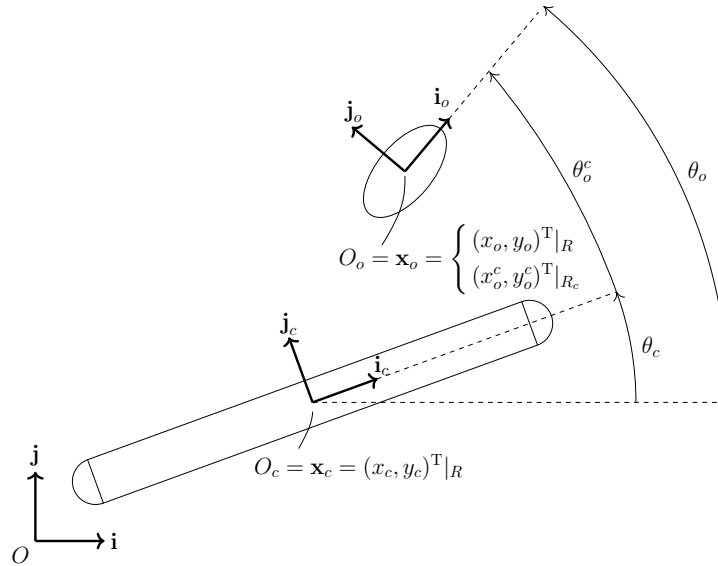


Figure 2.5: Parametrization of the scene using Cartesian coordinates. Because the problem is geometrically bi-dimensional, vectors \mathbf{k} , \mathbf{k}_c and \mathbf{k}_o were deliberately omitted for clarity.

are very suitable for currents modeling, as shown in chapter 3, and for the localization and shape

estimations tasks presented in chapter 5 and 6 respectively. Nevertheless, for the seeking object task described in chapter 4, Cartesian coordinates are not convenient and polar coordinates are preferred. Hence, we introduce another parametrization of the object's pose, by defining another sensor frame $R_p = (O_p, \mathbf{i}_c, \mathbf{j}_c)$, as shown in figure 2.6. In this frame, the object's center \mathbf{x}_o is

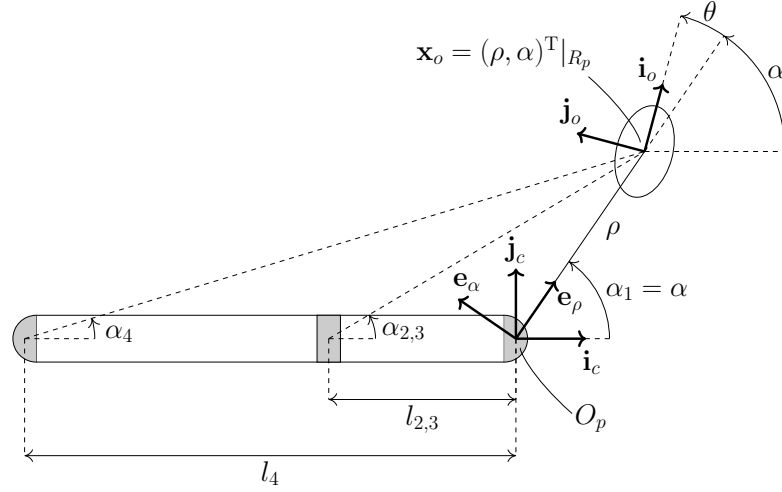


Figure 2.6: Parametrization of the object's center and orientation in polar coordinates. Only one cylindrical macro-electrode, denoted 2, 3, is represented for better clarity. The frame $R_p = (O_p, \mathbf{i}_c, \mathbf{j}_c)$ is attached to the sensor. The object's center is parametrized with $(\rho, \alpha)^T$ and its orientation with respect to the sensor axis with angle $\alpha + \theta$.

defined with polar coordinates (ρ, α) , and its orientation with respect to the sensor's main axis with angle $\alpha + \theta$.

2.3 Sensor's kinematics model

Here, we describe the sensor's kinematic model in both systems of coordinates.

In Cartesian coordinates, motion of the sensor in the fixed frame is described with the relationship between the vector of the sensor's pose $(x_c, y_c, \theta_c)^T$ (see figure 2.5) and the velocities input vector $(V_{\parallel}, V_{\perp}, \Omega)^T$ (see figure 2.2). Denoting \dot{x}_c , \dot{y}_c and $\dot{\theta}_c$ the temporal derivatives in R of the coordinates x_c , y_c and θ_c respectively, we have

$$\begin{cases} \dot{x}_c \mathbf{i} = V_{\parallel} \cos \theta_c \mathbf{i} + V_{\parallel} \sin \theta_c \mathbf{j}, \\ \dot{y}_c \mathbf{j} = -V_{\perp} \sin \theta_c \mathbf{i} + V_{\perp} \cos \theta_c \mathbf{j}, \\ \dot{\theta}_c \mathbf{k} = \Omega \mathbf{k}. \end{cases} \quad (2.2)$$

These equations are obtained by orthogonally projecting the vectors \mathbf{V}_{\parallel} and \mathbf{V}_{\perp} on fixed frame's vectors \mathbf{i} and \mathbf{j} . Projecting these equations on the basis vectors, we have the following sensor's

kinematics model

$$\begin{bmatrix} \dot{x}_c \\ \dot{y}_c \\ \dot{\theta}_c \end{bmatrix} = \begin{bmatrix} \cos \theta_c & -\sin \theta_c & 0 \\ \sin \theta_c & \cos \theta_c & 0 \\ 0 & 0 & 1 \end{bmatrix} \begin{bmatrix} V_{\parallel} \\ V_{\perp} \\ \Omega \end{bmatrix} \quad (2.3)$$

in Cartesian coordinates in the fixed frame R .

In polar coordinates, the pose vector is $(\rho, \alpha, \theta)^T$ (see figure 2.6). In order to establish the kinematics model with respect to that pose vector, we firstly express the velocity \mathbf{V}_0 , defined as the velocity of the center of the object, \mathbf{x}_0 , with respect to the sensor, in the frame R_p

$$\mathbf{V}_0 = \frac{d}{dt}(\mathbf{x}_0) \Big|_{R_p} = \frac{d}{dt}(\rho \cos \alpha \cdot \mathbf{i}_c + \rho \sin \alpha \cdot \mathbf{j}_c) = (\dot{\rho} \cos \alpha - \rho \dot{\alpha} \sin \alpha) \cdot \mathbf{i}_c + (\dot{\rho} \sin \alpha + \rho \dot{\alpha} \cos \alpha) \cdot \mathbf{j}_c. \quad (2.4)$$

The vector $(V_{\parallel}, V_{\perp}, \Omega)^T$ does not explicitly appear in this equation but with the use of another expression of \mathbf{V}_0 , it will. Indeed, the velocity \mathbf{V}_0 can also be written as a function of the velocity of the center of the sensor, denoted \mathbf{V}_c , which writes $\mathbf{V}_c = V_{\parallel} \cdot \mathbf{i}_c + V_{\perp} \cdot \mathbf{j}_c$ in R_p . The center of the object \mathbf{x}_0 being fixed with respect to R , the velocity \mathbf{V}_0 in R_p equals to the opposite of the velocity \mathbf{V}_c plus a term involving the distance between O_c and \mathbf{x}_0 and the rotation velocity Ω . Formally, we have

$$\mathbf{V}_0 = -\mathbf{V}_c + \left(\frac{l_4}{2} \cdot \mathbf{i}_c + \rho \cdot \mathbf{e}_\rho \right) \times \Omega \cdot \mathbf{k}_c = -\mathbf{V}_c + \left(\frac{l_4}{2} \cdot \mathbf{i}_c + \rho \cdot \cos \alpha \mathbf{i}_c + \rho \cdot \sin \alpha \mathbf{j}_c \right) \times \Omega \cdot \mathbf{k}_c, \quad (2.5)$$

where \times denotes the cross product. By developing the previous equation we get

$$\mathbf{V}_0 = (\rho \sin \alpha \Omega - V_{\parallel}) \cdot \mathbf{i}_c - \left(V_{\perp} + \frac{l_4}{2} \Omega + \rho \cdot \cos \alpha \Omega \right) \cdot \mathbf{j}_c, \quad (2.6)$$

and in virtue of the equality between (2.4) and (2.6) we obtain the following system

$$\begin{cases} \dot{\rho} \cos \alpha - \rho \dot{\alpha} \sin \alpha = \rho \sin \alpha \Omega - V_{\parallel} \\ \dot{\rho} \sin \alpha + \rho \dot{\alpha} \cos \alpha = -V_{\perp} - \frac{l_4}{2} \Omega - \rho \cdot \cos \alpha \Omega. \end{cases} \quad (2.7)$$

To get the expression of $\dot{\rho}$ (resp. $\dot{\alpha}$), we multiply the first equation of the previous system with $\cos \alpha$ (resp. $\sin \alpha$) and the second one with $\sin \alpha$ (resp. $\cos \alpha$), and then we calculate their sum (resp. differences). As a result, we have

$$\begin{cases} \dot{\rho} = -V_{\parallel} \cos \alpha - V_{\perp} \sin \alpha - \frac{l_4}{2} \sin \alpha \Omega \\ \dot{\alpha} = \frac{V_{\parallel} \sin \alpha}{\rho} - \frac{V_{\perp} \cos \alpha}{\rho} - \Omega \left(\frac{l_4 \cos \alpha}{2\rho} + 1 \right). \end{cases} \quad (2.8)$$

Finally, considering the relationship $\Omega = -\dot{\theta} - \dot{\alpha}$, we have as a third equation

$$\dot{\theta} = -\frac{V_{\parallel} \sin \alpha}{\rho} + \frac{V_{\perp} \cos \alpha}{\rho} - \Omega \frac{l_4 \cos \alpha}{2\rho}. \quad (2.9)$$

As a result, we have the following sensor's kinematics model in polar coordinates in the frame R_p

$$\begin{bmatrix} \dot{\rho} \\ \dot{\alpha} \\ \dot{\theta} \end{bmatrix} = \begin{bmatrix} -\cos \alpha & -\sin \alpha & -\frac{l_4 \sin \alpha}{2} \\ \frac{\sin \alpha}{\rho} & -\frac{\cos \alpha}{\rho} & -\left(\frac{l_4 \cos \alpha}{2\rho} + 1 \right) \\ -\frac{\sin \alpha}{\rho} & \frac{\cos \alpha}{\rho} & \frac{l_4 \cos \alpha}{2\rho} \end{bmatrix} \begin{bmatrix} V_{\parallel} \\ V_{\perp} \\ \Omega \end{bmatrix}. \quad (2.10)$$

Now the scene parametrization and the kinematics of the sensor are defined, let us detail its geometrical characteristics and how the active electro-sensing is implemented through it.

2.4 Sensor

In this section we describe in details the actual sensor. The elements that it is composed of and its dimensions are firstly presented. Then, the polarization and measurement strategy and electric circuit are introduced and finally, a study of the electrical impedance of the scene is presented.

2.4.1 Sensor's structure and dimensions

The sensor is cylindrical, 22cm long and 2cm diameter, see figure 2.7. It is composed of an in-

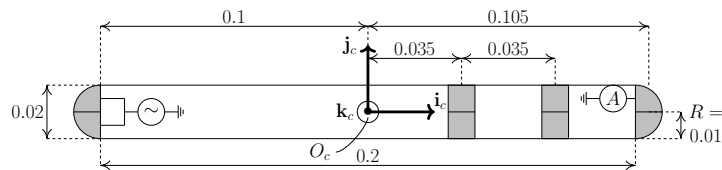


Figure 2.7: Dimensions of the sensor (in meter) and its related frame $R_c = (O_c, \mathbf{i}_c, \mathbf{j}_c, \mathbf{k}_c)$ (top view). Conducting parts (electrodes) are in grayed out. Inspired from [54].

insulating body and eight electrically isolated electrodes $e_{n=1,\dots,8}$. Electrodes are gathered in four pairs of left-right symmetrical electrodes, denoted $\mathcal{E}_{k=1,\dots,4}$ and named macro-electrodes (see figure 2.8). The voltage generator connected to \mathcal{E}_4 and the ampere-meter connected to e_1 in figure

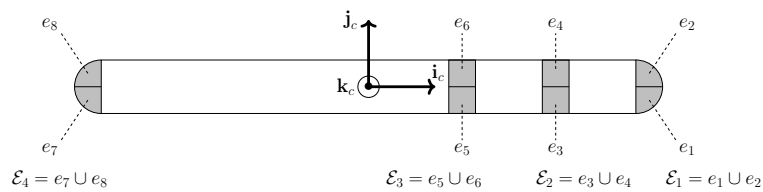


Figure 2.8: The electrodes $e_{n=1\dots 8}$ and macro-electrodes $\mathcal{E}_{k=1,\dots,4}$ numbering.

2.7 represent one of the macro-electrode polarization and electrode current measurement configuration that it is possible to perform with that sensor. Polarization and current measurement are details in the following section.

2.4.2 Implementation of the active electro-sensing

This sensor was designed to perform active electro-sensing, just like the weakly electric fish do. It implements the two fundamental functions of active electro-sensing 1) produce an electric field in the surroundings ; 2) acquire the electric image. We firstly introduce how the principles of the active electro-sensing are implemented and then, the involved electric circuit and digitalization process that allow this implementation. Finally, experiments and a theoretical study showing that the impedance of the scene can be reasonably considered as purely resistive are presented.

Field generation principle

One of the two functions of the active electro-sensing is the electric field generation. In order to produce that field (said as basal field) a macro-electrode is set under an electric potential with respect to the three others as shown in figure 2.7, where \mathcal{E}_4 is plugged to the sine wave generator. A software controlled switch allows each macro-electrode to be polarized in turn, so that four different basal fields can be produced, represented in figure 2.9. The basal field topology depends

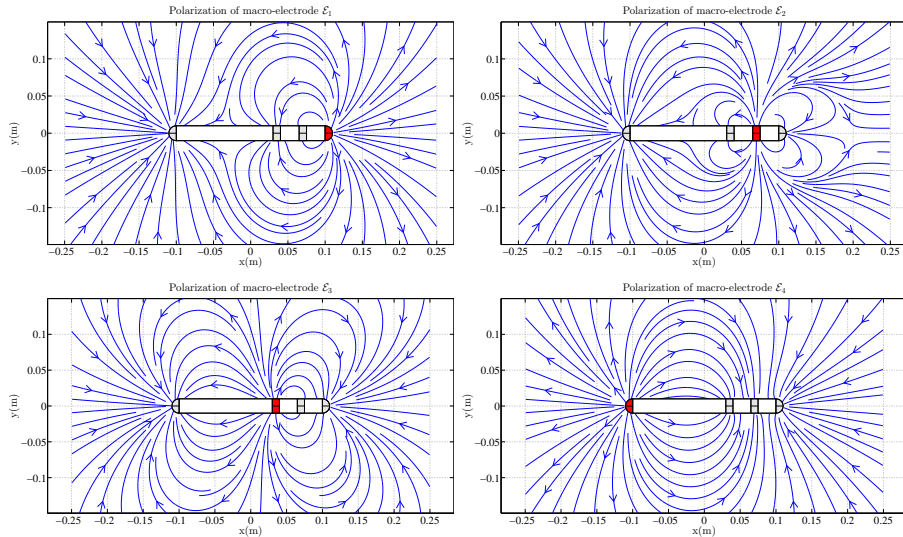


Figure 2.9: The basal field corresponding to the four possible polarizations of macro-electrodes, computed with the analytical model introduced in chapter 3.

on the sensor's geometry and on the relative electrodes' positions. The underlying physics that describes the electric field behavior is detailed in chapter 3.

Image acquisition principle

The second function consists in acquiring the electric image. It is performed by measuring the electric current flowing through each electrode, as shown in figure 2.7, where e_2 is plugged to the ampere-meter. Because the input quantity is a voltage (U) and the measured quantity is a

current (I), this strategy is named as U-I mode. The actual measurement system does not allow current measurement on the electrodes of the polarized macro-electrode. The table 2.2 sums

	Measurement electrodes							
	e_1	e_2	e_3	e_4	e_5	e_6	e_7	e_8
Polarized macro-electrodes	\mathcal{E}_1	×	×	✓	✓	✓	✓	✓
	\mathcal{E}_2	✓	✓	×	×	✓	✓	✓
	\mathcal{E}_3	✓	✓	✓	✓	×	×	✓
	\mathcal{E}_4	✓	✓	✓	✓	✓	✓	×

Table 2.2: Available current measurements (columns) for a given polarized macro-electrode (rows). Crosses (×) indicate non available measurements. Any other measurement is possible (✓).

up the available current measurements for a given polarized macro-electrode. So, for a given polarized macro-electrode, the electric currents flowing through the six available electrodes can be independently measured.

Electric circuit and digitalization process

The polarization and measurement scheme is given in figure 2.10, showing polarized electrode e_1 and current measurement on electrode e_k . Necessarily, according to table 2.2, electrode k represents any electrode $e_{i=3,\dots,8}$. The voltage sine generator polarizes electrode e_1 with respect

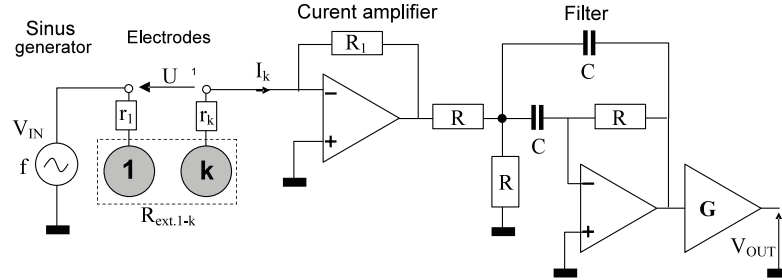


Figure 2.10: Polarization and measurement scheme, composed of a sine voltage generator, two electrodes e_1 and e_k , a current amplifier and a band-pass filter. G is the output gain of the filter. Electrode e_1 is polarized with a potential U , while current through electrode e_k denoted I_k is measured. Electric resistances of the electrodes' respective wires are represented with r_1 and r_k . $R_{\text{ext.1-k}}$ represents the external resistance of the scene between both electrodes. Taken from [81].

to e_k with voltage V_{IN} . This electromotive force induces an electric current in the scene and as a result, current I_k flows through e_k . The relationship between the input voltage U and the measured current I_k is given by

$$I_k = \frac{U}{Z_k}, \quad (2.11)$$

Z_k being the complex impedance corresponding to the wires and the scene. Here, the impedance of the wires and the scene are considered as purely resistive. This hypothesis holds when the

frequency of signal V_{IN} is set to $f = 22.5 \times 10^3$ Hz. This particular frequency was determined with a frequency sweeping process, described later in this section. Then, an analog conditioning of I_k is performed: amplification and band-pass which center frequency is f . The output voltage of the circuit is V_{OUT} . According to [81], V_{OUT} is a linear function of I_k

$$V_{OUT} = \frac{GR_1}{2} I_k. \quad (2.12)$$

The acquisition of voltage V_{OUT} is performed with a remote 16 bits resolution Dspace acquisition device. The measurement range is $\pm 10V$, leading to a 0.3mV voltage resolution. The sampling rate is determined by the signal V_{IN} frequency, by generating a square signal at the same frequency f . Both signals are synchronized, so that the maximum value of V_{IN} corresponds to the falling edge of the square signal, as shown in figure 2.11. Falling edges trigger the digitalization of

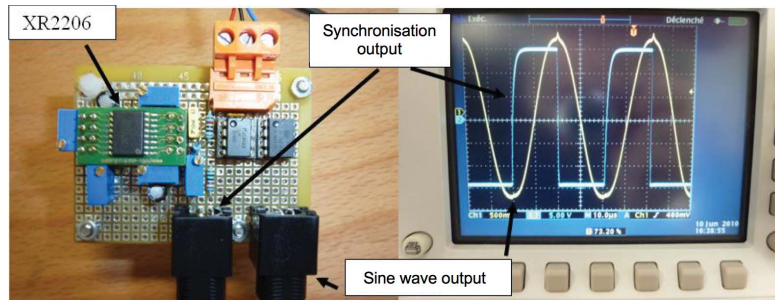


Figure 2.11: For amplitude variation measurement, a square signal is generated, synchronized with the polarization sine signal. Taken from [81].

V_{OUT} in order to have one measurement per signal period. Due to this acquisition strategy, only amplitude variation can be measured, and a phase shift between V_{OUT} and V_{IN} would produce amplitude measurement errors. But the following study shows that there is no phase shift in our problem.

Resistive behavior of the system

As explained above, the acquisition strategy is designed for a purely resistive behavior of the system (scene + electric circuit). Here, we show that in the context of robotics, which is largely composed of objects made of plastic (insulating) and metal (conductive) materials¹, this consideration is true. This presentation is split in two parts 1) we present the frequency response of the system without object in the scene and a convenient frequency is chosen so that the phase is canceled out ; 2) we present the electrical characteristics of different object's materials and show that materials of interest in robotics applications (plastic, metal) have a purely resistive response.

In [81], a measurement of the complex impedance Z_k is presented. It was carried out as follows. The sensor was immersed in three different tanks (25l, 150l and 1000l), with no other object, and a frequency sweeping of signal V_{IN} was performed while I_k was measured. As shown in figure

¹ Contrary to the natural environment of the fish, which is mostly composed of organic matter (plants and animals).

2.12, the phase of the complex impedance (due to the sensor itself, the wires, the water and the tank) is the lowest, close to 0, for frequencies between 5×10^3 Hz and 5×10^4 Hz. According to

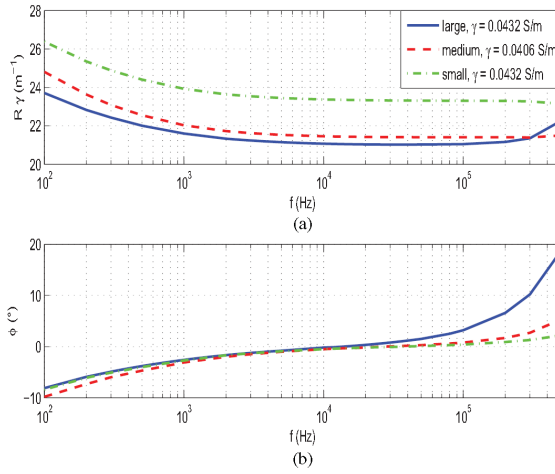


Figure 2.12: Bode diagram of the complex impedance for three different tank sizes. Top: module (db), bottom: phase. In the legend, γ refers to the actual conductivity of the water. Taken from [81].

[81], this behavior is mainly due to three contributions:

1. capacitance of the water is the lowest between 5×10^3 Hz and 5×10^4 Hz,
2. contact impedance between electrodes and water is low above 10^3 Hz,
3. impedance of the coaxial cable becomes significant above 10^5 Hz.

Hence, the chosen frequency for signal V_{IN} is 22.5×10^3 Hz, ensuring that no phase shift is observed between V_{IN} and V_{OUT} .

We now have to deal with the case in which an object is introduced. In fact, adding an object to the scene potentially introduce a phase shift between the polarization and measured signals, depending on the object's material. This was experimentally emphasized by Bai in [8] using the SensorPod showed in figure 1.23a. Figure 2.13 shows typical measurements presented in [8], where amplitude and phase shift are plotted against frequency for several objects. For insulating material (Nylon), amplitude and phase shift do not significantly vary with frequency. On the other hand, plant, grape and tomato produce non negligible phase around 22.5×10^3 Hz, the frequency under consideration for us. In order to complete these experimental results, we now present a theoretical study of the complex impedance of the scene depending on the object's material. We get as a starting point the Rasnow's model of potential perturbation due to a spherical object (1.1). In this expression, a complex number, denoted χ and named contrast factor, represents the dielectric contrast between the object and the medium

$$\chi = \frac{\rho_1 - \rho_2 + i\omega\rho_1\rho_2(\epsilon_2 - \epsilon_1)}{2\rho_2 + \rho_1 + i\omega\rho_1\rho_2(2\epsilon_1 + \epsilon_2)}, \quad (2.13)$$

where ρ_1 and ρ_2 are the resistivities of the medium and the object respectively, ϵ_1 and ϵ_2 are the dielectric permittivities of the medium and the object respectively, and ω is the angular

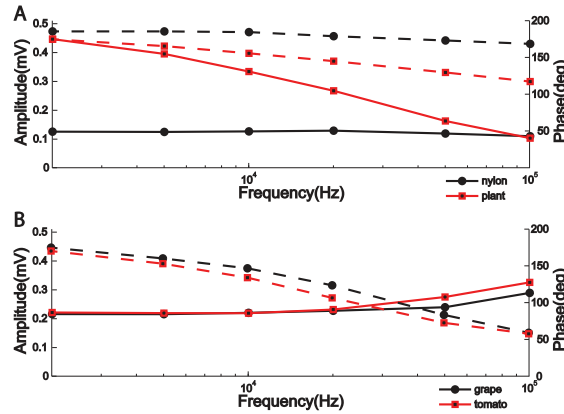


Figure 2.13: Amplitude and phase measurement for Nylon, plant, grape and tomato, using the SensorPod (straight lines: amplitude, dashed lines: phase). Taken from [8].

frequency of the basal electric field \mathbf{E}_0 (see figure 1.8). An object produces phase shift between polarization signal and measured signal when the imaginary part of χ is not zero. In order to study the imaginary part of χ relatively to the surrounding medium, we firstly define coefficients α and β as the ratios of the resistivities and permittivities respectively

$$\rho_2/\rho_1 = \alpha, \quad \epsilon_2/\epsilon_1 = \beta, \quad (2.14)$$

and then rewrite (2.13) as a function of (α, β)

$$\chi = \frac{1 - \alpha + i\omega\rho_1\epsilon_1\alpha(\beta - 1)}{2\alpha + 1 + i\omega\rho_1\epsilon_1\alpha(\beta + 2)}. \quad (2.15)$$

This formulation is more convenient in order to make the study relatively to the surrounding

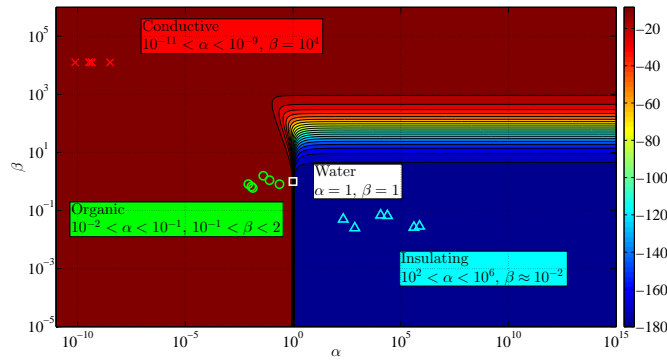


Figure 2.14: Angle $arg(\chi)$ as function of α and β , in degrees, at $f = 22.5\text{kHz}$. Water location ($\alpha = \beta = 1$) is represented with a white square, conductive materials with red crosses, insulating materials with blue triangles and organic materials with green circles. Material characteristics are taken from table A.1.

medium. The argument of complex number χ is

$$arg(\chi) = \arctan\left(\frac{\omega\rho_1\epsilon_1\alpha(\beta - 1)}{1 - \alpha}\right) - \arctan\left(\frac{\omega\rho_1\epsilon_1\alpha(\beta + 2)}{2\alpha + 1}\right). \quad (2.16)$$

At $f = 22.5$ kHz, $\arg(\chi)$ as a function of α and β is plotted in figure 2.14. In the (α, β) plan, $\arg(\chi)$ for conductive and insulating materials has constant values: $\arg(\chi) = 0^\circ$ and $\arg(\chi) = -180^\circ$ respectively. Organic materials, whose characteristics are close to that of the water, potentially introduce a non zero imaginary part. This is shown in figure 2.15a, where

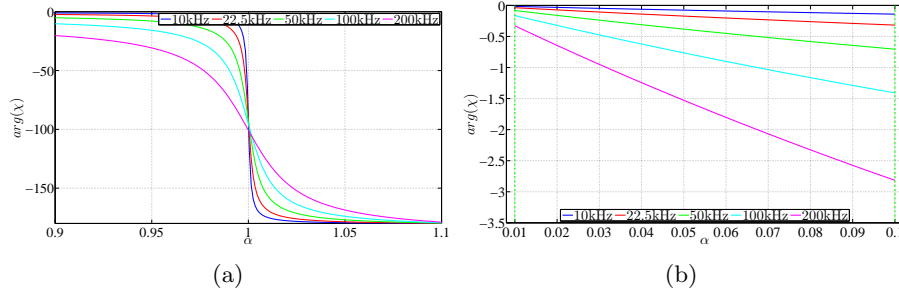


Figure 2.15: (a) Angle $\arg(\chi)$ as function of $\alpha \in [0.9; 1.1]$ for $\beta = 0.9$, in degrees, for several frequencies. (b) Same as (a) but in the range $\alpha \in [0.01; 0.1]$

$\arg(\chi)$ is plotted against α for $\beta = 0.9$. Particularly, in the range $\alpha \in [0.01; 0.1]$ which concerns the organic materials, figure 2.15b shows that phase shift can be in the range $[-2.8; 0]$, depending on the frequency. Such value of phase shift is quite small compare to the values in [8]. The reason is that figures 2.14, 2.15a and 2.15b only concern the materials themselves, whereas results in [8] are related to measurements with complete objects: tomatoes, grapes, plants, nylon, etc. With complete objects, other parameters have to be taken into account, such as the skin of the fruits which introduce capacitive effects, thus increasing the phase shift.

Now, let us look at the magnitude of χ , denoted $|\chi|$, as a function of α and β on figure 2.16, and which expression is

$$|\chi| = \left(\frac{(1 - \alpha)^2 + (\omega\rho_1\epsilon_1\alpha(\beta - 1))^2}{(2\alpha + 1)^2 + (\omega\rho_1\epsilon_1\alpha(\beta + 2))^2} \right)^{1/2}. \quad (2.17)$$

As for the argument in figure 2.14, $|\chi|$ for conductive and insulating has constant values 1 and

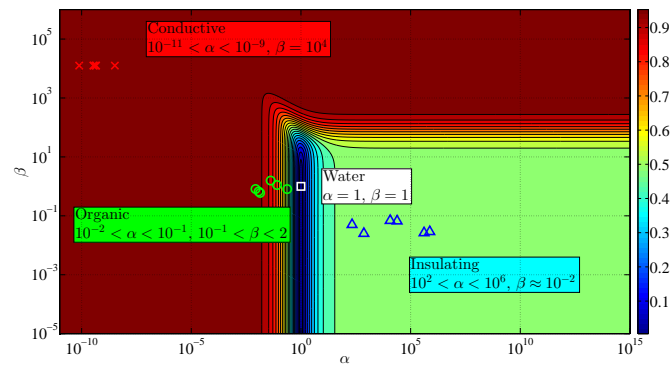


Figure 2.16: Magnitude $|\chi|$ as function of α and β , in degrees, at $f = 22.5$ kHz. Water location ($\alpha = \beta = 1$) is represented with a white square, conductive materials with red crosses, insulating materials with blue triangles and organic materials with green circles. Material characteristics are taken from table A.1.

1/2 respectively, in the (α, β) plan. Though, organic materials lead to different magnitude values depending on α and β as shown in figure 2.17.

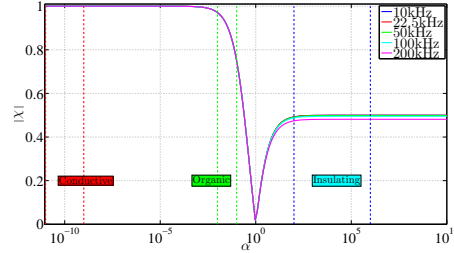


Figure 2.17: Magnitude $|\chi|$ as function of $\alpha \in [10^{-11}; 10^{10}]$ for $\beta = 0.9$, for several frequencies. Ranges of α for the conductive, organic and insulating materials are indicated with the vertical dotted lines.

As a conclusion, the materials with dielectric characteristics that strictly contrast with that of the water have a purely resistive behavior. In this case, the imaginary part of the contrast factor can be neglected with respect to its real part and equation (2.13) can be rewritten as

$$\chi \simeq \frac{\rho_1 - \rho_2}{2\rho_2 + \rho_1}, \quad (2.18)$$

or equivalently, in term of conductivities

$$\chi \simeq \frac{\gamma_o - \gamma}{2\gamma + \gamma_o}, \quad (2.19)$$

where γ and γ_o are the conductivities of the water and the object respectively. In our experiments, the material of the object is either aluminum ($\alpha \simeq 10^{-10}$, $\beta \simeq 10^4$) or PVC ($\alpha \simeq 10^3$, $\beta \simeq 10^{-2}$). This ensures the contrast factor to be either 1 (conductive) or -1/2 (insulating).

2.5 Currents measurements in practice

In practice, some precautions have to be taken when currents are measured in presence of an object. Firstly, the actual currents are necessarily vitiated with noise. Secondly the sensor does not navigate in an infinitely large aquarium, so the insulating walls has a non negligible effect on the measured currents. Thirdly, a special care has to be made about the support of the object, which holds it fixed in the scene. Here, we present some results about the measurement noise characterization, and then describe a standard measurement configuration, named as "fly-by test", which will help to evaluate the influence of the walls and the object's support on the measurements.

2.5.1 Noise characterization

The electronic noise of the experimental test bench was characterized and presented in [81], and we sum up the main results here. The sensor used for that study was composed of only two

hemispherical macro-electrodes: \mathcal{E}_1 and \mathcal{E}_4 in figure 2.8. It was placed at mid-height of the aquarium, like in figure 2.1b, but in radial contact to the wall. No displacement was set during this experiment but the motors of the gantry were let switched on. The current I was acquired for

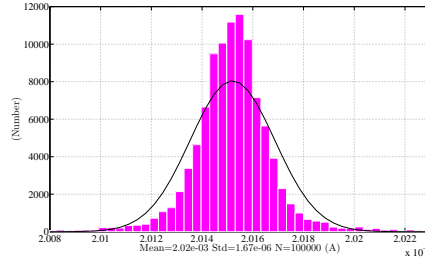


Figure 2.18: The noise distribution of current measurements obtained with a population of 100,000 individual measurements. Straight line: Gaussian function of same average and standard deviation as the distribution.

a population of 100,000 individual measurements, which led to the distribution shown in figure 2.18. The mean and standard deviation of this distribution are 2.02×10^{-3} A and 1.67×10^{-6} A respectively. This distribution does not fit the Gaussian function of same average and standard deviation, showing a non-Gaussian noise behavior of the noise. This is due to the non-random noise produced by the motors of the Cartesian robot. However, we take ± 3 standard deviation as the measurement error range (statistically covering 99.7% of the population), which leads to an error range expressed as the percentage of the mean value of $\pm 0.1\%$. This measurement noise characterization will be used in the next chapters in order to add representative noise on our simulated currents.

Now, we are interested in evaluate the effects of the aquarium and the object's support on the measurements. To that end, we have to firstly define a typical measurement configuration named as fly-by test. This is the purpose of the next section.

2.5.2 Fly-by test

In presence of an object, a typical measurement configuration is defined as the fly-by test. It consists in a straight line displacement of the sensor, passing by an object. The sensor longitudinal velocity V_{\parallel} is set as a constant whereas lateral velocity V_{\perp} and angular velocity Ω are set to 0. Thus, lateral distance y_c^c is constant. Figure 2.19a shows an example of fly-by test in which the trajectory of the object with respect to the sensor is drawn. While the sensor is moving, a macro-electrode is set to a constant potential with respect to the three others. Hence, the object is submitted to a variable basal field. With the analytical model (described in chapter 3), the basal field at the center of the object for 8 sample points of the trajectory are computed and shown in figure 2.19b. We observe that the object is submitted to a rotating field which varies in magnitude. The field magnitude is the lowest when the object is far form the sensor (positions 1 and 8) and gets its maximum value when the object is close to \mathcal{E}_4 (position 6).

Now, let us turn our attention to the currents that flow through the electrodes during this fly-by test. To that end, it is necessary to complete the description of the fly-by test above with some practical considerations. Indeed, the representation of figure 2.19a is an ideal case, where there

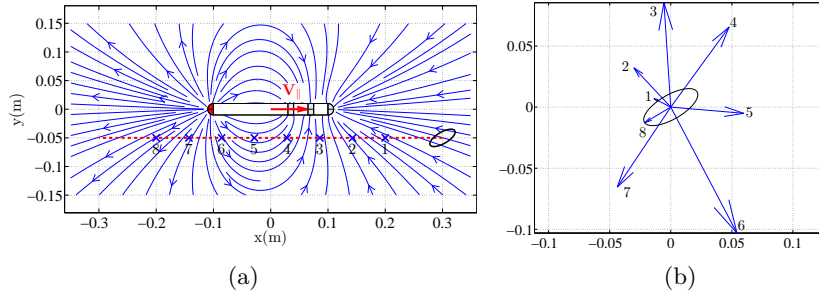


Figure 2.19: (a) A fly-by test with polarization of macro-electrode \mathcal{E}_4 . The object (represented at its initial position) is ellipsoidal and rotated with a constant angle θ_c^c with respect to the sensor's axis. The trajectory of its center with respect to the sensor is represented with the dashed straight line (constant lateral distance y_o^c). For 8 sample points of the trajectory, numbered 1 to 8, the basal field is plotted in figure 2.19b. Actually, the object is fixed and the sensor moves in straight line, this representation is a sensor point of view. (b) The ellipsoid and the 8 different basal fields to which it is submitted, corresponding to the 8 positions shown in figure 2.19a. The scale for this representation of the field is arbitrary, but the relative magnitudes are respected. This field was computed with the analytical model described in chapter 3.

is no other element in the scene than the sensor and the object. But, in actual conditions, the presence of the tank and the support that holds the object has to be taken into account. In

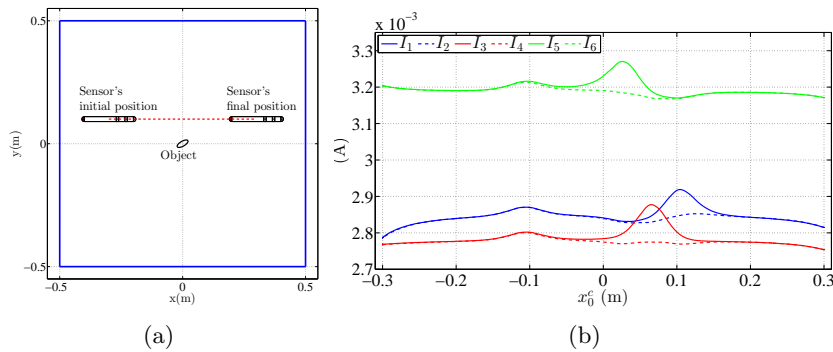


Figure 2.20: (a) The actual fly-by test configuration. The object is held at the center of the aquarium, the latter being represented with the blue solid lines. The sensor moves in straight line, the trajectory of its center being represented with the dashed line. At each end of its trajectory, the sensor is close to the walls. (b) Measured currents corresponding to the actual fly-by test. Horizontal axis represents the position of the object's center relatively to the sensor's center (x_o^c in figure 2.5), while vertical axis represents the currents' magnitude.

figure 2.20a is represented the actual configuration of the fly-by test: the object is fixed in the middle of the tank and the sensor, moved by the robot, passes by the object.

As an example, figure 2.20b shows the measured currents $I_{1,\dots,6}$ during an actual fly-by test with the following conditions

February 7, 2018

- Polarized macro-electrode: \mathcal{E}_4 ,
- Object 3 in table 2.3 (2cm radius conductive sphere),
- $x_0^c \in [-300; 300]$ mm,
- $y_0^c = -50$ mm (the object passes by the sensor on its right side).

Note that, in accordance with table 2.2, the currents I_7 and I_9 are not measured because macro-electrode \mathcal{E}_4 is polarized. The currents presented in figure 2.20b are composed of a superimposition of several contributions.

If we consider a scene that would be composed of the sensor only (no object, infinitely large tank), the sensor responds to its own basal field only. In this case, the currents that flow through the electrodes correspond to the polarized sensor's. Then, if we consider the sensor in a tank that is sufficiently small (our $1\text{m} \times 1\text{m} \times 1\text{m}$ tank can be considered as "sufficiently small", as shown in the next section), the insulating walls are polarized by the basal field. As a consequence, they produce an additive component on the currents, which adds up to the sensor's contribution. The sensor's and tank's contributions can be gathered and named as basal currents, represented by the vector of currents I^0 in chapter 3.

With an object that is introduced in the scene, located at the center of the aquarium, its response to the basal field adds up to the basal currents, if we assume that a polarized wall do not polarize in turn the object. This is a reasonable hypothesis, considering the distance between each wall and the object ($\simeq 50\text{cm}$).

Last but not least, the object's support potentially provides a supplementary component to the currents. The two following sections present the object's support and the basal currents contributions during an actual fly-by test.

2.5.3 Object's support effect

When performing a fly-by test in presence of an object, the latter has to be held static at the center of the aquarium, in the sensor horizontal plane. As it will be shown in the next section, the walls' effects can be canceled out by subtraction because there does not exist any mutual polarization between the walls and the object. For the object's support, this assumption does not hold because they are in contact with each other. So, the support has to produce minimal effect on the measurements. We have tested two means for the object fixing: the rigid stand and the Nylon string. Here, we describe both of them and evaluate their effects on the currents.

One of the means to hold an object static is the stand, fixed at the bottom of the tank and composed of

- a 1mm diameter conductive rod onto which it is sticked,
- an insulating support,
- a threaded end that is screwed in the bottom of the tank.

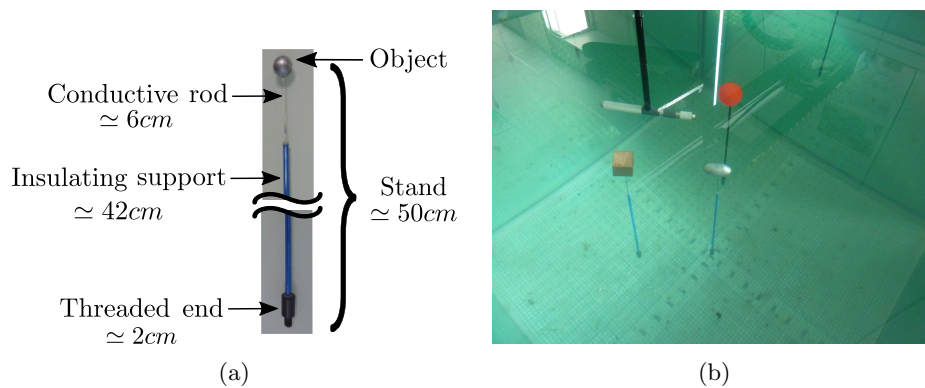


Figure 2.21: (a) A stand for the object. Total length is about 50cm. (b) The sensor with three objects, each being fixed on a stand described in (a).

Figure 2.21a describes this assembly. The total length is about 50cm so that the object's center is closely at the mid-height in the aquarium. Another solution for maintaining the objects static in the sensor plane is the Nylon string. The objects are drilled with a 1mm diameter hole and one can pass a 0.22mm diameter Nylon string through it. One end of the string is attached to an anchor in the bottom of the tank. The other end is attached to a rigid support above the water surface so that the string is maintained taut. See figures 2.22a and 2.22b. Now, let us

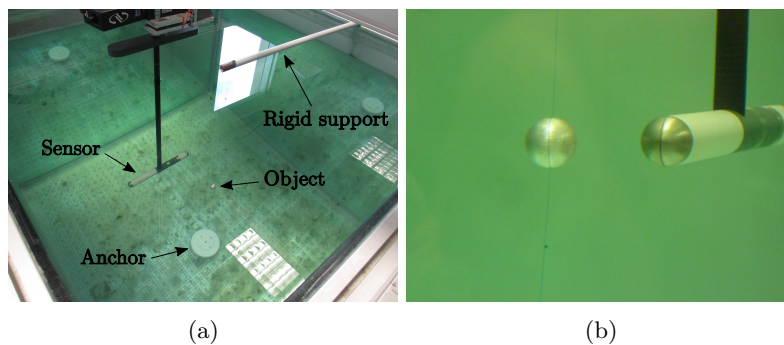


Figure 2.22: (a) A 1cm radius conductive sphere held with a 0.22mm diameter Nylon string, taut between an anchor and a rigid support. (b) Zoom on the object and the sensor in the same horizontal plane.

evaluate the effects of both the stand and the Nylon string on the measurements. For the stand, two experiments were performed. They both consist in fly-by tests with a scene composed of the stand only (no object on it), with and without a 60mm long conductive rod. Measurements were performed for different lateral distances d and heights h , with respect to the top of the insulating support, as described in figure 2.23a. For the first test, the conductive rod is removed in order to evaluate the effect of the insulating support only. The sensor was located at three different heights $h = \{10, 30, 60\}$ mm and at one lateral distance $d = 20$ mm. The current I_2 during the fly-by tests for these three positions are shown in figure 2.23b. We can see a global bending that is identical for the three currents. This is the walls' effects, which is detailed next section. Over that global variation, we observe current deviations only for the current that corresponds to $h = 10$ mm. The two other currents show that we have no current deviation due to the insulating

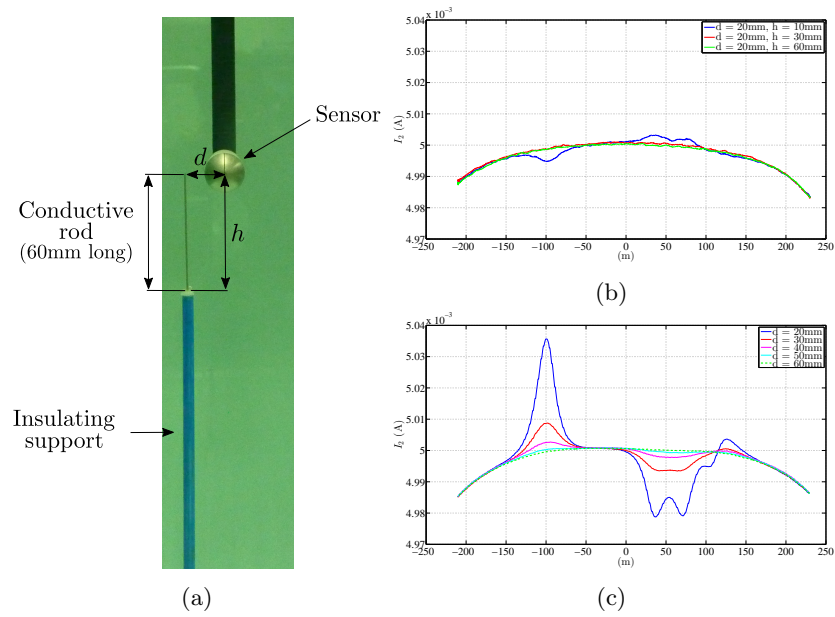


Figure 2.23: (a) Representation of the lateral distance d and height h . (b) Current I_2 without the conductive rod during a fly-by test for $d = 20\text{mm}$ and $h = \{10, 30, 60\}\text{mm}$. (c) Current I_2 with the conductive rod during a fly-by test for $h = 60\text{mm}$ and $d = \{20, 30, 40, 50, 60\}\text{mm}$.

support if $h \geq 30\text{mm}$. For the second test, the 60mm long conductive rod is placed on top of the insulating support in order to evaluate its effects on the currents. Sensor's height in remained constant, $h = 60\text{mm}$, and lateral distances $d = \{20, 30, 40, 50, 60\}\text{mm}$. In figure 2.23c, one can see that for $d \leq 50\text{mm}$, the conductive rod has a non negligible effect on the measurement. A fly-by test was performed with the Nylon string only (no object) at $d = 20\text{mm}$ in order check if it does not have an effect on the measurements. Figure 2.24a shows that its electrical response

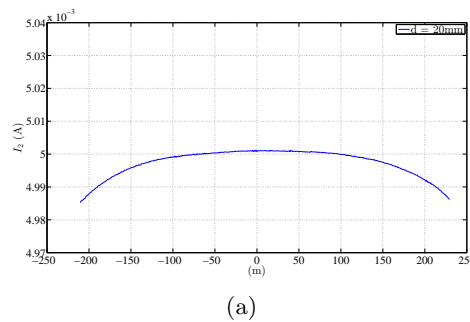


Figure 2.24: Current I_2 with a vertical Nylon string (no object) during a fly-by test for $d = 20\text{mm}$.

is not perceptible in the measurements.

As a conclusion, for fly-by tests where the lateral distance of the object with respect to the sensor ($|y_0^c|$) is below 50mm, the Nylon string must be used as object's support. By the way, all the experiments presented in this thesis were performed with the Nylon string as object's support.

2.5.4 Aquarium effects

In the previous section, we stated that the tank has an effect on the currents measurements, illustrated by the global bending of the current I_2 in figures 2.23b, 2.23c and 2.24a. Here, we propose to evaluate this effect for all the measured currents and show that it is possible to cancel out this contribution from the measurements. To that end, we perform a fly-by test, but with only the sensor in the tank. The resulting currents are shown in figure 2.25. We observe

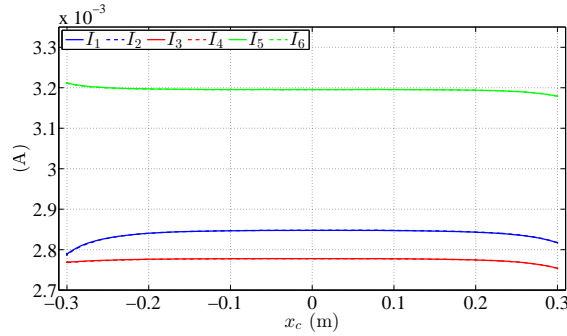


Figure 2.25: Measured currents corresponding to the fly-by test with no object in the tank. For each macro-electrode, both of the measured currents take the same value.

constant values when the sensor is close to the middle of the tank. In this case, the walls are sufficiently far from the sensor so that they have no effect on the measurements. Hence, the current values measured when the sensor is at the center of the tank can be considered as the sensor's contribution only. When the sensor approaches the walls ($|x_c| \geq 0.15\text{m}$), we observe non negligible currents' variations indicating that the walls are polarized by the basal field and thus have an influence on the currents. For a fly-by test with an object at the middle of the tank, these walls' effects are not desirable, but can easily be canceled out, assuming that a polarized wall do not polarize in turn the object. The respective contributions of the walls and of the object to the currents can be supposed as additive contributions. So, in practice, each fly-by test has to be performed twice 1) with the object ; 2) without the object. The currents of the second

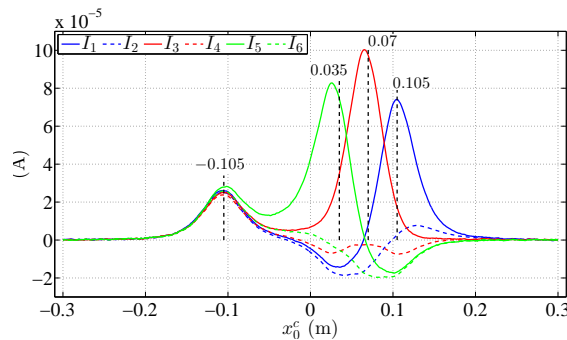


Figure 2.26: Currents from figure 2.20b (with object, held by the Nylon string) from which the currents from figure 2.25 (without object) were subtracted. The vertical dotted lines correspond to the longitudinal positions of the macro-electrodes in the sensor frame, with their respective values above.

round are subtracted to those of the first round, so that the walls' effects are deleted. See figure 2.26. Note that this currents' subtraction process also deletes the sensor's effect. The resulting currents only contain the object's contribution. That is why all the currents vanish when the object is far from the sensor, that is, for ($|x_0^c| \geq 0.2\text{m}$). The currents on the right side of the sensor (I_1 , I_3 and I_5) have much more variations compare to the currents on the left side (I_2 , I_4 and I_6). This is due to the fact that the object passed by the sensor on its right side during that test, and the left side of the sensor was less exposed to the field of the polarized object. Currents I_1 , I_3 and I_5 also have their maximum values when the object faces the corresponding electrode: $x_0^c \simeq 0.105\text{m}$ for current I_1 , $x_0^c \simeq 0.07\text{m}$ for current I_3 and $x_0^c \simeq 0.035\text{m}$ for current I_5 . This is in accordance with the electrodes' positions presented in figure 2.7.

At this point, we have presented the sensor, the tank in which it navigates thanks to the Cartesian robot and the equations of its locomotion. The objects were also introduced, made of either conductive or insulating material. It was shown that they produce a purely resistive electrical response when they are submitted to an electric field. Then, the electric circuit of the sensor, which was designed to measure such response, was detailed. Finally, a typical measurement configuration named as the fly-by test was presented. It was shown that the effects of the walls on the measurements could be subtracted afterward. Also, a particular attention has to be paid to the object's support: for measurements which lateral distance to the object is lower than 50mm, the object has to be held with a Nylon string in order to avoid non desirable additional components in the measurements.

The measured currents presented in this chapter are the expression of the interactions between the elements of the scene through the electric field produced by the sensor. In order to have a physical interpretation of these currents, we present in the next chapter the underlying physics of the electric sense. Also, two models for the computation of the currents for a given scene will be presented.

Chapter 3

Physics and models

In this chapter, we describe the direct problem of active electrolocation. A scene is considered, composed of insulating and conductive objects lying in a conductive medium. Some of the conductive boundaries can be set under a given electric potential. In this general framework, an electrostatics formulation for the electric potential is derived from the Maxwell's equations. A solution to this problem is presented, using the boundary elements method (BEM). It consists in formulating the electric potential problem as an integral boundary equation, and then, numerically solving it with a discretization of the boundaries of the scene. Finally, the electric currents flowing through the electrodes are computed using Ohm's law. BEM is considered as our first model. A second direct model is described, said as the analytical model, using actual properties of the scene, such as the slender shape of the sensor and the smallness of the object.

3.1 The active electrolocation direct problem formulation

Consider a scene composed of a water domain \mathcal{D} in which are immersed insulating and conductive sub-domains (see figure 3.1). The number of sub-domains and their shapes are arbitrary. The boundary of domain \mathcal{D} (water) is defined as $\partial\mathcal{D} = \partial\mathcal{D}_e \cup \partial\mathcal{D}_i \cup \partial\mathcal{D}_c$, where

- $\partial\mathcal{D}_e$ defines the boundaries that encircle all the sub-domains and delimits the scene,
- $\partial\mathcal{D}_i$ defines the insulating boundaries,
- $\partial\mathcal{D}_c$ defines the conductive boundaries.

Moreover, some of the conductive boundaries are set to a known electric potential (boundaries $\partial\mathcal{D}_{cu}$) whereas others are not (boundaries $\partial\mathcal{D}_{cf}$), such that $\partial\mathcal{D}_c = \partial\mathcal{D}_{cu} \cup \partial\mathcal{D}_{cf}$. For all point \mathbf{y} in $\partial\mathcal{D}$, a normal vector \mathbf{n} is defined, arbitrary oriented outwards \mathcal{D} .

Solving the direct problem consists in computing (analytically or numerically) the electric potential in the whole scene, when considering the imposed potential on $\partial\mathcal{D}_{cu}$, the materials and the geometry (i.e., $\partial\mathcal{D}$) as known. But, before being solved (which is the purpose of next section

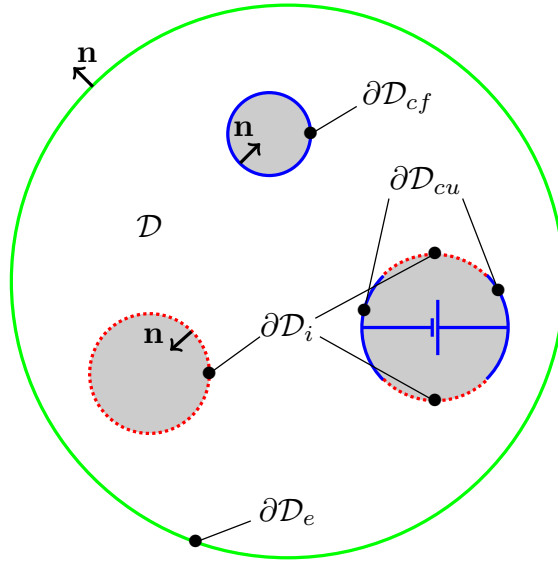


Figure 3.1: The different domains involved in the problem. The domain \mathcal{D} corresponds to the water. It is bounded by boundary $\partial\mathcal{D}_e$, the boundaries of the conductive objects $\partial\mathcal{D}_c$ (blue straight lines) and the boundaries of the insulating objects $\partial\mathcal{D}_i$ (red dotted lines). The conductive boundaries are split into imposed potential $\partial\mathcal{D}_{cu}$ and floating potential $\partial\mathcal{D}_{cf}$ boundaries. For all points in $\partial\mathcal{D}$, a normal unit vector \mathbf{n} is defined, arbitrary orientated outwards \mathcal{D} .

3.2), the problem has to be stated. To that end, we get as a starting point the local formulation of Maxwell's equations in media [48]

$$\nabla \times \mathbf{E} = -\frac{\partial \mathbf{B}}{\partial t} \quad (\text{Maxwell-Faraday}) \quad (3.1)$$

$$\nabla \cdot \mathbf{D} = \rho \quad (\text{Maxwell-Gauss}) \quad (3.2)$$

$$\nabla \times \mathbf{H} = \mathbf{j} + \frac{\partial \mathbf{D}}{\partial t} \quad (\text{Maxwell-Ampere}) \quad (3.3)$$

$$\nabla \cdot \mathbf{B} = 0 \quad (\text{Maxwell-Thomson}), \quad (3.4)$$

where

\mathbf{E} is the electric field (V/m)

\mathbf{H} is the magnetic field (A/m)

\mathbf{D} is the electric flux, or electric displacement (C/m²)

\mathbf{B} is the magnetic flux, or magnetic induction (T)

\mathbf{j} is the current density (A)

ρ is the electric charge density (C).

The symbol $\nabla \times$ denotes the rotational operator and $\nabla \cdot$ the divergence operator. The electric flux \mathbf{D} is related to the electric field \mathbf{E} through the relation $\mathbf{D} = \epsilon_0 \mathbf{E} + \mathbf{P}$. The vector field

\mathbf{P} is the polarization, which describes how the medium is polarized under the effect of the electric field \mathbf{E} . Similarly, the magnetic flux \mathbf{B} is related to the magnetic field \mathbf{H} through the relation $\mathbf{B} = \mu_0(\mathbf{H} + \mathbf{M})$. The vector field \mathbf{M} is the magnetization which describes how the medium magnetizes under the effect of the electric field \mathbf{H} . The constants $\epsilon_0 \simeq \frac{1}{36\pi}10^{-9}$ F/m and $\mu_0 = 4\pi10^{-7}$ H/m are the permittivity and the permeability of vacuum, respectively. Equations (3.1) to (3.4) describe how the fields and fluxes are related to their causes: charge ρ for \mathbf{D} and current density \mathbf{j} for \mathbf{H} . It also states that the magnetic flux divergence is zero. This general formulation of the electromagnetic problem can be simplified considering some reasonable properties concerning the scene

- \mathcal{P}_1 each domain in the scene is an electric and magnetic LHI material: linear, homogeneous and isotropic,
- \mathcal{P}_2 the conducting media (water and conductive objects) in the scene satisfy the generalized Ohm's law: there exists a linear relationship between the current density \mathbf{j} and the electric field \mathbf{E} ,
- \mathcal{P}_3 the excitation signal frequency f is set to 2.25×10^4 Hz (see chapter 2 for justification of that choice).

Property \mathcal{P}_1 is valid in each domain but not on the boundaries, where there exist sharp discontinuities in term of material properties. Thus, in the following, the problem is firstly stated inside each domain, and then, the particular case of the boundaries is addressed, using the jump conditions for the electric field.

3.1.1 The electric potential in domains

Here, only domains are considered, the case of the boundaries being treated in section 3.1.2. As a consequence of property \mathcal{P}_1 :

Linearity : For all M point of the material, the relationship between \mathbf{E} and \mathbf{P} is linear. There exists a tensor $\chi_e(M)$ so that $\mathbf{P} = \epsilon_0\chi_e(M)\mathbf{E}$.

Homogeneity : Tensor $\chi_e(M) = \chi_e$ is constant over the whole material.

Isotropy : Tensor χ_e is proportional to identity, so $\mathbf{P} = \epsilon_0\chi_e\mathbf{E}$, χ_e being the electric susceptibility of the material.

Hence, the electric flux is rewritten as $\mathbf{D} = \epsilon_0(1 + \chi_e)\mathbf{E}$. The coefficient $\epsilon = \epsilon_0(1 + \chi_e)$ is the permittivity of the material. So, the Maxwell-Gauss equation (3.2) is rewritten as

$$\nabla \cdot \epsilon \mathbf{E} = \rho. \quad (3.5)$$

In virtue of material uniformity, the permittivity ϵ is constant over each domain, so it does not depend on space variables and the expression above can be rewritten as

$$\epsilon \nabla \cdot \mathbf{E} = \rho. \quad (3.6)$$

With the same arguments about the magnetic LHI properties of the medium, the magnetic flux becomes $\mathbf{B} = \mu\mathbf{H}$ with μ the permeability of the material, and the Maxwell-Ampere equation (3.3) can be rewritten as

$$\nabla \times \mathbf{B} = \mu \left(\mathbf{j} + \epsilon \frac{\partial \mathbf{E}}{\partial t} \right). \quad (3.7)$$

Taking the divergence of (3.7) and using (3.6) one obtain the charge conservation law

$$\nabla \cdot \mathbf{j} + \frac{\partial \rho}{\partial t} = 0, \quad (3.8)$$

The current density \mathbf{j} can be split into a source component \mathbf{j}_s and an induced component \mathbf{j}_{ind} . The current density \mathbf{j}_s comes from the imposed source, so it is not affected by the fields. In contrast, the induced current density \mathbf{j}_{ind} exists as a response to the fields. According to property \mathcal{P}_2 , the current density \mathbf{j}_{ind} is linearly related to its corresponding electric field through the medium's conductivity γ and we have

$$\mathbf{j} = \mathbf{j}_s + \gamma \mathbf{E}. \quad (3.9)$$

Then, as shown in [31, 30], the fields \mathbf{E} and \mathbf{B} can be decoupled so that the problem can be considered as electroquasistatic (EQS). A condition for that is given by the relationship

$$\frac{L}{\lambda} \ll 1, \quad (3.10)$$

where L is the characteristic length of the system and $\lambda = \frac{1}{f\sqrt{\epsilon\mu}}$ is the wavelength of a propagating electromagnetic wave of frequency f . With a signal frequency $f = 22.5 \times 10^3$ Hz (property \mathcal{P}_3), typical characteristics of water $\mu \simeq 4\pi \times 10^{-7}$ H/m, $\epsilon \simeq 7 \times 10^{-10}$ F/m and typical length $L \leq 1\text{m}^1$, the order of magnitude of ratio L/λ is 10^{-4} . Thus, the inequality (3.10) is satisfied and the EQS approximation can be made, neglecting the right member of (3.1). This gives an irrotational behavior to field \mathbf{E}

$$\nabla \times \mathbf{E} = \mathbf{0}. \quad (3.11)$$

As a consequence, one can state that the field \mathbf{E} derives from a scalar potential field ϕ , so that $\mathbf{E} = -\nabla\phi$. At this point, we have four equations left for the description of our EQS problem: Gauss' law (3.6), charge conservation law (3.8), Ohm's law (3.9) and irrotational behavior of field \mathbf{E} (3.11). Injecting (3.6) and (3.9) in (3.8) one obtains the charge relaxation equation

$$\frac{\gamma}{\epsilon} \rho + \frac{\partial \rho}{\partial t} = -\nabla \cdot \mathbf{j}_s. \quad (3.12)$$

This first order differential equation indicates that a variation of the source \mathbf{j}_s does not have an instantaneous effect on the charge ρ (and thus, on the field \mathbf{E}). Instead of that, ρ varies according to the exponential

$$\rho(t) = C \cdot e^{-\frac{\gamma}{\epsilon} t} - \frac{\epsilon}{\gamma} \nabla \cdot \mathbf{j}_s, \quad (3.13)$$

where C is a constant depending on initial conditions. The time constant $\tau = \epsilon/\gamma$ is the relaxation time [21, 30, 31]. According to table A.1, typical values of relaxation time for fresh water and conductive materials are 10^{-6} s and 10^{-18} s respectively. For insulating materials, where there is no conduction, we have to consider the typical time for material polarization which is as short as 10^{-15} s. Those values are with no comparison with that of the excitation signal $1/f \simeq 10^{-4}$ s.

¹The assumption $L \leq 1\text{m}$ for the typical length is actually verified. For instance, it was shown in section 2.5.4 that the effects of the walls vanish when the distance from the sensor is above 0.2m.

So, in the following we will assume that a source variation has an effect on the charges (and thus, on the fields) with no delay². This situation correspond to the electrostatic equilibrium that is reached at any instant, even if the excitation signal is constantly varying. As a consequence, the charge conservation law (3.8) becomes

$$\nabla \cdot \mathbf{j} = 0. \quad (3.14)$$

Hence, it comes from (3.14), (3.11) and (3.6)

$$\Delta \phi = \nabla \cdot \mathbf{j}_s, \quad (3.15)$$

where operator $\Delta * = \nabla \cdot \nabla *$ is the Laplacian for any scalar field $*$. Because the source \mathbf{j}_s is only located on the boundaries of the electrodes on which an electric potential is imposed (this statement being explained in the next section), the above expression becomes

$$\Delta \phi = 0. \quad (3.16)$$

It is the Laplace equation for the potential ϕ . This formulation is only valid out of the boundaries, on which there is sharp discontinuities in term of ϵ and γ . For a complete formulation of the problem, matching conditions have to be determined on the boundaries.

3.1.2 Boundary conditions

We have shown in the previous section that our direct problem can be summed up with the Laplace equation for the potential (3.16). This is a linear, homogeneous, second order ordinary differential equation (ODE). It is not defined on the boundaries, but knowing the boundary conditions at all $\mathbf{x} \in \partial \mathcal{D}$, it is solvable in \mathcal{D} . Here, we firstly present the jump conditions for the electric field at the interface of two regions with different material properties. Then, these jump conditions for the field are turned to boundary conditions for the potential in our particular case, where the interface is either water/conductive material or water/insulating material.

Jump conditions for the electric field

Let us consider the boundary between two media of permittivity ϵ_1 and ϵ_2 respectively. Locally, a surface element can be considered as a plane, as shown in figure 3.2a. The orthonormal coordinate system $(O, \mathbf{s}, \mathbf{t}, \mathbf{n})$ is attached to this plane, with \mathbf{s} and \mathbf{t} lying in the plane and \mathbf{n} being orthogonal to the plane. A rectangular oriented contour is defined, leaned on \mathbf{t} and \mathbf{n} , which length is l and height is h . Its dimensions are small enough so that electric fields \mathbf{E}_1 and \mathbf{E}_2 on each side of the plane are uniform inside the contour. The circulation of the field around this contour is

$$\begin{aligned} \oint \mathbf{E} \cdot d\mathbf{l} &= \int_0^{h/2} \mathbf{E}_1 \cdot \mathbf{n} \cdot d\mathbf{l} + \int_0^l \mathbf{E}_1 \cdot \mathbf{t} \cdot d\mathbf{l} - \int_0^{h/2} \mathbf{E}_1 \cdot \mathbf{n} \cdot d\mathbf{l} \\ &\quad - \int_{-h/2}^0 \mathbf{E}_2 \cdot \mathbf{n} \cdot d\mathbf{l} - \int_0^l \mathbf{E}_2 \cdot \mathbf{t} \cdot d\mathbf{l} + \int_{-h/2}^0 \mathbf{E}_2 \cdot \mathbf{n} \cdot d\mathbf{l}. \end{aligned} \quad (3.17)$$

²Considering the sea water, due to the high conductivity, the relaxation time is even shorter. In the case of distilled water, the conductivity is significantly lower than that of fresh water and the relaxation time is no more negligible at 22.5×10^3 Hz.

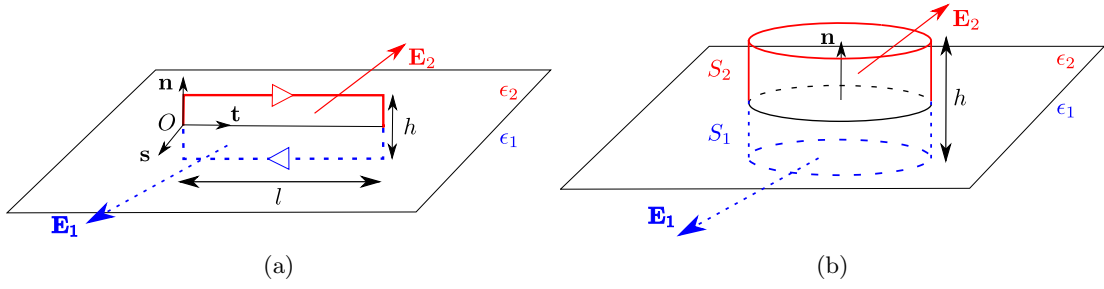


Figure 3.2: (a) An oriented contour through a planar surface for the field's tangential component jump condition. (b) A cylindrical volume through a planar surface for the field's normal component jump condition.

In order to evaluate the fields on the boundary, the limit of that circulation when $h \rightarrow 0$

$$\lim_{h \rightarrow 0} \oint \mathbf{E} \cdot d\mathbf{l} = \int_0^l \mathbf{E}_1 \cdot \mathbf{t} \cdot dl - \int_0^l \mathbf{E}_2 \cdot \mathbf{t} \cdot dl \quad (3.18)$$

shows that only the tangential components $\mathbf{E}_{1\parallel} = \mathbf{E}_1 \cdot \mathbf{t}$ and $\mathbf{E}_{2\parallel} = \mathbf{E}_2 \cdot \mathbf{t}$ remain. Recall that under EQS approximation the electric field is irrotational (3.11). This is equivalent to a circulation of \mathbf{E} that is zero over any closed contour $\oint \mathbf{E} \cdot d\mathbf{l} = 0$. As a result, we have continuity of the tangential component of the field through the boundary

$$\mathbf{E}_{1\parallel} = \mathbf{E}_{2\parallel}. \quad (3.19)$$

In order to handle the case of the field's normal component, let us define a cylindrical surface across the boundary as shown in figure 3.2b. It is composed of two symmetrical surfaces S_1 and S_2 , each of them composed of a circular base (S_{1b} and S_{2b}) and a cylindrical contour (S_{1c} and S_{2c}) of height $h/2$. Again, the dimensions of the cylinder are sufficiently small such that the fields \mathbf{E}_1 and \mathbf{E}_2 are constant in their respective volume. The flux of the field through the cylinder is

$$\oiint \epsilon \mathbf{E} \cdot d\mathbf{S} = \iint_{S_{1b}} \epsilon_1 \mathbf{E}_1 \cdot \mathbf{n} \cdot dS + \iint_{S_{1c}} \epsilon_1 \mathbf{E}_1 \cdot d\mathbf{S} - \iint_{S_{2b}} \epsilon_2 \mathbf{E}_2 \cdot \mathbf{n} \cdot dS + \iint_{S_{2c}} \epsilon_2 \mathbf{E}_2 \cdot d\mathbf{S}, \quad (3.20)$$

which limit when $h \rightarrow 0$ is

$$\lim_{h \rightarrow 0} \oiint \epsilon \mathbf{E} \cdot d\mathbf{S} = \iint_{S_{1b}} \epsilon_1 \mathbf{E}_1 \cdot \mathbf{n} \cdot dS - \iint_{S_{2b}} \epsilon_2 \mathbf{E}_2 \cdot \mathbf{n} \cdot dS. \quad (3.21)$$

Here, only the normal components $\mathbf{E}_{1\perp} = \mathbf{E}_1 \cdot \mathbf{n}$ and $\mathbf{E}_{2\perp} = \mathbf{E}_2 \cdot \mathbf{n}$ remain. Moreover, because fields are constant in S_1 and S_2 respectively, this last expression can be rewritten as

$$\lim_{h \rightarrow 0} \oiint \epsilon \mathbf{E} \cdot d\mathbf{S} = (\epsilon_1 \mathbf{E}_{1\perp} - \epsilon_2 \mathbf{E}_{2\perp}) S_b, \quad (3.22)$$

with S_b the surface of S_{1b} or S_{2b} . On the other hand, because the materials are LHI, we showed that Maxwell-Gauss relationship (3.2) could be simplified as (3.6), or equivalently, for any closed surface S

$$\oiint \epsilon \mathbf{E} \cdot d\mathbf{S} = Q, \quad (3.23)$$

with Q the electric charge in S . In this example, because $h \rightarrow 0$, the electric charge in the cylinder equals to the surface charge density, denoted σ , multiplied by the surface S_b . Hence we have

$$\sigma = \epsilon_1 \mathbf{E}_{1\perp} - \epsilon_2 \mathbf{E}_{2\perp}, \quad (3.24)$$

which is the jump condition for the normal component of the electric field. Note that, contrary to the tangential component (3.19), the normal component depends on both the properties of the medium and the unknown charge density σ . We can also add a third jump condition, which concerns the normal component of current density \mathbf{j} , using the same procedure as for the field normal component. Applying the charge conservation law (3.14) in its integral formulation

$$\oiint \mathbf{j} \cdot d\mathbf{S} = 0 \quad (3.25)$$

to the cylinder of figure 3.2b, the jump condition for the normal component of current density expresses as

$$\mathbf{j}_{1\perp} = \mathbf{j}_{2\perp}. \quad (3.26)$$

This relationship states that there is continuity of the normal component of \mathbf{j} at the interface.

Now, from the jump conditions in the general case, we derive boundary conditions for the potential in the particular cases of water/insulating material and water/conductive material interfaces.

In the following, subscript o will refer to the object's side whereas the absence of subscript will denote the water's side.

Boundary conditions at water/insulating material interface

Let us consider an object made of insulating material immersed in water. By definition, the electric current cannot flow in an insulating material, so $\mathbf{j}_o = 0$. In virtue of the jump condition (3.26), we necessarily have a zero normal component of current density \mathbf{j} in the water

$$\mathbf{j}_{\perp} = 0. \quad (3.27)$$

The water being an ohmic media (property \mathcal{P}_2), the current density \mathbf{j} is linearly related to the field \mathbf{E} through water conductivity γ

$$\mathbf{j} = \gamma \mathbf{E}. \quad (3.28)$$

Taking into account the property of the current density (3.27), we have for the field

$$\mathbf{E}_{\perp} = 0, \quad (3.29)$$

or, in term of potential

$$\nabla \phi(\mathbf{x}) \cdot \mathbf{n} = \frac{\partial \phi(\mathbf{x})}{\partial n} = 0, \forall \mathbf{x} \in \partial \mathcal{D}_i, \quad (3.30)$$

which is known as the Neumann boundary condition. However, the potential $\phi(\mathbf{x}), \forall \mathbf{x} \in \partial \mathcal{D}_i$ remains unknown.

Boundary conditions at water/conductive material interface

Let us now deal with the case of an object that is made of conductive material immersed in water. According to the previous section, the relaxation times of the materials are small with respect to the excitation signal period. So, any charge carrier in a conductor (which is free to move) is instantaneously set in motion under the effect of the external field. As a result, the charges accumulate on the boundary. According to the Gauss equation (3.6), and recall that $\nabla \times \mathbf{E} = \mathbf{0}$, electric field inside conductive object is necessarily zero³. This surface charge density, denoted σ , remains unknown. In virtue of the continuity of the tangential component of the field across the boundary (3.19), the tangential component is necessarily zero. Hence, the field is normal to the boundary or, equivalently, the potential is constant on the boundary. To sum up, we have

$$\begin{cases} \mathbf{E}_\perp(\mathbf{x}) = \frac{\partial\phi(\mathbf{x})}{\partial n} \text{ is unknown } \forall \mathbf{x} \in \partial\mathcal{D}_c, \\ \phi(\mathbf{x}) = \text{unknown constant}, \forall \mathbf{x} \in \partial\mathcal{D}_c, \end{cases} \quad (3.31)$$

on any water/conductive material interface. Now, we must distinguish two kinds of conducting boundary: electrodes, on which a potential is imposed, and conductive objects, on which the potential is floating.

On the electrodes (boundary $\partial\mathcal{D}_{cu}$ in figure 3.1), an electric potential u is imposed, so we have

$$\begin{cases} \frac{\partial\phi(\mathbf{x})}{\partial n} \text{ is unknown } \forall \mathbf{x} \in \partial\mathcal{D}_{cu}, \\ \phi(\mathbf{x}) = u, \forall \mathbf{x} \in \partial\mathcal{D}_{cu}, \end{cases} \quad (3.32)$$

which is named as the Dirichlet boundary condition.

Now considering a conductive object (boundary $\partial\mathcal{D}_{cf}$ in figure 3.1), the potential is floating and depends on the external applied field. So it remains unknown. In addition, the charge conservation law (3.14), expressed in its global formulation, states that the sum of the currents that flow through the object's boundary is zero. As a result

$$\begin{cases} \int_{\partial\mathcal{D}_{cf}} \frac{\partial\phi(\mathbf{x})}{\partial n} ds = 0, \forall \mathbf{x} \in \partial\mathcal{D}_{cf}, \\ \phi(\mathbf{x}) = \text{unknown constant}, \forall \mathbf{x} \in \partial\mathcal{D}_{cf}. \end{cases} \quad (3.33)$$

Boundary conditions for $\partial\mathcal{D}_e$

The boundary $\partial\mathcal{D}_e$ can be considered either as sufficiently far from the objects so that it is not influenced by the electric potential or as the insulating walls of an aquarium. In the first case, the potential and the field can be considered as zero. In the second case, boundary conditions for insulating objects applies.

³Actually, charges on the boundary arrange themselves in order to produce an electric field that is equal in magnitude and opposite to the external field, the total field being zero.

3.2 Solving the direct problem

We have now at our disposal a partial differential equation for the potential ϕ (3.16) and boundary conditions, either for ϕ or for $\frac{\partial\phi}{\partial n}$. In this section, a method is proposed to solve this problem in the water domain \mathcal{D} . It consists in turning our differential problem into a boundary integral equation which can be numerically solved using a discretization of the boundaries. This solving process is the boundary elements method (BEM).

3.2.1 Boundary integral formulation

First of all, we state that the problem described in previous section has a unique solution. Proofs of that statement can be found in [2, 11, 30, 31]. There exist two ways to obtain that solution:

1. A direct method: based on the use of Green's identities, it is the method described in the following. It was used for the electric sense modeling in [12].
2. An indirect method: using the concept of single and double layer potentials, it was employed in [2, 11] for the biological electric sense modeling.

Both methods are presented in [63]. Here, we use the direct method because it has a more physical meaning. Firstly, let us introduce the Dirac δ function $\delta(\mathbf{x}, \mathbf{y})$, in point \mathbf{x} , defined as

$$\int_V f(\mathbf{y})\delta(\mathbf{x}, \mathbf{y})dV(\mathbf{y}) = \begin{cases} 0 & \text{if } \mathbf{x} \neq \mathbf{y}, \\ f(\mathbf{x}) & \text{if } \mathbf{x} = \mathbf{y}, \end{cases} \quad (3.34)$$

where \mathbf{x} , \mathbf{y} are two position vectors of a volume V and f a function. Secondly, a function G is said as a Green's function if it is a fundamental solution of Laplace equation [42], that is

$$\Delta G(\mathbf{x}, \mathbf{y}) = -\delta(\mathbf{x}, \mathbf{y}), \quad (3.35)$$

so, using the δ function definition above

$$\int_V f(\mathbf{y})\Delta G(\mathbf{x}, \mathbf{y})dV(\mathbf{y}) = \begin{cases} 0 & \text{if } \mathbf{x} \neq \mathbf{y} \\ -f(\mathbf{x}) & \text{if } \mathbf{x} = \mathbf{y}. \end{cases} \quad (3.36)$$

Moreover, the normal derivative of a Green's function, denoted F , is also a Green's function [42]

$$\Delta F(\mathbf{x}, \mathbf{y}) = \Delta \frac{\partial G(\mathbf{x}, \mathbf{y})}{\partial n} = -\delta(\mathbf{x}, \mathbf{y}), \quad (3.37)$$

Thirdly, the second Green's identity [42] states that, for any two continuous functions u and v , defined in a volume V bounded by surface S

$$\int_V [u.\Delta v - v.\Delta u] dV = \int_S \left[u.\frac{\partial v}{\partial n} - v.\frac{\partial u}{\partial n} \right] dS. \quad (3.38)$$

Now, let $u(\mathbf{x}, \mathbf{y}) = G(\mathbf{x}, \mathbf{y})$ and $v(\mathbf{y}) = \phi(\mathbf{y})$ in the domain \mathcal{D} bounded by the $\partial\mathcal{D}$. We have

$$\int_{\mathcal{D}} [G(\mathbf{x}, \mathbf{y}).\Delta\phi(\mathbf{y}) - \phi(\mathbf{y}).\Delta G(\mathbf{x}, \mathbf{y})] dV(\mathbf{y}) \quad (3.39)$$

$$= \int_{\partial\mathcal{D}} \left[G(\mathbf{x}, \mathbf{y}).\frac{\partial\phi(\mathbf{y})}{\partial n} - \phi(\mathbf{y}).F(\mathbf{x}, \mathbf{y}) \right] dS(\mathbf{y}). \quad (3.40)$$

Left hand term of this equation can be simplified using (3.16) and (3.35)

$$\phi(\mathbf{x}) = \int_{\partial\mathcal{D}} \left[G(\mathbf{x}, \mathbf{y}) \cdot \frac{\partial\phi(\mathbf{y})}{\partial n} - \phi(\mathbf{y}) \cdot F(\mathbf{x}, \mathbf{y}) \right] dS(\mathbf{y}), \forall \mathbf{x} \in \mathcal{D}. \quad (3.41)$$

At this point, starting from the Laplace equation, we have turned the formulation of the problem to a boundary integral problem. Equation (3.41) verifies Laplace equation for all Green's function G . In the literature [5, 63], it is demonstrated that a suitable Green's function G for such problem in \mathbb{R}^3 is

$$G(\mathbf{x}, \mathbf{y}) = \frac{1}{4\pi|\mathbf{y} - \mathbf{x}|}, \quad (3.42)$$

and thus,

$$F(\mathbf{x}, \mathbf{y}) = \frac{\partial}{\partial n} \left(\frac{1}{4\pi|\mathbf{y} - \mathbf{x}|} \right) = -\frac{1}{4\pi} \frac{(\mathbf{y} - \mathbf{x})}{|\mathbf{y} - \mathbf{x}|^3} \cdot \mathbf{n}, \quad (3.43)$$

which, indeed, both satisfy (3.35). Equation (3.41) shows that potential at point $\mathbf{x} \in \mathcal{D}$ is the sum of two contributions which are both a weighted sum over the boundary. The 1st contribution is the sum of the normal derivatives of the potential, weighted by the function G whereas the 2nd contribution is the sum of the potential, weighted by the function F .

The equation (3.41) is the solution of our problem if and only if it verifies our boundaries conditions as well. Although functions G and F are singular on $\partial\mathcal{D}$, one can demonstrate [63] that

$$\frac{1}{2}\phi(\mathbf{x}) = \int_{\partial\mathcal{D}} \left[G(\mathbf{x}, \mathbf{y}) \cdot \frac{\partial\phi(\mathbf{y})}{\partial n} - \phi(\mathbf{y}) \cdot F(\mathbf{x}, \mathbf{y}) \right] dS(\mathbf{y}), \forall \mathbf{x} \in \partial\mathcal{D}. \quad (3.44)$$

This equation, in addition to Laplace equation in \mathcal{D} in its integral form (3.41), entirely describes the potential for a given scene. In the next section, a numerical method is proposed to solve (3.44). Then, the potential and its normal derivative will be known on all boundaries and thus, the potential at any point in \mathcal{D} may be calculated using (3.41).

3.2.2 Boundaries discretization and direct problem solving

In order to numerically solve (3.44), boundary $\partial\mathcal{D}$ is meshed into N surface elements

$$\partial\mathcal{D} = \bigcup_{j=1}^N \mathcal{S}_j. \quad (3.45)$$

As an example, figure 3.3 shows a virtual scene composed of the sensor and an object, whose boundaries are meshed.

Under the assumption of sufficiently small elements, the potential $\phi_{i=1, \dots, N}$ and its normal derivative $\frac{\partial\phi_i}{\partial n_i}$ are assumed to be constant over surface \mathcal{S}_i , and according to (3.44)

$$\frac{1}{2}\phi_i = \sum_{j=1}^N \frac{\partial\phi_j}{\partial n_j} \int_{\mathcal{S}_j} G(\mathbf{x}_i, \mathbf{y}) dS - \sum_{j=1}^N \phi_j \int_{\mathcal{S}_j} F(\mathbf{x}_i, \mathbf{y}) dS, \forall i = 1, \dots, N. \quad (3.46)$$

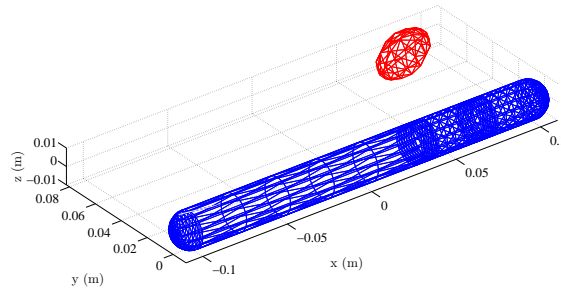


Figure 3.3: A virtual scene composed of the sensor and an ellipsoidal object.

These N equations can be gathered in a linear system

$$\frac{1}{2} \begin{bmatrix} \phi_1 \\ \vdots \\ \phi_N \end{bmatrix} = \begin{bmatrix} g_{11} & \cdots & g_{1N} \\ \vdots & \ddots & \vdots \\ g_{N1} & \cdots & g_{NN} \end{bmatrix} \cdot \begin{bmatrix} \frac{\partial \phi_1}{\partial n_1} \\ \vdots \\ \frac{\partial \phi_N}{\partial n_N} \end{bmatrix} - \begin{bmatrix} f_{11} & \cdots & f_{1N} \\ \vdots & \ddots & \vdots \\ f_{N1} & \cdots & f_{NN} \end{bmatrix} \cdot \begin{bmatrix} \phi_1 \\ \vdots \\ \phi_N \end{bmatrix} \quad (3.47)$$

where $g_{ij} = \int_{S_j} \frac{1}{4\pi|\mathbf{x}_i - \mathbf{y}|} dS$ and $f_{ij} = \int_{S_j} \frac{\partial}{\partial n_j} \frac{1}{4\pi|\mathbf{x}_i - \mathbf{y}|} dS$. This system has only one unknown for each equation. Indeed, if surface S_i in which we calculate potential ϕ_i (i^{th} line of the system) belongs to

- an insulating boundary ($\partial\mathcal{D}_i$): according to (3.30), $\frac{\partial \phi_i}{\partial n_i} = 0$ and ϕ_i is unknown,
- a conductive boundary with an imposed potential u ($\partial\mathcal{D}_{cu}$): according to (3.32), $\phi_i = u$ and $\frac{\partial \phi_i}{\partial n_i}$ is unknown,
- a conductive boundary with no imposed potential ($\partial\mathcal{D}_{cf}$): according to (3.33), $\phi_i =$ unknown constant and $\sum_{i=1}^M \frac{\partial \phi_i}{\partial n_i} ds = 0$, with M the number of surface elements of the discretized boundary $\partial\mathcal{D}_{cf}$.

Gathering the unknowns in a vector denoted X , a linear system in the form $\mathbf{A}X = \mathbf{b}$ is built, with \mathbf{A} a $[N \times N]$ matrix and \mathbf{b} a vector of dimension N . This system is then solved with an iterative solver GMRES (generalized minimum residual).

With that computation tool, the electric current I_n flowing through the electrode $e_{n=1,\dots,8}$ are computed for a given scene as

$$I_n = \gamma \int_{e_n} \frac{\partial \phi(\mathbf{y})}{\partial n} \cdot \mathbf{n} \cdot dS(\mathbf{y}), \quad (3.48)$$

in virtue of Ohm's law in the conductive medium.

The BEM model has the advantage of providing accurate simulated currents, without practical constraints and measurement noise. Also, even if a commercial software (for instance ANSYS or COMSOL) could have been used for that task, we preferred to design and code our own tool in order to get a very good comprehension of the involved physics.

February 7, 2018

However, solving the system (3.47) is time consuming. As an example, for a scene composed of 2540 boundary elements, it takes around 72 seconds to solve the system on a desktop computer, equipped with an Intel Core i7 processor, 24Go of RAM and running Windows 7. The implementation of inversion algorithm on such model could be very hard to implement on an embedded robot. That is why a simplified direct model, named as analytical model was derived. It was firstly presented in [12], and we recall it in the next section.

3.3 Analytical direct model

As we showed in previous section, the BEM model is a powerful and accurate tool for off-line simulations of currents for a given scene. It is valid for any size and shape of sensor and object. But, considering the sensor's characteristics and some other properties about the scene, one can reassess the integral formulation (3.44) and obtain a much simpler analytical model for the direct problem [12]. These properties are

\mathcal{P}_4 the sensor has a slender shape: it has a cylindrical shape, and its diameter is small compare to its length, see its actual dimensions in figure 2.7,

\mathcal{P}_5 there is only one object in the scene, either perfectly conductive or perfectly insulating, with prolate ellipsoidal shape ($a \geq b = c$ in figure 2.4),

\mathcal{P}_6 the object is far enough from the sensor, that is, if r represents the distance of the object to the sensor, $r \geq 3R = 3\text{cm}$,

\mathcal{P}_7 the object is considered as "small", that is, its typical dimension is of the order of the sensor radius $R = 1\text{cm}$,

\mathcal{P}_8 the object and the sensor lie in the same plane, represented in red in figure 2.1b.

In the following, properties \mathcal{P}_4 to \mathcal{P}_8 will be considered as satisfied in addition to the general properties \mathcal{P}_1 to \mathcal{P}_3 . As explained in [12], the analytical model does not describe the currents flowing through the electrodes $e_{1,\dots,8}$ but two combinations of them, named as axial and lateral currents. So, let us firstly introduce the concepts of axial and lateral currents and then detail the method to obtain their analytical formulations.

3.3.1 Axial and lateral currents

In order to present the concept of axial current, let us consider the sensor immersed in an external electric potential, as shown in figure 3.4a.

The location of the macro-electrode \mathcal{E}_i is denoted \mathbf{x}_i , $\forall i \in \{1, 2, 3, 4\}$. Because of the slender shape, we consider each macro-electrode \mathcal{E}_i narrow enough so that both of its constitutive electrodes are submitted to the same potential $\phi(\mathbf{x}_i)$. So, the sensor is axially set to potential differences $\phi(\mathbf{x}_i) - \phi(\mathbf{x}_j)$. The sensor being submitted to these axial voltages, it flows through the macro-electrode \mathcal{E}_i an axial current denoted $I_{\text{ax},i} \forall i \in \{1, \dots, 4\}$. Because this solicitation is axial, the left and right resulting currents for a given macro-electrode are the same, and the

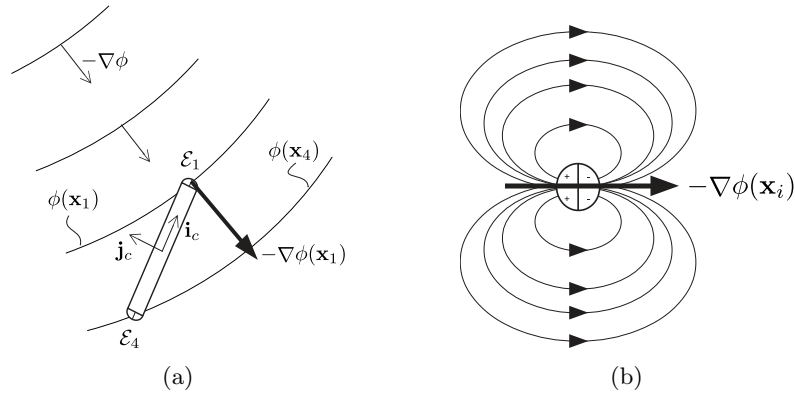


Figure 3.4: (a) The sensor in an external electric potential. Only macro-electrodes \mathcal{E}_1 and \mathcal{E}_4 are represented for the sake of simplicity. Their positions are denoted \mathbf{x}_1 and \mathbf{x}_4 , respectively. The potential difference between two macro-electrodes leads to an axial polarization of the sensor and as a consequence, current named as *axial* flows through the electrodes. (b) The lateral polarization of the i^{th} macro-electrode which produces the lateral current $I_{lat,i}$.

axial current $I_{ax,i}$ is defined as half the sum of the two components. The four lateral currents are gathered in vector I_{ax} as follows

$$I_{ax} = \begin{bmatrix} I_{ax,1} \\ I_{ax,2} \\ I_{ax,3} \\ I_{ax,4} \end{bmatrix} = \begin{bmatrix} \frac{I_1+I_2}{2} \\ \frac{I_3+I_4}{2} \\ \frac{I_5+I_6}{2} \\ \frac{I_7+I_8}{2} \end{bmatrix} \quad (3.49)$$

As it will be shown in the following, the potential $\phi(\mathbf{x}_i)$ can either be produced by the sensor itself (polarization of the macro-electrodes) or produced by a remote polarized object. In both cases, the relationships between these potentials and the resulting vector I_{ax} are linear and the corresponding matrices which encode the properties of the sensor and the properties of the object, respectively, will be described later in this section.

Each macro-electrode \mathcal{E}_i is also submitted to the gradient of $\phi(\mathbf{x}_i)$, denoted $-\nabla\phi(\mathbf{x}_i)$, see figure 3.4a. Under the effect of that field, \mathcal{E}_i polarizes as shown in figure 3.4b, and as a result, it flows a current through each of the two electrodes. The lateral current $I_{lat,i}$ is defined as half the difference of the currents flowing through both electrodes of \mathcal{E}_i .

$$I_{lat} = \begin{bmatrix} I_{lat,1} \\ I_{lat,2} \\ I_{lat,3} \\ I_{lat,4} \end{bmatrix} = \begin{bmatrix} \frac{I_1-I_2}{2} \\ \frac{I_3-I_4}{2} \\ \frac{I_5-I_6}{2} \\ \frac{I_7-I_8}{2} \end{bmatrix} \quad (3.50)$$

Unlike the axial currents, each lateral current is independent from the three others. Also, when the field is due to the sensor's polarization only (no object or other field source), the lateral component is necessarily zero.

Now the concept of axial and lateral currents are presented, a method to derive an analytical model for these currents is introduced. This method was firstly presented in [12]. It makes the use of the successive reflexions method which is based on the truncation of the series expansion formulation of the direct problem

$$\phi = \sum_{i=0}^{\infty} \phi_i. \quad (3.51)$$

As shown in figure 3.5, the component ϕ_0 is the electric potential that exists as the consequence

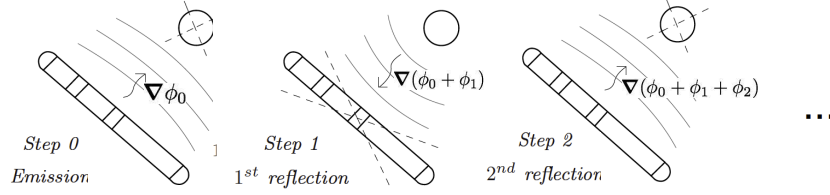


Figure 3.5: Illustration of the 3 first steps of the successive reflexions method. Taken from [14].

of the polarization of an electrode of the sensor, the object being ignored. Solving the direct problem for ϕ_0 is Step 0, or emission. Potential ϕ_1 is the electric potential induced by the object when it is polarized under the effect of ϕ_0 . Solving the direct problem for $\phi_0 + \phi_1$ is Step 1, or 1st reflexion, considering that the sensor is absent from the scene. Step 2, or 2nd reflexion, consists in solving the problem for $\phi_0 + \phi_1 + \phi_2$, ϕ_2 being the perturbation of $\phi_0 + \phi_1$ due to the sensor.

This process is theoretically infinite, but in practice, because $|\phi_i|$ decreases as the inverse of a power of two, the series truncation after the third component (ϕ_2) is a reasonable approximation

$$\phi \simeq \phi_0 + \phi_1 + \phi_2. \quad (3.52)$$

In the following, we will use the general integral formulation (3.41) for each of these three steps, taking into account the additional properties \mathcal{P}_4 to \mathcal{P}_7 .

3.3.2 Model for the emission (Step 0)

Here, only the sensor is present in the scene. Before computing the potential $\phi(\mathbf{x}), \forall \mathbf{x} \in \mathcal{D}$, we define the currents vector denoted $I^0 \in \mathbb{R}^4$ which each component k corresponds to the electric current that flows through the macro-electrode \mathcal{E}_k

$$I^0 = [I_1^0 \quad I_2^0 \quad I_3^0 \quad I_4^0]^T \quad (3.53)$$

where

$$I_k^0 = \int_{\mathcal{E}_k} \mathbf{j}(\mathbf{y}) \cdot \mathbf{n}(\mathbf{y}) \cdot dS(\mathbf{y}) = \gamma \int_{\mathcal{E}_k} \frac{\partial \phi_0(\mathbf{y})}{\partial n} dS(\mathbf{y}), \forall k \in \{1, \dots, 4\} \quad (3.54)$$

in virtue of Ohm's law (3.9). Knowing the water conductivity γ , a numerical solution of the equation system (3.47) provides a good approximation of I^0 . It also shows that I^0 is in linear combination with the polarization vector $U \in \mathbb{R}^4$, which k^{th} component is the electric potential imposed onto macro-electrode \mathcal{E}_k

$$U = [u_1 \quad u_2 \quad u_3 \quad u_4]^T. \quad (3.55)$$

The relationship between I^0 and U is given by the $[4 \times 4]$ real symmetric matrix C^0

$$I^0 = C^0 U \quad (3.56)$$

which was computed with BEM (see [12])

$$C^0 = \frac{\gamma}{100} \begin{bmatrix} 7.6534 & -3.1370 & -2.3053 & -2.1829 \\ -3.1370 & 8.3933 & -3.2027 & -2.0804 \\ -2.3053 & -3.2027 & 7.8032 & -2.3190 \\ -2.1829 & -2.0804 & -2.3190 & 6.6052 \end{bmatrix}. \quad (3.57)$$

Now, let us compute the potential $\phi(\mathbf{x})$, $\forall \mathbf{x} \in \mathcal{D}$ using the integral equation (3.41), decomposing boundary $\partial\mathcal{D}$ into insulating boundary ($\partial\mathcal{D}_i$) and the four boundaries of the polarized macro-electrodes \mathcal{E}_k

$$\phi_0(\mathbf{x}) = -\frac{1}{4\pi} \int_{\partial\mathcal{D}_i} \phi_0(\mathbf{y}) \frac{\partial\phi_0(\mathbf{y})}{\partial n} dS(\mathbf{y}) + \sum_{i=1}^4 \frac{1}{4\pi} \int_{\mathcal{E}_i} \left(\frac{1}{r} \frac{\partial\phi_0(\mathbf{y})}{\partial n} - u_i \frac{\partial(1/r)}{\partial n} \right) dS(\mathbf{y}), \quad (3.58)$$

with $r = |\mathbf{y} - \mathbf{x}|$. In [12] a proof is given for a perturbation series expansion of this expression with respect to the small quantity R/r (property \mathcal{P}_5), which is

$$\phi_0(\mathbf{x}) = \frac{1}{4\pi} \sum_{i=1}^4 \frac{1}{r_i} \int_{\mathcal{E}_i} \frac{\partial\phi_0(\mathbf{y})}{\partial n} dS(\mathbf{y}) + \mathcal{O}(R/r) \quad (3.59)$$

with $r_k = |\mathbf{r}_k| = |\mathbf{x} - \mathbf{x}_k|$, \mathbf{x}_k being the position of the geometrical center of macro-electrode k . Using the current I_k^0 definition (3.54), the above equation becomes

$$\phi_0(\mathbf{x}) = \frac{1}{4\pi\gamma} \sum_{i=1}^4 \frac{I_i^0}{r_i} + \mathcal{O}(R/r). \quad (3.60)$$

Then, the electric field $\mathbf{E}^0(\mathbf{x})$ is computed as the opposite of the gradient of $\phi_0(\mathbf{x})$

$$\mathbf{E}^0(\mathbf{x}) = \frac{1}{4\pi\gamma} \sum_{i=1}^4 \frac{\mathbf{r}_i}{r_i^3} I_i^0. \quad (3.61)$$

In the following, \mathbf{E}^0 will refer to this electric field, evaluated at the center of the object \mathbf{x}_o , that is $\mathbf{E}^0(\mathbf{x}_o) \rightarrow \mathbf{E}^0$. The field \mathbf{E}^0 can be rewritten in the matrix form

$$\mathbf{E}^0 = \frac{1}{4\pi\gamma} G^T C^0 U, \quad (3.62)$$

where the matrix G , expressed in the sensor's frame, being defined as

$$G = \begin{bmatrix} \frac{x_o^c - x_1}{r_1^3} & \frac{y_o^c}{r_1^3} & 0 \\ \frac{x_o^c - x_2}{r_2^3} & \frac{y_o^c}{r_2^3} & 0 \\ \frac{x_o^c - x_3}{r_3^3} & \frac{y_o^c}{r_3^3} & 0 \\ \frac{x_o^c - x_4}{r_4^3} & \frac{y_o^c}{r_4^3} & 0 \end{bmatrix}, \quad (3.63)$$

with $r_k = \sqrt{(x_o^c - x_k)^2 + y_o^{c2}}$, $\forall k \in \{1, \dots, 4\}$. The last column of G is 0 because the sensor and the object lie in the same plane. In the fixed frame $(O, \mathbf{i}, \mathbf{j})$, the components of \mathbf{E}^0 on \mathbf{i} and \mathbf{j} are respectively

$$E_x^0 = \frac{1}{4\pi\gamma} \sum_{i,j=1}^4 \frac{x_o^c - x_i}{r_i^3} C_{ij}^0 u_j, \quad E_y^0 = \frac{1}{4\pi\gamma} \sum_{i,j=1}^4 \frac{y_o^c}{r_i^3} C_{ij}^0 u_j. \quad (3.64)$$

3.3.3 Model for the 1st reflexion (Step 1)

Here, we focus on the electrical behavior of the object when it is submitted to the field \mathbf{E}^0 (3.62). The background theory that describes this behavior is given in [5]. It is based on the concept of generalized polarization tensors (GPTs) which describes the relationship between the electric potential produced by a polarized object and the external field that initiated this polarization. In our context, the external field is \mathbf{E}^0 and the produced potential evaluated at distance r from the origin is denoted $\phi_1(r)$. This relationship, expressed in a coordinate system attached to the object, is given by

$$\phi_1(r) = \frac{1}{4\pi} \sum_{|\alpha|, |\beta|=1}^{+\infty} \frac{(-1)^{|\alpha|}}{\alpha! \beta!} \frac{\partial^{|\alpha|} 1/r}{\partial r^{|\alpha|}} P_{\alpha\beta}(\gamma_o, \mathcal{D}_o) \partial^\beta \phi_0(\mathbf{0}), \quad (3.65)$$

where

- α, β are the multi-indices $\alpha = (\alpha_1, \alpha_2, \alpha_3)$, $\beta = (\beta_1, \beta_2, \beta_3)$,
- $\frac{\partial^{|\alpha|} 1/r}{\partial r^{|\alpha|}}$ is the $|\alpha|^{th}$ derivative of the Green's function G defined in (3.42), evaluated in $(\mathbf{0}, \mathbf{x})$ with $r = |\mathbf{x}|$
- ∂^β is the differential operator $\partial^\beta = \frac{\partial^{\beta_1}}{\partial x^{\beta_1}} \cdot \frac{\partial^{\beta_2}}{\partial y^{\beta_2}} \cdot \frac{\partial^{\beta_3}}{\partial z^{\beta_3}}$,
- $P_{\alpha\beta}(\gamma_o, \mathcal{D}_o)$ is the generalized polarization tensor, which only depends on the object's conductivity γ_o and boundary $\partial\mathcal{D}_o$. In the following, the explicit dependence in term of γ_o and $\partial\mathcal{D}_o$ will be deliberately omitted: $P_{ij}(\gamma_o, \mathcal{D}_o) \rightarrow P_{ij}$.

The equation (3.65) is an infinite sum of contributions of GPTs and it is proven in [5] that the knowledge of all GPTs uniquely determines the geometry and the conductivity of the object. This expression can be simplified in the case of ellipsoidal objects, using lemma 4.4 in [5] which states that for symmetrical objects, if $|\alpha| + |\beta|$ is odd, then $P_{\alpha\beta}$ is zero. Hence, if we consider only the two first terms of this expansion we have the following approximation

$$\phi_1(r) \simeq \frac{\mathbf{r}}{4\pi r^3} P_{11} \cdot \mathbf{E}^0 + \frac{\mathbf{r}}{8\pi r^4} P_{22} : \partial^1 \mathbf{E}^0, \quad (3.66)$$

where the symbol $:$ denotes the tensor product. The field \mathbf{E}^0 explicitly appears remarking that $\partial^1 \phi_0(\mathbf{0}) = \mathbf{E}^0$. These first and second terms correspond to a dipolar and a quadrupolar response of the object, respectively. We describe both of them now.

Dipolar response of the object

Let us denote the dipolar contribution to potential $\phi_1(\mathbf{x})$ as $\phi_{1d}(\mathbf{x})$, so that

$$\phi_{1d}(r) = \frac{\mathbf{r}}{4\pi r^3} P_{11} \cdot \mathbf{E}^0. \quad (3.67)$$

The generalized polarization tensor P_{11} is named as Pólya-Szegö polarization tensor [88]. It is represented, in the object's frame, as a $[3 \times 3]$ diagonal matrix. Submitted to an electric field \mathbf{E}^0 , the object behaves as an electric dipole \mathbf{p}

$$\mathbf{p} = P_{11} \cdot \mathbf{E}^0, \quad (3.68)$$

which produces potential $\phi_{1d}(r)$ through the propagating function $\mathbf{r}/(4\pi r^3)$. Figure 3.6 represents

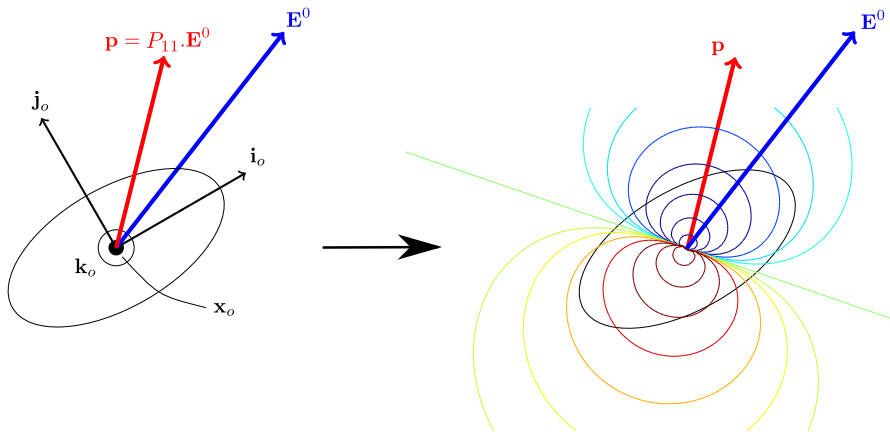


Figure 3.6: Representation of the electric field \mathbf{E}^0 and the dipolar moment \mathbf{p} for an ellipsoidal object (left). Potential $\phi_{1d}(\mathbf{x})$ represented with its iso-values (right).

the field \mathbf{E}^0 , the dipolar moment \mathbf{p} and the induced potential for an ellipsoidal object. The vector \mathbf{p} is obtained through the linear transformation P_{11} which scales and rotates the vector \mathbf{E}^0 . This linear transformation depends on the intrinsic properties of the object. Explicit relationships between object's properties and components of P_{11} were proposed in [5, 44] for an ellipsoidal object. These relationships are of great interest for the shape recognition algorithm (chapter 6) so we describe them in details here.

Explicit expression of the Pólya-Szegö tensor P_{11}

With semi-axis denoted a , b and c , as represented in figure 2.4, we have, in the ellipsoid's frame $(O_o, \mathbf{i}_o, \mathbf{j}_o, \mathbf{k}_o)$

$$P_{11} = (\gamma_o - \gamma) \mathcal{V} \begin{pmatrix} \frac{1}{\gamma + A(\gamma_o - \gamma)} & 0 & 0 \\ 0 & \frac{1}{\gamma + B(\gamma_o - \gamma)} & 0 \\ 0 & 0 & \frac{1}{\gamma + C(\gamma_o - \gamma)} \end{pmatrix} \quad (3.69)$$

where constants A , B et C are defied as

$$A = \frac{bc}{a^2} \int_1^{+\infty} \frac{1}{t^2 \sqrt{t^2 - 1 + \left(\frac{b}{a}\right)^2} \sqrt{t^2 - 1 + \left(\frac{c}{a}\right)^2}} dt, \quad (3.70)$$

$$B = \frac{bc}{a^2} \int_1^{+\infty} \frac{1}{\left(t^2 - 1 + \left(\frac{b}{a}\right)^2\right)^{\frac{3}{2}} \sqrt{t^2 - 1 + \left(\frac{c}{a}\right)^2}} dt, \quad (3.71)$$

$$C = \frac{bc}{a^2} \int_1^{+\infty} \frac{1}{\sqrt{t^2 - 1 + \left(\frac{b}{a}\right)^2} \left(t^2 - 1 + \left(\frac{c}{a}\right)^2\right)^{\frac{3}{2}}} dt, \quad (3.72)$$

constants γ and γ_o being the water and object's conductivities respectively. $\mathcal{V} = \frac{1}{3}abc$ is the volume of the object, divided by 4π . For prolate ellipsoids, $a \geq b = c$ (property \mathcal{P}_5), coefficients A , B and C simplify

$$A = \left(\frac{b}{a}\right)^2 \int_1^{+\infty} \frac{1}{t^2 \left(t^2 - 1 + \left(\frac{b}{a}\right)^2\right)} dt, \quad (3.73)$$

$$B = \left(\frac{b}{a}\right)^2 \int_1^{+\infty} \frac{1}{\left(t^2 - 1 + \left(\frac{b}{a}\right)^2\right)^2} dt, \quad (3.74)$$

$$C = \left(\frac{b}{a}\right)^2 \int_1^{+\infty} \frac{1}{\left(t^2 - 1 + \left(\frac{b}{a}\right)^2\right)^2} dt, \quad (3.75)$$

B and C being equal.

In the particular case of a sphere, we have $a = b = c$ and it is possible to evaluate the integrals A , B and C which are equal to $1/3$. So, we get

$$P_{11} = a^3 \frac{\gamma_o - \gamma}{2\gamma + \gamma_o} \begin{pmatrix} 1 & 0 & 0 \\ 0 & 1 & 0 \\ 0 & 0 & 1 \end{pmatrix}. \quad (3.76)$$

The coefficient $\frac{\gamma_{obj} - \gamma_o}{2\gamma_o + \gamma_{obj}}$ is χ in the Rasnow's perturbation model (1.1), here in the case of real values conductivities. For a conductive object, $\gamma_o \gg \gamma$ so $\chi \simeq 1$, and for an insulating object $\gamma_o \ll \gamma$ so $\chi \simeq -1/2$, which indeed correspond to the values deduced in section 2.4.2.

If the object is perfectly conductive or perfectly insulating (property \mathcal{P}_5), the formulation of coefficients of P_{11} (3.69) can be simplified again. With a water conductivity γ in the order of 10^{-2} , one can discriminate two cases

- The object is insulating: no charge circulation exists in the material so that $\gamma_o \rightarrow 0$ and $\gamma_o - \gamma \simeq -\gamma$. The matrix P_{11} is rewritten as

$$P_{11} \simeq \mathcal{V} \begin{pmatrix} \frac{1}{A-1} & 0 & 0 \\ 0 & \frac{1}{B-1} & 0 \\ 0 & 0 & \frac{1}{B-1} \end{pmatrix}. \quad (3.77)$$

- The object is conductive: $\gamma_o \simeq 10^7$ and $\gamma_o - \gamma \simeq \gamma_o$. In this case

$$P_{11} \simeq \gamma_o \mathcal{V} \begin{pmatrix} \frac{1}{\gamma + A\gamma_o} & 0 & 0 \\ 0 & \frac{1}{\gamma + B\gamma_o} & 0 \\ 0 & 0 & \frac{1}{\gamma + B\gamma_o} \end{pmatrix}. \quad (3.78)$$

Then, looking at the values of A et B against the aspect ratio $\eta = a/b$ (see figure 3.7) one can see that they are both in the order of magnitude of 10^{-1} . Hence, the denominators of the diagonal coefficients can be simplified

$$\gamma + A\gamma_o \simeq A\gamma_o \quad (3.79)$$

$$\gamma + B\gamma_o \simeq B\gamma_o, \quad (3.80)$$

and finally P_{11} becomes

$$P_{11} \simeq \mathcal{V} \begin{pmatrix} \frac{1}{A} & 0 & 0 \\ 0 & \frac{1}{B} & 0 \\ 0 & 0 & \frac{1}{B} \end{pmatrix}. \quad (3.81)$$

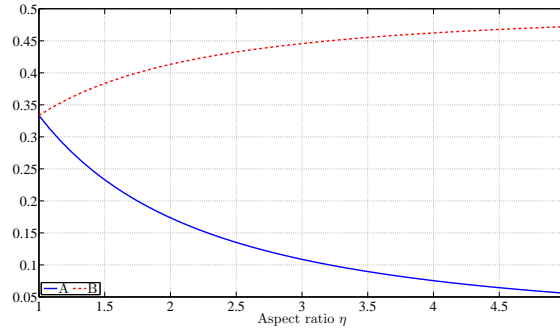


Figure 3.7: Coefficients A and B against aspect ratio η .

In the following chapters, it will be convenient to express tensor P_{11} in the sensor frame. Because sensor and object lie in the same plane (property \mathcal{P}_8), this transformation is performed with a rotation matrix of angle θ_o^c about the \mathbf{k}_o axis, defined as

$$R = \begin{pmatrix} \cos \theta_o^c & -\sin \theta_o^c & 0 \\ \sin \theta_o^c & \cos \theta_o^c & 0 \\ 0 & 0 & 1 \end{pmatrix}, \quad (3.82)$$

the angle θ_o^c corresponding to that it is shown in figure 2.5. Thus, one obtain the tensor P_{11}^c in the sensor frame

$$P_{11}^c = R.P_{11}.R^T. \quad (3.83)$$

Finally, P_{11}^c writes

$$P_{11}^c = \begin{pmatrix} \lambda_u \cos^2(\theta_o^c) + \lambda_v \sin^2(\theta_o^c) & (\lambda_u - \lambda_v) \cos(\theta_o^c) \sin(\theta_o^c) & 0 \\ (\lambda_u - \lambda_v) \cos(\theta_o^c) \sin(\theta_o^c) & \lambda_u \sin^2(\theta_o^c) + \lambda_v \cos^2(\theta_o^c) & 0 \\ 0 & 0 & \lambda_w \end{pmatrix}, \quad (3.84)$$

with $\lambda_u = \mathcal{V}/A$ and $\lambda_v = \mathcal{V}/B$ for a conductive object and $\lambda_u = \mathcal{V}/(A-1)$ and $\lambda_v = \mathcal{V}/(B-1)$ for an insulating object. In both cases we have $\lambda_w = \lambda_v$. For more convenience, let us denote

the components of P_{11}^c as

$$P_{11}^c = \begin{bmatrix} p_{11}^c & p_{12}^c & 0 \\ p_{21}^c & p_{22}^c & 0 \\ 0 & 0 & \lambda_w \end{bmatrix}. \quad (3.85)$$

Because P_{11} is diagonal and R is unitary, P_{11}^c is symmetric, so $p_{21}^c = p_{12}^c$.

Last but not least, one can introduce the decomposition of P_{11} into two components

$$P_{11} = \bar{P}_{11} + \hat{P}_{11}, \quad (3.86)$$

where \bar{P}_{11} is named as the isotropic component

$$\bar{P}_{11} = \begin{bmatrix} \frac{1}{2}(\lambda_u + \lambda_v) & 0 & 0 \\ 0 & \frac{1}{2}(\lambda_u + \lambda_v) & 0 \\ 0 & 0 & \frac{1}{2}\lambda_w \end{bmatrix} = \begin{bmatrix} \bar{\lambda} & 0 & 0 \\ 0 & \bar{\lambda} & 0 \\ 0 & 0 & \frac{1}{2}\lambda_w \end{bmatrix}, \quad (3.87)$$

and \hat{P}_{11} is named as the anisotropic component

$$\hat{P}_{11} = \begin{bmatrix} \frac{1}{2}(\lambda_u - \lambda_v) & 0 & 0 \\ 0 & \frac{1}{2}(\lambda_v - \lambda_u) & 0 \\ 0 & 0 & \frac{1}{2}\lambda_w \end{bmatrix} = \begin{bmatrix} \hat{\lambda} & 0 & 0 \\ 0 & -\hat{\lambda} & 0 \\ 0 & 0 & \frac{1}{2}\lambda_w \end{bmatrix}. \quad (3.88)$$

Now the dipolar response of the object is described, let us focus on the second contribution in (3.66).

Quadrupolar response of the object

Let the quadrupolar contribution to potential $\phi_1(\mathbf{x})$ be $\phi_{1q}(\mathbf{x})$, defined as

$$\phi_{1q}(r) = \frac{\mathbf{r}}{8\pi r^4} P_{22} : \partial^1 \mathbf{E}^0. \quad (3.89)$$

This contribution arises when the field \mathbf{E}^0 is not constant in the object, that is, when the first derivative of \mathbf{E}^0 , denoted $\partial^1 \mathbf{E}^0$, is not zero and makes the tensor P_{22} to express. Unlike the tensor P_{11} , there does not exist yet in the literature an explicit expression of P_{22} for ellipsoidal objects. In other words, we cannot evaluate the potential $\phi_{1q}(r)$ from the knowledge of the properties of the object. So, we shall not be able to get quantitative values of that potential. But, the multipole expansion for the potential is a standard problem in physics [42] and we can use this approach in order to have a qualitative representation of $\phi_{1q}(\mathbf{x})$. The term $\frac{1}{2}P_{22}\partial^1 \mathbf{E}^0$ can be identified to the term $u_r^T Q u_r$ in the physics literature, where $u_r = r/|r|$ and Q is the quadrupole moment tensor represented with a $[3 \times 3]$ matrix. A quadrupolar potential can be produced with four particles carrying charge $\pm q$, placed at the tops of a square. The induced potential is represented with its iso-values in figure 3.8. Because the potential $\phi_{1q}(\mathbf{x})$ cannot be explicitly related to the field \mathbf{E}^0 and the objects properties, this representation is only qualitative. That is why, in the following chapters, the algorithms only consider the dipolar response of the object, and neglect the quadrupolar response. However, this representation provides good intuition about this second contribution and this will be essential for the understanding of the reasons of the limits of these algorithms.

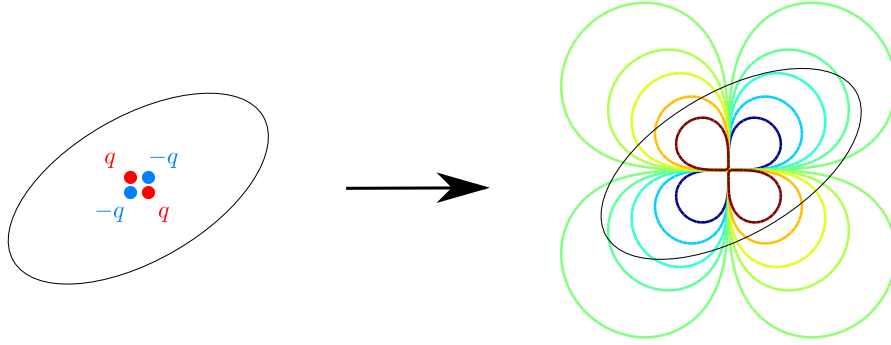


Figure 3.8: Representation of the four charges (left) that produce the potential $\phi_{1q}(\mathbf{x})$ represented with its iso-values (right).

3.3.4 Model for the 2nd reflexion (Step 2)

Here, we calculate the effect of the electric response of the sensor to the combination of both ϕ_0 and $\phi_1 \simeq \phi_{1d}$. Firstly, we define another electric currents vector, denoted δI_{ax} and defined as

$$I_{\text{ax}} = I^0 + \delta I_{\text{ax}}, \quad (3.90)$$

where δI_{ax} is an additive component due to the presence of object. As I^0 , which is the consequence of a given polarization vector U through C^0 , δI_{ax} is the consequence of the potentials $\phi_1(\mathbf{x})$ evaluated at the macro-electrodes centers, through C^0 as well

$$\delta I_{\text{ax}} = C^0 \cdot \Phi_1, \quad (3.91)$$

where Φ_1 is the vector of potentials $\phi_1(\mathbf{x})$ evaluated at each macro-electrodes center \mathbf{x}_k

$$\Phi_1 = [\phi_1(\mathbf{x}_1) \quad \phi_1(\mathbf{x}_2) \quad \phi_1(\mathbf{x}_3) \quad \phi_1(\mathbf{x}_4)]^T. \quad (3.92)$$

Note that the relationship (3.91) is established considering the smallness of the lateral dimensions of the sensor (slender shaped sensor, property \mathcal{P}_4) and approximating ϕ_1 as being uniform on each \mathcal{E}_k and equal to $\phi_1(\mathbf{x}_k)$. With the expressions of the field \mathbf{E}^0 (3.62) and the potential ϕ_1 (3.67), the vector δI_{ax} can be written in the matrix form

$$\delta I_{\text{ax}} = -\frac{1}{4\pi\gamma} C^0 G P_{11} G^T C^0 U. \quad (3.93)$$

Recall the matrix product $-\frac{1}{4\pi\gamma} P_{11} G^T C^0 U = P_{11} \cdot \mathbf{E}^0 = \mathbf{p}$ (3.68). As a consequence, the vector δI_{ax} is the projection onto the axial currents space of the dipolar moment \mathbf{p} through the matrix $C^0 G$

$$\delta I_{\text{ax}} = C^0 G \mathbf{p}. \quad (3.94)$$

Also, we define the real and symmetric conductance variation matrix δC , such that $\delta I_{\text{ax}} = \delta C \cdot U$

$$\delta C = -\frac{1}{4\pi\gamma} C^0 G P_{11} G^T C^0. \quad (3.95)$$

The matrix δC encodes the conductance variation of the environment due to the presence of the object. The current $\delta I_{\text{ax},k}$, measured on a given macro-electrode k as half the sum of the

currents I_{2k} and I_{2k-1} , can be written from (3.93) as

$$\delta I_{\text{ax},k} = - \sum_{i=1}^4 \frac{C_{ki}^0}{r_i^3} [(x_o^c - x_i) \cdot E_x^0 \cdot p_{11}^c + y_o^c \cdot E_y^0 \cdot p_{22}^c + ((x_o^c - x_i) \cdot E_y^0 + y_o^c \cdot E_x^0) \cdot p_{12}^c], \quad (3.96)$$

with E_x^0 and E_y^0 given by (3.64).

The second measurable currents vector is denoted I_{lat} and is defined as

$$I_{\text{lat}} = -\frac{1}{4\pi} P_{\perp} H P_{11} G^T C^0 U, \quad (3.97)$$

where P_{\perp} is a constant diagonal matrix which components only depend on the electrodes' geometry

$$P_{\perp} = 10^{-4} \begin{bmatrix} 5.2860 & 0 & 0 & 0 \\ 0 & 6.7360 & 0 & 0 \\ 0 & 0 & 6.9156 & 0 \\ 0 & 0 & 0 & 5.5189 \end{bmatrix}. \quad (3.98)$$

The values of P_{\perp} where determined experimentally with a calibration process. The matrix H is defined as

$$H = \begin{bmatrix} \frac{3y_o^c(x_o^c - x_1)}{r_1^5} & \frac{2y_o^{c2} - (x_o^c - x_1)^2}{r_1^5} & 0 \\ \frac{3y_o^c(x_o^c - x_2)}{r_2^5} & \frac{2y_o^{c2} - (x_o^c - x_2)^2}{r_2^5} & 0 \\ \frac{3y_o^c(x_o^c - x_3)}{r_3^5} & \frac{2y_o^{c2} - (x_o^c - x_3)^2}{r_3^5} & 0 \\ \frac{3y_o^c(x_o^c - x_4)}{r_4^5} & \frac{2y_o^{c2} - (x_o^c - x_4)^2}{r_4^5} & 0 \end{bmatrix}, \quad (3.99)$$

with $r_k = \sqrt{(x_o^c - x_k)^2 + y_o^{c2}}, \forall k \in \{1, \dots, 4\}$. The vector I_{lat} can also be interpreted as the projection onto the lateral currents space of the dipolar moment \mathbf{p} through the matrix $P_{\perp} H$

$$I_{\text{lat}} = P_{\perp} H \mathbf{p}. \quad (3.100)$$

The current $I_{\text{lat},k}$, measured on a given macro-electrode k as half the difference of the currents I_{2k} and I_{2k-1} , can be written from (3.97) as

$$I_{\text{lat},k} = -\frac{p_{\perp k}}{r_k^5} \left(3y_o^c(x_o^c - x_k) \cdot E_x^0 \cdot p_{11}^c + 2y_o^{c2} - (x_o^c - x_k)^2 \cdot E_y^0 \cdot p_{22}^c \right. \\ \left. + (3y_o^c(x_o^c - x_k) \cdot E_y^0 + (2y_o^{c2} - (x_o^c - x_k)^2) \cdot E_x^0) \cdot p_{12}^c \right) \quad (3.101)$$

with $p_{\perp k}$ the k^{th} component of the diagonal of P_{\perp} and E_x^0 and E_y^0 given by (3.64). Whereas $\delta I_{\text{ax},k}$ is a linear combination of the four electric potential $\phi_1(\mathbf{x}_{k=1,\dots,4})$, $I_{\text{lat},k}$ is proportional to the corresponding normal component of electric field $\mathbf{E}_1(\mathbf{x}_k) = -\nabla \cdot \phi_1(\mathbf{x}_k)$. The multiplicative coefficient being $p_{\perp k}$

$$I_{\text{lat},k} = -p_{\perp k} \mathbf{E}_1(\mathbf{x}_k) \cdot \mathbf{n}. \quad (3.102)$$

3.3.5 Currents model in polar coordinates

The currents model described above was described in Cartesian coordinates. But, for the seeking object task (chapter 4), this formulation is not the most suitable. The polar coordinates system,

as described in figure 2.6, is a more convenient coordinates' system for such a task and the currents' expressions are reformulated here. Moreover, using the polarization tensor decomposition (3.86), $\delta I_{\text{ax},k}$ and $I_{\text{lat},k}$ can be both decomposed into an isotropic (*bar* symbol) and an anisotropic contribution (*hat* symbol)

$$\delta I_{\text{ax},k} = \delta \bar{I}_{\text{ax},k} + \delta \hat{I}_{\text{ax},k} \quad (3.103)$$

$$I_{\text{lat},k} = \bar{I}_{\text{lat},k} + \hat{I}_{\text{lat},k}, \quad (3.104)$$

and the currents expressions are

$$\delta \bar{I}_{\text{ax},k} = -\frac{\bar{\lambda}}{4\pi\gamma} \sum_{i,j=1}^4 \frac{C_{kj}^0 I_i^0}{\rho_i^3 \cdot \rho_j^3} (l_i l_j + (l_i + l_j)\rho \cos \alpha + \rho^2). \quad (3.105)$$

$$\begin{aligned} \delta \hat{I}_{\text{ax},k} = & -\frac{\hat{\lambda}}{4\pi\gamma} \sum_{i,j=1}^4 \frac{C_{kj}^0 I_i^0}{\rho_i^3 \cdot \rho_j^3} (l_i l_j \cos(2(\theta + \alpha)) \\ & + (l_i + l_j)\rho \cos(2\theta + \alpha) + \rho^2 \cos(2\theta)) \end{aligned} \quad (3.106)$$

$$\begin{aligned} \bar{I}_{\text{lat},k} = & -\frac{p_{\perp k} \bar{\lambda}}{4\pi\rho_k^3} \sum_{i=1}^4 \frac{I_i^0}{\rho_i^3} (l_i 3 \sin(\alpha_k) \cos(\alpha_k) \\ & + \rho (3 \sin(\alpha_k) \cos(\alpha - \alpha_k) - \sin(\alpha))). \end{aligned} \quad (3.107)$$

$$\begin{aligned} \hat{I}_{\text{lat},k} = & -\frac{p_{\perp k} \hat{\lambda}}{4\pi\rho_k^3} \sum_{i=1}^4 \frac{I_i^0}{\rho_i^3} (l_i (3 \sin(\alpha_k) \cos(2\theta + 2\alpha - \alpha_k) - \sin(2(\theta + \alpha))) \\ & + \rho (3 \sin(\alpha_k) \cos(2\theta + \alpha - \alpha_k) - \sin(2\theta + \alpha))) \end{aligned} \quad (3.108)$$

where $\rho_i = \|l_i \mathbf{e}_{\parallel} + \rho \mathbf{e}_{\rho}\|, \forall i \in \{1, \dots, 4\}$.

Now the analytical model is entirely described, it can be implemented in order to compute the currents vectors δI_{ax} and I_{lat} for a comparison with actual measurements and BEM simulated currents. Figure 3.9 shows the currents for the fly-by test introduced in figure 2.20a. There is a good correlation between the actual measurements (straight lines) and BEM computed currents (thin straight lines with crosses). The differences can mainly be explained by 1) the effect of the rigid epoxy fiber which is not modeled in the BEM ; 2) the not perfect shape of the constitutive elements of the actual sensor, which is a manufactured device. Despite of these small differences, both models fairly describe the currents' behavior. This shows that the BEM model is accurate enough to provide reliable simulated currents and the relevance of the analytical model, which will be used as a basis for the inverse problem solving in the next chapters.

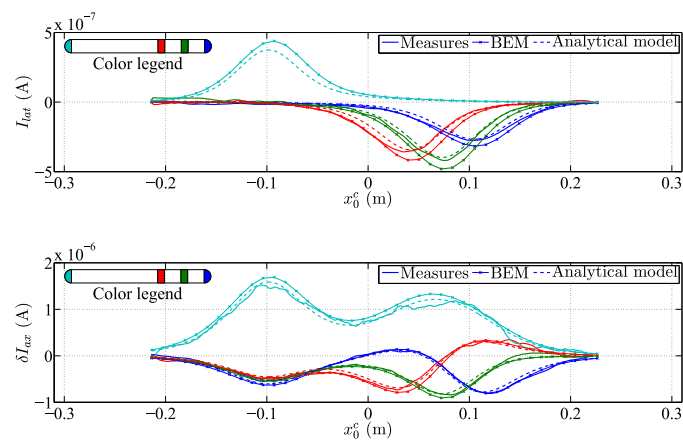


Figure 3.9: Top (resp. bottom): the currents I_{lat} (resp. δI_{ax}) for the fly-by test described in figure 2.20a. Solid lines: measured currents. Solid lines with crosses: BEM currents. Dashed lines: currents calculated with the analytical model. The horizontal axis represents the longitudinal component of the object in the sensor frame, denoted x_0^c in figure 2.5.

Chapter 4

Object's inspection

As previously mentioned in the introduction, we consider the sensor navigating in an unknown environment as a starting point. Just like the fish which detects an object and navigates in its surroundings using a sensorimotor loop (see figure 1.15), we propose in this chapter several algorithms that allow the sensor to have a similar behavior. These algorithms enable the sensor to detect the presence of an object, adapt its trajectory in order to reach it and rotate around it. Also, we will show that the object's material can easily be discriminated as well as its position with respect to the sensor's axis.

To sum up, the term "object's inspection" is used to gather these different tasks. Let us list them and describe each of them in details

1. object's detection,
2. object's material discrimination,
3. object's left/right position discrimination with respect to the sensor's axis,
4. seek the object and rotate around it by following its boundaries.

The three first tasks correspond to three simple algorithms which consist in checking if some particular measured currents are zero, positive or negative. The fourth task is performed with a more complex algorithm, divided into three phases, and partly inspired by the behavior of the fish when it reaches an external electric dipole, as represented in figure 1.14 and studied in [78, 70].

4.1 Object's detection

Checking the presence of an object in the sensor's surroundings is the first task to perform before any other. Indeed, the implementation of an algorithm for object's localization or characterization in the absence of any object would have no sense.

The presence of an object can be determined by comparing the current measurements with the measurements that are expected in the absence of any object. According to (3.90), if the sensor is far from any object, the measured axial currents vector boils down to I^0 , which is known because it only depends on the sensor characteristics and the water conductivity. Hence, the absence of an object in the sensor's surroundings leads to

$$I_{\text{ax}} - I^0 = \mathbf{0}. \quad (4.1)$$

So, a simple object's detection algorithm consists in checking if this equality is true or not. In actual conditions, a threshold can be experimentally defined in order to take into account the measurement uncertainties and noise [81]. Hence, in practice, the presence of an object will be assessed if the following inequality is verified

$$|I_{\text{ax}} - I^0| \geq \text{noise}. \quad (4.2)$$

This algorithm requires very low computing resources and can be implemented at any moment during the sensor's movement. In the following, we will assume that the presence of the object is unambiguously known.

4.2 Material discrimination

When an object is detected in the surroundings, its material can be discriminated. Recall that in this thesis, the objects are considered as either conductive or insulating. The principle for material characterization is based on the global conductivity variation due to the object. For a scene with no object, the measured vector $I_{\text{ax}} = I^0$. Adding an object in the scene will make the global conductivity to change and this will have an influence on the measured currents. The variation with respect to I^0 will be positive or negative depending on the object's material. For instance, suppose the macro-electrode \mathcal{E}_4 to be set to a voltage u and the three others to 0V. Hence, the current flowing through \mathcal{E}_4 is given by $I_{\text{ax},4} = I_4^0 + \delta I_{\text{ax},4}$. So, the sign of current $\delta I_{\text{ax},4}$ can be used to discriminate the object's material. Unfortunately, as explained in section 2.4.2, measuring the current of a polarized electrode is not technically feasible. But, due to the charge conservation in the whole scene, the sum of all currents in the scene equals to zero. Thus, $\delta I_{\text{ax},4}$ can be computed as $\delta I_{\text{ax},4} = -\sum_{i=1}^3 \delta I_{\text{ax},i}$.

In order to illustrate that, four fly-by tests were performed in simulation, with two 1cm radius spheres, one being conductive and the other being insulating, each one passing by the sensor on each side. To sum up, the currents were recorded during the four following fly-by tests

1. Conductive sphere, passing by the sensor on the left side,
2. Conductive sphere, passing by the sensor on the right side,
3. Insulating sphere, passing by the sensor on the left side,
4. Insulating sphere, passing by the sensor on the right side.

See the test conditions in figure 4.1, top row. As a result, the sum $\sum_{i=1}^3 \delta I_{\text{ax},i}$, denoted $\Sigma \delta I_{\text{ax}}$, is positive for the conductive sphere (figure 4.1, second row), and is negative for the insulating sphere (figure 4.1, bottom row), independently of the side. Hence, the following algorithm is defined

1. If $\Sigma\delta I_{ax} > 0$, then the object is a conductor,
2. If $\Sigma\delta I_{ax} < 0$, then the object is an insulator.

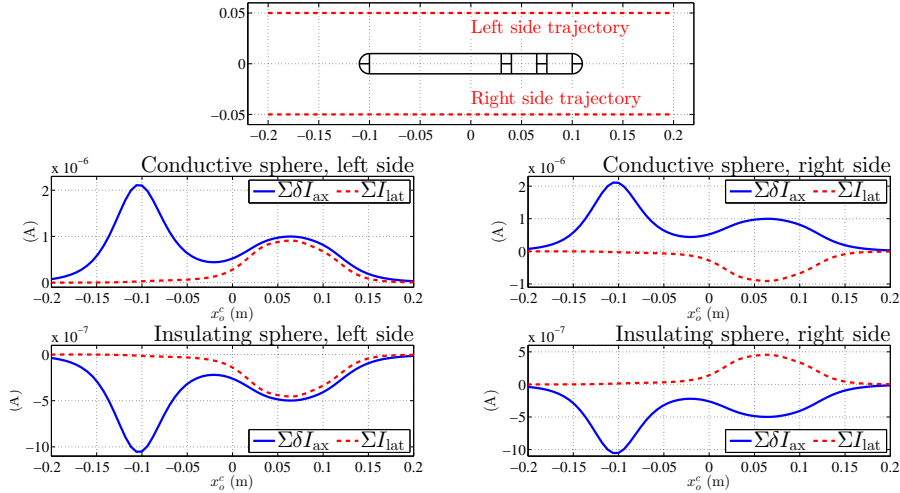


Figure 4.1: Top row: the two trajectories of the spheres with respect to the sensor. Middle row: the currents' sums $\Sigma\delta I_{ax}$ and ΣI_{lat} during the fly-by test with the conductive sphere. Bottom row: similar to the middle row but for the insulating sphere.

Like the previous algorithm, a threshold can be experimentally defined in order to take into account the measurement noise.

Also, one can see that the sign of the sum of the lateral currents, denoted ΣI_{lat} , depends on both the object's material and the side. This is useful to determine on which side of the sensor the object is. This is presented in the next section.

4.3 Left/right discrimination

We saw in the previous section that the sign of $\Sigma\delta I_{ax}$ allows for material discrimination. Using similar observation on the sum of the $I_{lat,k=1,2,3}$ currents, denoted ΣI_{lat} , one can discriminate on which side of the sensor the object is.

As already mentioned in chapter 3, the lateral current measured on a given macro-electrode is proportional to the normal component of the electric field \mathbf{E}_1 at the location of that macro-electrode, see equation 3.102. Also, recall that \mathbf{E}_1 is the field that is produced by the polarized object. In figure 3.4a is represented the field $\mathbf{E}_1(\mathbf{x}_1)$ for an object placed on the left side of the sensor. If this object would be placed symmetrically on the right side of the sensor, the sign of the normal component of $\mathbf{E}_1(\mathbf{x}_1)$ would be changed.

This is confirmed by the simulations presented in figure 4.1: the middle row shows that a conductive sphere on the left side produces a positive value of ΣI_{lat} , whereas this object on the right side produces a negative value of ΣI_{lat} . The bottom row in figure 4.1 shows the same

principle with the insulating sphere, but with opposite sign. The material of the object being discriminated with the algorithm described in the previous section, one can define the following algorithm

1. If $\Sigma I_{\text{lat}} = 0$, there is no object in the scene, or there is one object facing macro-electrode \mathcal{E}_1 or \mathcal{E}_4 ,
2. If $\Sigma I_{\text{lat}} > 0$, a conductive object is on the left or an insulating object is on the right,
3. If $\Sigma I_{\text{lat}} < 0$, an insulating object is on the left or a conductive object is on the right,

where ΣI_{lat} implicitly represents the sum $\sum_{i=1}^3 I_{\text{lat},i}$. As an example, the material and the left/right discriminations can be performed by reading the signs of currents shown in figure 3.9, which indeed, were obtained with an conductive object ($\Sigma \delta I_{\text{ax}} > 0$) on the right side of the sensor ($\Sigma I_{\text{lat}} < 0$). Again, in actual conditions a zero value has no sense, but may be replaced by the noise level.

At this point, we are able to detect the presence of an object in the sensor's surroundings, discriminate its material and on which side it is with respect to the sensor's axis. Let us now set our sensor in motion, using another algorithm which allows the sensor to reach the object and rotate around it by following its boundaries.

4.4 Seek the object

The displacement toward an object and the rotation around it by following its boundaries necessarily requires a controlled motion of the sensor. A controlled strategy was proposed in [14, 56] in order to reach that goal. It is composed of three distinct phases. We will firstly describe the whole algorithm and then focus on its first phase in this section, which correspond to the displacement toward the object. The second and third phases of the algorithm correspond to the rotation about the object, which will be the purpose of the next two sections.

The whole algorithm is presented in figure 4.2a. Firstly, the object is sought with a constant forward velocity $V_{\parallel} \mathbf{i}_c$, and a controlled angular velocity $\Omega \mathbf{k}_c$ (from A to B in 4.2b). It corresponds to the first phase denoted "Seek an object" in figure 4.2a. This phase is ended by a transition, which corresponds to the zero crossing of the current $\delta I_{\text{ax},2}$. Secondly, V_{\parallel} is set to 0 and a rotation about the vertical axis is performed in order to remove the sensor from the electric influence of the object (from B to B' in 4.2b). This corresponds to the second phase denoted "Flee from the electric influence" in 4.2a, which lasts until the minimum value of $|\delta I_{\text{ax},1}|$ is reached, which represents the second transition. Finally, a constant V_{\parallel} is applied and Ω is controlled so that the sensor follows the boundaries of the object (from B' to C in 4.2b). It corresponds to the third phase denoted "Follow the boundaries" in 4.2a. All along the process, only \mathcal{E}_4 is polarized with a constant value and measurements are performed on the three other macro-electrodes.

Here we describe the first phase of the algorithm, which consists in seeking an object. The control strategy proposed is inspired by the fish's behavior, which follows the field lines in order to reach an electric dipole as presented in figure 1.14. This strategy can be easily reproduced with our sensor, taking benefits from its slender shape and using the lateral current $I_{\text{lat},1}$. As shown by

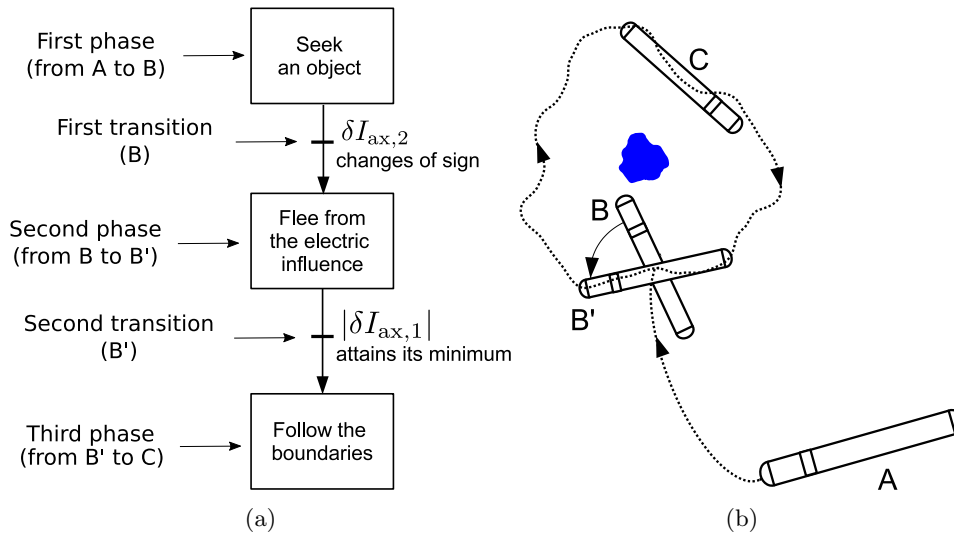


Figure 4.2: (a) The three phases and the two transitions of the algorithm. (b) A representation of the sensor's path during the algorithm's implementation.

their definition (3.50), the I_{lat} currents are calculated as half the difference between the currents measured on the left and right electrodes of each macro-electrode. Intuitively, we can feel that this difference would be zero if the sensor would be aligned with a current line. This is shown with the analytical model, which indicates that the lateral current measured on macro-electrode k is proportional to the component of the electric field that is normal to the electrode (3.102). Hence, a convenient criteria to evaluate the sensor alignment with a current line is the value of an I_{lat} current.

One have to mention that contrary to the experiment with the fish presented in [78], where the dipole presented to the fish was artificially turned on and off, in our context the dipole is due to the polarization of an electrically passive object. Nevertheless, the principle of the field lines following can be reproduced. This was firstly introduced in [14] for spherical objects. It consists in a proportional feedback control law of the rotation velocity Ω while a constant value is imposed for the linear velocity V_{\parallel}

$$V_{\parallel} = V_d, \Omega = k \cdot I_{lat,1}, \quad (4.3)$$

where V_d is a constant positive value and k is the gain of the proportional law. It was shown in [14] that the sensor could reach any contrasted spherical object using this control law. We firstly describe the case of a spherical object and then extend the results to ellipsoidal objects [56].

Let us note that, in the following, we will use the scene's parametrization described in figure 2.6. We will use the associated sensor's kinematics written as a function of the state vector (ρ, α, θ) , and the currents' analytical model described with equations (3.105) to (3.108).

4.4.1 Spherical objects

In the case of a spherical object, the angle θ in figure 2.6 does not exist and the state vector defined in (2.10) simplifies to $x = (\rho, \alpha)^T$. Also, the object's response is restricted to the isotropic component, so the control law ensures that $I_{\text{lat},1} = \bar{I}_{\text{lat},1} = 0$. The figures 4.3a and 4.3b show

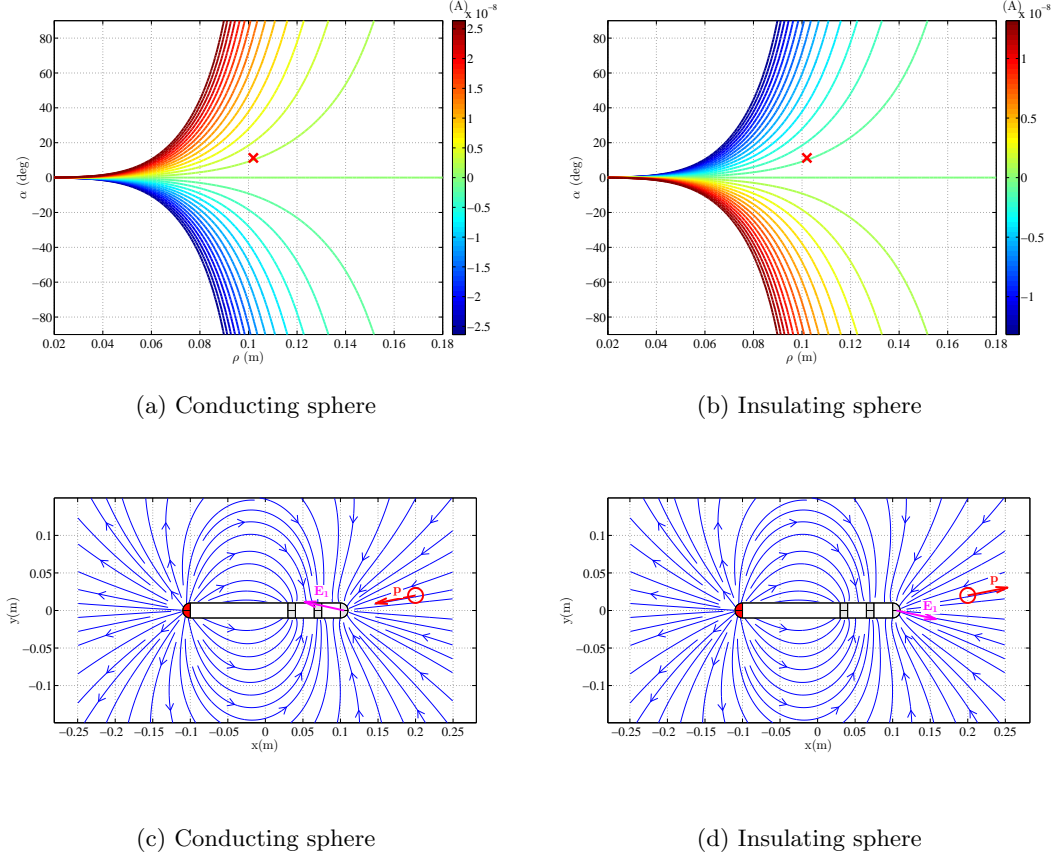


Figure 4.3: First row: $\bar{I}_{\text{lat},1}$ iso-values in the plan (ρ, α) for a conducting sphere (a) and for an insulating sphere (b). The red crosses indicate the coordinates of the sphere represented in the figures of the second row $(0.102\text{m}, 11.3^\circ)$. Second row: representation of the electric field $\mathbf{E}_1(\mathbf{x}_1)$ due to a spherical conducting (c) and insulating (d) object. The dipolar moment \mathbf{p} is tangent to the electric field line \mathbf{E}^0 and $\mathbf{E}_1(\mathbf{x}_1) \cdot \mathbf{n} \neq 0$.

some iso-values of $\bar{I}_{\text{lat},1}$ as a function of ρ and α . One can see that the root locus is given for $\alpha = 0$ and any value of ρ , that is, $\bar{I}_{\text{lat},1}$ cancels out when the sphere is aligned with the sensor's axis. As an example, figures 4.3c and 4.3d show a spherical object located at $(\rho, \alpha) = (0.102\text{m}, 11.3^\circ)$, plunged into the basal field produced by the sensor which macro-electrode \mathcal{E}_4 is polarized. The dipolar moment \mathbf{p} is tangent to the electric field line \mathbf{E}^0 because the tensor P_{11} for the sphere is proportional to the identity matrix, see (3.76). As a result, $\mathbf{E}_1(\mathbf{x}_1)$ is not aligned with the sensor's axis, so the current $\bar{I}_{\text{lat},1} \neq 0$ (recall $\bar{I}_{\text{lat},1}$ is proportional to the normal component of $\mathbf{E}_1(\mathbf{x}_1)$, see (3.102)). The only way for $\bar{I}_{\text{lat},1}$ to vanish is to approach the object from the sensor's axis, that is, set α to zero.

Now, let us turn our attention to the choice of gain k . Firstly, suppose an object on the left side, as shown in figure 2.6. With a positive gain k in the control law (4.3), a positive value of $\bar{I}_{\text{lat},1}$ will set Ω to a positive value. This will make the sensor to turn on the left. So, if the object is conducting, the rotation will continue until $\bar{I}_{\text{lat},1}$ cancels out when the sensor points out toward the object's center. But, if the object is insulating, current $\bar{I}_{\text{lat},1}$ is negative (see 4.3b) so the sensor will turn on the right, fleeing from the object. Symmetrically, an insulating object on the right side would also be fled. Hence, the sign of the gain k has to be adapted to the material of the object, using the material discrimination algorithm described in section 4.2. So, the gain shall be divided by $\delta I_{\text{ax},4} = \Sigma \delta I_{\text{ax}}$, which is positive for a conducting object and negative for an insulating object (see section 4.2). This normalization has another advantage: the water conductivity γ is canceled out in the ratio $I_{\text{lat},1}/\Sigma \delta I_{\text{ax}}$, which makes the control law independent of the water. Then, k has to be large enough with respect to the constant velocity V_d . Indeed, as

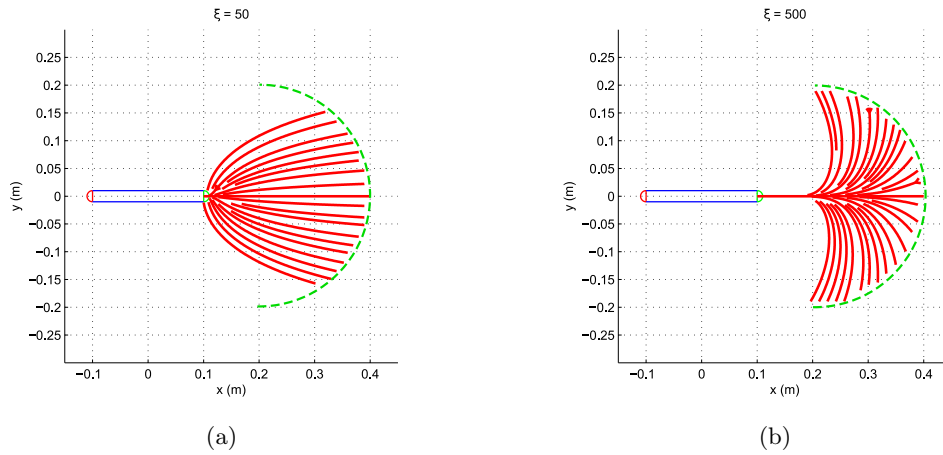


Figure 4.4: The trajectories of a sphere in the sensor frame ($O_p, \mathbf{i}_c, \mathbf{j}_c$) during the seeking object phase, for a reactivity $\xi = 50$ (a) and $\xi = 500$ (b). Each red line represents the trajectory of a sphere, from the sensor point of view. The green dashed lines represent the detection range.

shown in 4.4a, if the reactivity ξ , defined as $\xi = k/V_{\parallel}$, is set to 50 the sensor reaches the object before canceling out angle α . On the other hand, with a sufficiently high reactivity ($\xi = 500$ in figure 4.4b), the sensor rotates towards the object's center first ($\alpha = 0$) and then goes forward to reach it. To sum up, in practice the control law (4.3) becomes

$$V_{\parallel} = V_d, \Omega = \frac{500 \cdot V_d}{\Sigma \delta I_{\text{ax}}} I_{\text{lat},1}. \quad (4.4)$$

4.4.2 Ellipsoidal objects

In the case of an ellipsoidal object, the orientation angle θ plays a role and both $\bar{I}_{\text{lat},1}$ and $\hat{I}_{\text{lat},1}$ have to be taken into account, that is $I_{\text{lat},1} = \bar{I}_{\text{lat},1} + \hat{I}_{\text{lat},1}$. This is illustrated in figures 4.5a and 4.5b, in which we can see that the $I_{\text{lat},1}$ root locus depends on θ . Particularly, figure 4.5b shows that there exist some orientations $\theta + \alpha$ which cancel out $I_{\text{lat},1}$ even if the object is not aligned with sensor's axis. Despite of this θ -dependency, it is possible to use the same control law as for the spherical objects (4.4), the attractive behavior being preserved as shown in figure

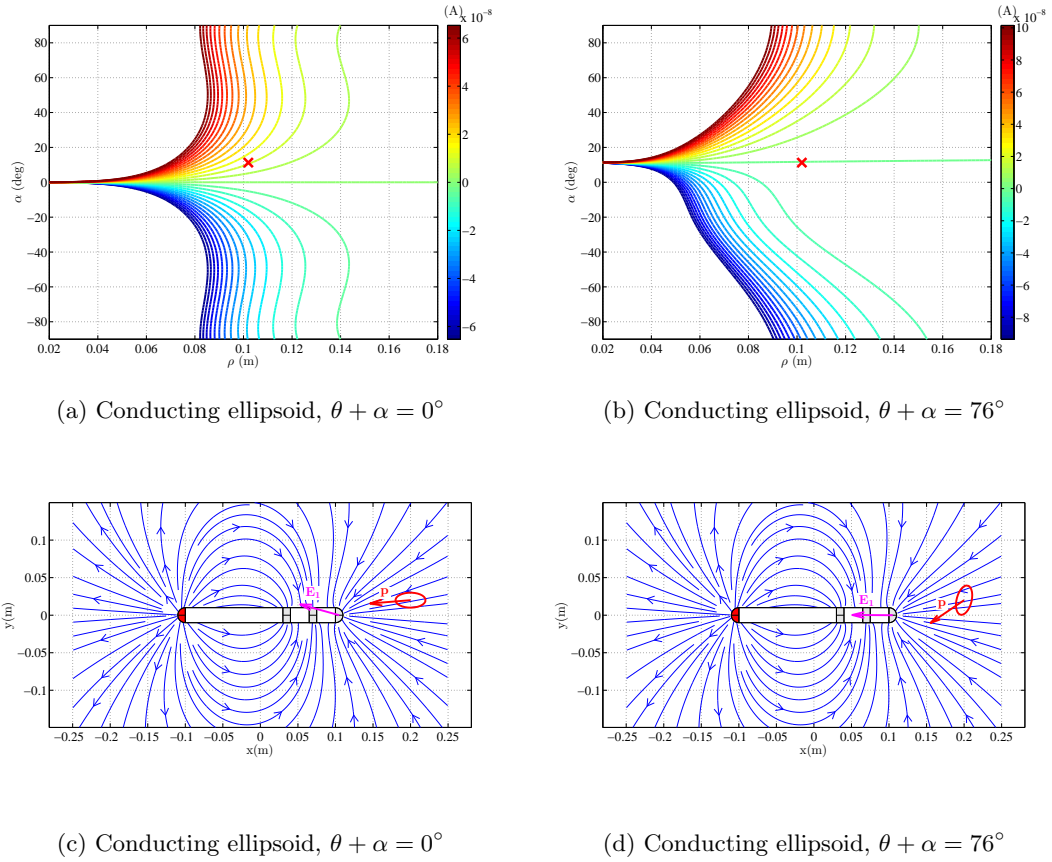


Figure 4.5: First row: $\bar{I}_{\text{lat},1}$ iso-values in the plan (ρ, α) for a conducting ellipsoid with $\theta + \alpha = 0^\circ$ (a) and $\theta + \alpha = 76^\circ$ (b). The red crosses indicate the coordinates $(0.102\text{m}, 11.3^\circ)$ which are the coordinates of the ellipsoid's center represented in the figures of the second row. Second row: representation of the electric field $\mathbf{E}_1(\mathbf{x}_1)$ due to an ellipsoidal conducting object rotated with an angle of $\theta + \alpha = 0^\circ$ (c) and $\theta + \alpha = 76^\circ$ (d). Because P_{11} has an anisotropic component \hat{P}_{11} , the dipolar moment \mathbf{p} is not necessarily tangent to the field lines. In (d), the normal component of $\mathbf{E}_1(\mathbf{x}_1)$ equals to zero, leading to $I_{\text{lat},1} = 0$, even if the object's center is not aligned with the sensor's axis.

4.6. In the sensor frame, the object is not attracted along a straight line as observed for the sphere, but within a cone defined with the aperture angle. The aperture angle depends on both the angle $\theta + \alpha$, as shown in figure 4.7a and on the object's aspect ratio, as shown in figure 4.7b.

4.4.3 First transition: stop while facing the object

Whereas $I_{\text{lat},1}$ was used for the first phase, here current $\delta I_{\text{ax},2}$ is used to end this first phase. According to the equation (3.94), this current has the following expression

$$\delta I_{\text{ax},2} = C_2^0 \cdot G \cdot \mathbf{p} \quad (4.5)$$

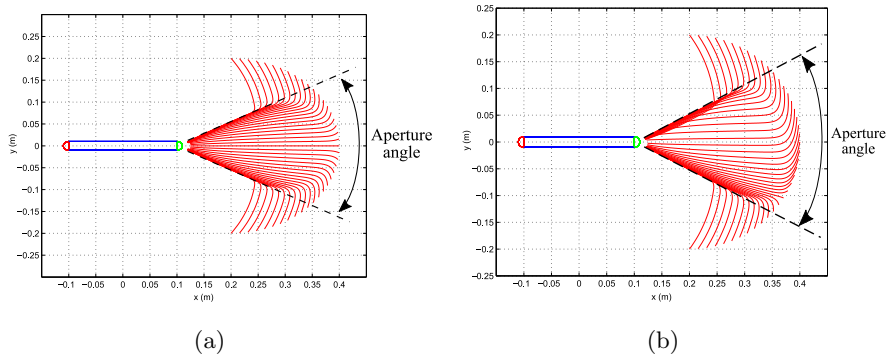


Figure 4.6: Trajectories of an ellipsoid in the sensor frame ($O_p, \mathbf{i}_c, \mathbf{j}_c$) for a reactivity $\xi = 500$. Initial angle $\theta + \alpha = 0^\circ$ (a) and $\theta + \alpha = 30^\circ$ (b).

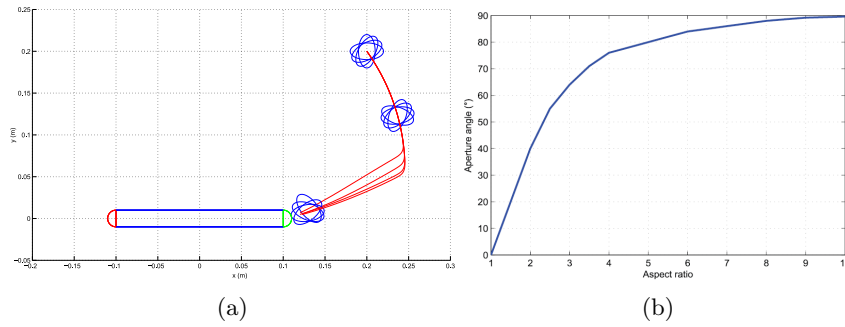


Figure 4.7: (a) The trajectories of an ellipsoid in the sensor frame ($O_p, \mathbf{i}_c, \mathbf{j}_c$) for a reactivity $\xi = 500$ and $\theta + \alpha = \{0^\circ, 30^\circ, 60^\circ, 90^\circ\}$. (b) The aperture angle as a function of the aspect ratio of the object.

where C_2^0 is the second line of matrix C^0 (3.57), G is the matrix defined in (3.63) and \mathbf{p} is the dipolar moment of the object. The vector $\mathbf{C}_2 = C_2^0 \cdot G \in \mathbb{R}^3$ is a function of the sensor's geometrical properties and of ρ and α only. Hence, it is independent of the properties of the object, encoded in the vector \mathbf{p} .

There exist two cases in which $\delta I_{ax,2}$ changes its sign: either $\mathbf{C}_2(\rho, \alpha) = \mathbf{0}$ or $\mathbf{C}_2(\rho, \alpha) \perp \mathbf{p}$. The case $\mathbf{p} = \mathbf{0}$ is not considered here because it corresponds to a scene with no object. The root locus of $\delta I_{ax,2}$ is represented in figure 4.8, as a function of ρ and α for three different sensor's geometries, defined by three different values of l_2 (recall that l_2 was defined in figure 2.6). This shows that for a given distance l_2 , the distance ρ between the macro-electrode \mathcal{E}_1 and the object's center when the sensor stops its motion lies between two bounds. Considering that $l_2 = 0.035$ on our sensor, the first phase will stop for ρ in the range $[0.08; 0.09]$ m.

At this point, we have described the seeking object task, which corresponds to the first phase and the first transition of the algorithm shown in 4.2a. Let us continue with the description of the next phase of the algorithm, which corresponds to flee from the object's influence.

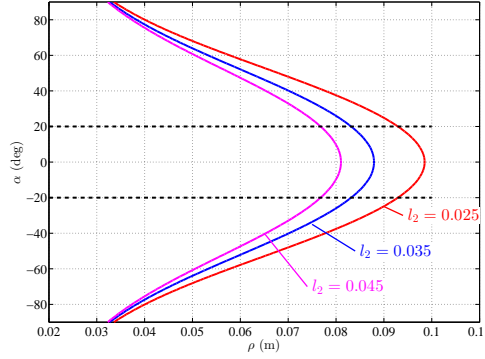


Figure 4.8: Current $\delta I_{ax,2}$ root locus in the (ρ, α) plane for three different values of l_2 , calculated with the analytical model for a conducting sphere. Note that the root locus is in the range of detection. The dashed lines represent the aperture angle for an aspect ratio of 2, that is, $\pm 20^\circ$ as shown in figure 4.7b.

4.5 Flee from the object's influence

For the second phase, which consists in rotating the sensor about the vertical axis until the effect of the objects cancels out (from B to B' in 4.2b), the following control law is defined

$$V_{\parallel} = 0, \Omega = -k \cdot \delta I_{ax,1}, \quad (4.6)$$

where k is a positive gain. Contrary to previous control law (4.3), the minus sign ensures the sensor to flee from the object. The normalization of k with $\Sigma \delta I_{ax}$ shall also be used in order to indistinctly deal with conducting and insulating objects. The velocity V_{\parallel} is set to 0 in order to maintain the distance between sensor's and object's centers to the value given at the end of the first phase. Hence, the control law for the object clearance is defined as

$$V_{\parallel} = 0, \Omega = -k \cdot \frac{\delta I_{ax,1}}{\Sigma \delta I_{ax}}. \quad (4.7)$$

The value of k is the same as the seeking object control law (4.4). This sensor's rotation is described with respect to the angle μ , as shown in figure 4.9a. The angle $\mu = 0$ corresponds to the sensor's position when it reached the first transition. The control law defined above makes the sensor rotate counter-clockwise, hence making μ increase. While performing this rotation, the current $\delta I_{ax,1}$ decreases and increases, as shown in figure 4.9b.

Whatever the angle θ , $\delta I_{ax,1}$ takes a minimum value for μ around 90° and 270° and a maximum value around 0° and 180° . This trend is explained regarding the expression (3.94), showing that the vector δI_{ax} is a function of the object's dipolar moment \mathbf{p} through the matrix $C^0 G$. The factors r_i^{-3} in G (see (3.63)) make the measured currents for a close object to be higher (in norm) compare to a far object. Thus, for μ close to 0° , the current $\delta I_{ax,1}$ takes high values because the object is close to macro-electrode \mathcal{E}_1 . For μ close to 90° , $\delta I_{ax,1}$ takes its minimum value because the object is far from all macro-electrodes. Then, for $\mu > 90^\circ$, the object become closer to the macro-electrode \mathcal{E}_4 and that makes $\delta I_{ax,1}$ to increase again until μ being close to 180° . A symmetric pattern for $\delta I_{ax,1}$ is obtained for $180^\circ < \mu < 360^\circ$. So, the control law (4.7) makes

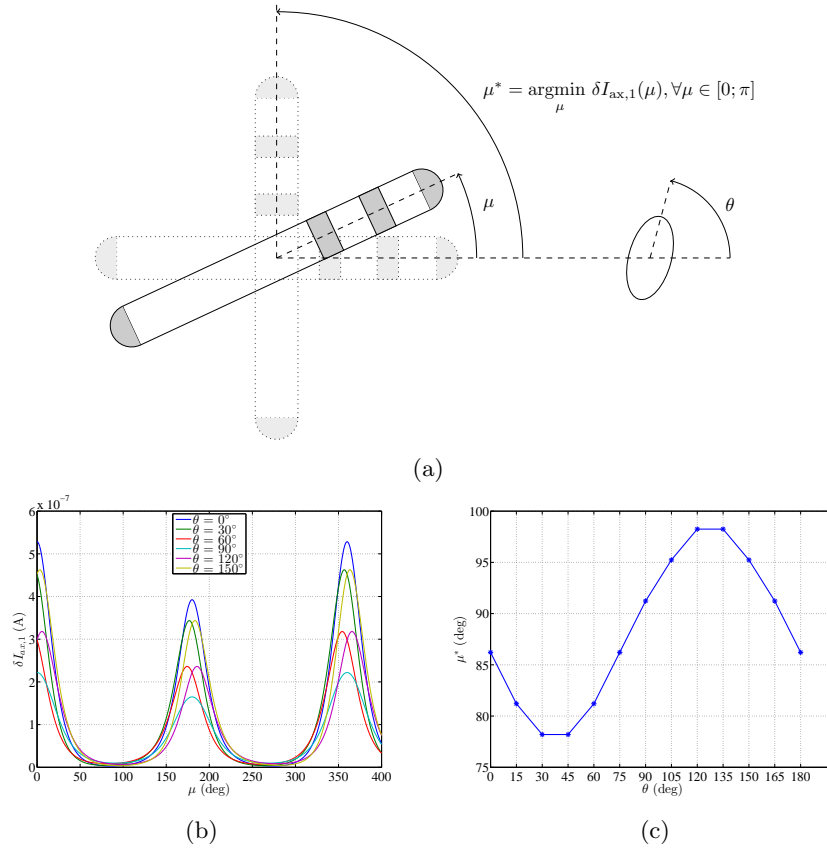


Figure 4.9: (a) A representation of the angles μ and μ^* . (b) The current $\delta I_{ax,1}$ as a function of μ for different object's angle θ , calculated with the analytical model. (c) The angle μ^* as a function of θ , obtained with the analytical model as well.

the sensor rotate until the minimum value of $\delta I_{ax,1}$ is reached. At this point, the control law is stopped. Let us denote μ^* the corresponding value of μ , that is,

$$\mu^* = \operatorname{argmin}_{\mu} \delta I_{ax,1}(\mu). \quad (4.8)$$

In figure 4.9c one can see the evolution of μ^* as a function of θ . This variation does not call into question the object clearance strategy and will only impact on the object's boundaries following described in next section. It can be mentioned that $\mu^*(0) \neq 90^\circ$ and $\mu^*(90) \neq 90^\circ$. This is due to the positions of the electrodes that are not symmetric respect to the vertical axis. Once the minimum value of $\delta I_{ax,1}$ is reached, the object clearance is considered as ended and the $\delta I_{ax,1}$ value is memorized.

4.6 Following the object's boundaries

After the sensor have fled from the object's influence, it follows the object boundaries with the following control law

$$V_{\parallel} = V_d, \Omega = k' \cdot (\delta I_{ax,1} - \delta I_{ax,1}^d), \quad (4.9)$$

where V_d is a constant positive value and k' a second steering gain that differs from k in (4.4) and (4.7). The current $\delta I_{ax,1}^d$ is the memorized value at the end of the second phase, so the control law (4.9) makes the sensor to track an iso-value $\delta I_{ax,1} = \delta I_{ax,1}^d$, thus revolving around the object. Trajectories around a sphere are shown in figure 4.10a for three values of reactivity ξ' , defined as

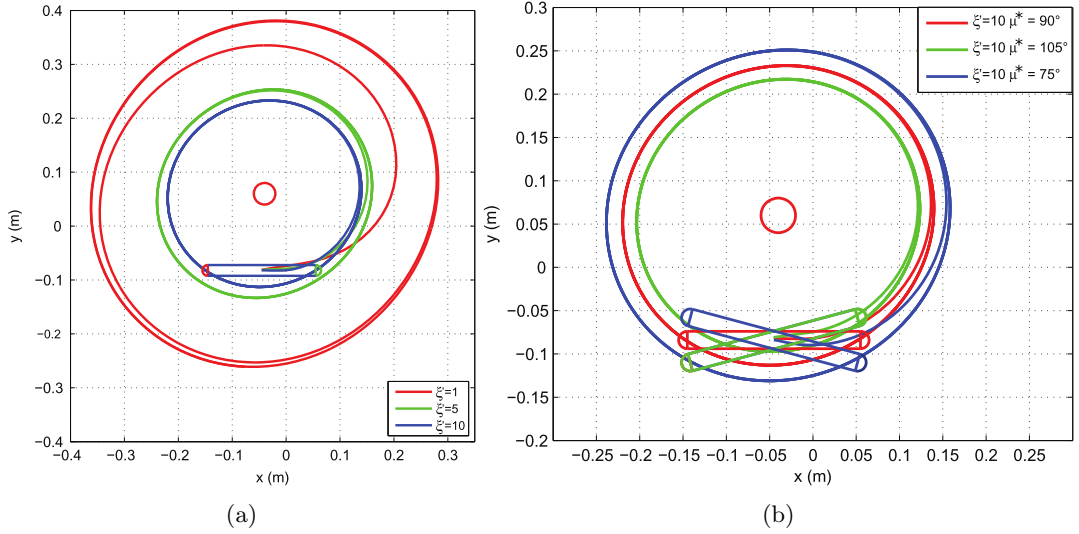


Figure 4.10: (a) Trajectories of the sensor for $\xi' \in \{1, 5, 10\}$ and with $\mu^* = 90^\circ$. (b) Trajectories of the sensor for $\xi' = 10$ and with $\mu^* \in \{90^\circ, 105^\circ, 75^\circ\}$.

$\xi' = k'/V_{\parallel}$. As shown in figure 4.9b, the minimum value of $\delta I_{ax,1}$ is reached for different values of μ , depending on the angle θ . As a result, the angle μ^* , which corresponds to the minimum value of $\delta I_{ax,1}$, is not necessarily 90° . So, during rotation around a non-spherical object, μ^* varies and the lateral distance between sensor and the object's boundary is not preserved during the revolution, as shown on figure 4.11. However, these simulation results show that the rotation around the object is preserved.

Now the entire algorithm for seeking an object and rotate around it was described with simulations, let us now focus on its experimental implementation.

4.7 Experimental implementation of the overall strategy

Here, we present some experimental results of the implementation of the whole algorithm described in figure 4.2b. In figure 4.12, first row, are shown the trajectories of the sensor for three insulating objects: a sphere, an ellipsoid, and a cube. The cube was tested twice, rotated by angles 0° and 45° . Looking at the sensor's trajectories, we notice that the sensor firstly reaches

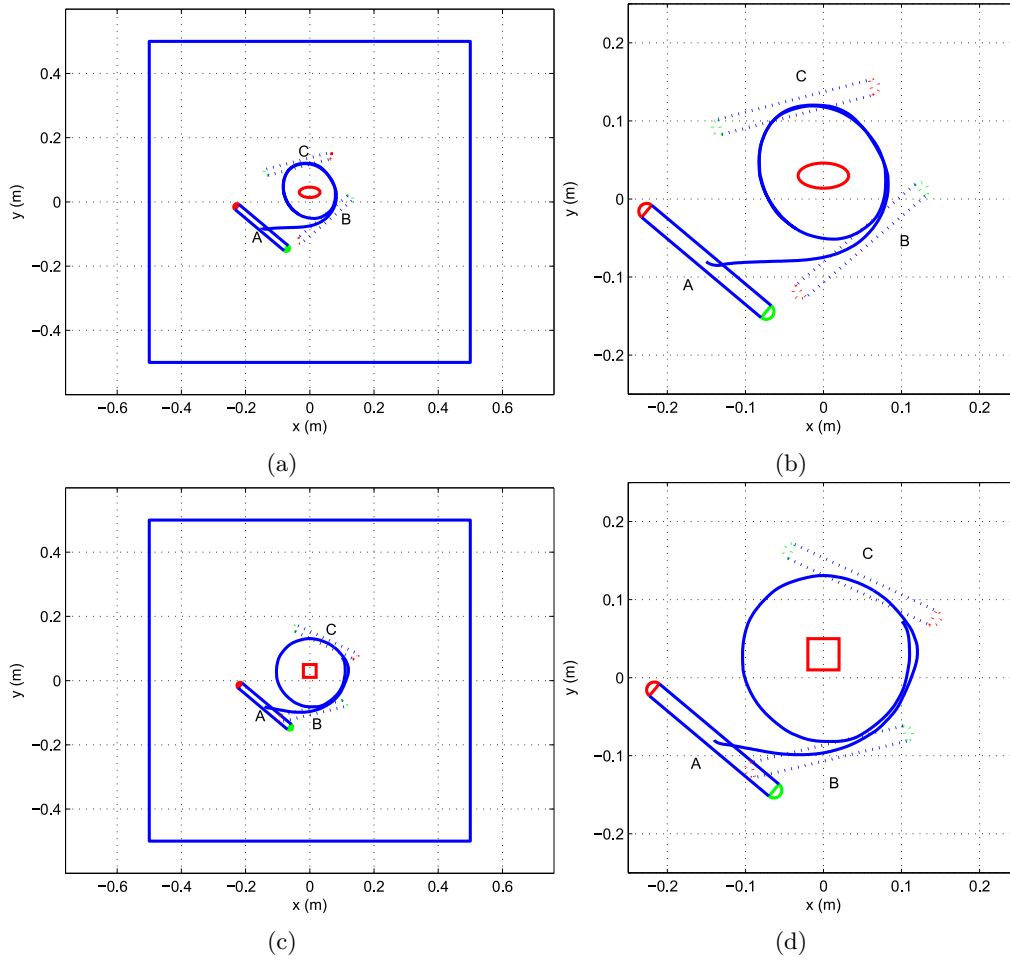


Figure 4.11: Implementation of the algorithm with non-spherical object. (a) Path of the sensor around a conductive ellipsoid. (b) Magnified view of the sensor's path in (a). (c) Path of the sensor around a conductive cube. (d) Magnified view of the sensor's path in (c).

the object and stops while facing it. This position is referenced as B. Then, it rotates in order to flee from the object's influence until it reaches the position B'. Finally, it rotates around the object, following an almost circular trajectory centered on the object.

The time evolution of the currents $\delta I_{ax,1}$ and $\delta I_{ax,2}$ during the experiment with the cube are plotted in figure 4.12d and 4.12e. From A to B, corresponding the first phase, the current $\delta I_{ax,2}$ increases as the sensor approaches the objects, until it reaches 0, at $t \simeq 8.5$ s. Then, the second phase begins, from B, during which the sensor rotates about its vertical axis until the minimum value of $\delta I_{ax,1}$ is reached (at $t \simeq 20$ s, B'). Finally, this value of $\delta I_{ax,1}$ is preserved thanks to the control law by rotating about the object during this third phase.

This algorithm was also experimentally tested with large objects. In the example represented in figure 4.13a, an insulating wall was placed at the center of the aquarium. After the seeking object phase starting in A, the sensor stops in front of this wall, and then orbits around it. The

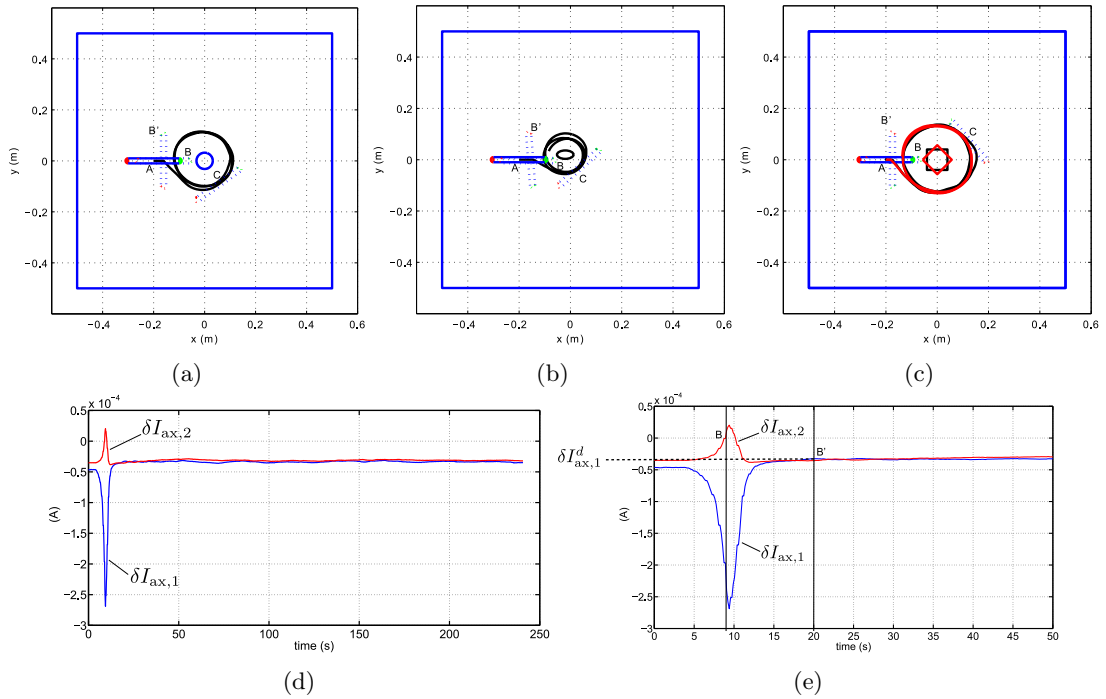


Figure 4.12: Top row: the path of the sensor when the algorithm is applied. (a) Insulating sphere (object 3 in table 2.1). (b) Insulating ellipsoid (object 5 in table 2.1). (c) Insulating cube (object 8 in table 2.1), rotated by 0° and 45° . Bottom row: the measured currents $\delta I_{ax,1}$ (blue) and $\delta I_{ax,2}$ (red) as a function of time during the experiment shown in (c). (d) Full experiment. (e) Focus on the 50 first seconds of the experiment.

path of the sensor is not symmetric with respect to the wall. It is due to the proximity of the walls of the aquarium, which have a non negligible effect on the measurements. Modifying the initial pose does not have an effect on the sensor's path during the third phase.

A second example is presented in figure 4.13b, in which an insulating wall is placed at the bottom left corner of the aquarium. As observed in the previous example, the sensor stops when it faces the wall, then rotates about its vertical axis and then follows the wall. The measured currents during these movements are represented in 4.13c and 4.13d. At $t \simeq 35$ seconds, the current $\delta I_{ax,1}$ decreases because the sensor approaches the wall that it is facing. So, in order to make the error $\delta I_{ax,1} - \delta I_{ax,1}^d$ as small as possible, the control law (4.9) adjusts the angle velocity Ω so that the sensor passes by the corner. As a result, we can see that the current $\delta I_{ax,1}$ increases until it reaches $\delta I_{ax,1}^d$ again. This way, the sensor follows the boundaries of the aquarium. During its second turn, the insulating wall in the bottom left corner is removed. One can see that the sensor adapts its trajectory to this new configuration.

Through these experiments, we showed that the object's inspection algorithm described in figure 4.2a is implementable with our sensor. Composed of three simple proportional control laws and using only thresholds' detections, this algorithm requires very low computing resources. Also, it does not require any physical model. It is a big advantage for a real time implementation on an autonomous underwater robot.

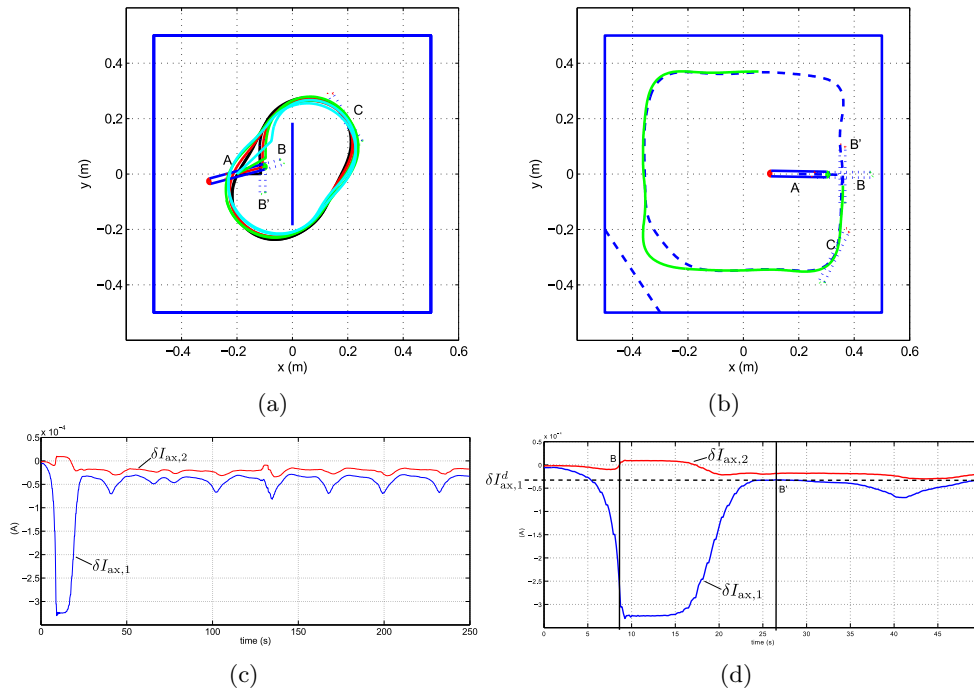


Figure 4.13: Top row: the path of the sensor when the algorithm is applied. (a) An insulating wall in the middle of the tank. The different colors correspond to different initial poses of the sensor. (b) A removable insulating corner. The dashed line corresponds to the first path with the corner, the solid line corresponds to the second turn, without the removable wall. Bottom row: the measured currents $\delta I_{ax,1}$ (blue) and $\delta I_{ax,2}$ (red) as a function of time during experiment shown in (b). (c) Full experiment. (d) Focus on the 50 first seconds of the experiment.

We can note that the sensor geometry is essential. The axis-symmetry allows the current's line following and the distance l_2 is a key parameter in the stopping distance for the first transition.

This object's inspection is of great interest in the reconstruction of a scene using the electric sense. However, it does not provide accurate localization and shape description of the object yet. So, in order to go one step further in the scene reconstruction and get some more details about the object, we propose in the two next chapters some other algorithms that deal with object's localization and shape estimation.

Chapter 5

Localization

At this point, according to the previous chapter, the object was detected, its material and side discriminated. Also, we showed that the sensor is able to automatically move towards it and revolve around it at an almost constant distance. Now, the problem is to accurately localize its center and then estimate its geometrical properties. These two tasks can be decoupled thanks to the use of the MUSIC (multiple signal classification) algorithm. One of its advantages is that it enables an electric dipole localization regardless of its orientation and strength. In our context, this corresponds to the localization of the geometrical center of the object, independently of its intrinsic properties (semi-axis a and b) and orientation angle θ_o . The algorithm in charge of estimating these three parameters will be presented in chapter 6. The scheme of figure 5.1 represents

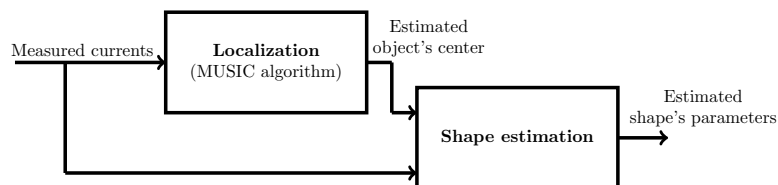


Figure 5.1: The scheme of the two stages strategy for object's localization and shape estimation. As an input, the measured currents are firstly used for the MUSIC algorithm for object's center estimation. Knowing that localization, the shape estimation can be performed.

this process. This two stages strategy was firstly proposed in [2, 11] in the context of electric fish modeling and showed its relevance. In this chapter, we focus on the localization of the object with the MUSIC algorithm. In the first section, we will introduce the principles of the algorithm, and then, present some simulation results based on the analytical model. In order to get closer to the actual conditions, some implementations of MUSIC with BEM currents will be presented, showing that the localization errors are mainly due to some approximations in the analytical model, onto which MUSIC is based. Finally, we will propose a new localization strategy, based on four MUSIC implementations and some sensor motions, in order to significantly reduce these large errors. At the end, in actual conditions, the objects listed in table 2.1 are localized with an absolute error below 3mm.

5.1 Principle of MUSIC algorithm

In this section we present the principle of the MUSIC algorithm, which provides an estimation of the object's localization in the sensor frame. So, for the sake of simplicity, the sensor pose will be considered as $(x_c, y_c, \theta_c) = (0, 0, 0)$ in the fixed frame R (see figure 2.5). In this case, the poses (x_o, y_o, θ_o) and $(x_o^c, y_o^c, \theta_o^c)$ are equal, and the superscript c will be deliberately omitted in the three first sections of this chapter.

MUSIC was firstly developed for passive antennas arrays in order to estimate radio signals' directions of arrival [79]. It was then showed that the algorithm principle could be extended to active arrays, in order to localize passive scatterers [24]. Generally speaking, an active array is composed of electrodes which can both emit and measure a signal. For an electrode configured as the emitter, all the electrodes measure the back propagating signal at their respective locations. This first set of measurements forms the first column of the multi-static response matrix, or MSRM. Then, by sequentially setting each electrode as emitter, the measured MSRM is completed. This measurement sequence can be performed with our sensor. Recall equations (3.93) and (3.95), describing the relationships between the polarization vector U and measured vector δI_{ax}

$$\delta I_{\text{ax}} = \delta C.U. \quad (5.1)$$

The matrix δC is our MSRM. The polarization of the macro-electrode \mathcal{E}_1 with a potential u implies a vector $U = [u \ 0 \ 0 \ 0]$ and the corresponding measured vector δI_{ax} forms the first column of δC . The process is repeated three more times, by polarizing the three other macro-electrodes one after the other, in order to complete the matrix. It should be mentioned that neither the object nor the sensor move during this measurement process.

Then, a singular value decomposition (SVD) [37] is performed, so that

$$\delta C = V.\Sigma.W^T, \quad (5.2)$$

where V and W are 4×4 matrices which columns are the singular vectors and Σ a diagonal 4×4 matrix which diagonal contains the singular values sorted in increasing order. According to the linear algebra [37, 87], the columns of V (left singular vectors) that are related to the non zero singular values form a basis of the image of the linear transformation δC . The image is the vector space in which the vector δI_{ax} lies. It is called the signal subspace and is denoted \mathcal{S} . It also exists the noise subspace, denoted \mathcal{N} , which is orthogonal to \mathcal{S} , such that $\mathbb{R}^4 = \mathcal{S} \oplus \mathcal{N}$. A basis of \mathcal{N} is composed of the columns of V that are related to the zero singular values. See a 2-D representation of these subspaces and their relative bases in figure 5.2.

Then, let us recall another expression for δI_{ax} (3.94), which explicitly highlights the dipolar moment $\mathbf{p} = [p_x \ p_y \ p_z]^T$

$$\delta I_{\text{ax}} = C^0 G \mathbf{p}. \quad (5.3)$$

Because of the top-down symmetry of the problem, the third component p_z equals to zero. Thus, the vector δI_{ax} is a linear combination of the two first columns of the matrix $C^0 G$

$$\delta I_{\text{ax}} = C^0 \begin{bmatrix} \frac{x_o - x_1}{r_1^3} \\ \frac{x_o - x_2}{r_2^3} \\ \frac{x_o - x_3}{r_3^3} \\ \frac{x_o - x_4}{r_4^3} \end{bmatrix} p_x + C^0 \begin{bmatrix} \frac{y_o}{r_1^3} \\ \frac{y_o}{r_2^3} \\ \frac{y_o}{r_3^3} \\ \frac{y_o}{r_4^3} \end{bmatrix} p_y, \quad (5.4)$$

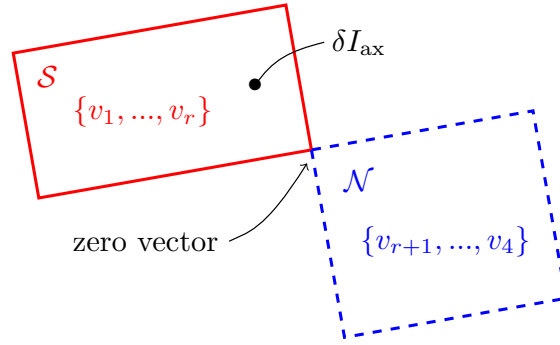


Figure 5.2: A representation of the signal subspace \mathcal{S} (solid lines rectangle) and the noise subspace \mathcal{N} (dashed lines rectangle). Denoting r the rank of δC , \mathcal{S} is spanned by the r first singular vectors $\{v_1, \dots, v_r\}$ and \mathcal{N} is spanned by the $4 - r$ last singular vectors $\{v_{r+1}, \dots, v_4\}$. The vector δI_{ax} belongs to \mathcal{S} and the intersection between \mathcal{S} and \mathcal{N} is the zero vector. Inspired by [87].

see the expression of the matrix G (3.63).

The vectors $\left[\frac{x_o - x_1}{r_1^3} \quad \frac{x_o - x_2}{r_2^3} \quad \frac{x_o - x_3}{r_3^3} \quad \frac{x_o - x_4}{r_4^3} \right]^T$ and $\left[\frac{y_o}{r_1^3} \quad \frac{y_o}{r_2^3} \quad \frac{y_o}{r_3^3} \quad \frac{y_o}{r_4^3} \right]^T$ are denoted G_x and G_y , respectively. Because δI_{ax} is known to belong to \mathcal{S} , the columns $C^0 G_x$ and $C^0 G_y$ necessarily form a basis of \mathcal{S} . This basis is not necessarily orthogonal. Thus, both \mathcal{S} and \mathcal{N} are of dimension two ($r = 2$ in figure 5.2). Note that this basis only depends on the sensor's properties (which are known) and on the object's center, the information about the intrinsic properties of the object being contained in coefficients p_x and p_y . Now, let us define the two following functions

$$\begin{cases} S_x: \mathbb{R}^2 \rightarrow \mathbb{R}^4, \\ (x, y) \mapsto C^0 \left[\frac{x - x_1}{r_1^3} \quad \frac{x - x_2}{r_2^3} \quad \frac{x - x_3}{r_3^3} \quad \frac{x - x_4}{r_4^3} \right]^T, \end{cases} \quad (5.5)$$

and

$$\begin{cases} S_y: \mathbb{R}^2 \rightarrow \mathbb{R}^4, \\ (x, y) \mapsto C^0 \left[\frac{y}{r_1^3} \quad \frac{y}{r_2^3} \quad \frac{y}{r_3^3} \quad \frac{y}{r_4^3} \right]^T. \end{cases} \quad (5.6)$$

In the literature, these functions are called *steering vectors* [24]. When they are evaluated in $(x, y) = (x_o, y_o)$, the steering vectors equal to the columns $C^0 G_x$ and $C^0 G_y$ respectively, and thus belong to \mathcal{S} . Equivalently, their projections onto \mathcal{N} equal to zero. In other words, the following imaging function is infinite for $(x, y) = (x_o, y_o)$

$$\begin{cases} F: \mathbb{R}^2 \rightarrow \mathbb{R}, \\ (x, y) \mapsto \frac{1}{\|P_{\mathcal{N}} \cdot S_x(x, y)\| + \|P_{\mathcal{N}} \cdot S_y(x, y)\|}, \end{cases} \quad (5.7)$$

where $P_{\mathcal{N}}$ is a projector onto the subspace \mathcal{N} . This projector is obtained with the singular vectors v_3 and v_4 according to

$$P_{\mathcal{N}} = V_{34} \cdot (V_{34}^T \cdot V_{34})^{-1} \cdot V_{34}^T, \quad (5.8)$$

where V_{34} is the 4×2 matrix formed with the two column vectors v_3 and v_4 [87].

In practice, a search area is defined as a grid in the plane $(O, \mathbf{i}, \mathbf{j})$ (see figure 5.5). For each node of that grid, the imaging function (5.7) is evaluated. The coordinates of the node for which the imaging function is the highest is considered as the object's center localization. See in figure 5.3 a geometric representation of this procedure. To sum up, the MUSIC implementation consists

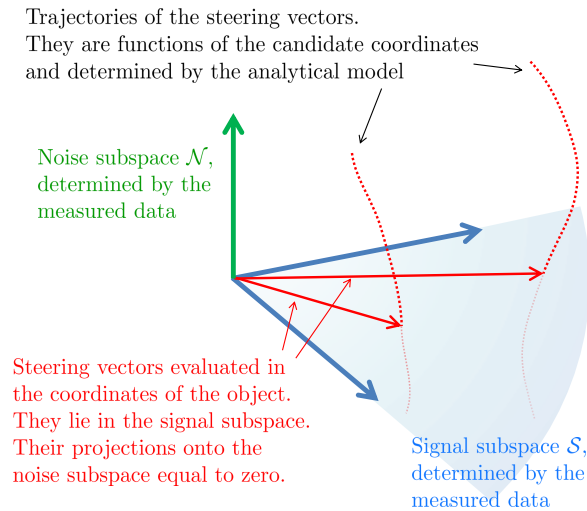


Figure 5.3: Geometric representation of MUSIC principle in dimension 3.

in the following steps

1. MSR matrix δC is constructed by polarizing each macro-electrode one after the other,
2. SVD of δC is computed,
3. a projector P_N onto \mathcal{N} is computed using the two last columns of matrix V ,
4. for each node of a grid attached to the sensor frame, the imaging function F (5.7) is evaluated,
5. the node for which function F is the highest is considered as the object's center localization.

The dipolar moment \mathbf{p} being absent of this process, the localization is totally independent of the object's shape and orientation. Also, considering our sensor's geometry (four aligned macro-electrodes), some particularities have to be considered:

1 - Left side search: due to the linear alignment of the macro-electrodes, the sign of y_o (representing on which side of the sensor the object is) can be factored out in the second column in (5.4). Thus, it cannot be discriminated with MUSIC. In fact, MUSIC gives two symmetrical solutions with respect to the sensor axis. But, in chapter 4 an algorithm was proposed to make a left/right discrimination. Hence, the search area of MUSIC will arbitrarily limited to the left side of the sensor, and the sign of the estimated lateral coordinate will be adjusted, if needed.

2 - Signal subspace dimension: the columns in (5.4) were assumed to be a non collinear set of vectors, so that the dimension of \mathcal{S} is two. We have to consider the particular cases in which these vectors can be collinear or equal to the zero vector, which cases would lead to a reduction of the subspace dimension.

1. The collinearity between G_x and G_y would impose the equality between the four numerators $(x_o - x_i), i = 1, \dots, 4$, which is not true $\forall x_o$.
2. If the object's center is aligned with the sensor axis, thus $y_o = 0$ and the second column of $C^0 G$ equals to the zero vector. Such situation is avoided using the algorithm described in chapter 4 which allows to detect an object facing \mathcal{E}_1 or \mathcal{E}_4 . A rotation of the sensor ensures that the object is not aligned and avoids this situation.
3. The case in which G_x or G_y belongs to the kernel of C^0 would also produce the zero vector. A basis of the kernel of C^0 is the vector $[1 \ 1 \ 1 \ 1]^T$ because in each line (or column) of C^0 , each component is equal to the opposite of the sum of the three others, in virtue of the charge conservation. Neither G_x nor G_y belongs to the kernel of $C^0, \forall(x_o, y_o)$.

To sum up, the dimension of the subspace \mathcal{S} is 2, except when $y_o = 0$, in which case it equals to 1. But, using the left/right discrimination algorithm described in chapter 4, this situation is always avoided. As a result, the dimension of \mathcal{S} shall always be 2, at least theoretically. The following section presents a MUSIC implementation with the analytical model currents as input.

5.2 Implementation of MUSIC algorithm with analytical model data

An example of MUSIC implementation with the matrix δC components computed with the analytical model is now presented. The properties of the scene are as follows:

Object: Conductive ellipsoid,

Object's dimensions: $a = 0.01m, b = 0.0045m$ ($\eta = 2.22, \mathcal{V} = 8.48 \times 10^{-7}$),

Localization and orientation: $(x_o, y_o) = (-0.034m, 0.072m), \theta_o = 50^\circ$.

Once the matrix δC that corresponds to this scene is constructed, the SVD is computed. Looking at the singular values in figure 5.4 (the diagonal components of matrix Σ in (5.2)), one can see that the two last ones are equal to zero, as expected.

Then, a search area of dimension $(0.2m \times 0.1m)$ is defined on the left side of the sensor, with a $0.005m$ discretization step, as shown in figure 5.5. At each node of that grid, the imaging function F is computed. The coordinates of the node that corresponds to the maximum value of F are $(-0.035m, 0.07m)$ in this example. Let us denote (\hat{x}_o, \hat{y}_o) this estimated object's center. The localization error can be evaluated using the euclidean norm of vector $(\hat{x}_o - x_o, \hat{y}_o - y_o)$, according to the following definition

$$e = \sqrt{(\hat{x}_o - x_o)^2 + (\hat{y}_o - y_o)^2}, \quad (5.9)$$

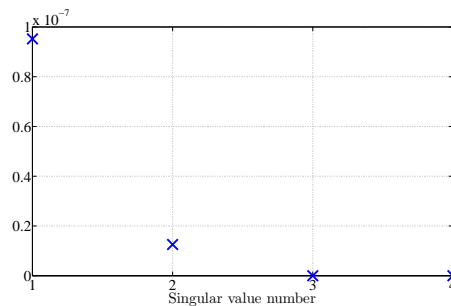


Figure 5.4: The singular values of the matrix δC of the example described above.

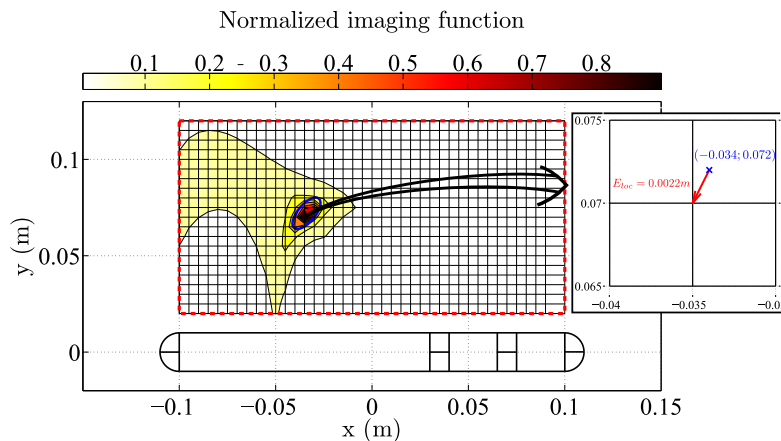


Figure 5.5: An example of MUSIC implementation with analytical model currents as input. The object is a conducting ellipsoid with $(a, b, \theta_o) = (0.01m, 0.0045m, 50^\circ)$ and $(x_o, y_o) = (-0.034m, 0.072m)$. The red dashed line represents boundaries of the search area, which discretization step is $0.005m$. The coordinates of the imaging function's maximum value is $(-0.035m, 0.07m)$. This leads to a localization error $e = 0.0022m$.

which is equal to $0.0022m$ in this example (see zoomed part of figure 5.5). Obviously, the less the discretization step, the less the localization error would be obtained. The maximum error is reached when the center of the object coincides with the center of a square of the grid. In such case, the error is given by half the diagonal of the square, that is

$$e \leq \frac{s}{\sqrt{2}}, \quad (5.10)$$

s being the discretization step. The localization of an object which center would correspond to a search grid node would be zero. This is due to the fact that both the matrix δC and the steering vectors are calculated with the analytical model. However, for an actual MUSIC implementation, the measured currents (so the matrix δC) are not in total accordance with those of the analytical model. In such case, the relationship (5.10) is no longer valid because some additional sources of localization error arise, for instance due to the model approximations or the measurement noise. In order to identify and evaluate these additional sources of error, we will use in the next section the BEM model currents as an input for the MUSIC algorithm.

5.3 Implementation of MUSIC algorithm with BEM data

In the previous section, the currents computed with the analytical model were used as input. In order to get closer to the actual conditions, here we use the currents computed with the BEM model (see section 3.2.2). They have the advantages of

1. including all the components that are not taken into account in the analytical model, that is, all the components involved in the object's electrical response 3.65,
2. being free of any noise, the measurement noise could be artificially added in a second phase in order to estimate its effects.

Hence, the goal of this section is to identify and to understand the localization error sources thanks to the currents computed with the BEM model. To that end, several objects were numerically designed and their surfaces were meshed. These virtual objects are described in table 5.1 and are represented at their localization in the scene in figure 5.6.

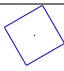





						
Number	1	2	3	4	5	6
Shape	Cube	Cube	Ellipsoid	Ellipsoid	Ellipsoid	Sphere
Material	Insul.	Cond.	Cond.	Insul.	Cond.	Cond.
a ($\text{m} \times 10^{-3}$)	10	10	8	10	10	10
b ($\text{m} \times 10^{-3}$)	10	10	6.7	5	4	10
\mathcal{V} (cm^3)	8	8	1.5	1.05	0.67	4.2
η	1	1	1.2	2	2.5	1
x_o ($\text{m} \times 10^{-3}$)	0	110	70	-40	130	± 200
y_o ($\text{m} \times 10^{-3}$)	60	80	70	90	50	30 to 100
θ_o (deg)	30	0	-20	-70	35	-

Table 5.1: The objects' representations and their corresponding features. For the cubes, semi-axis a and b are defined as half of the edge length.

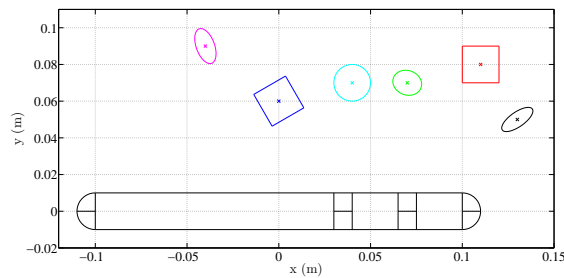


Figure 5.6: Representation of the tested objects in simulation. Sphere is represented at position $(x_o, y_o) = (0.04; 0.07)$.

5.3.1 Evaluation of a favorable area for the localization

Here, we evaluate the localization error depending on the localization of the object with respect to the sensor frame. To that end, an evaluation of the MUSIC performance is carried out with the 0.01m radius conducting sphere (object 6 in table 5.1). An area of size $0.4\text{m} \times 0.07\text{m}$ is defined on the left side of the sensor, discretized with a 0.01m step on each direction, as represented in figure 5.7a. This leads to a $41 \times 8 = 328$ points grid. To each point of that grid correspond

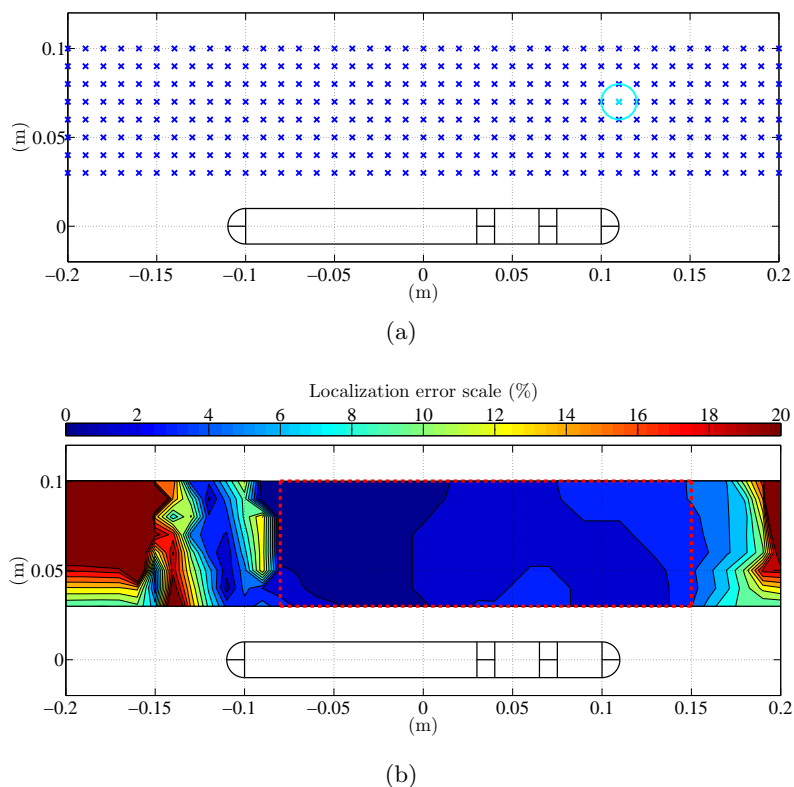


Figure 5.7: (a) A $0.4 \times 0.07\text{m}$ discretized area on the left side of the sensor (step = 0.01m). Each cross represents a localization of the sphere, which is represented at point $(x_o, y_o) = (0.11, 0.07)$ as an example. For each sphere's localization in this grid, MUSIC is applied. (b) The localization error map, built with the localizations given by MUSIC, when evaluated for the sphere at each point of the grid introduced in (a). The scale is expressed in percentage of the sensor length. The dashed rectangle defines an area in which the error is below 4.5%, that is, below the sphere radius = 1cm.

a localization of the sphere, the construction of a matrix δC , a MUSIC implementation and, thus, a localization error. An error map was built, represented in figure 5.7b, on which the area facing the sensor gives error below 4.5% of the sensor length (dashed rectangle). An error of 4.5% corresponds to one sphere radius (1cm). On the other hand, when the object is too far, for instance when $(x_o, y_o) = (-0.16, 0.09)$, error can reach at least 20% ($\simeq 4.4\text{cm}$). This poor

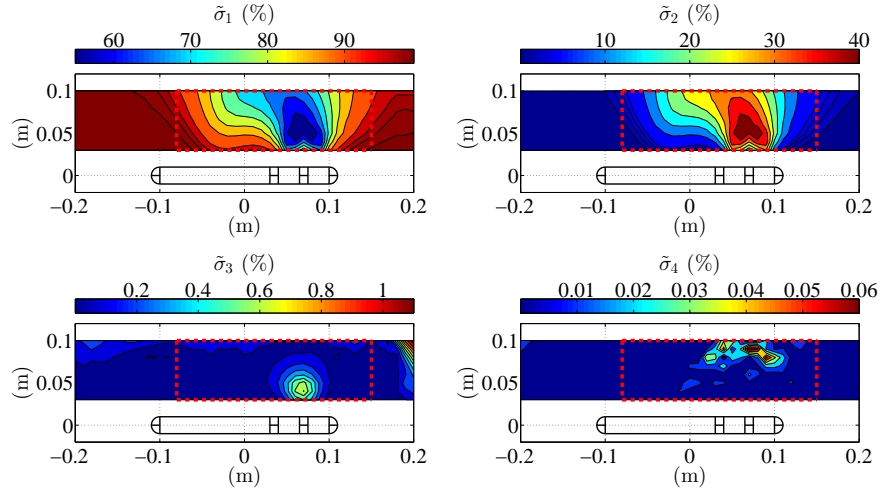


Figure 5.8: The maps of the four normalized singular values of matrix δC corresponding to the grid defined in figure 5.7a. The dashed rectangle is identical to that of figure 5.7b (localization error below 4.5%).

localization estimation out of the area facing the sensor can be illustrated with the maps of the normalized singular values $\tilde{\sigma}_{i=1,\dots,4}$, see figure 5.8. These maps were obtained by computing the singular value decomposition of each matrix δC that correspond to each sphere position of the grid in figure 5.7a. The normalization of the singular values was proceeded according to

$$\tilde{\sigma}_i = \frac{\sigma_i}{\text{trace}(\Sigma)} \cdot 100, \forall i \in \{1, \dots, 4\}, \quad (5.11)$$

where $\tilde{\sigma}_i$ is the i^{th} normalized singular value, σ_i is the i^{th} singular value and $\text{trace}(\Sigma)$ is the sum of the four diagonal components of matrix Σ in (5.2). This normalization highlights the contribution of each singular value with respect to the three others. Looking at the four maps in 5.8, one can make the following observations

Rank of δC is not 2 Contrary to the theory given in section 5.1, $\tilde{\sigma}_3$ and $\tilde{\sigma}_4$ are not equal everywhere to zero. This shows that there exist some additional contributions to the currents that are not taken into account in the analytical model (5.4). However, $\tilde{\sigma}_3$ and $\tilde{\sigma}_4$ are very low compare to $\tilde{\sigma}_1$ and $\tilde{\sigma}_2$, so these additional contributions are very weak and can be considered as noise. Most of the information is included in the two dimensional subspace \mathcal{S} , which is in accordance with theory. We will see in the following the effect of these additional contributions on the localization.

$\tilde{\sigma}_2$ tends toward 0 far from the sensor In the area facing the sensor, $\tilde{\sigma}_1$ is in the range [50%; 90%] whereas $\tilde{\sigma}_2$ is in the range [10%; 50%]. This shows the repartition of the information along the two axis v_1 and v_2 respectively. Out of the area facing the sensor, $\tilde{\sigma}_1$ tends toward 100% and $\tilde{\sigma}_2$ tends toward 0%, showing that axis v_1 monopolizes majority of the information. At first glance, this corresponds to a one dimensional signal subspace \mathcal{S} . So, MUSIC produces large errors since it is based on the principle of a two dimensional signal subspace.

At this point, we identified a favorable area, facing the sensor, that corresponds to a minimal localization error. Now, in order to get closer to actual conditions, we add a random noise of 2% on the components of each matrix δC , and the error map of figure 5.7b was computed again. As

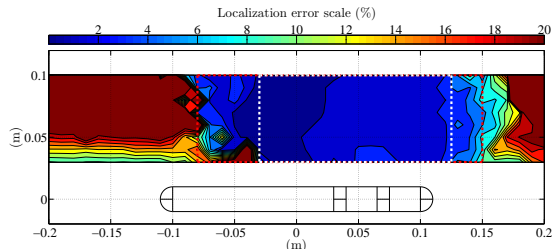


Figure 5.9: Localization error map obtained with similar conditions as map 5.7b, but with an additive random noise of 2% on the components of the matrix δC . The white dashed rectangle indicates the area in which error is below 4.5%, while the red dashed rectangle is the same as that of map 5.7b (4.5% error without noise).

a result, we get the error map in figure 5.9. The red dashed rectangle is the same as that of map 5.7b and the white dashed rectangle delimits the area in which localization error is below 4.5% with additive noise on the measurements. Comparing these two rectangles, we can see that the noise tends to reduce the favorable area, and focus it in front of the macro-electrodes \mathcal{E}_1 to \mathcal{E}_3 . This is due to the fact that the four δI_{ax} currents' magnitude are the highest when the object faces these macro-electrodes (see δI_{ax} currents in figure 3.9).

According to these observations, we can consider the area facing the macro-electrodes \mathcal{E}_1 to \mathcal{E}_3 as the best place for the object to be, in order to get the lowest localization error. When an object in this area, the measured vector δI_{ax} is ensured to lie in a two dimensional signal subspace, and the localization is more robust with respect to noise.

5.3.2 Error behavior with respect to the object's properties

Now, let us turn our attention to the dependency of MUSIC toward the properties of the object. In theory, as introduced above, the localization process with MUSIC is independent of the object's orientation and of the intrinsic properties (aspect ratio and volume). In order to evaluate that independence, the objects presented in table 5.1 were localized with MUSIC and the results are shown in figure 5.10.


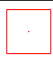




						
Number	1	2	3	4	5	6
e_x (m $\times 10^{-3}$)	0	2	0	0	1	0
e_y (m $\times 10^{-3}$)	-5	-7	-5	-3	-8	-5
e (%)	2.3	3.3	2.3	1.4	3.7	2.3

Table 5.2: BEM objects' localization results, corresponding to figure 5.10.

Note that, according to the previous remarks about the singular values, their actual localization

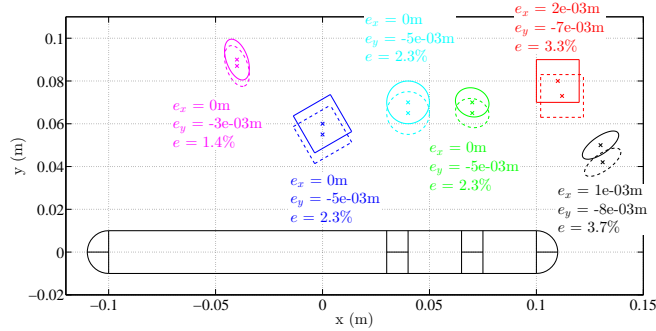


Figure 5.10: Actual objects (solid lines) and localized objects (dashed lines) using MUSIC. Even if they are represented all together here, only one object was present in the scene when MUSIC was applied. For each object, the absolute longitudinal and lateral errors (denoted e_x and e_y respectively) are given in meters and the localization error (denoted e , calculated according to (5.9)) is given in percentage of the sensor length. See table 5.2 in which the results are summed up.

were deliberately chosen inside the area delimited by the red dashed line in figure 5.7b. For all the non spherical objects, the localization error (denoted e and calculated according to (5.9)) is in accordance with that of the sphere, that is, below 4.5%, whatever the object's shape or orientation.

Now separately looking at the longitudinal and lateral components of the error (respectively denoted e_x and e_y), we observe that e_y is systematically higher than e_x in magnitude, and negative. The lateral distance is always under estimated. In order to understand this behavior, we have to have a look at the basal field to which the objects are submitted. For instance, the basal field inside the sphere, localized at $(x_o, y_o) = (0.04; 0.07)$, is plotted in figure 5.11, for each of the four polarizations. The field lines are somewhat parallel, showing that the field is almost uniform in term of direction. On the other hand, the magnitude of the field varies inside the object in a non negligible manner. The field's magnitude fall in the object is of 46.2%, 52%, 54.7% and 39.4% for the polarization of macro-electrode \mathcal{E}_1 , \mathcal{E}_2 , \mathcal{E}_3 and \mathcal{E}_4 respectively. This is due to the behavior of \mathbf{E}^0 with respect to the distance, which is a function of the inverse of a power of three, as described by the analytical model (3.64). Hence, we cannot actually consider the basal field as uniform in the object. This necessarily leads to a second term for the potential $\phi_1(\mathbf{x})$, which expresses when the gradient of the basal field is not zero, as shown in expression (3.66). This additional component is a quadrupolar contribution to the potential $\phi_1(\mathbf{x})$, described previously in (3.89). Unfortunately, unlike the tensor P_{11} for the dipolar component in (3.67), there does not exist in the literature any explicit relationship between the object's properties and this quadrupolar component of the potential. In other words, there does not exist any explicit analytical formulation for the tensor P_{22} yet. So, we have to deal with that issue with qualitative arguments only. Despite of that, by observing the behavior of the basal field, the localization errors' origin will make sense and we will find good comprehension of the problem at the end.

Considering the four images in figure 5.11, we observe that the basal field preferably polarizes the part of the object that is close to the sensor, for each of the four polarizations. Hence, we can consider that it is this part of the object which responds, and thus is localized. In order to confirm that, the MUSIC algorithm was performed with several ellipsoids (one after

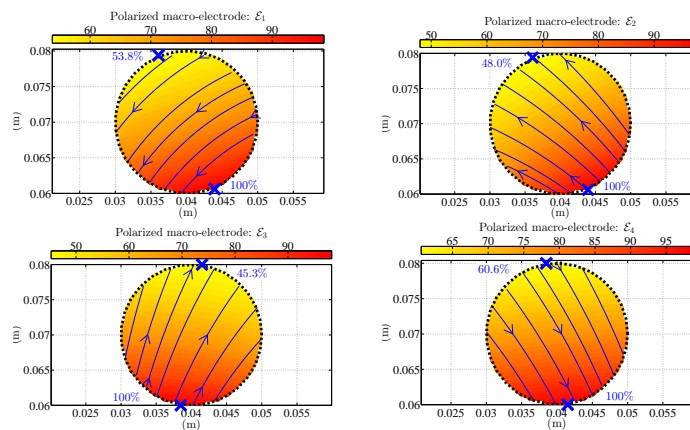


Figure 5.11: Representation of the basal field to which a 1cm radius sphere located at $(x_o, y_o) = (0.04; 0.07)$ is submitted, for each of the four possible polarizations (computed with BEM model). The blue oriented lines represent the field lines and the graduated shading represents the normalized field's magnitude. For each polarization, the localization inside the object of the maximum and minimum values of the field's magnitude is indicated.

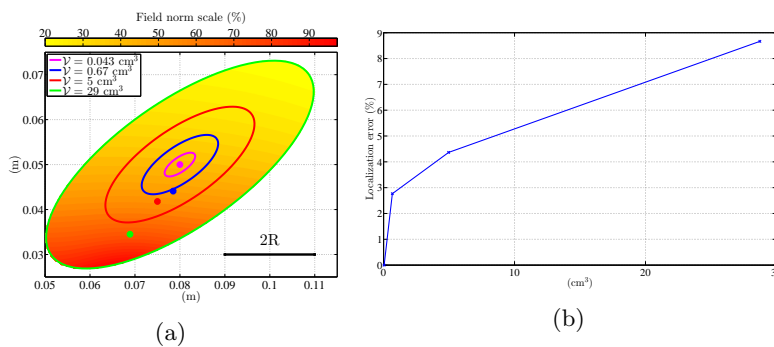


Figure 5.12: (a) Four ellipsoids localized with MUSIC. The estimated localizations are represented with the corresponding colored dots. The normalized basal field for the polarization of macro-electrode \mathcal{E}_4 in the largest object is represented. The sensor diameter ($2R$) is also represented for scale comparison. (b) The localization error as a function of the ellipsoid's volume.

the other) of different volumes. These ellipsoids only differ in term of volume and have same localization and orientation in the sensor frame ($(x_o, y_o) = (0.08; 0.04)$ and $\theta_o = 35^\circ$), same aspect ratio ($\eta = 2.5$) and same material (conductive). Figure 5.12a shows a representation of these ellipsoids and their estimated localizations. Also, the normalized field for polarization \mathcal{E}_4 is plotted in the largest ellipsoid. For the smaller ellipsoid (magenta), the currents used as input for the MUSIC algorithm were computed with the analytical model. Thus, the localization error is zero, as expected. For each of the three other ellipsoids (blue, red and green), the currents were computed with the BEM model. As a result, the localization returned by MUSIC tends to follow the most illuminated part of the object, as it was observed for the sphere.

The phenomenon is also observed when the aspect ratio varies, all other things being equal, as shown in figures 5.13a and 5.13b. The five ellipsoids have the same localization and orientation

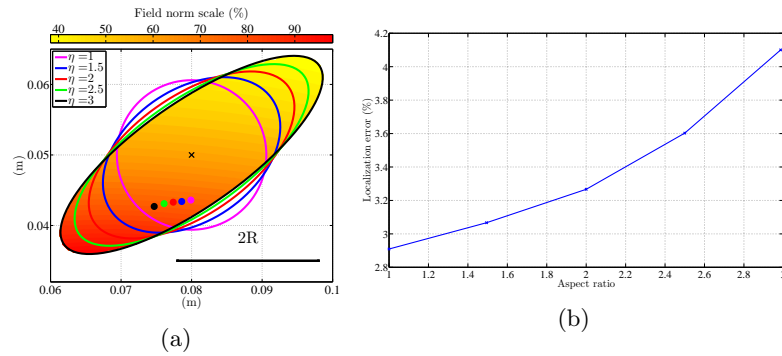


Figure 5.13: (a) Five ellipsoids localized with MUSIC. The estimated localizations are represented with the corresponding colored dots. The normalized basal field for the polarization of macro-electrode \mathcal{E}_4 in the largest object is represented. The sensor diameter ($2R$) is also represented for scale comparison. (b) The localization error as a function of the ellipsoid's aspect ratio.

as in the previous example ($(x_o, y_o) = (0.08; 0.04)$ and $\theta_o = 35^\circ$), and have the same volume ($\mathcal{V} = 2.5$) and the same material (conductive). We observe a similar trend, that is, a localization of the part of the object that is the most illuminated. These simulation results show a non negligible localization errors using the MUSIC algorithm, due to the non uniformity of the basal field inside the object.

At this point, we have identified three causes of the localization's accuracy reduction: the signal subspace dimension that tends toward one when the object is far from the sensor, the presence of an additive noise and the truncation of the object's response at the first term in the analytical model. In addition, we can mention at least three others sources of localization errors that necessarily occur in experimental conditions and that have not been taken into account until now

- uncertainty on the water conductivity measurement (leading to a non desirable offset on the measurements),
- non perfect sensor's geometry (uncertainties on electrodes' positions),
- experimental imprecisions, in particular on the object's and sensor's positions.

It is hard to quantitatively evaluate these additional uncertainties and we now present the results obtained in actual conditions, keeping in mind that they necessarily play a role in the localization error.

5.4 Implementation of MUSIC algorithm with experimental data

In the previous section, the localization algorithm was fed with BEM currents. Here, we present the results obtained with actual measurements.

Note that in experimental conditions, it is not possible to have a correspondence between the fixed frame and the sensor frame as we supposed in the previous sections. Hence, the superscript c is introduced in order to unambiguously distinguish (x_o, y_o, θ_o) and $(x_o^c, y_o^c, \theta_o^c)$. Recall that the sensor pose in the fixed frame is supposed to be known at any instant, so the object's localization in R can be recovered using the following affine transformation

$$\begin{bmatrix} x_o \\ y_o \end{bmatrix} = \begin{bmatrix} x_c \\ y_c \end{bmatrix} + \begin{bmatrix} \cos \theta_c & -\sin \theta_c \\ \sin \theta_c & \cos \theta_c \end{bmatrix} \begin{bmatrix} x_o^c \\ y_o^c \end{bmatrix}. \quad (5.12)$$

First of all, we have to present the detection range that we have in experimental conditions, which is smaller than that we observed with BEM currents, for a similar object.

5.4.1 From small to large objects

With BEM currents, we showed that the simulations worked up to a lateral distance of 0.1m far from the sensor, even in presence of noise (see figure 5.9). But, as we will see now, it is not the case with experimental currents. Particularly, for insulating objects, the signal amplitude is very low. As an example, figure 5.14a shows the current $\delta I_{ax,1}$ during fly-by tests for a 0.01m

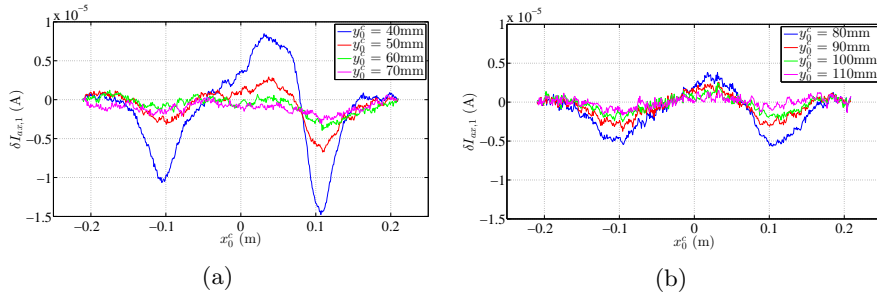


Figure 5.14: Current $\delta I_{ax,1}$ during fly-by tests at several lateral distances with polarization of macro-electrode \mathcal{E}_4 . (a) Insulating sphere (object 2 in table 2.1). (b) Insulating ellipsoid (object 7 in table 2.1), semi-major axis aligned with the sensor.

radius insulating sphere, at several lateral distances. When the object is the closest to the sensor ($y_o \leq 50\text{mm}$), we observe an alternating current depending on the longitudinal coordinate x_o^c . Facing the macro-electrodes \mathcal{E}_1 and \mathcal{E}_4 ($x_o^c \simeq 0.1\text{m}$ and $x_o^c \simeq -0.1\text{m}$ respectively), the currents are negative while they are positive for $-0.05\text{m} \leq x_o^c \leq 0.085$. But, for $y_o > 50\text{mm}$, this sign change does not occur due to the weak response of such a small object. As a result, even if this object is detectable when facing macro-electrodes \mathcal{E}_1 and \mathcal{E}_4 at a lateral distance of 70mm, the MUSIC algorithm cannot be implemented for $y_o > 50\text{mm}$, which is a very short distance for applications in robotics.

So, in order to increase the range of our experimental measurements, we chose to use large objects, numbered from 3 to 6 in table 2.1. They have a higher response level and lead to a range of 100mm as it is shown in figure 5.14b. The counterpart of using large objects is that they do not respect a priori the hypothesis of our analytical model, as shown in simulation in the previous section. As an example, the localization map for ellipsoid 4 in table 2.1, rotated with an angle of -30° is shown in 5.15. We can see the same main characteristic as in simulation,

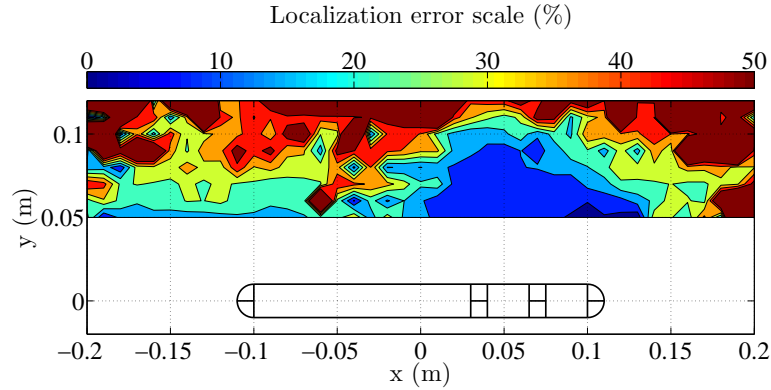


Figure 5.15: Localization error map obtained with similar conditions as maps 5.7b and 5.9, but with the ellipsoid numbered 4 in table 2.1, rotated with an angle of -30° with respect to the sensor axis.

that is, a favorable area that faces the macro-electrodes \mathcal{E}_1 to \mathcal{E}_3 (dark blue), in which the error is below 15%. As an example, this ellipsoid at $(x_o^c, y_o^c) = (0.05; 0.07)$ is represented in figure 5.17, the error being of 8.9% in that particular case.

These results obtained with actual measurements are in accordance with our study based on simulations in the previous section: the localization accuracy decreases when using large objects, due to the non uniformity of the basal field. Multipolar terms in the object's response must contribute to the measured currents. These multipolar contributions are not taken into account in the analytical model on which the steering vectors are based. As a result, the algorithm localizes the part of the object that is the best illuminated by the basal field, that is, the closest to the sensor. Also, the measurement noise and other unavoidable experimental uncertainties lead to a reduced favorable area, facing macro-electrodes \mathcal{E}_1 to \mathcal{E}_3 . Because it is important to have the object in this area in order to get the lower localization error, we propose in the next section a strategy based on sensor motions that ensures that situation. Moreover, we will see that by repeating this procedure four times according to a specific sensor trajectories, it is possible to significantly reduce the localization error.

5.4.2 New localization strategy for large objects

Here, we propose to improve the preceding results by applying MUSIC four times with the same object, at four different object positions with respect to the sensor, involving sensor motion. The barycenter of the four localizations will be considered as the object's localization.

The first thing to consider is to place the sensor so that the object is in the favorable area. To do so, we use the concepts of t-images and peak position observed by the biologists in the fish and introduced in section 1.1.4. Indeed, we remark that, for a polarization of \mathcal{E}_4 , the lateral current $I_{lat,i}, \forall i \in \{1, 2, 3\}$, gets its maximum absolute value when the object faces the macro-electrode \mathcal{E}_i . This is illustrated by the fly-by test currents in figure 3.9 (top). With our sensor, we can consider the lateral currents during a fly-by test as our t-images (compare with the t-image of

the fish in figure 1.13). As a result, we can define a peak position, using the $I_{lat,2}$ current, as the longitudinal coordinate of the object in the sensor frame which corresponds to the maximum absolute value of $I_{lat,2}$. Strictly, the definition of our peak position, denoted x_{pp} , is

$$x_{pp} = \operatorname{argmax}_{x_o^c} |I_{lat,2}|. \quad (5.13)$$

Let us recall that the relationship between $I_{lat,2}$ and x_o^c is given by (3.101). As we can see in

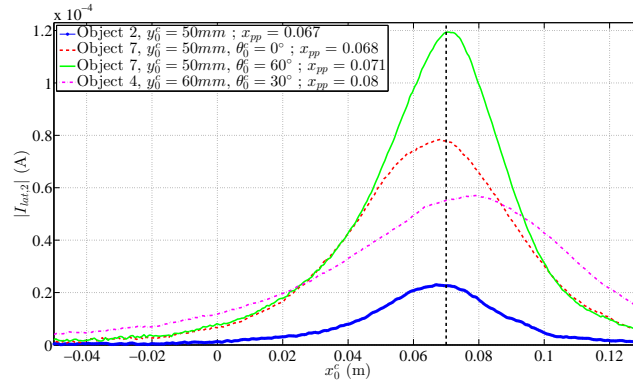


Figure 5.16: Four absolute values of current $I_{lat,2}$ corresponding to different fly-by tests. The conditions of these tests are indicated in the legend, followed by the corresponding peak positions. The vertical dotted line corresponds to the longitudinal position of the macro-electrode \mathcal{E}_2 , that is, 0.07m (see sensor scheme 2.7).

figure 5.16, the peak position is not strictly independent of the object's intrinsic properties but it is accurate enough to make sure that the object lies in the favorable area. Practically, the sensor moves in straight line, with constant polarization of macro-electrode \mathcal{E}_4 and stops when the peak position is reached. At this point, the multi polarization is performed in order to construct the matrix δC and the MUSIC algorithm is applied. As a result, we get a localization estimation as

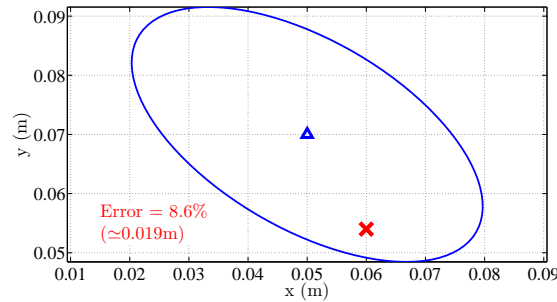


Figure 5.17: Representation of that ellipsoid at $(x_o^c, y_o^c) = (0.05; 0.07)$ and its estimated localization. Blue triangle: true localization ; red cross: estimated localization.

illustrated in the example in figure 5.17. Then, the sensor moves in straight line for a distance of half of its axial length (= 0.11m), ensuring that the tail has passed the object, and stops. Then, it is rotated by $\pi/2$ and starts again a straight line motion with constant polarization

of macro-electrode \mathcal{E}_4 , until the peak position is reached, for a second MUSIC localization. This principle is repeated four times, the trajectory of the sensor drawing a rectangular shaped trajectory around the object, as represented in figure 5.18. Figure 5.19 shows, in the sensor

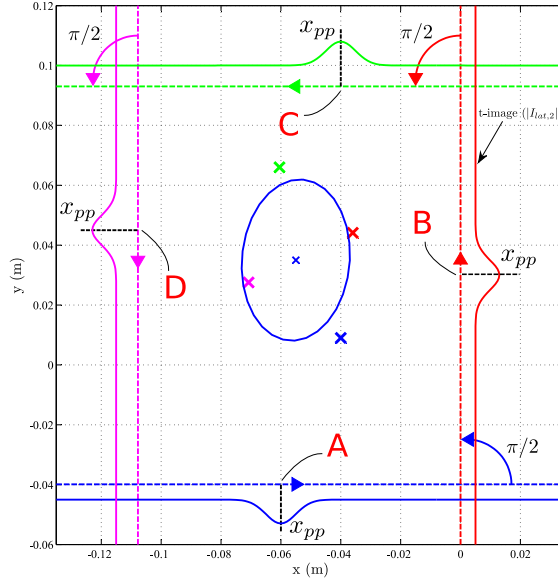


Figure 5.18: Scheme of the localization strategy for a large object (object 7 in table 2.1). The four dotted and orientated lines represent the straight line trajectories followed by the sensor. The corresponding t-images (currents $|I_{\text{lat},2}|$) are superimposed along these four paths. To each peak position correspond an estimated localization provided by MUSIC, represented by a cross of same color as the path on which the localization is performed.

point of view, the four localizations of object 4 in table 2.1 during this process. Finally, once the four localizations obtained with MUSIC are collected during this process, their barycenter is computed and is considered as the object's center estimation. We have observed on several trials that this procedure significantly reduces the localization error compare to a single MUSIC implementation.

As an example, we now consider the conductive ellipsoid numbered 4 and the insulating one numbered 7 in table 2.1. Each of the two objects was positioned in the tank's center, and this localization strategy was applied with the probe starting at a lateral distance of 52mm for object 4, and 63mm for object 7. Object 4 was rotated by -30° , and object 7 rotated by 90° . In figure 5.20a and 5.20b are represented these two objects, as well as their four localizations estimated by MUSIC and their barycenter. The resulting localization errors are 2.6mm and 1.6mm respectively. Even if the four independent localization errors are important, their barycenter correspond to a reduced error. Hence, we proved the feasibility of this strategy in experimental conditions. We showed that it leads to very small localization errors compare to a single MUSIC implementation, which tends to localize the part of the object that is the closest to the sensor.

In the process shown in figure 5.1, we are now able to provide an estimated object's center to the shape estimation algorithm, which is the purpose of the next chapter.

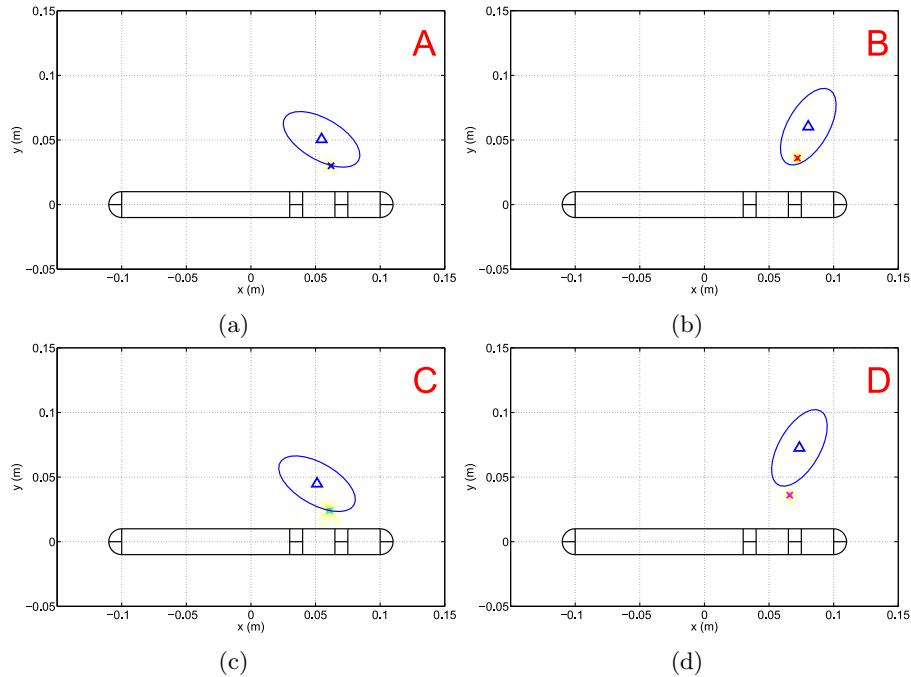


Figure 5.19: Snapshots of the scene in the sensor frame when MUSIC is performed, that is, when the peak position is reached for the object 4 in table 2.1. In each figure, the triangle and the cross indicate the actual and estimated localizations, respectively. The letters A, B, C, D correspond to the peak positions in figure 5.18.

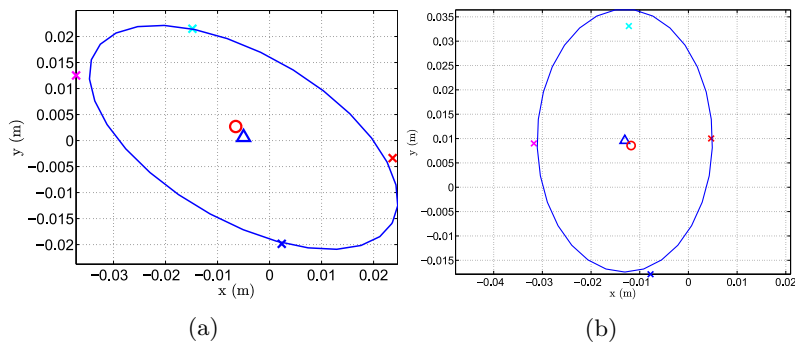


Figure 5.20: Representation of two localized object with the strategy for large objects. Triangles represent the actual objects' centers, crosses represent the estimated localizations with MUSIC and the circles represent their barycenter. (a) Conductive ellipsoid (Object 4). Error = 2.6mm. (b) Insulating ellipsoid (object 7). Error = 1.6mm.

Chapter 6

Shape estimation

According to the two stages strategy represented in figure 5.1, now we have to solve the shape estimation problem, with measured currents and estimated localization as inputs. This is in accordance with the strategy used by the fish, which is able to separate the localization and size estimation tasks, as it was shown in section 1.1.4. In this chapter, we will assume that the object's material (conductive or insulating) is determined and its localization is estimated thanks to the algorithms presented in chapters 4 and 5 respectively. Referring to the scene parametrization given in figures 2.4 and 2.5, the three left parameters for a complete scene reconstruction are the ellipsoid's semi-axis length (a,b) , or equivalently the volume \mathcal{V} and the aspect ratio η , and the angle between the sensor's axis and the semi-major axis, denoted θ_o^c . The algorithm that estimates these parameters was firstly proposed in [2, 11] in the case of the electric fish modeling. It can be decomposed into two consecutive steps

Step one Estimation of the object's polarization tensor P_{11}^c , whose components explicitly appear in the currents' models (3.96) and (3.101), using an optimization algorithm.

Step two Estimation of the parameters \mathcal{V} , η and θ_o^c using the estimated polarization tensor and by inverting its analytical expression (3.84).

In this chapter, the first section is dedicated to the description of the principles of this algorithm. Then, in the second section, the relevance of the method will be shown using BEM data as input, with no measurement noise and no error of the object's localization. After that, the robustness of the shape estimation with respect to the measurement noise and to the localization uncertainty will be evaluated, and an improved version of the algorithm will be presented, which is less sensitive to the noise. Finally, implementation of the algorithm with experimental data will be presented in the third section, showing its applicability in actual conditions

6.1 Principle of the shape estimation algorithm

As explained in introduction, the shape estimation strategy is decomposed into two consecutive steps. We describe both of them in this section. Recall that the localization of the object is

needed and considered as known at this point.

6.1.1 Step one : Estimation of the object's polarization tensor

Here, we present an algorithm, based on the least squares method [64], that estimates the components of the object's polarization tensor, expressed in the sensor frame. It is denoted P_{11}^c in chapter 3 and its analytical expression is given by (3.84). It is symmetric, that is, the components p_{12}^c and p_{21}^c are equal. Moreover, the component λ_w plays no role in the problem, due to the top-bottom symmetry of the scene. Indeed, according to the expression of matrix G (3.63), which last column is zero, the basal field \mathbf{E}^0 has no vertical component at the center of the object. This is due to the fact that the sensor and the object both lie in the same horizontal plan. Thus, the component λ_w is not excited. At the end it leads to a component p_z of the dipolar moment that is zero, as it was mentioned in the previous chapter and illustrated in equation (5.4). Finally, we have three components to estimate: p_{11}^c , p_{22}^c and p_{12}^c .

The analytical model shows that the axial and the lateral currents measured on a given macro-electrode can be written as a linear combinations of these three components, as shown in the equations (3.96) and (3.101). Let us recall them here, subscript $k = 1, \dots, 4$ denoting the k^{th} macro-electrode

$$\delta I_{ax,k} = \varphi_{1,k} \cdot p_{11}^c + \varphi_{2,k} \cdot p_{22}^c + \varphi_{3,k} \cdot p_{12}^c, \quad (6.1)$$

$$I_{lat,k} = \psi_{1,k} \cdot p_{11}^c + \psi_{2,k} \cdot p_{22}^c + \psi_{3,k} \cdot p_{12}^c, \quad (6.2)$$

where the functions $\varphi_{1,k}$, $\varphi_{2,k}$, $\varphi_{3,k}$, $\psi_{1,k}$, $\psi_{2,k}$ and $\psi_{3,k}$ are defined as

$$\varphi_{1,k} = - \sum_{i=1}^4 \frac{C_{ki}^0}{r_i^3} (x_o^c - x_i) \cdot E_x^0, \quad (6.3)$$

$$\varphi_{2,k} = - \sum_{i=1}^4 \frac{C_{ki}^0}{r_i^3} y_o^c \cdot E_y^0, \quad (6.4)$$

$$\varphi_{3,k} = - \sum_{i=1}^4 \frac{C_{ki}^0}{r_i^3} ((x_o^c - x_i) \cdot E_y^0 + y_o^c \cdot E_x^0) \quad (6.5)$$

$$\psi_{1,k} = - \frac{P_{\perp k}}{r_k^5} \cdot 3y_o^c (x_o^c - x_k) \cdot E_x^0, \quad (6.6)$$

$$\psi_{2,k} = - \frac{P_{\perp k}}{r_k^5} \cdot 2y_o^c{}^2 - (x_o^c - x_k)^2 \cdot E_y^0, \quad (6.7)$$

$$\psi_{3,k} = - \frac{P_{\perp k}}{r_k^5} \cdot \left(3y_o^c (x_o^c - x_k) \cdot E_y^0 + (2y_o^c{}^2 - (x_o^c - x_k)^2) \cdot E_x^0 \right). \quad (6.8)$$

These functions only depend on the sensor properties through the components of C^0 and P_{\perp} and on the object's localization in the sensor frame (x_o^c, y_o^c) . For a given controlled trajectory of the sensor, these functions can be computed at sampling instants t_i , $i \in \{1, \dots, N\}$, and paired with the corresponding currents $\delta I_{ax,k}(t_i)$ and $I_{lat,k}(t_i)$. For a trajectory composed of N sample

points, we get the following linear system of $6N$ equations in three unknowns

$$\begin{bmatrix} \delta I_{\text{ax},1}(t_1) \\ \delta I_{\text{ax},2}(t_1) \\ \delta I_{\text{ax},3}(t_1) \\ I_{\text{lat},1}(t_1) \\ I_{\text{lat},2}(t_1) \\ I_{\text{lat},3}(t_1) \\ \vdots \\ \delta I_{\text{ax},1}(t_N) \\ \delta I_{\text{ax},2}(t_N) \\ \delta I_{\text{ax},3}(t_N) \\ I_{\text{lat},1}(t_N) \\ I_{\text{lat},2}(t_N) \\ I_{\text{lat},3}(t_N) \end{bmatrix} = \begin{bmatrix} \varphi_{1,1}(t_1) & \varphi_{2,1}(t_1) & \varphi_{3,1}(t_1) \\ \varphi_{1,2}(t_1) & \varphi_{2,2}(t_1) & \varphi_{3,2}(t_1) \\ \varphi_{1,3}(t_1) & \varphi_{2,3}(t_1) & \varphi_{3,3}(t_1) \\ \psi_{1,1}(t_1) & \psi_{2,1}(t_1) & \psi_{3,1}(t_1) \\ \psi_{1,2}(t_1) & \psi_{2,2}(t_1) & \psi_{3,2}(t_1) \\ \psi_{1,3}(t_1) & \psi_{2,3}(t_1) & \psi_{3,3}(t_1) \\ \vdots & \vdots & \vdots \\ \varphi_{1,1}(t_N) & \varphi_{2,1}(t_N) & \varphi_{3,1}(t_N) \\ \varphi_{1,2}(t_N) & \varphi_{2,2}(t_N) & \varphi_{3,2}(t_N) \\ \varphi_{1,3}(t_N) & \varphi_{2,3}(t_N) & \varphi_{3,3}(t_N) \\ \psi_{1,1}(t_N) & \psi_{2,1}(t_N) & \psi_{3,1}(t_N) \\ \psi_{1,2}(t_N) & \psi_{2,2}(t_N) & \psi_{3,2}(t_N) \\ \psi_{1,3}(t_N) & \psi_{2,3}(t_N) & \psi_{3,3}(t_N) \end{bmatrix} \cdot \begin{bmatrix} p_{11}^c \\ p_{22}^c \\ p_{12}^c \end{bmatrix}, \quad (6.9)$$

which models the measured currents over the whole trajectory. Because we have three linearly independent $\delta I_{\text{ax},k}$ and three $I_{\text{lat},k}$ available measurements in actual conditions, we only get the measurements on the macro-electrodes \mathcal{E}_1 , \mathcal{E}_2 and \mathcal{E}_3 , the macro-electrode \mathcal{E}_4 being polarized with a constant value u . Also, the chosen trajectory being that of a fly-by test, the angle θ_o^c remains constant, so are the components of P_{11}^c .

This linear model structure allows the implementation of the least squares method in order to estimate the tensor's components. We recall the basics of this approach here, which can be found in details in [64]. To that end, let us firstly add some notations. The $6N$ components vector of currents on the left side in (6.9) is denoted $\tilde{\mathbf{I}}$. The *tilde* symbol indicates that it corresponds to a modeled vector of currents. On the other hand, the corresponding measured vector is simply denoted \mathbf{I} . The $6N \times 3$ matrix on the right side is denoted Ψ and the vector of the three unknown parameters is denoted Θ . Hence, the system (6.9) is rewritten as

$$\tilde{\mathbf{I}} = \Psi \cdot \Theta. \quad (6.10)$$

Also, we define the prediction error, denoted ε , as the difference between the measured vector \mathbf{I} and the modeled vector defined by (6.10), that is

$$\varepsilon = \mathbf{I} - \Psi \cdot \Theta. \quad (6.11)$$

This error represents the ability for the model to predict a vector $\tilde{\mathbf{I}}$ for a given vector Θ and a given trajectory of the sensor, when compared to measured data \mathbf{I} . The best model produces the smallest prediction error.

The smallness of the error has to be quantified. Here we use the least squares criterion, denoted L_s and defined as half the square of the Euclidean norm of ε

$$L_s = \frac{1}{2} \|\varepsilon\|^2 = \frac{1}{2} (\mathbf{I} - \Psi \cdot \Theta)^T (\mathbf{I} - \Psi \cdot \Theta), \quad (6.12)$$

The principle of the least squares method consists in finding the vector $\hat{\Theta}$, an estimate of Θ , that minimizes L_s . The advantage of this criterion is that it is a quadratic function of Θ so it has a global minimum and the estimate that cancels out its first derivative with respect to Θ can be analytically calculated [64]. It is given by

$$\hat{\Theta} = [\Psi^T \cdot \Psi]^{-1} \cdot \Psi^T \cdot \mathbf{I}. \quad (6.13)$$

Note that we recognize the Moore-Penrose pseudo inverse matrix $\Psi^+ = [\Psi^T \cdot \Psi]^{-1} \cdot \Psi^T$ [37, 87].

In this standard least squares algorithm, each line of the system (6.9) plays an equivalent role in the solution. But some of the measurements can be particularly affected by the noise or being non relevant in regard to the linear model structure. This was showed in the chapter 5, in which the best localizations were obtained when the object faced the electrodes \mathcal{E}_1 to \mathcal{E}_3 , see figure 5.15. Hence, we have to deal with the reliability of each sample point during a fly-by test. This can be done by weighting each component of the vector ε depending on the reliability of the corresponding measured data. To that end, we define a *weighted* prediction error, denoted ε_w , as

$$\varepsilon_w = Q \cdot \varepsilon, \quad (6.14)$$

where Q is a $6N \times 6N$ diagonal matrix which contains on its diagonal the weights that are affected to each line of the system (6.9). As a result, we get the weighted least squares criterion

$$L_{sw} = \frac{1}{2} (\mathbf{I} - \Psi \cdot \Theta)^T Q^2 (\mathbf{I} - \Psi \cdot \Theta), \quad (6.15)$$

and the corresponding estimate

$$\hat{\Theta}_w = [\Psi^T \cdot Q \cdot \Psi]^{-1} \cdot \Psi^T \cdot Q \cdot \mathbf{I}. \quad (6.16)$$

In [53], the choice for the components of the matrix Q was the Euclidean norm of the basal electric field \mathbf{E}^0 , evaluated at the estimated center of the object. The matrix Q was defined as

$$Q = \begin{bmatrix} \|\mathbf{E}^0(t_1)\| & & 0 \\ & \ddots & \\ 0 & & \|\mathbf{E}^0(t_N)\| \end{bmatrix}. \quad (6.17)$$

This weighting allowed to give less importance to the data that correspond to the object far from the sensor, that is, the data that are more affected by the noise. Figure 6.1a shows the

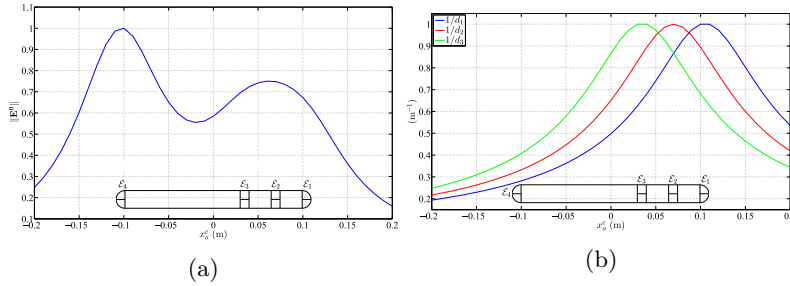


Figure 6.1: (a) The normalized value of $\|\mathbf{E}^0\|$ during a fly-by test. See also the representation of \mathbf{E}^0 during a fly-by test in figure 2.19b. (b) The inverse of the normalized distances d_1 , d_2 and d_3 between \mathcal{E}_1 , \mathcal{E}_2 and \mathcal{E}_3 and the object's center during a fly-by test. In both figures, the sensor is also represented .

normalized value of $\|\mathbf{E}^0\|$ during a fly-by test. One can see that, indeed, the measured samples that correspond to the object far from the sensor ($|x_s^c| > 0.12$) are down weighted. However, this choice for Q gives the highest weight when the object faces the macro-electrode \mathcal{E}_4 . This is not in accordance with figure 5.15, in which we can see that the best correspondence between model

and measurement is obtained when $0 \leq x_o^c \leq 0.14$. Moreover, figure 3.9 shows that $I_{\text{lat},1,2,3}$ are close to zero when the object faces \mathcal{E}_4 and provide no information to the system. Hence, we propose different weighting here, based on the distance between each macro-electrode and the object's center. Each current $\delta I_{\text{ax},k}$ and $I_{\text{lat},k} \forall k \in \{1, 2, 3\}$ at instant t_i will be weighted with the inverse of the corresponding Euclidean distance

$$d_k(t_i) = \sqrt{(x_o^c(t_i) - x_k)^2 + y_o^c(t_i)^2}, \quad (6.18)$$

x_k being the coordinate of \mathcal{E}_k along the axis \mathbf{i}_c . So, one can define N matrices $Q_i, \forall i \in \{1, \dots, N\}$ as

$$Q_i = \begin{bmatrix} 1/d_1(t_i) & & & & & & 0 \\ & 1/d_2(t_i) & & & & & \\ & & 1/d_3(t_i) & & & & \\ & & & 1/d_1(t_i) & & & \\ & & & & 1/d_2(t_i) & & \\ & 0 & & & & 1/d_3(t_i) & \\ & & & & & & 1/d_3(t_i) \end{bmatrix}, \quad (6.19)$$

and gather them in the weighting matrix Q such that

$$Q = \begin{bmatrix} Q_1 & & 0 \\ & \ddots & \\ 0 & & Q_N \end{bmatrix}. \quad (6.20)$$

Looking at figure 6.1b, one can see that this choice for the weights is more suitable for our problem, providing more importance to the samples when object is close to macro-electrodes \mathcal{E}_1 , \mathcal{E}_2 and \mathcal{E}_3 . In the following, only this weighted version of the least squares will be used.

At this point, using this algorithm, we can get an estimation of the components of P_{11}^c . We could stop our study here because all the parameters that define the currents in the analytical model are estimated. But, this estimated tensor does not explicitly represent the geometry of the object. So, we have to proceed to a transformation of the estimated tensor's components into estimated geometrical parameters. This is the purpose of the second step of the shape estimation process.

6.1.2 Step two : Object's shape parameters estimation

Once the tensor's components are estimated, the second and last step consists in extracting the geometrical properties of the object: volume \mathcal{V} , aspect ratio η and angle θ_o^c . This will be performed by inverting the relationships (3.84) that relate the geometrical parameters to the tensor's components. Let us recall them here

$$\begin{cases} p_{11}^c = \mathcal{V} \cdot [f(\eta) \cdot \cos^2(\theta_o^c) + g(\eta) \cdot \sin^2(\theta_o^c)], \\ p_{22}^c = \mathcal{V} \cdot [f(\eta) \cdot \sin^2(\theta_o^c) + g(\eta) \cdot \cos^2(\theta_o^c)], \\ p_{12}^c = \mathcal{V} \cdot [f(\eta) - g(\eta)] \cos(\theta_o^c) \cdot \sin(\theta_o^c), \end{cases} \quad (6.21)$$

were the functions f and g are defined as

$$\begin{cases} f = 1/A \text{ and } g = 1/B \text{ for a conductive object} \\ f = 1/(A - 1) \text{ and } g = 1/(B - 1) \text{ for an insulating object} \end{cases} \quad (6.22)$$

with the functions A and B being defined as

$$\begin{cases} A(\eta) = \eta^{-2} \int_1^{+\infty} \frac{1}{t^2(t^2 - 1 + \eta^{-2})} dt, \\ B(\eta) = \eta^{-2} \int_1^{+\infty} \frac{1}{(t^2 - 1 + \eta^{-2})^2} dt. \end{cases} \quad (6.23)$$

In practice, the following alternative and equivalent system of equations is used

$$\begin{cases} p_{11}^c + p_{22}^c = \mathcal{V} \cdot (f(\eta) + g(\eta)), \\ p_{11}^c - p_{22}^c = \mathcal{V} \cdot (f(\eta) - g(\eta)) \cdot \cos(2\theta_o^c), \\ 2 \cdot p_{12}^c = \mathcal{V} \cdot (f(\eta) - g(\eta)) \cdot \sin(2\theta_o^c). \end{cases} \quad (6.24)$$

Indeed, this alternative system has two advantages: 1) it allows to easily distinguish a sphere from an ellipsoid ; 2) the estimation of the intrinsic properties of the object \mathcal{V} and η can be decoupled from the angle estimation, as it will be shown below.

Looking at equation (3.76), the tensor that corresponds to a sphere is proportional to the identity matrix, so we have the following rule

$$\text{If } p_{12}^c = p_{11}^c - p_{22}^c = 0, \text{ the object is a sphere and } \theta_o^c \text{ is arbitrary.} \quad (6.25)$$

If this rule is not verified, the object is an ellipsoid and the angle θ_o^c is computed according to

$$\theta_o^c = \frac{1}{2} \arctan(2 \cdot p_{12}^c / (p_{11}^c - p_{22}^c)). \quad (6.26)$$

In practice, the function `atan2` will be used, with $2 \cdot p_{12}^c$ and $p_{11}^c - p_{22}^c$ as the first and the second parameter respectively. Then, we get a sub-system of two equations in two unknowns \mathcal{V} and η , by adding the square of the two last lines of the system (6.24) and combining the result with its first equation

$$\begin{cases} \mathcal{V} \cdot f(\eta) = \frac{1}{2} \left(p_{11}^c + p_{22}^c + \sqrt{(p_{11}^c - p_{22}^c)^2 + 4(p_{12}^c)^2} \right), \\ \mathcal{V} \cdot g(\eta) = \frac{1}{2} \left(p_{11}^c + p_{22}^c - \sqrt{(p_{11}^c - p_{22}^c)^2 + 4(p_{12}^c)^2} \right). \end{cases} \quad (6.27)$$

The ratio between these two equations only depends on η , and its analytical expression can be calculated using (6.22). Their representative curves are given in figure 6.2, top row, for a conductive and an insulating object. These functions having only one solution over the range $[0; 2.5]$, η can be estimated by reading these plots. In practice, in the case of an autonomous robot a look-up table can be used. Obviously, either the function f/g or the function g/f can be used. In the following, for a conducting object, we will use the function f/g because the absolute value of its slope is higher than that of the function g/f . Hence, the use of f/g would introduce a smaller error on η , compare to g/f . For an insulating object, the function g/f will be used for the same reason.

Finally, once η is estimated, we can get an estimation of \mathcal{V} using one of the two equations (6.27), multiplying it by $1/f$ for the first one and $1/g$ for the second one. Functions $1/f$ and $1/g$ are represented in figure 6.2, bottom row. In practice, for both conductive and insulating objects, we will use the first equation in (6.27) and function $1/f$ because the absolute value of its slope is higher than that of $1/g$.

This ends the introduction of the principles of the shape estimation algorithm. The next sections present its implementation with BEM data and with experimental data.

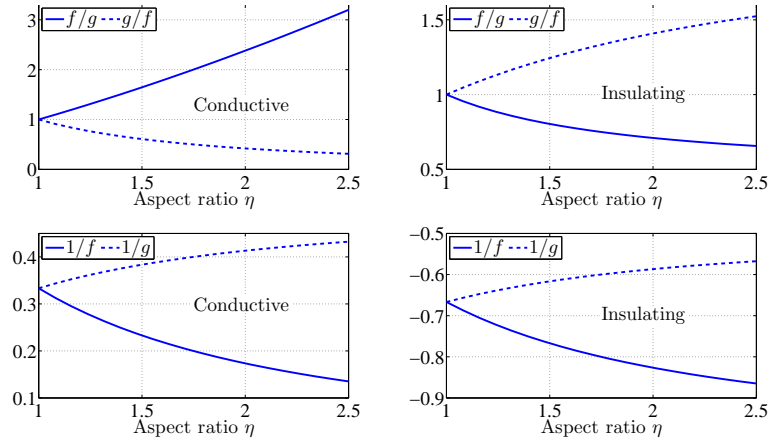


Figure 6.2: Representation of the functions f/g and g/f (top row) and $1/f$ and $1/g$ (bottom row) for conductive (left column) and insulating (right column) objects.

6.2 Implementation of the shape estimation with BEM data

Here, as in chapter 5 for the localization, we firstly evaluate the performances of the shape estimation algorithm with BEM data as input. The goal is to analyze the algorithm's behavior with neither localization error nor measurement noise. The only source of uncertainty will be the approximations of the analytical model. The localization errors and the measurement noise will be artificially included in a second phase in order to evaluate their effects.

6.2.1 Neither localization error nor measurement noise

As a starting point we use the simulated objects of table 5.1 (those that were used to evaluate the MUSIC algorithm in chapter 5), and apply the shape estimation algorithm to each of them. The trajectory of the sensor is defined as a fly-by test, that is, with constant values of y_o^c and θ_o^c , that are indicated for each object in table 5.1. There are $N = 41$ samples over the trajectory, with $-0.2m \leq x_o^c \leq 0.2m$, i.e, one sample every centimeter. No localization error nor measurement noise are present. Once the geometrical parameters are estimated, one can plot the estimated objects using the parametric equations

$$\begin{cases} x(t) = \hat{x}_o^c + \hat{a} \cdot \cos t \cdot \cos \hat{\theta}_o^c - \hat{b} \cdot \sin t \cdot \sin \hat{\theta}_o^c, \\ y(t) = \hat{y}_o^c + \hat{a} \cdot \cos t \cdot \sin \hat{\theta}_o^c + \hat{b} \cdot \sin t \cdot \cos \hat{\theta}_o^c, \end{cases} \quad (6.28)$$

where $t \in [0; 2\pi[$ and the symbol *hat* indicate that it concerns estimated values. Because the algorithm provides estimates of the parameters \mathcal{V} and η , we have to get the corresponding values

of the parameters \hat{a} and \hat{b} , which can easily be calculated with the following relationships

$$\hat{a} = \sqrt[3]{\frac{3 \cdot \hat{\mathcal{V}} \cdot \hat{\eta}^2}{4 \cdot \pi}}, \quad (6.29)$$

$$\hat{b} = \frac{\hat{a}}{\hat{\eta}}.$$

The six actual and estimated objects are represented in figure 6.3 using these equations. Qualitatively,

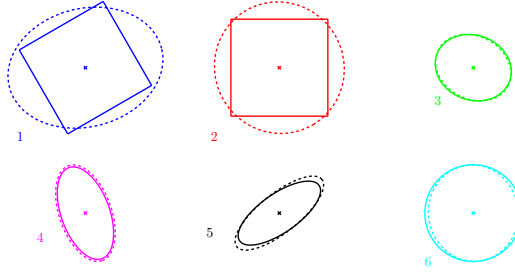


Figure 6.3: Actual objects (solid lines) and estimated objects (dashed lines).

one can see that the estimation is very good for the six objects, showing the relevance of the method. Quantitatively, the actual and estimated values are given in table 6.1. In order to

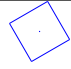
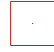




						
Number	1	2	3	4	5	6
Material	Insul.	Cond.	Cond.	Insul.	Cond.	Cond.
a ; \hat{a} ($\text{m} \times 10^{-3}$)	10 ; 15.92	10 ; 13.65	8 ; 8.09	10 ; 10.39	10 ; 11.32	10 ; 9.98
b ; \hat{b} ($\text{m} \times 10^{-3}$)	10 ; 12.38	10 ; 13.37	6.7 ; 6.51	5 ; 5.39	4 ; 4.05	10 ; 9.28
\mathcal{V} ; $\hat{\mathcal{V}}$ (cm^3)	8 ; 10.22	8 ; 10.22	1.5 ; 1.44	1.05 ; 1.26	0.67 ; 0.78	4.2 ; 3.60
η ; $\hat{\eta}$	1 ; 1.28	1 ; 1.02	1.2 ; 1.24	2 ; 1.93	2.5 ; 2.79	1 ; 1.07
θ_o^c ; $\hat{\theta}_o^c$ (deg)	30 ; 13.60	0 ; -61.82	-20 ; -27.28	-70 ; -70.43	35 ; 37.71	- ; -84.17
e_s (%)	0.36	5.53	1.81	3.48	0.46	5.06
e_θ ($^\circ$)	16.40	61.82	7.28	0.43	2.71	-

Table 6.1: BEM objects' shape estimation results, corresponding to figure 6.3.

evaluate and compare these results we define a shape error, denoted e_s , defined as

$$e_s = \sqrt{\frac{(a - \hat{a})^2 + (b - \hat{b})^2}{a^2 + b^2}} \cdot 100 \quad (6.30)$$

expressed in percent, and the angle error, denoted e_θ , defined as

$$e_\theta = |\theta_o^c - \hat{\theta}_o^c| \quad (6.31)$$

expressed in degrees. The shape error and the angle error are given in table 6.1, in the second to last and in the last row, respectively. The shape errors are spread from 0.46% to 5.53%.

For the particular cases of the cubes, because the model on which is based the algorithm is that of an ellipsoid, they are necessarily estimated as ellipsoids. In order to calculate the shape error as a percentage, a sphere with same volume was used as reference, that is, a sphere with 12.4mm radius. Note that their estimated aspect ratios are close to one ($\hat{\eta} = 1.28$ for object 1 and $\hat{\eta} = 1.02$ for object 2). This is because the electrical response of a polarized cube can be approximated to a sphere at leading order [46] and this is in accordance with [59], in which the algorithm, based on a Kalman filter, estimates the cubes with circumscribed spheres. Their estimated volumes equal to that of a sphere of radius $a = 13.5\text{mm}$ for both of them

$$\hat{V} = 10.22\text{cm}^3 \Leftrightarrow a = \sqrt[3]{\frac{3 \times 10220}{4\pi}} = 13.5\text{mm}. \quad (6.32)$$

Now looking at the angle errors, objects 3, 4 and 5 show errors between 0.43° and 7.28° . For the sphere (object 6), the algorithm provides an angle value, even if this has no significance. This is due to the fact that the estimated tensor component \hat{p}_{12}^c is not zero, and the estimated components \hat{p}_{11}^c and \hat{p}_{22}^c are not equal, as it would be the case for a sphere. For instance, the first step of the algorithm provided the following estimated tensor components for object 6

$$\begin{cases} \hat{p}_{11}^c = 8.4 \times 10^{-7}, \\ \hat{p}_{22}^c = 9.1 \times 10^{-7}, \\ \hat{p}_{12}^c = -7.4 \times 10^{-9}, \end{cases}$$

leading to an estimated angle of -84.17° . But, because the aspect ratio is close to one, this estimated angle has a weak influence on the object's shape reconstruction, as illustrated in figure 6.3, object 6. In fact, we can consider that as the estimated aspect ratio becomes closer to one, the estimated angle becomes less significant gradually. But this has a counterpart: the estimation of the angle for the ellipsoids which aspect ratio is close to one is fragile. This will be highlighted in the case of experimental data in the next section.

6.2.2 With localization errors and no measurement noise

In the examples above, because the localization is considered as known, that is $(\hat{x}_o^c, \hat{y}_o^c) = (x_o^c, y_o^c)$, and because there is no measurement noise on the currents, the differences between actual and estimated values can only be attributed to the difference between BEM and analytical model currents. Now, let us focus on how the localization error impacts these results. To that end, we define a set of localization errors with polar coordinates, as shown in figure 6.4. It is defined by 3 circles of $\rho = \{1, 2, 3\}\text{mm}$ radius and by 20 equidistant angles $\theta \in [0^\circ; 360^\circ]$, leading to a set of 60 different localization errors. Hence, for each of these 60 errors, the actual localization is altered according to

$$\begin{cases} \tilde{x}_o^c = x_o^c + \rho \cdot \cos(\theta), \\ \tilde{y}_o^c = y_o^c + \rho \cdot \sin(\theta), \end{cases} \quad (6.33)$$

where $(\tilde{x}_o^c, \tilde{y}_o^c)$ is the altered object's localization. For a given object and a given altered localization, we compute a matrix $\Psi(\tilde{x}_o^c, \tilde{y}_o^c)$ and the shape estimation algorithm is applied. As a result, we get 60 shape estimations for each of the six previously tested objects. Figure 6.5 shows these 60 estimations for each of them. The corresponding shape and angle errors are given in figures 6.6a and 6.6b respectively.

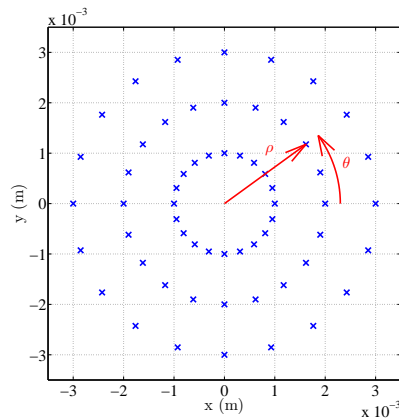


Figure 6.4: The 60 localization errors. Each blue cross represents a localization error, defined with a radius ρ and an angle θ .

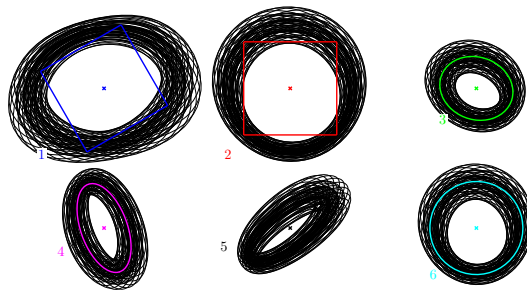


Figure 6.5: The actual objects (colored solid lines) and the estimated objects (black solid lines). The estimated objects are represented at the true localization.

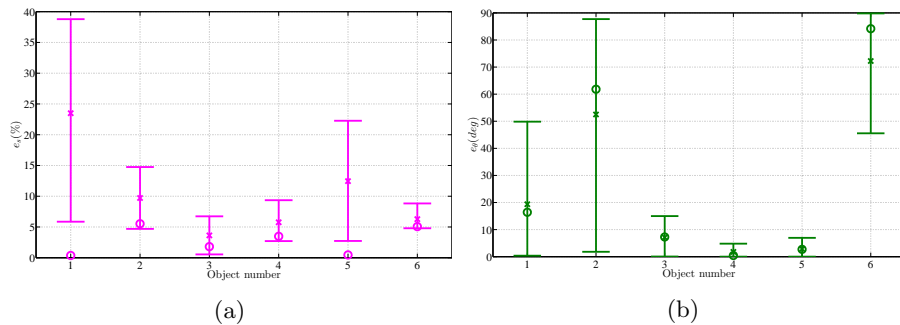


Figure 6.6: (a) The shape errors for the six objects. (b) The angles error for the six objects. In both graphs, the circles represent the error value with no localization error. The crosses represents the mean error over the 60 trials, and the error bar indicate the error range.

Firstly, let us focus on the results about the shape estimation, and we will deal with the angle estimation in a second phase. For each object, the mean shape error (crosses) over the 60 trials is higher than the error obtained without localization error (circles). On the other hand, the

minimal shape error of objects 2, 3, 4 and 6 is lower than the error without localization error. This shows that there exist some altered matrices $\Psi(\tilde{x}_o^c, \tilde{y}_o^c)$ such that the modeled currents fit the measured currents better than the model with the matrix with no localization error $\Psi(x_o^c, y_o^c)$. This produces at the end a better estimation of the shape.

Also, the shape error range for the objects 1 and 5 is wider than the four others, showing that they are more sensitive to localization errors. These two objects differ in term of material, shape, aspect ratio and volume. But, they have in common the fact that they are the closest to the sensor: $y_o^c = 0.06\text{m}$ for object 1 and $y_o^c = 0.05\text{m}$ for object 5. The lateral distance of the four other objects are greater or equal to 0.07m , see figure 5.6. So, in order to evaluate if it is this shorter lateral distance which leads to a higher sensitivity for objects 1 and 5, we define two new objects, denoted 1' and 5', which differ from objects 1 and 5 only in term of lateral distance, which is set to 0.08m for both of them. The same 60 localization errors were defined and the 60 shape estimation were performed for both objects 1' and 5'. Figure 6.7 shows that the shape

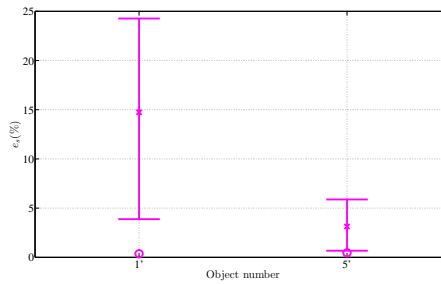


Figure 6.7: Shape error for the two objects 1' and 5'.

error range is significantly reduced, compare to objects 1 and 5. The maximum shape error is 25% for object 1', whereas it is 38% for object 1. Similarly, the maximum shape error is 6% for object 5', whereas it is 22% for object 5. This shows that increasing the lateral distance significantly improves the robustness of the shape estimation with respect to the localization error. This is in accordance with the hypothesis of the analytical model (property \mathcal{P}_6) which states that the object must be at least 3cm far from the sensor. Here, even if this requirement is strictly respected, we can see that the lateral distance has a non negligible effect on the shape estimation.

Let us focus on the angle error now. See figure 6.6b. One can see that the minimal shape error is lower than the error without localization error for the six objects. Same conclusion can be draw as the shape error case: there exist some localization errors that make the model to better describe the measured currents than the model with no localization error.

Also, the objects that are the less sensitive to localization errors are the objects 3, 4 and 5, with maximal angle errors between 5° (object 4) and 15° (object 3). On the other hand, the object 1, 2 and 6 present wide range of error. These objects have in common their aspect ratio $\eta = 1$. We find again the observation made on the sphere without any localization error: for such spheroidal objects, the angle has no importance in the scene description, the tensor being proportional to the identity matrix. Hence, the absolute values of the angle error has no meaning. But, this wide variation in term of angle estimation informs us about the algorithm's behavior: if the object's tensor is proportional to the identity matrix, there is a supplementary and non necessary degree of freedom in the algorithm which, at the end, estimates the angle within a wide

range for spheroidal objects. In fact, we could consider that this is not crucial because any angle is suitable for such objects, and the object is well represented at the end. But, as a counterpart, the angle estimation is less accurate for non spheroidal objects with aspect ratio close to one. This drawback will be highlighted with experimental data in the next section.

Now we have explored the effects of the localization errors without any measurement noise, let us evaluate the effect of an additive noise on the measurements when the localization is known.

6.2.3 With measurement noise and no localization error

Here, we investigate the effects of an additive measurement noise, without localization error. Adding a 5% random noise on the measurements, with no localization error, we get the results

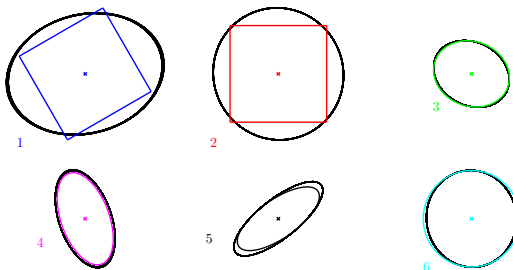


Figure 6.8: The actual objects (colored solid lines) and 500 estimated objects (black solid lines), each corresponding to a realization of the additive random noise.

shown in figure 6.8. We can see that the deviation from the initial estimation is almost zero (compare with figure 6.3), showing that the algorithm is robust with respect to the noise. This is due to the least squares methods which has a averaging behavior [64].

As a conclusion, we showed that the proposed algorithm provides good shape estimations with BEM data as input. The maximal shape error we observed over all of our tests is 25% (object 1'), the maximal shape error of the five other objects being below 15%. These results were obtained with a lateral distance greater than or equal to 0.07m. With a shorter lateral distance, we showed that the sensitivity to the localization error significantly increases.

The maximal observed angle error over all the tests (for the non spheroidal objects) is 15° (object 3). We also showed that the algorithm provides a wide range of angle errors for spheroidal objects.

The additive noise on the measurements led to very small shape and angle errors, close to zero, showing that the localization error has a significantly much more important effect compare to the noise.

Despite these shape and angle errors, each of the six tested objects are clearly identifiable, showing that this method is relevant.

As described in the previous chapter 5, supplementary sources of errors are present in experimental conditions, such as the uncertainty on the water conductivity measurement, the non perfect

sensor's geometry and experimental imprecisions on the object's and sensor's positions. In the next section we present the performances of the shape estimation algorithm in these experimental conditions.

6.3 Shape estimation with experimental data

In order to validate the shape estimation in actual conditions, we performed many fly-by tests with the ellipsoidal objects numbered 4 to 7 in figure 2.3. Again, these objects are considered as large, that is, they do not meet the model's hypothesis. But, we use them anyway in order to have a wider range of detection (see section 5.4.1). For each object, 35 fly-by tests were performed: 7 different lateral distances $y_o^c \in \{50, 60, 70, 80, 90, 100, 110\}$ mm and 5 different angles $\theta_o^c \in \{-30, 0, 30, 60, 90\}$ degrees. Only four test are missing: short lateral distance (50mm) and angle of 90° for objects 4 and 5, for which the sensor was too close to the object. Also, for object 7 at lateral distance $y_o^c = 110$ mm and angles 60° and 90° for which the data were unusable because of particularly low SNR (recall the example given in figure 5.14b). This leads to 136 different experiments. The trajectories were performed along $2L = 440$ mm long trajectories.

The methodology we will use here consists in

1. observe the results gathered in the four tables in table 6.9 (denoted Table A, Table B, Table C and Table D),
2. extract the main trends from the results.

We will give some explanations about these trends using the observations made with the BEM shape estimation (previous section).

Table 6.9.A is divided in four blocks, each of them corresponding to an object. In each block, each row corresponds to a lateral distance and each column corresponds to an angle. The shape estimation error varies in the range from 1.5% to 47.7%, with an overall average of 16.3%. The shapes of the actual and estimated objects for such error values are shown in figure 6.10 as examples. One can see that a 1.5% shape error (figure 6.10(a)) is almost indistinguishable. The object's is very well estimated. The example in figure 6.10(b) corresponds to a 16.7% shape error. In this particular case, the estimation of the aspect ratio is under estimated: $\hat{\eta} = 1.12$, whereas $\eta = 1.5$. This leads to an error on the semi-axis b that is greater than the error on the semi-axis a . On the other hand, the third example in figure 6.10(c) shows an over estimated aspect ratio.

In the last line of the table A is indicated the mean shape error for each object's angle. We observe that the mean shape error is in the range [14%; 18.7%]. About the angle estimation, one can see that it is well estimated for object 4 (the maximum error is obtained for $y_o^c = 100$, $\theta_o^c = 90^\circ$ and equals to 15.94°). For objects 5, 6 and 7, the angle estimation is not as good as that of object 4. The error can even reach more than 85° in some cases. Let us note that this poor angle estimation does not affect much the shape estimation results. These first observations from the results in table 6.9 lead to the following trend:

Trend 1: angle estimation is fragile.

Table A

	Lat. dist. (mm)	-30		0		30		60		90	
		Shape error (%)	Angle error (°)	Shape error (%)	Angle error (°)	Shape error (%)	Angle error (°)	Shape error (%)	Angle error (°)	Shape error (%)	Angle error (°)
Conductive a 0.033 b 0.016 Object 4	50	17.64	7.69	8.71	1.24	5.41	4.01	21.95	6.23	-	-
	60	8.62	5.90	9.49	0.39	8.68	4.89	8.16	3.61	22.68	14.00
	70	4.09	5.20	13.02	1.71	11.72	5.28	3.99	4.29	12.17	13.34
	80	2.31	4.23	13.19	4.44	13.74	5.96	6.82	1.83	6.68	12.29
	90	2.98	0.21	15.06	4.34	11.86	9.11	8.59	1.32	3.52	12.17
	100	3.70	0.59	12.17	1.49	16.39	8.39	7.20	2.58	2.06	15.94
	110	4.24	5.99	20.36	6.80	15.79	11.00	14.57	7.75	1.51	13.12
Insulating a 0.033 b 0.016 Object 5	50	12.50	85.70	30.76	27.91	19.38	54.97	47.74	65.48	-	-
	60	24.00	70.12	24.59	2.18	12.47	39.32	10.79	65.49	18.67	74.74
	70	31.75	6.84	20.08	2.91	7.86	26.69	24.28	36.60	27.77	33.36
	80	29.51	24.58	8.74	1.43	14.19	18.92	23.30	7.34	25.68	21.02
	90	19.95	6.30	3.65	7.32	4.77	20.70	19.25	23.61	11.53	8.62
	100	28.78	46.45	21.00	3.02	19.95	11.55	7.22	7.24	22.91	7.62
	110	11.31	5.33	16.42	32.36	22.63	5.51	33.85	33.96	20.92	9.06
Conductive a 0.027 b 0.018 Object 6	50	3.27	5.94	13.89	27.58	13.69	6.38	23.53	9.73	15.70	36.89
	60	9.62	3.58	14.80	15.72	14.17	12.14	15.55	7.33	3.78	38.40
	70	13.34	9.25	18.80	20.27	15.16	15.79	15.04	4.66	4.75	36.55
	80	19.11	7.03	17.03	7.71	15.71	5.75	18.99	2.71	10.37	44.64
	90	16.75	51.02	17.07	48.36	14.91	3.85	23.69	28.77	13.83	54.03
	100	17.14	71.57	16.09	66.28	16.70	5.90	27.04	21.32	16.66	56.06
	110	17.33	41.50	19.92	50.02	24.90	10.08	30.07	33.80	17.24	9.89
Insulating a 0.027 b 0.018 Object 7	50	31.52	76.53	16.69	78.00	11.83	48.86	18.07	17.48	39.66	32.89
	60	12.11	73.50	9.74	78.96	10.73	41.18	16.60	1.16	19.18	22.17
	70	11.13	61.24	9.87	84.07	10.74	39.76	21.31	10.48	30.38	15.31
	80	11.12	56.01	11.46	85.25	9.04	42.70	18.82	18.61	45.04	4.06
	90	11.07	33.82	13.36	54.20	21.51	63.12	22.37	29.77	24.41	2.38
	100	26.67	37.69	16.80	65.05	13.05	56.22	14.92	26.14	23.30	2.20
	110	13.26	39.42	42.73	61.05	16.40	61.11	-	-	-	-
Mean error		14.81	30.11	16.27	30.00	14.05	22.83	18.66	17.75	17.61	23.63

Table B

	Shape error (%)	Angle error (°)
Object 4	9.97	6.10
Object 5	19.95	26.30
Object 6	16.16	24.87
Object 7	18.94	43.04

Table C

Lat. dist. (mm)	Shape error (%)	Angle error (°)
50	19.55	32.97
60	13.72	28.74
70	15.36	21.68
80	16.04	18.82
90	14.01	23.15
100	16.49	25.66
110	19.08	24.32

} Mean shape: 15,1%
Mean angle: 23,6°

Table D

	Conductive		Insulating		$\eta = 2$		$\eta = 1,5$	
	Shape (%)	Angle (°)	Shape (%)	Angle (°)	Shape (%)	Angle (°)	Shape (%)	Angle (°)
Mean error	12.30	15.64	17.95	31.58	13.83	14.35	16.42	32.87
Standard deviation	5.87	18.70	8.18	25.69	8.23	17.86	6.83	25.40

Figure 6.9: The results of the experiments. Table A: the errors of shape (pink) and angle (green) for 136 different experiments: four objects, five angles (-30, 0, 30, 60 and 90°) and seven distances (50, 60, 70, 80, 90, 100 and 110 mm). The last line shows the mean of each column. Table B: the mean errors of shape and angle for each object. Table C: the mean errors of shape and angle for all objects at each distance. Table D: the mean errors of shape and angle for conductive objects, insulating objects, and aspect ratio 2 and 1.5 in the distance interval [60 ; 100] (100 experiments).

This will be confirmed by looking at the data in table B.

Also, note that object 4 is better estimated in both term of shape and angle, compare to the three other objects. This is clearly illustrated by table B, which shows the mean of the shape and angle errors for each object. See also figure 6.11a in which the distribution of the shape error for all the 136 experiments is represented. This distribution has a mean value equal to 16.3% and spreads from 1.5% to 47.7%, as already said before. But, the errors above 35% are just four particular cases over the 136 tests, so that 97% of the experiments have shape errors lower or equal 35%.

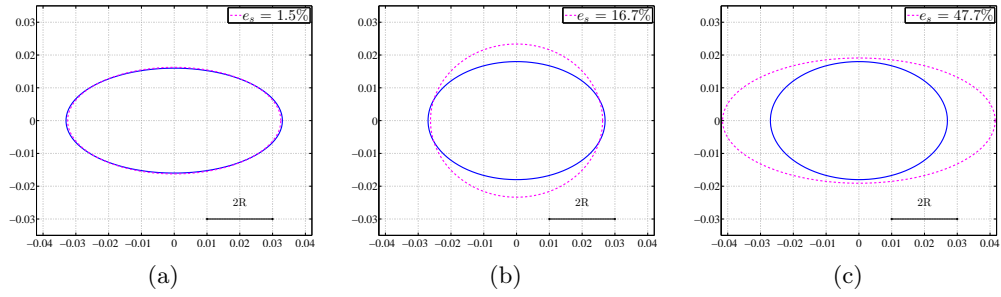


Figure 6.10: Three examples of shape estimation, represented with $\theta_o^c = 0^\circ$. Solid blue lines: actual objects ; dashed pink lines: estimated objects. (a) Object 4, $\theta_o^c = 0^\circ$, $y_o^c = 110\text{mm}$, $e_s = 1.5\%$ (b) Object 6, $\theta_o^c = 30^\circ$, $y_o^c = 100\text{mm}$, $e_s = 16.7\%$ (c) Object 5, $\theta_o^c = 60^\circ$, $y_o^c = 50\text{mm}$, $e_s = 47.7\%$. The sensor diameter ($2R$) is also represented for comparison.

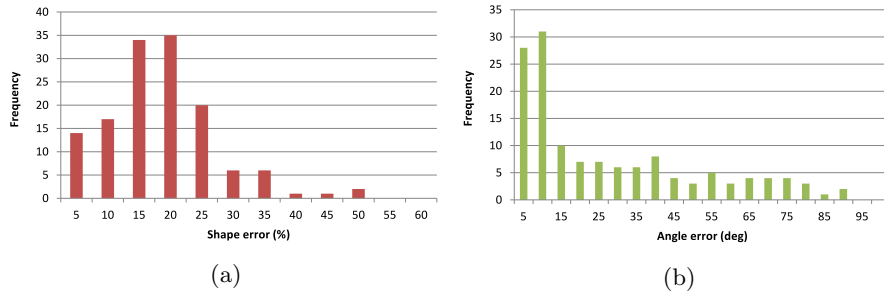


Figure 6.11: The shape error (a) and the angle error (b) distributions among the 136 experiments of figure 6.9.

On the other hand, the angle error has a mean value of 25° , and spreads from 0.2° to 85.7° , as shown in figure 6.11b. Even though almost 60 experiments have angle errors lower or equal 10° , more than half of the experiments have angle errors greater than or equal 15° . This confirms the trend 1 which states that the angle estimation is fragile.

This trend was already observed with BEM data when a localization error is introduced, see figures 6.5 and 6.6b. It showed that the angle estimation is not accurate for objects with an aspect ratio close to one. This is the case with experimental data, for objects 6 and 7. The angle estimation of object 5, which has an aspect ratio equal to 2, is also inaccurate. This is due its insulating material, as it will be explained below.

Table C gathers the shape and angle mean errors for each lateral distance. This highlights an interval in term of lateral distance, in which both errors are the lowest: $y_o^c \in [60\text{mm}; 100\text{mm}]$. In this interval, the mean shape error over all objects, angles and distances is 15.1% . For the angle error, it is equal to 23.6° .

Trend 2: the best interval is $y_o^c \in [60\text{mm}; 100\text{mm}]$ in term of shape and angle estimation.

The lower bound (60mm) can be explained by the fact that the analytical model on which is based the method is theoretically valid when the object is not too close to the sensor ($y_o^c \geq 3R$

according to [12]). On the other hand, the upper bound (100mm) corresponds to the limit beyond which the signal to noise ratio makes the algorithm performances to decrease. This was already mentioned in section 5.4.1 and illustrated in figures 5.14a and 5.14b.

Finally, the table D shows the means and the standard deviations of the errors, computed for objects of same material (conductive and insulating objects in the first and second column respectively) and for objects of same aspect ratio ($\eta = 2$ and $\eta = 1.5$ in the third and fourth column respectively). One can see that the shape and the angle of conductive objects are significantly better estimated than insulating objects: 5.6% better for the shape and 15.9° better for the angle. So, a third trend is drawn:

Trend 3: conductive objects are better estimated than insulating objects in both terms of shape and angle.

In order to give an explanation to this trend let us have a look at the four figures 6.12, in which the lateral current $I_{\text{lat},2}$ for two similar objects which only differ in term of material are plotted. In figure 6.12a, one can see that the peak position (already defined in section 5.4.2) varies as a

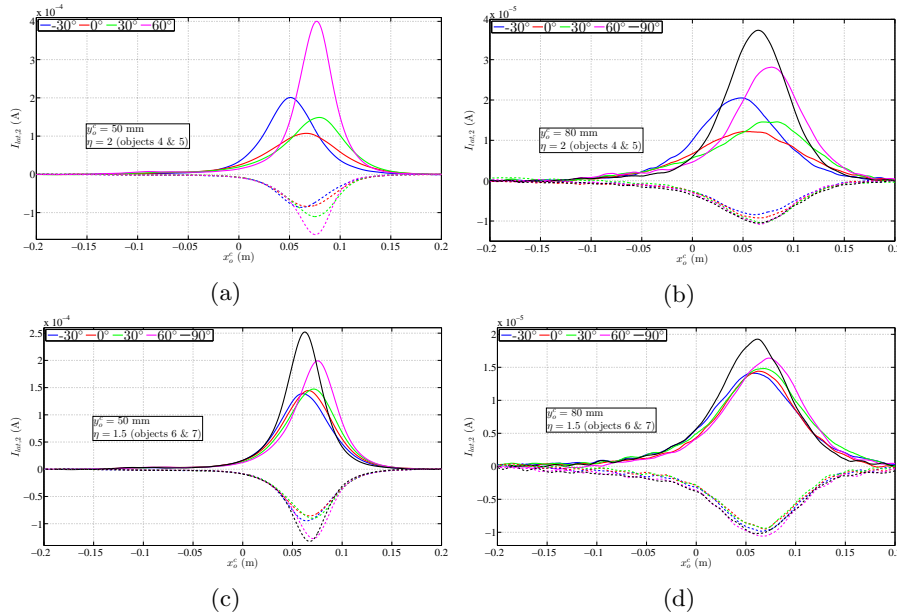


Figure 6.12: The current $I_{\text{lat},2}$ measured during fly-by tests for different angles θ_o^c . In each figure, the currents correspond to two different objects which only differ in term of material. Solid lines: conductive objects, dashed lines: insulating objects. (a) Objects 4 and 5 at lateral distance $y_o^c = 50\text{mm}$. (b) Objects 4 and 5 at lateral distance $y_o^c = 80\text{mm}$. (c) Objects 6 and 7 at lateral distance $y_o^c = 50\text{mm}$. (d) Objects 6 and 7 at lateral distance $y_o^c = 80\text{mm}$.

function of θ_o^c , for both of the conductive and the insulating objects. Note that this variation is lower for the insulating object than for the conductive one. Same observation can be made about the amplitude: amplitude variation versus the angle θ_o^c is lower for an insulating object. When increasing the lateral distance, all other things being equal (figure 6.12b), this phenomenon is emphasized. Whereas the currents are significantly different for the conducting object, they are very similar for the insulating one. In short, the currents are less sensitive to θ_o^c when the object

is made of insulating material. As a consequence, it is necessarily difficult for the algorithm to clearly discriminate two different objects, and hence, accurately estimate the parameters \mathcal{V} , η and θ_o^c with such small currents' variations.

Similarly, the ellipsoids with larger aspect ratio are better estimated. The shape estimation is 2.6% better and the angle estimation is 18.5°. As a conclusion, we have the fourth trend:

Trend 4: objects with aspect ratio $\eta = 2$ are better estimated than objects with aspect ratio $\eta = 1.5$ in both terms of shape and angle.

The currents' sensitivity with respect to the aspect ratio can be qualitatively evaluated in the same way as for trend 3. Looking at figure 6.12c, one can see that the peak position and the amplitude variations are weak compare to that of objects with $\eta = 2$. Again, when the lateral distance increases the phenomenon becomes very clear, as shown in figure 6.12d, where the differences between the measured currents are not significant. As a result, the algorithm cannot accurately estimate the shape and the angle.

All these results were obtained with no localization error. Now, let us add such an error as input in order to evaluate its influence.

6.3.1 Evaluation of the influence of the localization uncertainty on the shape estimation

In this section we show the effects of a localization error on the shape estimation. This was performed in the same way as the previous section with the BEM data. The configuration for the localization error is defined with three radius $\rho \in \{2, 4, 6\}$ and fifty angles $\theta \in [0; 2\pi]$ with a step of $2\pi/50$. See a representation of this configuration in figure 6.13c. Note that the maximum localization error is quite large (6mm) compare to that it was chosen in the previous section (3mm), in order to adapt it the object's size. The localization error made with the MUSIC algorithm (chapter 5) are also shown in figure 6.13c as a comparison.

In figure 6.13a are presented the object 4 (blue straight lines), its estimated shape with no localization error (dashed pink) and the 150 estimated ellipsoids with the localization errors defined above (pale blue straight lines). The variation in term of shape and angle is qualitatively low.

Quantitatively, the figure 6.13b shows the average shape error over the 50 values of each radius ρ . It points out that the shape error increases form 10% with no localization error to 13.7% on average with 6mm localization error. This shows a relative robustness of the shape recognition with respect to the localization error. These results are reported in 6.2, in which is also indicated the shape error obtained with the MUSIC localization error. This test was also performed with object 7, and the results are indicated in table 6.2 as well. Like the object 4, the shape error is higher when the MUSIC localization is introduced (18.7%) compare with the case with no localization error (17.9%). The shape error significantly increases to 35.1%, in average, for a 6mm localization error. These results confirm that were obtained with the BEM data: the shape estimation for the insulating objects with lower aspect ratio is more sensitive to localization errors.

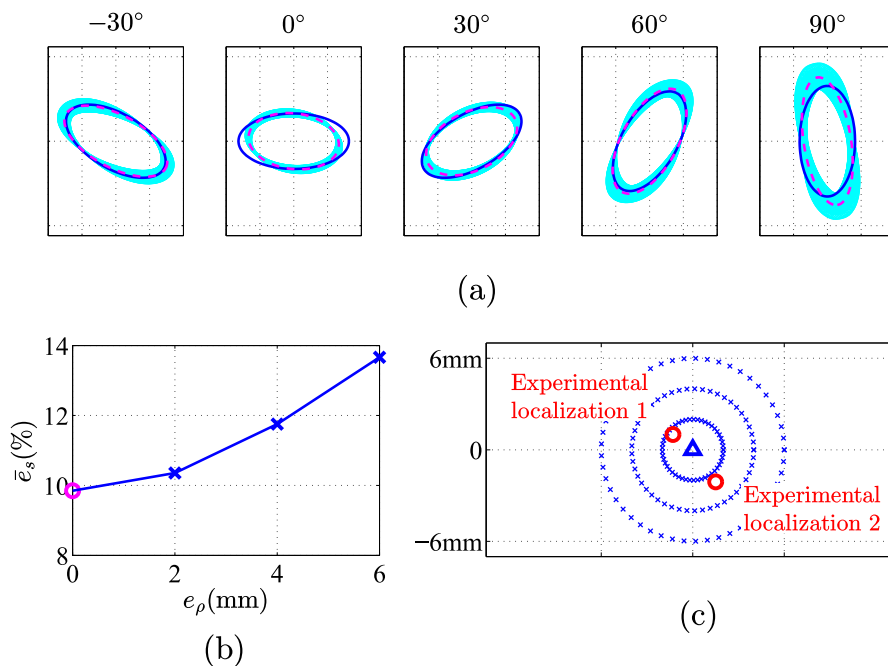


Figure 6.13: Shape estimation of object 1 in Table 2.1 at 60mm for 5 orientations (from left to right: -30° , 0° , 30° , 60° , 90°) when additional errors e_ρ on the localization are introduced as inputs of shape estimation, according to the polar grid of sub-figure (c). (a) Estimated ellipsoid for the 3×50 erroneous localization (pale blue); real shape (blue); estimated shape when the localization is perfect (pink dashed lines). (b) Mean averaged shape error \bar{e}_s as a function of the localization error e_ρ . (c) Localization error grid centered on the real value. It is defined by 3 circles of $\{2, 4, 6\}$ mm radius and by 50 equidistant angles from 0° to 360° . The two red dots represent the two experimental localizations as estimated in section 6.

	Localization error		
	No error	MUSIC error	50 pts with 6mm error
Shape error Object 4	8.7%	10.3%	13.7% (mean)
Shape error Object 7	17.9%	18.7%	35.1% (mean)

Table 6.2: Shape errors examples with different localization errors for a conductive (object 4, -30° , 60mm) and an insulating ellipsoid (object 7, 90° , 60mm).

For the angle estimation, the four trends described above are in agreement with the fact that the angle is particularly difficult to estimate. That is why we propose in the next section another strategy for the angle estimation based on an additional controlled movement of the sensor. Then, the shape parameters η and \mathcal{V} are estimated using the algorithm described above.

6.3.2 Improved shape estimation strategy

As observed on the experimental results, the angle estimation is fragile when it is estimated along with the geometry parameters η and \mathcal{V} . In this last section of this chapter, we propose an improved strategy which consists in decoupling the angle and shape estimations.

The principle consists in a self alignment of the sensor with one of the symmetry axis of the ellipsoidal object. The idea of such an alignment was presented in [9], implemented as discrete sequence of successive displacements. Here, we propose to achieve the alignment using a continuous reactive law, of the same kind as those presented in chapter 4. Specifically, it is possible to apply the following feedback control law

$$\begin{cases} V_{\parallel} = k_1 \cdot \delta I_{ax,3} \\ V_{\perp} = k_2 \cdot I_{lat,4} \\ \Omega = k_3 \cdot I_{lat,3} \end{cases} \quad (6.34)$$

with the set of gains $k_{i=1,2,3}$ able to steer the sensor in a stable pose aligned with the minor axis of the ellipsoid. This control law was implemented in simulation with the gains $k_1 = 1$, $k_2 = 10$

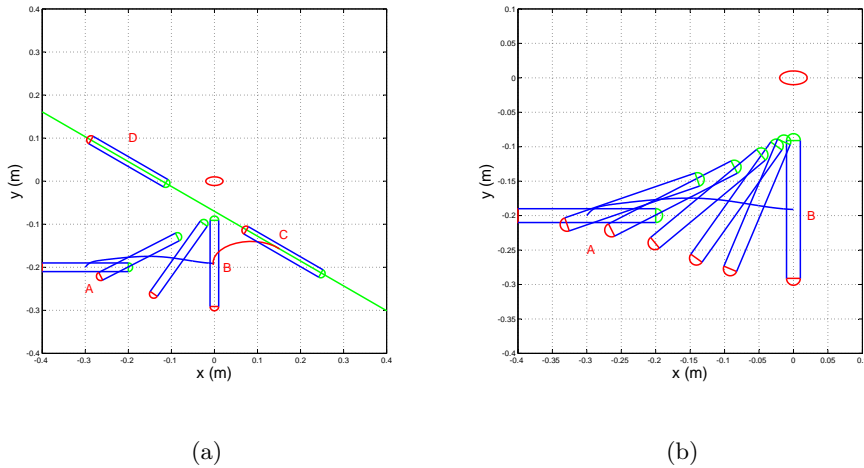


Figure 6.14: The improved strategy for the shape estimation. (a) Simulated motion of the probe. The lines (AB), (BC) and (CD) represent the path of the sensor's center. The probe starts from a pose A and thanks to the control law (6.34), it is steered to the pose B, in which its main axis is aligned with the minor axis of the ellipsoid. From point B, the sensor is moved in open loop in order to reach the first point of the fly-by test denoted C. (b) Zoom on the first phase, between A and B.

and $k_3 = 100$, and the induced sensor's trajectory is shown in figures 6.14a and 6.14b, from label A to label B. At this point (sensor in position B), the angle θ_o^c is known and equals to 90° . Recall that the center of the object is also known, thanks to the localization algorithm proposed in the previous chapter. It is then easy to move the sensor with an open loop control in order to perform a fly-by test, with a convenient lateral distance (chosen in the range [60mm; 100mm]) according to the trend 2) and with a desired angle θ_o^c .

The trajectory of the sensor from B to the first position of the fly-by test, denoted C, is represented in figure 6.14a. Then, the straight line trajectory of the sensor during the fly-by test is represented with the line (CD). Finally, the shape estimation algorithm is applied, with the currents measured during that fly-by test as input.

Because the angle θ_o^c is known, a new matrix Ψ in (6.9) is defined, taking into account the angle. It becomes a $6N \times 2$ matrix because there are only two parameters to estimate: p_{11} and p_{22} , the components of the tensor expressed in the object's basis, denoted P_{11} in chapter 3. As an example, this new shape estimation was applied to the objects 4 to 7, rotated with an angle $\theta_o^c = -30^\circ$, and for the seven lateral distances $y_o^c \in \{50, 60, 70, 80, 90, 100, 110\}$ mm. For each

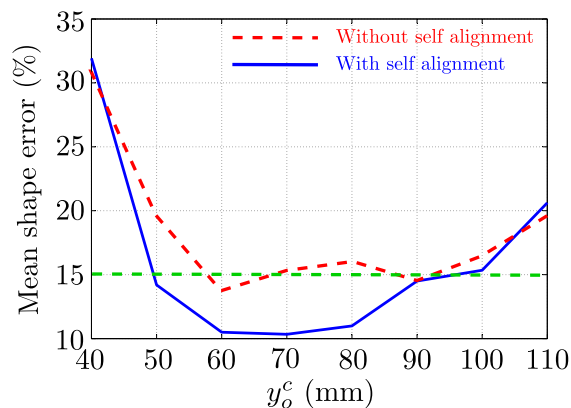


Figure 6.15: The shape error as a function of the lateral distance for $\theta_o^c = -30^\circ$.

lateral distance, the mean of the shape errors was calculated and they are represented in figure 6.15. This curve explicitly shows a favorable lateral distance, between 60mm and 80mm. The lowest shape error is obtained for $y_o^c = 70$, and it is equal to 10.3%. This has to be compared with the mean shape error obtained without this alignment procedure, which is around 15% according to the tables in 6.9. Also, we observe that in a lateral distance range [50 ; 90]mm, the object's shape is estimated with an error below 15% on average. These results are particularly encouraging for a shape estimation improvement.

Nevertheless, the angle estimation performed using this strategy was only tested in simulation until now. It should be tested in experimental conditions, in order to validate its feasibility and also to evaluate the angle error that it would provide.

Chapter 7

Conclusion

In this thesis, we proposed new methods for an ellipsoidal object's inspection, localization and shape estimation using a sensor inspired by the weakly electric fish. We showed their relevance in both simulation and experimental conditions.

In chapter 4, we showed that an ellipsoidal object could be detected, its material discriminated as well as its left/right position with respect to the sensor's axis. Then, three reactive control laws could be implemented for the sensor to reach the object and rotate around it by following its boundaries, taking benefit from the axis-symmetry of the sensor. Moreover, the proposed algorithm was tested with other objects, such as insulating cube and walls, showing its versatility.

In order to localize the object, we proposed to use the MUSIC algorithm in chapter 5. With the choice of larger objects than the hypothesis of the analytical model allows, we showed the difficulty to get an accurate result. We clearly identified that the non uniformity of the electric field to which the object is submitted causes these large imprecisions. But, using movements of the sensor and four implementations of the algorithm we were able to get a reasonable localization error, below 3mm.

The shape and the orientation were finally estimated using a least squares algorithm and the inversion of the analytical model of an ellipsoidal object's polarization tensor (presented in chapter 6). Thanks to the plentiful experiments we performed, we could extract some trends about the algorithm's behavior. Especially, we highlighted a favorable range in term of lateral distance in which the shape estimation is the best: [60 ; 100]mm. Below 60mm, the analytical model is not accurate enough to provide good estimations. Above 100mm, the lack of accuracy comes from the weakness of the electrical object's response with respect to the noise level. If the lateral distance of the object is in this range, we showed that the mean shape estimation and the mean angle estimation are 15.1% and 23.6° respectively. Also, the difficulty to obtain an accurate angle estimation with this method was emphasized, especially for the objects with aspect ratio equal to 1.5, which are close a sphere. A improvement strategy was proposed, which consists in an alignment of the sensor axis with the minor axis of the ellipsoid using reactive control laws. While some more experiments need to be performed to validate this strategy in experimental conditions, it would make the mean shape error to decrease to 10.3%.

These results are encouraging for the artificial electric sense research. The drawbacks of the proposed methods were highlighted and, finally, they represent a good starting point for future works. So, let us now propose some areas of research based on the results we obtained.

Perhaps, the main difficulty of this work was to deal with the gap between the analytical model's currents and the measured currents. Because it is difficult to respect the requirements of the model in actual conditions (ie. the smallness of the object), this gap can be quite large, and the final results suffer from that. One of the first ideas that come to mind is to take into account the quadrupole contribution of the object's response (3.89) in the analytical model, which was not considered until now.

For the localization with MUSIC, this new contribution would lead to the definition of new steering vectors, associated with this quadrupole contribution. So, we suggest for future work to analytically calculate these new steering vectors and define a new imaging function that takes them into account.

For the shape estimation, because we do not have any explicit expression of the quadrupole moment, we would not be able to directly use the tensor P_{22} as we did with P_{11} . But, the principle of the least squares algorithm could be preserved, this time estimating the components of both P_{11} and P_{22} . This would provide a better estimate for the components of P_{11} . Then, the second phase of the algorithm, which consists in estimating the parameters η , \mathcal{V} and θ_o^c , would not be modified. Hence, the better estimation of P_{11} would provide better accuracy in the geometrical parameters estimation.

Instead of making shape estimation as we proposed in this thesis another paradigm would be performing shape recognition, by the use of a dictionary, putting in touch a given object's shape and a given polarization tensor. This strategy significantly differs from that it is proposed in this thesis because the shape is not *estimated* but rather *identified*. This was already implemented in the field of applied maths [4, 3, 11, 46]. The dictionary would be created beforehand using the BEM and/or actual measurements, and saved into the robot's memory. Then, the least squares method could be used for tensor's components estimation, and finally the shape would be identified by reading in this dictionary.

Last but not least, we now propose another improvement that could get the system toward a more autonomous behavior. Although the algorithms were presented sequentially (see figure 1.28) and could easily be automatically implemented one after the other in this order, this was not tested yet. We provided in this thesis all the ingredients to perform such a set up, and now it would be very interesting to implement it in actual conditions. The articulations between these ingredients are still lacking. Even more, the three phases (object's inspection, localization and shape estimation) could be merged. The localization and the shape estimation could be performed during the object's inspection phase. Indeed, if the measurement of the matrix δC would be continuously performed during its trajectory around the object, the principle of the four localizations presented at the end of chapter 5 would be applicable, even with more than four points. Also, with a recording of the currents during that trajectory, the least squares algorithm would be performed, and then, the shape and the angle estimated. The object would be localized and its shape estimated by automatically rotating around it.

Appendix A

Dielectric properties of materials

As shown in the chapters 2 and 3, the dielectric characteristics of the materials involved in the scene are the permittivity ϵ and the conductivity γ (or, equivalently, the resistivity $\rho = 1/\gamma$). The typical values of these quantities for different materials are needed. But, in the literature, the dielectric properties of the materials can be expressed as other physical quantities, such as the dielectric constant denoted ϵ' and the loss factor denoted ϵ'' . Here, some definitions of these quantities are recalled and the relationships between them are given, so that the needed permittivity and the conductivity can be computed. All the definitions and notations are taken from [77], and some typical values for common materials are given in table A.1.

The permittivity represents the linear relationship between electric field \mathbf{E} and electric flux \mathbf{D}

$$\mathbf{D} = \epsilon \mathbf{E}. \quad (\text{A.1})$$

Usually, ϵ is expressed as a function of the permittivity of vacuum, denoted ϵ_0

$$\epsilon = \epsilon_r \epsilon_0 \quad (\text{A.2})$$

where ϵ_r is the relative permittivity of the material and $\epsilon_0 \simeq \frac{1}{36\pi} 10^{-9}$ F/m is defined as

$$\epsilon_0 = \frac{1}{c^2 \mu_0} \quad (\text{A.3})$$

with $c \simeq 3.10^8$ m/s the speed of light and $\mu_0 = 4\pi 10^{-7}$ H/m the magnetic permeability of the vacuum. The relative permittivity ϵ_r is a complex quantity

$$\epsilon_r = \epsilon' - i\epsilon'' \quad (\text{A.4})$$

where

ϵ' is the dielectric constant,

ϵ'' is the loss factor,

and i is the complex unit. In the vacuum, $\epsilon' = 1$ and $\epsilon'' = 0$. The ratio ϵ''/ϵ' is called the dielectric loss tangent, denoted $\tan(\delta)$

$$\tan(\delta) = \epsilon''/\epsilon'. \quad (\text{A.5})$$

The loss factor can be expressed as a function of the conductivity γ (S/m) and the angular frequency $\omega = 2\pi f$

$$\epsilon'' = \frac{\gamma}{\omega\epsilon_0}. \quad (\text{A.6})$$

The resistivity ρ ($\Omega\cdot\text{m}$) of a material is defined as the inverse of the conductivity

$$\rho = \frac{1}{\gamma}. \quad (\text{A.7})$$

In the literature, one can find some dielectric properties for different materials [40, 27, 32, 45, 10]. The dielectric constant and the loss factor (or the loss tangent) are given for waters, dielectrics and organic materials, so the conductivity and the resistivity can be deduced with the relationships (A.5), (A.6) and (A.7). The conductors, for which the loss factor is close to zero, are defined with their conductivities, whereas their relative permittivity is set to 1.

	Relative permittivity ϵ'	Relative loss factor ϵ''	Loss tangent $\tan(\delta)$	Measurement frequency f (Hz)	Conductivity γ (S/m)	Resistivity ρ ($\Omega\cdot\text{m}$)	Source
WATERS							
Distilled	80.1	0.03		27.10 ⁶	7.2.10 ⁻⁶	1.4.10 ⁵	[40]
Fresh	79.6	18.9		27.10 ⁶	4.5.10 ⁻³	2.2.10 ²	[40]
Sea	29.1	34.1		23.8.10 ⁹	7.2	0.14	[27]
METALS & ALLOYS							
Iron	1				1.10 ⁷	9.7.10 ⁻⁸	[32]
Stainless steel 304	1				1.39.10 ⁶	7.2.10 ⁻⁷	[32]
Aluminum alloy 360	1				1.33.10 ⁷	7.5.10 ⁻⁸	[32]
Copper	1				5.88.10 ⁷	1.7.10 ⁻⁸	[32]
Nickel	1				1.10 ⁷	1.10 ⁻⁷	[32]
Zinc	1				1.67.10 ⁷	6.10 ⁻⁸	[32]
DIELECTRICS							
Porcelain	5.5	4.4.10 ⁻²	8.10 ⁻³	10 ⁶	3.9.10 ⁻⁷	2.57.10 ⁶	[45]
Polyethylene	2.3	6.9.10 ⁻⁴	3.10 ⁻⁴	10 ⁶	6.1.10 ⁻⁹	1.64.10 ⁸	[45]
Teflon	2.1	4.2.10 ⁻⁴	2.10 ⁻⁴	3.10 ⁶	1.1.10 ⁻⁸	9.10 ⁷	[45]
Polyvinyl chloride (PVC)	4	2.4.10 ⁻¹	6.10 ⁻²	10.10 ⁶	2.1.10 ⁻⁵	4.7.10 ⁴	[45]
Glass	5.3	2.1.10 ⁻²	4.10 ⁻³	10 ⁶	1.87.10 ⁻⁷	5.3.10 ⁶	[45]
ORGANIC MATERIALS							
Apple flesh	64.3	80.8		27.10 ⁶	1.93.10 ⁻²	5.18.10 ¹	[40]
Cherry flesh	88.1	234.9		27.10 ⁶	5.61.10 ⁻²	1.78.10 ¹	[40]
Codling moth slurry	125.3	458.4		27.10 ⁶	1.09.10 ⁻¹	9.14	[40]
Raw beef	47.7	13.4		2.8.10 ⁹	3.32.10 ⁻¹	3.01	[10]
Raw porc	53.2	15.7		2.8.10 ⁹	3.89.10 ⁻¹	2.57	[10]
Mashed potatoes	64.6	21.7		2.8.10 ⁹	5.37.10 ⁻¹	1.86	[10]
Wood (walnut, dry)	2	0.07	0.035	10.10 ⁶	6.19.10 ⁻⁶	1.62.10 ⁵	[45]

Table A.1: The dielectric characteristics for different materials.

Bibliography

- [1] ALCOGER, A., OLIVEIRA, P., AND PASCOAL, A. Study and implementation of an ekf gib-based underwater positioning system. *Control Engineering Practice* 15, 6 (2007), 689 – 701. Cited on page [12](#).
- [2] AMMARI, H., BOULIER, T., AND GARNIER, J. Modeling active electrolocation in weakly electric fish. *SIAM Journal on Imaging Sciences* 6, 1 (2013), 285–321. Cited on pages [8](#), [65](#), [96](#), and [114](#).
- [3] AMMARI, H., BOULIER, T., GARNIER, J., JING, W., KANG, H., AND WANG, H. Target identification using dictionary matching of generalized polarization tensors. *Foundations of Computational Mathematics* 14, 1 (2014), 27–62. Cited on pages [10](#) and [135](#).
- [4] AMMARI, H., BOULIER, T., GARNIER, J., AND WANG, H. Shape recognition and classification in electro-sensing. *Proceedings of the National Academy of Sciences of the United States of America* 111, 32 (2014), 11652–11657. Cited on pages [10](#) and [135](#).
- [5] AMMARI, H., AND KANG, H. *Polarization and moment tensors, with applications to inverse problems and effective medium theory*. Springer-Verlag New York, 2007. Cited on pages [6](#), [66](#), [72](#), and [73](#).
- [6] ASSAD, C., RASNOW, B., AND STODDARD, P. Electric organ discharges and electric images during electrolocation. *Journal of Experimental Biology* 202, 10 (1999), 1185–1193. Cited on pages [4](#), [20](#), and [22](#).
- [7] BAFFET, G., BOYER, F., AND GOSSIAUX, P. B. Biomimetic localization using the electrolocation sense of the electric fish. In *Robotics and Biomimetics, 2008. ROBIO 2008. IEEE International Conference on* (2009), pp. 659–664. Cited on page [32](#).
- [8] BAI, Y., SNYDER, J., SILVERMAN, Y., PESHKIN, M., AND MACIVER, M. Sensing capacitance of underwater objects in bio-inspired electrosense. In *2012 IEEE/RSJ International Conference on Intelligent Robots and Systems (IROS)* (2012), pp. 1467–1472. Cited on pages [5](#), [30](#), [46](#), [47](#), and [48](#).
- [9] BAI, Y., SNYDER, J. B., PESHKIN, M., AND MACIVER, M. A. Finding and identifying simple objects underwater with active electrosense. *The International Journal of Robotics Research* (2015). Cited on pages [5](#), [9](#), [31](#), and [132](#).
- [10] BENGTTSSON, N. E., AND RISMAN, P. O. Dielectric properties of food at 3 ghz as determined by a cavity perturbation technique. *Journal of Microwave Power* 6, 2 (1971), 101–106. Cited on pages [A2](#) and [A3](#).

- [11] BOULIER, T. *Modélisation de l'électro-localisation active chez les poissons faiblement électriques*. PhD thesis, Ecole Polytechnique, 2013. Cited on pages 8, 10, 65, 96, 114, and 135.
- [12] BOYER, F., GOSSIAUX, P., JAWAD, B., LEBASTARD, V., AND POREZ, M. Model for a sensor inspired by electric fish. *IEEE Transactions on Robotics* 28, 2 (2012), 492–505. Cited on pages 6, 32, 65, 68, 70, 71, and 129.
- [13] BOYER, F., AND LEBASTARD, V. *Exploration of Objects by an Underwater Robot with Electric Sense*. Springer Berlin Heidelberg, 2012, pp. 50–61. Cited on page 5.
- [14] BOYER, F., LEBASTARD, V., CHEVALLEREAU, C., AND SERVAGENT, N. Underwater reflex navigation in confined environment based on electric sense. *Robotics, IEEE Transactions on* 29, 4 (2013), 945–956. Cited on pages 5, 32, 33, 70, 84, and 85.
- [15] BULLOCK, T. H., HOPKINS, C. D., POPPER, A. N., AND FAY, R. R. *Electroreception*. Springer-Verlag New York, 2005. Cited on pages 4, 12, 18, 21, and 22.
- [16] CAPUTI, A. A. Contributions of electric fish to the understanding sensory processing by reafferent systems. *Journal of Physiology-Paris* 98, 1–3 (2004), 81 – 97. Cited on page 22.
- [17] CASTELLO, M., AGUILERA, P., TRUJILLO-CENOZ, O., AND CAPUTI, A. Electroreception in gymnotus carapo: pre-receptor processing and the distribution of electroreceptor types. *Journal of Experimental Biology* 203, 21 (2000), 3279–3287. Cited on page 22.
- [18] CAZENAVE, F., ZOOK, R., CARROLL, D., FLAGG, M., AND KIM, S. Development of the ROV SCINI and deployment in McMurdo Sound, Antarctica. *Journal of Ocean Technology* 6, 3 (2011), 39–58. Cited on page 14.
- [19] CHETTY, G., AND RUSSELL, A. *Electric Field Based Obstacle Avoidance*. Springer London, London, 1998, pp. 364–368. Cited on pages 5, 12, and 29.
- [20] CHRIST, R., AND WERNLI, R. *The ROV manual, A user guide for remotely operated vehicles, second edition*. Butterworth-Heinemann, 2014. Cited on pages 4, 13, 14, and 15.
- [21] CLAYTON, R. P., AND N., S. A. *Introduction to electromagnetic fields, second edition*. New York: McGraw-Hill, 1987. Cited on page 60.
- [22] CRUZ, N. *Autonomous Underwater Vehicles*. InTech, 2011. Cited on page 12.
- [23] DAMUS, R., DESSET, S., MORASH, J., POLIDORO, V., HOVER, F., CHRYSSTOMIDIS, C., VAGANAY, J., AND WILLCOX, S. *A new paradigm for ship hull inspection using a holonomic hover-capable AUV*. Springer Netherlands, 2006, pp. 195–200. Cited on page 14.
- [24] DEVANEY, A. J. Super-resolution processing of multi-static data using time reversal and music. Preprint, available at <http://www.ece.neu.edu/faculty/devaney/ajd/preprints.htm> (Accessed on June 15, 2017), 2000. Cited on pages 97 and 98.
- [25] DIMBLE, K. D., FADDY, J. M., AND HUMBERT, J. S. Electrolocation-based underwater obstacle avoidance using wide-field integration methods. *Bioinspiration and Biomimetics* 9, 1 (2014). Cited on pages 5 and 30.
- [26] DIMBLE, K. D., RANGANATHAN, B. N., KESHAVAN, J., AND HUMBERT, J. S. Computationally efficient underwater navigational strategy in electrically heterogeneous environments using electrolocation. In *2015 IEEE International Conference on Robotics and Automation (ICRA)* (2015), pp. 1172–1177. Cited on pages 5 and 30.

- [27] ELLISON, W., BALANA, A., DELBOS, G., LAMKAOUCHI, K., EYMARD, L., GUILLOU, C., AND PRIGENT, C. New permittivity measurements of seawater. *Radio Science* 33, 3 (1998), 639–648. Cited on pages A2 and A3.
- [28] ENGELMANN, J., BACELO, J., METZEN, M., PUSCH, R., BOUTON, B., MIGLIARO, A., CAPUTI, A., BUDELLI, R., GRANT, K., AND VON DER EMDE, G. Electric imaging through active electrolocation: implication for the analysis of complex scenes. *Biological Cybernetics* 98, 6 (2008), 519–539. Cited on pages 4, 21, and 22.
- [29] GIRIJA, C., AND RUSSELL, A. *Electric Field Based Sensing for Underwater Vehicle Guidance*. IEEE, Institute of Electrical and Electronics Engineers, United States, 1998, pp. 139 – 140. Cited on page 12.
- [30] HAUS, H. A., AND MELCHER, J. R. *Electromagnetic fields and energy*. Massachusetts Institute of Technology: MIT OpenCourseWare. <http://ocw.mit.edu>. Accessed: 2016-08-29. Cited on pages 6, 60, and 65.
- [31] HAUS, H. A., AND MELCHER, J. R. *Electromagnetic fields and energy*. Prentice Hall, 1989. Cited on pages 6, 60, and 65.
- [32] HAYNES, W. *CRC Handbook of Chemistry and Physics 93rd Ed.* CRC Press/Taylor and Francis, Boca Raton, 2012. Cited on pages A2 and A3.
- [33] HOFMANN, V., GEURTEN, B. R. H., SANGUINETTI-SCHECK, J. I., GÓMEZ-SENA, L., AND ENGELMANN, J. Motor patterns during active electrosensory acquisition. *Frontiers in Behavioral Neuroscience* 8 (2014). Cited on pages 5, 24, and 26.
- [34] HOFMANN, V., SANGUINETTI-SCHECK, J. I., GOMEZ-SENA, L., AND ENGELMANN, J. From static electric images to electric flow: towards dynamic perceptual cues in active electroreception. *Journal of Physiology-Paris* 107, 1–2” (2013), 95 – 106. Cited on pages 5, 23, and 24.
- [35] HOFMANN, V., SANGUINETTI-SCHECK, J. I., KÜNZEL, S., GEURTEN, B., GÓMEZ-SENA, L., AND ENGELMANN, J. Sensory flow shaped by active sensing: sensorimotor strategies in electric fish. *Journal of Experimental Biology* 216, 13 (2013), 2487–2500. Cited on pages 24 and 25.
- [36] HOPKINS, C. Electrical perception and communication. In *Encyclopedia of Neuroscience*, L. R. Squire, Ed. Academic Press, 2009, pp. 813 – 831. Cited on pages 18 and 21.
- [37] HORN, R. A., AND JOHNSON, C. R. *Matrix Analysis*. Cambridge University Press, New York, NY, USA, 1986. Cited on pages 97 and 117.
- [38] HOVER, F. S., EUSTICE, R. M., KIM, A., ENGLT, B., JOHANNSSON, H., KAESS, M., AND LEONARD, J. J. Advanced perception, navigation and planning for autonomous in-water ship hull inspection. *The International Journal of Robotics Research* 31, 12 (2012), 1445–1464. Cited on page 14.
- [39] HYSLOP, A., AND HUMBERT, J. Autonomous navigation in three-dimensional urban environments using wide-field integration of optic flow. *Journal of Guidance Control Dynamics* 33 (2010), 147–159. Cited on page 30.

- [40] IKEDIALA, J., HANSEN, J., TANG, J., DRAKE, S., AND WANG, S. Development of a saline water immersion technique with {RF} energy as a postharvest treatment against codling moth in cherries. *Postharvest Biology and Technology* 24, 2 (2002), 209 – 221. Cited on pages A2 and A3.
- [41] INZARTSEV, A. V. *Underwater vehicles*. In-Tech, 2009. Cited on pages 4, 12, 14, 15, and 16.
- [42] JACKSON, J. D. *Classical Electrodynamics Third Edition*, third ed. Wiley, 1998. Cited on pages 6, 30, 65, and 76.
- [43] JAWAD, B., GOSSIAUX, P. B., BOYER, F., LEBASTARD, V., GOMEZ, F., SERVAGENT, N., BOUVIER, S., GIRIN, A., AND POREZ, M. Sensor model for the navigation of underwater vehicles by the electric sense. In *Robotics and Biomimetics (ROBIO), 2010 IEEE International Conference on* (2010), pp. 879–884. Cited on page 32.
- [44] KANG, H., AND KYOUNGSUN, K. Anisotropic polarization tensors for ellipses and ellipsoids. *Journal of computational mathematics* 25, 2 (2007), 157–168. Cited on pages 6 and 73.
- [45] KAYE&LABY. Tables of physical and chemical constants. http://www.kayelaby.npl.co.uk/general_physics/2_6/2_6_5.html, jan 2017. Cited on pages A2 and A3.
- [46] KHAIRUDDIN, T. K. A., AND LIONHEART, W. R. B. Fitting ellipsoids to objects by the first order polarization tensor. *Malaya Journal of Matematik* 1 (2013), 44–53. Cited on pages 10, 122, and 135.
- [47] KOCAK, D. M., AND CAIMI, F. M. The current art of underwater imaging with a glimpse of the past and vision of the future. *Marine Technology Society Journal* 39, 3 (2005), 5–26. Cited on pages 4 and 15.
- [48] KRAICHMAN, M. B. *Handbook of electromagnetic propagation in conducting media*. University of Michigan Library, 1970. Cited on page 58.
- [49] KRAMER, B. *Electroreception and communication in fishes*. Progress in zoology, 1996. Cited on pages 4, 12, 18, 19, and 21.
- [50] KRIM, H., AND VIBERG, M. Two decades of array signal processing research: the parametric approach. *Signal Processing Magazine, IEEE* 13, 4 (1996), 67–94. Cited on page 30.
- [51] LAKHTAKIA, A., AND MARTÍN-PALMA, R. J. *Engineered Biomimicry*. Elsevier, 2013. Cited on page 16.
- [52] LANE, D. M., MAURELLI, F., KORMUSHEV, P., CARRERAS, M., FOX, M., AND KYRIAKOPOULOS, K. *PANDORA: Persistent Autonomy through Learning, Adaptation, Observation and Re-planning*, vol. 48-2. International Federation of Automatic Control (IFAC), 2012, pp. 238–243. Cited on pages 4, 12, and 14.
- [53] LANNEAU, S., BOYER, F., LEBASTARD, V., AND BAZEILLE, S. Model based estimation of ellipsoidal object using artificial electric sense. *The International Journal of Robotics Research* 36, 9 (2017), 1022–1041. Cited on pages 4, 33, and 117.
- [54] LANNEAU, S., LEBASTARD, V., AND BOYER, F. Object shape recognition using electric sense and ellipsoid’s polarization tensor. In *In Proceedings of the IEEE International Conference on Robotics and Automation (ICRA)* (2016), pp. 4692–4699. Cited on pages 4 and 42.

- [55] LEBASTARD, V., BOYER, F., CHEVALLEREAU, C., AND SERVAGENT, N. Underwater electro-navigation in the dark. In *Robotics and Automation (ICRA), 2012 IEEE International Conference on* (2012), pp. 1155–1160. Cited on page 33.
- [56] LEBASTARD, V., BOYER, F., AND LANNEAU, S. Reactive underwater object inspection based on artificial electric sense. *Bioinspiration & Biomimetics* 11, 4 (2016). Cited on pages 4, 84, and 85.
- [57] LEBASTARD, V., CHEVALLEREAU, C., AMROUCHE, A., JAWAD, B., GIRIN, A., BOYER, F., AND GOSSIAUX, P. B. Underwater robot navigation around a sphere using electro-location sense and kalman filter. In *Intelligent Robots and Systems (IROS), 2010 IEEE/RSJ International Conference on* (2010), pp. 4225–4230. Cited on pages 5 and 32.
- [58] LEBASTARD, V., CHEVALLEREAU, C., GIRIN, A., BOYER, F., AND GOSSIAUX, P. B. Localization of small objects with electric sense based on kalman filter. In *Robotics and Automation (ICRA), 2012 IEEE International Conference on* (2012), pp. 1137–1142. Cited on page 32.
- [59] LEBASTARD, V., CHEVALLEREAU, C., GIRIN, A., SERVAGENT, N., GOSSIAUX, P.-B., AND BOYER, F. Environment reconstruction and navigation with electric sense based on a kalman filter. *The International Journal of Robotics Research* 32, 2 (2013), 172–188. Cited on pages 5, 32, and 122.
- [60] LEWIS, J. E., AND MALER, L. Blurring of the senses: common cues for distance perception in diverse sensory systems. *Neuroscience* 114, 1 (2002), 19 – 22. Cited on page 22.
- [61] LISSMANN, H. W. Continuous electrical signals from the tail of a fish, *Gymnarchus niloticus* cuv. *Nature* 167, 4240 (1951), 201–202. Cited on pages 4, 12, and 17.
- [62] LISSMANN, H. W., AND MACHIN, K. E. The mechanism of object location in *Gymnarchus Niloticus* and similar fish. *Journal of Experimental Biology* 35, 2 (1958), 451–486. Cited on pages 4, 12, and 17.
- [63] LIU, Y. *Fast multipole boundary element method*. Cambridge University Press, New York, NY, USA, 2009. Cited on pages 6, 65, and 66.
- [64] LJUNG, L. *System identification (2nd ed.): theory for the user*. Prentice Hall PTR, 1999. Cited on pages 115, 116, and 125.
- [65] MAALOUF, D., CREUZE, V., AND CHEMORI, A. State feedback control of an underwater vehicle for wall following. In *2012 20th Mediterranean Conference on Control Automation (MED)* (2012), pp. 542–547. Cited on pages 4, 14, and 15.
- [66] MACIVER, M. A., AND NELSON, M. E. Towards a biorobotic electrosensory system. *Autonomous Robots* 11, 3 (2001), 263–266. Cited on pages 5 and 29.
- [67] MARTÍN-PALMA, R., AND LAKHTAKIA, A. Engineered biomimicry for harvesting solar energy: a bird’s eye view. *International Journal of Smart and Nano Materials* 4, 2 (2013), 83–90. Cited on page 16.
- [68] MAURELLI, F., CARRERAS, M., SALVI, J., LANE, D., KYRIAKOPOULOS, K., KARRAS, G., FOX, M., D., L., KORMUSHEV, P., AND CALDWELL, D. The pandora project: A success story in auv autonomy. In *OCEANS 2016 - Shanghai* (2016), pp. 1–8. Cited on pages 4 and 12.

- [69] MIGLIARO, A., CAPUTI, A. A., AND BUDELLI, R. Theoretical analysis of pre-receptor image conditioning in weakly electric fish. *PLoS computational biology* 1, 2 (2005), 123–131. Cited on page 22.
- [70] MOLLER, P. *Electric fishes, history and behavior*. Chapman & Hall, 1995. Cited on pages 4, 7, 12, 17, 18, 19, 21, 28, and 81.
- [71] NELSON, M. E. Electric fish. *Current Biology* 21, 14 (2011), R528–R529. Cited on page 17.
- [72] NEVELN, I. D., BAI, Y., SNYDER, J. B., SOLBERG, J. R., CURET, O. M., LYNCH, K. M., AND MACIVER, M. A. Biomimetic and bio-inspired robotics in electric fish research. *Journal of Experimental Biology* 216, 13 (2013), 2501–2514. Cited on page 16.
- [73] NGUYEN, N. AN WIEGAND, I., AND JONES, D. L. Sparse beamforming for active underwater electrolocation. In *2009 IEEE International Conference on Acoustics, Speech and Signal Processing* (2009), pp. 2033–2036. Cited on pages 5 and 29.
- [74] POLAR ROV. <https://bitbucket.org/polarrov/polarrov/wiki/Home>. Accessed: 2017-03-27. Cited on page 14.
- [75] RASNOW, B. The effects of simple objects on the electric field of *Apteronotus*. *Journal of Comparative Physiology A* 178, 3 (1996), 397–411. Cited on pages 4 and 20.
- [76] RASNOW, B., AND BOWER, J. M. The electric organ discharges of the gymnotiform fishes: I. *apteronotus leptorhynchus*. *Journal of Comparative Physiology A* 178, 3 (1996), 383–396. Cited on pages 4, 19, and 20.
- [77] RISMAN, P. Terminology and notation of microwave power and electromagnetic energy. *Journal of Microwave Power and Electromagnetic Energy* 26, 4 (1991), 243–250. Cited on page A1.
- [78] SCHLUGER, J. H., AND HOPKINS, C. D. Electric fish approach stationary signal sources by following electric current lines. *Journal of Experimental Biology* 130, 1 (1987), 359–367. Cited on pages 7, 25, 81, and 85.
- [79] SCHMIDT, R. Multiple emitter location and signal parameter estimation. *IEEE Transactions on Antennas and Propagation* 34 (1986), 276–280. Cited on page 97.
- [80] SCHWARZ, S., AND VON DER EMDE, G. Distance discrimination during active electrolocation in the weakly electric fish *gnathonemus petersii*. *Journal of Comparative Physiology A* 186, 12 (2001), 1185–1197. Cited on pages 5 and 27.
- [81] SERVAGENT, N., JAWAD, B., BOUVIER, S., BOYER, F., GIRIN, A., GOMEZ, F., LEBASTARD, V., STEFANINI, C., AND GOSSIAUX, P.-B. Electrolocation sensors in conducting water bio-inspired by electric fish. *Sensors Journal, IEEE* 13, 5 (2013), 1865–1882. Cited on pages 31, 44, 45, 46, 49, and 82.
- [82] SMITH, C. U. M. *Biology of Sensory Systems, second edition*. John Wiley & Sons, Ltd, 2008. Cited on page 18.
- [83] SOLBERG, J. R., LYNCH, K. M., AND MACIVER, M. A. Active electrolocation for underwater target localization. *The International Journal of Robotics Research* 27, 5 (2008), 529–548. Cited on pages 5 and 29.

- [84] STANFORD ROBOTICS LAB. Ocean One. <http://cs.stanford.edu/group/manips/ocean-one.html>. Accessed: 2017-03-27. Cited on page 14.
- [85] STODDARD, P. K., AND MARKHAM, M. R. Signal cloaking by electric fish. *Bioscience* 58, 5 (2008), 415–425. Cited on pages 4 and 19.
- [86] STOKEY, R. P., ROUP, A., VON ALT, C., ALLEN, B., FORRESTER, N., AUSTIN, T., GOLDSBOROUGH, R., PURCELL, M., JAFFRE, F., PACKARD, G., AND KUKULYA, A. Development of the remus 600 autonomous underwater vehicle. In *Proceedings of OCEANS 2005 MTS/IEEE* (2005), pp. 1301–1304. Cited on pages 13 and 14.
- [87] STRANG, G., AND BORRE, K. *Linear algebra, geodesy, and GPS*. Wellesley-Cambridge Press, Wellesley, MA, 1997. Cited on pages 97, 98, and 117.
- [88] SZEGÖ, G., AND PÓLYA, G. *Isoperimetric inequalities in mathematical physics*. Annals of mathematics studies 27. Princeton University Press, 1951. Cited on pages 6 and 73.
- [89] TOERRING, M. J., AND BELBENOIT, P. Motor programmes and electroreception in mormyrid fish. *Behavioral Ecology and Sociobiology* 4, 4 (1979), 369–379. Cited on page 26.
- [90] TOERRING, M. J., AND MOLLER, P. Locomotor and electric displays associated with electrolocation during exploratory behavior in mormyrid fish. *Behavioural Brain Research* 12, 3 (1984), 291 – 306. Cited on pages 5 and 26.
- [91] TRICAS, T. C. *The neuroecology of the elasmobranch electrosensory world: why peripheral morphology shapes behavior*. Springer Netherlands, 2001, pp. 77–92. Cited on page 18.
- [92] VAGANAY, J., BELLINGHAM, J., AND LEONARD, J. Comparison of fix computation and filtering for autonomous acoustic navigation. *International Journal of Systems Science* 29 (1998), 1111–1122. Cited on pages 4 and 12.
- [93] VON DER EMDE, G. Active electrolocation of objects in weakly electric fish. *Journal of Experimental Biology* 202, 10 (1999), 1205–1215. Cited on pages 4 and 21.
- [94] VON DER EMDE, G. Distance and shape: perception of the 3-dimensional world by weakly electric fish. *Journal of Physiology-Paris* 98, 1–3 (2004), 67 – 80. Cited on pages 4, 5, 23, and 27.
- [95] VON DER EMDE, G., AMEY, M., ENGELMANN, J., FETZ, S., FOLDE, C., HOLLMANN, M., METZEN, M., AND PUSCH, R. Active electrolocation in gnathonemus petersii: Behaviour, sensory performance, and receptor systems. *Journal of Physiology-Paris* 102, 4–6 (2008), 279 – 290. Cited on pages 5 and 27.
- [96] VON DER EMDE, G., BEHR, K., BOUTON, B., ENGELMANN, J., FETZ, S., AND FOLDE, C. 3-dimensional scene perception during active electrolocation in a weakly electric pulse fish. *Front Behav Neurosci* 4 (2010). Cited on pages 5, 27, and 28.
- [97] VON DER EMDE, G., AND FETZ, S. Distance, shape and more: recognition of object features during active electrolocation in a weakly electric fish. *Journal of Experimental Biology* 210, 17 (2007), 3082–3095. Cited on pages 5, 27, and 28.
- [98] VON DER EMDE, G., SCHWARZ, S., GOMEZ, L., BUDELLI, R., AND GRANT, K. Electric fish measure distance in the dark. *Nature* 395, 6705 (1998), 890–894. Cited on pages 5 and 23.

- [99] WEBB, B. Can robots make good models of biological behaviour? *Behavioral and Brain Sciences* 24, 6 (2001), 1033–1050. Cited on page [16](#).

Thèse de Doctorat

Sylvain LANNEAU

Localisation et estimation basées modèle d'un objet ellipsoïdal avec le sens électrique artificiel

Model based localization and estimation of an ellipsoidal object using artificial electric sense

Résumé

Le but de cette thèse est de contribuer à la perception sous-marine pour des applications de robotique grâce à un champ électrique. Nous proposons de nouvelles méthodes pour l'inspection, la localisation et l'estimation de forme d'un objet ellipsoïdal en utilisant un capteur inspiré des poissons faiblement électriques. Premièrement, nous montrons que l'objet peut être détecté et que son matériau et sa position par rapport à l'axe du capteur peuvent être discriminés en utilisant de simples détections de seuils sur les courants mesurés. Ensuite, nous proposons l'implémentation successive de trois lois de contrôle réactives permettant au capteur de se diriger vers l'objet et d'effectuer une révolution autour de celui-ci en suivant ses frontières. Puis, nous utilisons l'algorithme MUSIC afin de localiser le centre de l'objet. Enfin, les paramètres géométriques de l'objet et son orientation sont estimés grâce à une méthode d'optimisation basée sur les moindres carrés et sur l'inversion du modèle analytique du tenseur de polarisation d'un objet ellipsoïdal. Nous montrons que ces algorithmes fonctionnent en conditions expérimentales. Pour les algorithmes de localisation et d'estimation de forme, des techniques impliquant des déplacements du capteur sont proposées, afin de réduire significativement les imprécisions dues aux écarts entre le modèle et les mesures de courant.

Mots clés

Bio-inspiration, Robotique sous-marine, Sens électrique artificiel, Inspection d'objet, Localisation, Estimation de forme.

Abstract

The aim of this thesis is to contribute to the underwater perception for robotics applications using an electric field. We propose new methods for the inspection, the localization and the shape estimation of an ellipsoidal object using a sensor inspired by the weakly electric fish. Firstly, we show that the object can be detected and its material and position relative to the sensor axis discriminated, using simple threshold detections on the measured currents. Then, we propose the successive implementations of three reactive control laws allowing the sensor to head for the object and revolve around it by following its boundaries. After that, we use the MUSIC algorithm in order to localize the object's center. Finally, the geometrical parameters of the object and its orientation are estimated thanks to an optimization algorithm based on the least squares method and the inversion of the analytical model of the polarization tensor of an ellipsoidal object. We show that these algorithms can be experimentally implemented. For the localization and the shape estimation algorithms, some additional techniques involving sensor movements are proposed in order to significantly reduce the imprecisions due to the gap between the model and the actual currents' measurements.

Key Words

Bio-inspiration, Underwater robotics, Artificial electric sense, Object's inspection, Localization, Shape estimation.